LOW-MOLECULAR WEIGHT MOLECULES AS SELECTIVE CONTACTS FOR PEROVSKITE SOLAR CELLS

Ece Aktaş

UNIVERSITAT ROVIRA i VIRGILI

Low-Molecular Weight Molecules as Selective Contacts for Perovskite Solar Cells

ECE AKTAŞ

DOCTORAL THESIS

2021

UNIVERSITAT ROVIRA I VIRGILI
LOW-MOLECULAR WEIGHT MOLECULES AS SELECTIVE CONTACTS FOR PEROVSKITE SOLAR CELLS
Ece Aktaş

UNIVERSITAT ROVIRA I VIRGILI
LOW-MOLECULAR WEIGHT MOLECULES AS SELECTIVE CONTACTS FOR PEROVSKITE SOLAR CELLS
Ece Aktaş

UNIVERSITAT ROVIRA I VIRGILI
LOW-MOLECULAR WEIGHT MOLECULES AS SELECTIVE CONTACTS FOR PEROVSKITE SOLAR CELLS
Ece Aktaş

Doctoral Thesis

Low-Molecular Weight Molecules as Selective Contacts for Perovskite Solar Cells

Ece Aktaş

Supervised by Prof. Emilio Palomares Gil.

Universitat Rovira i Virgili

Institut Català d'Investigació Química

Tarragona – September 2021

UNIVERSITAT ROVIRA I VIRGILI
LOW-MOLECULAR WEIGHT MOLECULES AS SELECTIVE CONTACTS FOR PEROVSKITE SOLAR CELLS
Ece Aktaş

Prof. Dr. Emilio J. Palomares Gil, group leader at the Institute of Chemical Research of Catalonia (ICIQ) in Tarragona and Research Professor at the Catalan Institution for Advanced Studies (ICREA) in Barcelona

I STATE that the present study, entitled "Low-Molecular Weight Molecules as Selective Contacts for Perovskite Solar Cells", presented by Ece Aktaş to receive the degree of doctor, has been carried out under my supervision at the Department of Chemical Science and Technology of this University (URV) and Institute of Chemical Research of Catalonia (ICIQ), that she fulfills the requirements to obtain the distinction of an international doctor.

Tarragona, July 1st 2021

Prof. Dr. Emilio J. Palomares Gil

Doctoral thesis supervisor

UNIVERSITAT ROVIRA i VIRGILI

ICIQ Institut Català d'Investigació Química

UNIVERSITAT ROVIRA I VIRGILI
LOW-MOLECULAR WEIGHT MOLECULES AS SELECTIVE CONTACTS FOR PEROVSKITE SOLAR CELLS
Ece Aktaş

Acknowledgements

First and foremost, I would like to express my gratitude toward my Ph.D. supervisor Prof. Dr. Emilio Palomares for his tremendous support. Thank you for providing me guidance when I needed and for always being generous and considerate so that I could balance my personal life and my work. I am also grateful for the support of Prof. Dr. Antonio Abate during my short-term research stay.

Thanks to all Palomarians for creating a friendly, enjoyable, and helpful laboratory environment. Thanks to Werther, Dr. Jesus, Dr. Cristina, Dr. Sofia, Dr. Ilario, Dr. Maria, Dr. Georgiana, Dr. Rajesh, Dr. Eugenia, Dr. Tsung Yu, Dr. Lijun, Dr. Jose, Sarika, Dora, Eyüp, Bea, Dr. Carlos, and Pollito (Joan Marc), for having coffee breaks (even I could not join all of them), the great collaborations and for the friendships. Of course, huge thanks to Santi for being there always for me and his endless support! Likewise, thanks to Sorania, Beatriz, Aurora, and Eva for their kind help! I am grateful to be one Palomarian!

On my journey, I cannot thank enough Dr. Nga Phung for the scientific adventures and her endless support with patience. I also want to thank to Dr. Jorge Pascual Mielgo for joining our coffee breaks and bringing all the time his favourite chocolate. The words are not enough to describe their contribution to last year Ph.D. and even so on.

Thanks to the Abate group, Marion A. Flatken, Dr. Silver Hamil Turren Cruz, Hans Köbler, Laura Canil, Guixiang, and Dr. Meng Li for having

kindly laboratory environment, making even strange coronavirus time so and Friday dinners.

I would like to thank to my chosen family (Friends), Dr. Naime, Hande, Özge, Çağla, Duygu, Dr. Şevki, Dr. Doğukan, and Doğuşcan who have supported me since my master. Thanks to Deniz, Dr. Zeynep, Nihal, and their lovely family for making Tarragona feel like home! Thanks to Pau, Caro, Dr. Nataliia, Dr. Paulina, Dr. Federico, Dr. Marta, Dr. Franzi, Dr. Justine, Ivo for listening to me when I was feeling down and sharing all the nice memories with me in Tarragona. Also, thanks for the yoga sessions we had together during covid times.

Thanks to Sema, Büşra, Burçin, Mazi, and Nurgül for sending me online hugs and supports from Turkey whole the time. Thanks to Deniz, Merve, and Rıfkı for the emotional support and motivation talks!

Last but not least, I am really thankful for having support from my family for making my dreams come true.

"Becoming is better than being."

Carol S. Dweck

Dedicated;

To my beloved parents and brothers,

To Demir Mert and Aybars

Abstract

Photovoltaic technology is one of the most promising clean, renewable energy sources to reduce the environmental impacts of fossil fuels over the last decades. In this context, perovskites are a recently developed new photovoltaic material, which have drawn important attention due to their ability to achieve very high efficiencies. However, the large-scale industrial application of perovskite solar cells stays in the background of silicon-based solar cells, because of their dramatically shorter lifetime under operating conditions. The charge selective layers play a crucial role in the rapid rise in device performance and stability of perovskite solar cells. Recently, the application of self-assembled monolayers as charge selective layers in perovskite solar cells has gained tremendous attention, owing to advantages like cost-effectiveness, stability, and the absence of additives.

The aim of this thesis is to design and synthesise novel molecules able to form self-assembled monolayers that act as hole selective materials in perovskite solar cells for achieving high power conversion efficiency and exceptionally durable operational lifetime. To determine the real working conditions of complete devices, custom-built high throughput ageing setup is used. This ageing setup estimates the energy output of a solar cell in operation by obtaining the accurate efficiency value from the maximum power point.

Moreover, charge selective layers are responsible for the transport of photogenerated charges out of the solar cell and are in intimate contact

with the perovskite absorber. For that reason, the carrier recombination order in the newly synthesized Lewis base-made interlayer and in the self-assembled monolayer are investigated in functional devices, using advanced characterisation techniques, such as photo-induced charge extraction, photo-induced transient photovoltage, photo-induced transient photocurrent, and differential capacitance.

Resumen

La tecnología fotovoltaica es una de las fuentes de energía limpia y renovable más prometedoras para reducir el impacto ambiental de los combustibles fósiles en las últimas décadas. En este contexto, las perovskitas son un material cuya aplicación en dispositivos fotovoltaicos ha atraído recientemente una atención importante debido a su capacidad para lograr eficiencias muy elevadas. Sin embargo, la aplicación industrial a gran escala de las celdas solares de perovskita está menos desarrollada con respecto a las celdas solares basadas en silicio, debido a que su vida útil es más corta en condiciones operativas. Las capas de carga selectiva juegan un papel crucial en el rápido aumento del rendimiento del dispositivo y la estabilidad de las celdas solares de perovskita. Recientemente, la aplicación de moléculas capaces de formar monocapas autoensambladas que funcionan como capas selectivas de carga en celdas solares de perovskita han demostrado su potencial debido a las ventajas que proporcionan como la rentabilidad, la estabilidad y la ausencia de aditivos.

El objetivo de esta tesis es el diseño y síntesis de moléculas novedosas capaces de formar monocapas autoensambladas que funcionen como capas selectivas de huecos en celdas solares de perovskita para lograr una alta eficiencia de conversión de energía y una vida útil excepcionalmente larga. Para determinar las condiciones de trabajo reales de los dispositivos, se ha utilizado una configuración de medida del tiempo de vida de alto rendimiento hecha a medida. Esta configuración estima la

producción de energía de una celda solar en funcionamiento al obtener el valor de eficiencia preciso en el punto de máxima potencia.

Además, las capas selectivas de carga son responsables de transportar fuera de la celda solar las cargas fotogeneradas, y están en íntimo contacto con la capa de perovskita. Por esta razón, se ha investigado el orden de recombinación en la capa intermedia formada por una base de Lewis y en la monocapa autoensamblada en un dispositivo funcional, utilizando técnicas de caracterización avanzadas, como extracción de carga fotoinducida, fotovoltaje transitorio fotoinducido, fotocorriente transitoria fotoinducida y capacitancia diferencial.

Resum

La tecnologia fotovoltaica és una de les fonts d'energia neta i renovable més prometedores per reduir l'impacte ambiental dels combustibles fòssils en les últimes dècades. En aquest context, les perovskites són un material que ha atret recentment una atenció important a causa de la seva capacitat per aconseguir eficiències de conversió molt elevades. No obstant, l'aplicació industrial a gran escala de les cel·les solars de perovskita està menys desenvolupada respecte a les cel·les solars basades en silici, per la seva vida útil extremadament més curta en condicions funcionals. Les capes de càrrega selectiva juguen un paper crucial en el ràpid augment del rendiment del dispositiu i en l'estabilitat de les cel·les solars de perovskita. Recentment, l'aplicació de monocapes auto-assemblades formades per molècules orgàniques que funcionen com a capes selectives de càrrega en cel·les solars de perovskita ha atret una gran atenció a causa d'avantatges com la rendibilitat, l'estabilitat i l'absència d'additius.

L'objectiu d'aquesta tesi és el disseny i la síntesi de noves molècules que formen monocapes auto-assemblades que funcionin com a capes selectives de buits en cel·les solars de perovskita per aconseguir una eficiència de conversió alta d'energia i una vida útil excepcionalment llarga. Per determinar les condicions de treball reals dels dispositius, s'utilitza una configuració de mida d'envelliment d'alt rendiment feta a mida. Aquesta configuració estima la producció d'energia d'una cel·la solar en funcionament a l'obtenir el valor d'eficiència precís en el punt de màxima potència.

A més, les capes selectives de càrrega són responsables de transportar fora de la cel·la solar les càrregues fotogeneradas, i estan en íntim contacte amb la capa de perovskita. Per aquesta raó, s'ha investigat l'ordre de recombinació en la capa intermèdia formada per una base de Lewis i en la monocapa auto-assemblada en un dispositiu funcional, utilitzant tècniques de caracterització avançades com extracció de càrrega fotoinduïda, fotovoltaje transitori fotoinduït, fotocorrent transitòria fotoinduïda i capacitància diferencial.

Contributions to Scientific Literature

The following publications are based on the work described in this thesis:

1. **Ece Aktas**, Jesús Jiménez-López, Cristina Rodríguez-Seco, Rajesh Pudi, Manuel A. Ortuño, Núria López, and Emilio Palomares; '*Supramolecular Coordination of Pb^{2+} Defects in Hybrid Lead Halide Perovskite Films Using Truxene Derivatives as Lewis Base Interlayers*' *ChemPhysChem* **2019**, 20, 2702-2711. DOI: 10.1002/cphc.201900068
2. **Ece Aktas**, Jesús Jiménez-López, Kobra Azizi, Tomas Torres and Emilio Palomares; *'Self-assembled Zn Phthalocyanine as a robust p-type selective contact in Hybrid Lead Halide Perovskite Solar Cells' Nanoscale Horizons*, **2020**, 5, 1415-1419. DOI: 10.1039/D0NH00443J
3. **Ece Aktas**, Nga Phung, Hans Köbler, Dora A. González, Maria Méndez, Ivona Kafedjiska, Silver Hamill Turren-Cruz, Robert Wenisch, Iver Lauermann, Antonio Abate, and Emilio Palomares; *'Understanding the perovskite/self-assembled selective contact interface for ultra-stable p-i-n and highly efficient perovskite solar cells' Energy & Environmental Science,* ***2021.*** DOI: 10.1039/d0ee03807e

Oral and Poster Presentations at Conferences

- ✓ ***International Conference on Hybrid and Organic Photovoltaics (HOPV-18);*** Poster Presentation *'The Effect of Passivation Layer in Perovskite Solar Cells by 3-Fluoropyridine-Substituted Truxene Derivative Based Small Molecule'* Benidorm, Spain
- ✓ ***ICIQ 3rd PhD Day 2019;*** Poster Presentation *'Supramolecular Coordination of Pb^{2+} Defects in Hybrid Lead Halide Perovskite Films Using Truxene Derivatives as Lewis Base Interlayers'* Tarragona, Spain
- ✓ ***4th Asia-Pacific International Conference on Perovskite, Organic Photovoltaics and Optoelectronics 2020 (IPEROP-20);*** Oral Presentation *'Self-Assembled Hole Transporting Monolayer to Improve PiN Type Perovskite Solar Cell Performance'* Tsukuba, Japan
- ✓ ***13th International Hybrid and Organic Photovoltaics 2021 (HOPV-21);*** ePoster (Online) *'The Role of Terminal Group Position in Triphenylamine Based Self-Assembled Hole-Selective Monolayers in Perovskite Solar Cells' World*
- ✓ ***Materiales Orgánicos Disruptivos para Energía Fotovoltaica (RED MODE fotovoltaica);*** Oral Presentation (Online) *'Self-Assembled Hole Selective Small Molecules for Highly Efficient and Stable Perovskite Devices' Spain*

List of Acronyms

ASP	aerosol spray pyrolysis
ACN	acetonitrile
AFM	atomic force microscopy
AM	air mass
ASP	aerosol spray pyrolysis
BE	binding energy of the electron
brs	broad singlet coupling constants
CBM	conduction band maximum
CsFAMA	$Cs_{0.1}(MA_{0.15}FA_{0.85})_{0.9}Pb(I_{0.85}Br_{0.15})_3$
CV	cyclic voltammetry
d	doublet coupling constant
DCM	dichloromethane
CF	chloroform
dd	doublet of doublets coupling constant
DiffCap	different capacitance
DSSCs	dye-sensitised solar cells

dt	doublet of triplets coupling constant
E_F	Fermi energy level
ESEM	environmental scanning electron microscopy
EtOAc	ethyl acetate
EQE	external quantum efficiency
FF	fill factor
FTO	fluorine-doped tin oxide
GIXRD	grazing incidence x-ray diffraction
HI	hysteresis index
HOMO	highest occupied molecular orbital
HR-MS	High Resolution Mass Spectra
HSLs	hole selective layers
IPCE	incident-photon-to-current-efficiency
ITO	indium tin oxide
J_{SC}	short-circuit current
J-V	current density-voltage
K_B	Boltzmann constant

LUMO	lowest unoccupied molecular orbital
m	multiplet coupling constant
MALDI	matrix-assisted laser desorption/ionization
MALDI-TOF	matrix-assisted laser desorption/ionization time-of-flight
MPP	maximum power point
MS	mass spectrometry
NMR	nuclear magnetic resonance
PCE	power conversion efficiency
PEDOT:PSS	poly(3,4-ethylenedioxythiophene) polystyrene sulfonate
PI-CE	photo-induced charge extraction
PI-TPC	photo-induced transient photocurrent
PI-TPV	photo-induced transient photovoltage
PMMA	poly(methyl methacrylate)
PSC	perovskite solar cell
PV	photovoltaic
PTAA	poly[bis(4-phenyl)(2,4,6-trimethyl-phenyl)amine

q	elementary charge
Q	charge density
QFLS	quasi-Fermi level splitting
s	singlet coupling constant
SAMs	self-assembled monolayers
SASM	self-assembled small molecule
SCLC	space-charge limited current
SEM	Scanning Electron Microscope
Spiro-OMeTAD	2,2',7,7'-Tetrakis[N,N-di(4-methoxyphenyl)amino]-9,9'-spirobifluorene
SRH	Shockley-Read-Hall recombination
STC	standard test conditions
t	triplet coupling constant
T	temperature
T_c	crystallization temperature
TCSPC	time-correlated single-photon counting
T_{des}	decomposition temperature
T_g	glass transition temperature

TGA	thermogravimetric analysis
THF	tetrahydrofuran
TLC	thin layer chromatography
T_m	melting point temperature
TPA	triphenylamine
TRPL	time resolved photoluminescence
truxene	10,15-dihydro-5*H*-diindeno[1,2-a:1',2'-c]fluorene
UV-vis	ultraviolet and visible radiation
VBM	valence band maximum
V_{OC}	open-circuit voltage
XPS	x-ray photoelectron spectroscopy
XRD	x-ray diffraction

Table of Contents

List of Figures

List of Tables

Chapter 1

Introduction

Introduction

In the last centuries, the depletion of fossil fuel reserves and increasing environmental pollution has urged attention toward alternative, renewable energy sources. Fossil fuels are used as main sources of heat and energy around the World and these burnt fossil fuels increase the amount of carbon dioxide which is a highly potent greenhouse gas.[1,2] Greenhouse gases trap heat in the atmosphere which causes extreme weather events such as drought, flooding, etc.[3] To have a viable World, we should take an action like having durable renewable energy sources and environmentally consumption cycles. Renewable energy will play a vital role in the decarbonisation of our energy systems in the coming decades. For instance, hydropower (15%), wind energy (8%), and solar energy (2%) make up to one-fourth of the year energy production. Solar energy is one of the viable sources, and capable enough to fully cover the electricity demand around the globe. For instance, if all incoming light is absorbed, its total yearly energy consumption is around 150 TWh.[4,5]

First-generation conventional silicon-based photovoltaic (PV) technology is one of the key players in the field for large area static solar harvesting. It has been developed and commercialized for several years because of its advantages such as having a long-term stability. On the other hand, because of its intrinsic properties, Si-based PV has several disadvantages such as a low absorption coefficient due to its indirect bandgap, and high production cost. Silicon-based solar panels need to be made of pure material that causes to have the cost-intensive manufacturing process. Further, because of low absorption, the absorber needs to be in hundreds of micrometres thick, which makes them rigid and unsuitable for flexible solar panels.[6,7]

Introduction

Over the last three decades, many emerging types of PV technologies that are focused on the production of thin and flexible devices have attracted notable attention and are being developed. The advantages of emerging photovoltaic technologies are plentiful and employ inexpensive materials; they can be a solution-processible for low-cost energy production and flexible surfaces in the future, reducing the production costs of large-scale print applications, enabling the global transition to a carbon-free society.

Grätzel and co-workers reported a low-cost solar cell, which is named as dye-sensitised solar cells (DSSCs) and have its place in the thin-film solar cell group in 1991. It is a photoelectrochemical system and based on a light-absorbing organic or organometallic dye as the sensitizer and redox electrolyte.[8] Lately, Yao et al. have also shown a record power conversion efficiency (PCE) of 13% based on dithienopicenocarbazole organic dye.[9] Nonetheless, DSSCs have instability problems like leakage and corrosion issues by reason of the redox electrolyte. These disadvantages are important roadblocks for influencing their commercialization.[10]

In the attempts to increase the PCE of DSSCs, an enormous development in PCE has been reached by switching traditional dyes to organic-inorganic hybrid perovskite material. It was soon realised that the perovskite can be an independent solar absorber similar to the inorganic PV material. Since the first report in 2009, perovskite solar cells (PSCs) have rapidly become the hottest topic in photovoltaics due to their outstanding optoelectronic properties.[11] Fast development of device engineering allowed to prepare solar cells with PCE from 9% to over 25%

within ten years, already exceeding those of commercialized polycrystalline silicon solar cells.[12]

1.1. Perovskite Solar Cells

The term "perovskite" is attributed to the crystal structure of calcium titanate ($CaTiO_3$), discovered in 1839 by the German mineralogist Gustav Rose and named in honour of the Russian mineralogist Lev Perovski. It gives its name to the class of compounds with the same type of crystalline structure represented by the general formula ABX_3. **Figure 1.1** illustrates the perovskite structure, where A can be a small monovalent organic molecule such as methylammonium ($CH_3NH_3^+$, MA) or formamidinium ($NH_2{=}CH_3NH_2^+$, FA) or cations like Rb^+, and Cs^+, B is a divalent cation (Pb^{2+}, Ge^{2+}, and Sn^{2+}) and X stands for halide anion (I^-, Br^-, or Cl^-). As it can be seen in **Figure 1.1**, the A cation is 12-fold coordinated by the X anion in a cuboctahedral arrangement and the B cation is 6-fold coordinated by X in an octahedral configuration. The shown crystalline structure represents the most common orthorhombic structure, where the lattice constants (a, b, c) all have different lengths ($a \neq b \neq c \neq a$). The Goldschmidt tolerance factor (t)[13] has been used to significantly predict the stability of perovskite structure based only on the chemical formula ABX_3, as the following equation:

$$t = \frac{r_A + r_X}{\sqrt{2}(r_B + r_X)} \qquad \text{Equation 1.1}$$

where r_A, r_B and r_X is the ionic radius of the corresponding ions on A,B, and X-sites. A perfect packed structure corresponds to t = 1.0 and only a

tolerance factor in the range $0.8 < t < 1.0$ occurs. They could be distorted due to bending of the BX_6 octahedral and lowering of the symmetry, although in the lower part of this range. If $t > 1$, the A-site cation is larger, preventing it from forming the perovskite, which is photoactive, and if $t<0.8$, the cation is smaller, again frequently causing alternative structures.[14]

The organic–inorganic hybrid halide-based perovskites were commonly studied in the 1990s for the application in transistor technology and light-emitting diodes, due to their outstanding optoelectronic properties and solution processability. This material attracted later important attention for its application in photovoltaic devices owing to its low exciton binding energy, high absorption coefficient, long charge carrier lifetime, diffusion length, and tuneable bandgap. Even though hybrid lead halide perovskites have been known to have a superior charge transporting property for over a decade, Miyasaka and co-workers published the first work with the perovskite as absorbing material in the photovoltaic cell in 2009.[11] Here, they have used two different metal halide perovskite nanocrystals, $CH_3NH_3PbBr_3$ ($MAPbBr_3$) and $CH_3NH_3PbI_3$ ($MAPbI_3$, MAPI), as absorbing materials. Especially, MAPI shows superior optoelectronic properties because it covers nearly all the visible region with a bandgap of 1.54 eV, corresponding to an absorption onset of about 800 nm.[11]

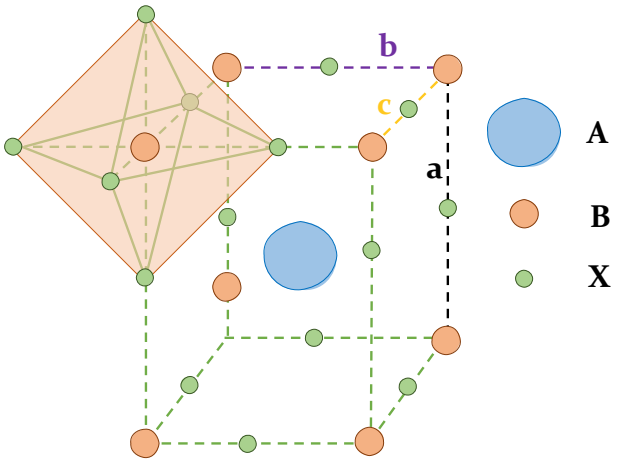

Figure 1.1. *Perovskite lattice representations, following the ABX_3 chemical formula. Note that the shown crystalline structure represents the most general orthorhombic structure.*

Still, despite having remarkable progress on the PSC efficiency, its long-term stability is one of the main roadblocks towards industrialization. First of all, the halide perovskite layer stability enhancement is essential to improve all device's stability. To achieve this goal, more complex multi-cation and mixed-anion composited perovskite absorber layers are investigated. In 2016, Saliba and co-workers achieved great improvement in stability and reproducibility by the incorporation of Cs^+.[15] After that, $Cs_{0.1}(MA_{0.15}FA_{0.85})_{0.9}Pb(I_{0.85}Br_{0.15})_3$ (CsFAMA) composition turned out to be a standard intrinsic semiconductor in perovskite solar cells for achieving high PCE and long-term stability.

1.1.1. Perovskite Device Architectures and Operating Mechanisms

The PSCs have mainly five components: (1) a metal-based cathode or anode, (2) a hole selective layer (HSL), (3) perovskite absorber layer, (4)

an electron selective layer (ESL), and (5) transparent conductive oxide (TCO). The charge selective layers play a crucial role in the photovoltaic performance of the PSC. When an n-type semiconductor is deposited onto the TCO, the device configuration is denoted as a planar or mesoporous n–i–p type (conventional) PSC. In contrast, when a p-type organic semiconductor thin film is deposited onto the TCO, the solar cell configuration is denoted as a planar p–i–n type (inverted) perovskite solar cell. Schematic illustration of the above-mentioned perovskite device architectures is shown in **Figure 1.2**.

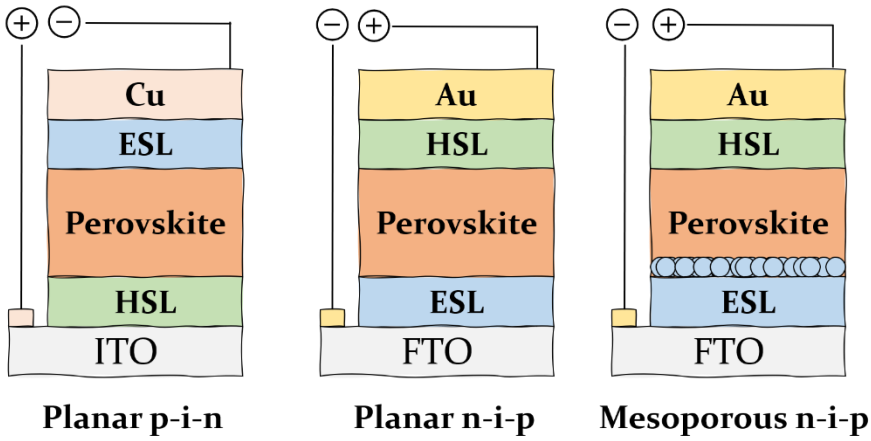

Figure 1.2. *Typical three sandwiched structures of the PSCs. The compact ESL and HSL are used in planar p-i-n and n-i-p structures, the bilayer of compact and mesoporous material consists of the ESL in mesoporous n-i-p device structure, respectively.*

Firstly, the perovskite layer absorbs photons and generates excitons (electron-hole pairs) during exposure to sunlight. These excitons can become free carriers (free electrons and holes) to produce a current. The carrier diffusion distance and lifetime are dependent on the perovskite material's low carrier recombination probabilities. For instance, MAPI

perovskite's carrier diffusion distance is at least 100 nm and longer than 1 μm for $MAPbI_{3-x}Cl_x$.[16,17] The lifetime and long diffusion distance of carriers are the main reason for the excellent performance of the PSC. Subsequently, these free holes and electrons are collected by the HSL and the ESL. The holes are transferred from the perovskite layer to HSL, which is finally collected by the metal electrode. Meanwhile, the electrons are transferred to the ESL and collected by TCO. After all, the photocurrent is generated in the outer circuit by connecting the TCO and the metal electrode in n-i-p architecture perovskite solar cells.

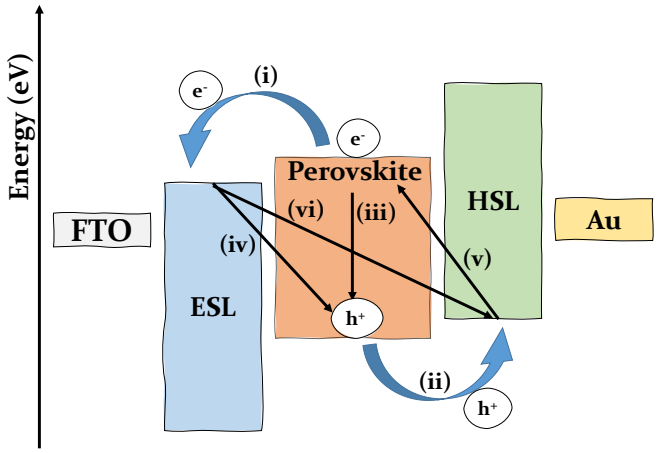

Figure 1.3. *Schematic diagram illustration of energy levels and transport processes of holes and electrons in an n-i-p architecture perovskite solar cell.*

In 2014, Marchioro et al. assumed that the electrons and holes can be extracted at the two heterojunction interfaces of ESL/perovskite and HSL/perovskite, followed by electrons injecting into ESL (process (i)) and holes injecting into HSL (process (ii)) to achieve charge transport.[18] Simultaneously, a series of behaviours that are detrimental to the cell's performance, such as exciton annihilation (process (iii)),

photoluminescence, or non-radiative recombination, as well as reverse transmission of electrons and holes (process (iv) and (v)) and recombination at the ESL/HSL interface (process (vi)) will also occur. All transport processes of electrons and holes in an HSL/perovskite/ESL cell are shown in **Figure 1.3**.

In order to achieve high performance from photovoltaic devices, the extraction of photogenerated charge carriers is all-important, therefore, it is necessary to use charge selective contacts, hole and/or electron transport materials to facilitate moving the carrier to the corresponding electrode. The energy levels alignment of charge selective contacts with the perovskite absorber layer should be considered when deciding the device architecture. For instance, in the case of the HSLs, it is interesting to have a higher lowest unoccupied molecular orbital (LUMO) level that will act as an electron blocking layer while a lower highest occupied molecular orbital (HOMO) level that will effectively extract holes from the perovskite absorber layer in p-i-n configuration PSCs. [19] Even if, the favourable HSL has energy offset between the perovskite valence band maximum (VBM) and HOMO level of the HSL for hole injection, it will introduce a non-radiative recombination component that will alter the final device open-circuit voltage (V_{OC}).[20]

In this section, the recombination of charge carrier types will be explained. Long carrier lifetimes are desirable to obtain highly efficient device performance, for this reason, the charge carrier recombination in perovskite devices has a very important role. The photoexcitation carrier density rules the predominant recombination mechanism. For instance,

while trap-assisted recombination will be dominating at low carrier densities (<10^{15} cm^{-3}), the band-to-band bimolecular recombination will be the dominant recombination mechanism after all the trap states are filled at intermediate carrier densities (10^{15}-10^{17} cm^{-3}). Furthermore, the dominant recombination mechanism will be Auger recombination at even higher carrier densities. All the recombination mechanism types are illustrated in **Figure 1.4**.

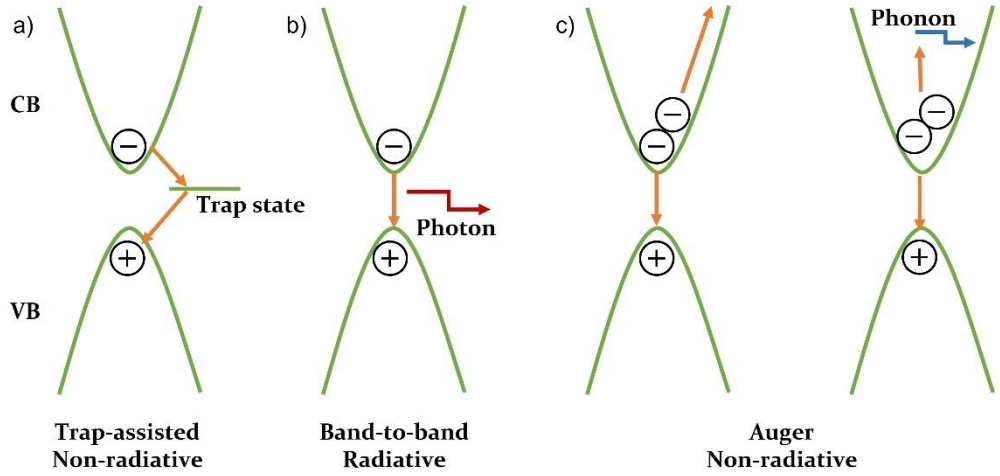

Figure 1.4. *Schematic illustration of recombination mechanism types in PSCs. a) Trap-assisted non-radiative recombination. b) Band-to-band bimolecular radiative recombination. c) Auger recombination.*

Trap-Assisted Non-Radiative Recombination

Trap-assisted recombination occurs when an electron falls into a trap state, which is an energy level within the bandgap. When the electron occupies the trap state, another electron cannot fill this trap, and the occupying electron moves into an empty VB state in a second step, in that way the recombination process is completed.[21] This process can be thought of as a two-stage transition of an electron from the CB to the VB,

or the destruction of the electron and hole that meet each other in the trap. This process is also referred as Shockley-Read-Hall (SRH) recombination.[22,23]

Perovskite solar cells combine their high carrier mobility with long carrier lifetimes and high radiation efficiency. However, full devices suffer from significant trap-assisted recombination losses that limit their V_{OC} to values well below the Shockley-Queisser limit.[24] Solar cells operate in the low carrier density regime where trap-assisted recombination is predominant at 1 Sun conditions. These traps states are caused by point defects of the perovskite lattice or the presence of a foreign atom.

Hence, most of the research groups focused on the passivation of the trap states. The main focus was to reduce trap-assisted recombination at defects in the perovskite bulk or grain boundaries. Indeed, significant improvements have been made through improved perovskite fabrication schemes for increasing particle size, improving crystallinity, and the invention of multiplication and/or multihalide formulations.[25] In addition, their studies confirmed that surface recombination is more important than recombination within crystalline particles and at inner grain boundaries.

Molecular modifiers are one of the most common application to passivate the surface traps. Guo and co-workers managed to decrease the trap densities in both grain interior and at the boundaries by using a bifunctional Lewis base additive, resulting in an enhanced carrier lifetime. In this study, the champion PCE of the MAPI-based device is

enhanced from ~16% to ~18% upon an optimised addition of IT-4F.[26] It is made of carbonyl (C=O), cyano (C≡N) and thiophene groups, which are reported to be excellent passivating agents. Carbonyl and cyano groups (Lewis bases) act as electron-withdrawing end groups that can effectively passivate the trap state at the surface and grain boundaries of perovskite thin films through Lewis acid-base reaction with the under-coordinated Pb^{2+}.[27,28]

Band-to-band bimolecular radiative recombination

Band-to-band radiative recombination occurs when the state changes from an electron CB state to the empty VB state associated with the hole. This band-to-band transition is typically also a direct radiation transition in bandgap semiconductors.[21,29] The radiative recombination is equal to the carrier generation, following the principle of detailed balance.[30] If we consider this situation in terms of perovskite devices, high radiative recombination rates will be expected due to its strong absorption feature.[29,31] Moreover, the charge carrier diffusion lengths were calculated in the micron regime, which is larger than the average thickness of perovskite solar cell devices using a thin layer of around 500-600 nm.[32] Having a higher absorption coefficient is significantly advantageous for photovoltaic devices operating in a low carrier density regime, even if they have high radiative recombination rates.[31]

Auger recombination

Auger recombination is a process where an electron and a hole are recombined in the transition from band-to-band, but now the resulting

energy is given to another electron or hole. The incorporation of a third particle affects the recombination rate, so Auger recombination is different than band-to-band recombination. Most likely, this process is also supported by the phonon through the absorption or emission of phonons.[33,34]

For solar cell application, Auger recombination is of little importance compared to carrier recombination rates, as it only works in high carrier density regimes (> 10^{17} cm^{-3}).

1.1.1.1. Perovskite Absorber

The main component is a metal halide perovskite layer in all possible device configurations for absorbing the photons and producing free carriers. The perovskite layer's fascinating optoelectronic properties, simple manufacturability, and low-cost precursors caused it to get attention in solar cell applications. The bandgap of perovskite materials for the engineering material properties and especially for solar cell applications has recently been realized by changing the material composition. These perovskites can be processed by numerous techniques and have an adjustable bandgap of about 1.2 to 3.0 eV by replacing the aforementioned cations,[35] metals,[36,37] or halides.[38] In the meantime, the wide bandgap makes perovskites desirable for different applications such as laser,[39] light-emitting devices,[40] photodetectors,[41] etc. This also provides a variety of options for photovoltaic applications.

MAPI is the simplest and most studied one lead-based perovskite which can achieve band gaps between 1.55 and 1.62 eV. It is nearly ideal for

single-junction thin-film photovoltaic technology. To use a small amount of Sn in Sn/Pb metal mixtures can be an option to achieve the Schockley-Quessier optimum for single-junction at 1.42 eV. The Schockley-Quessier limit asserts the maximum achievable efficiency is intrinsically limited to 31% due to thermalisation and transmission losses.[42] The tuneable bandgap of the perovskite enables it to be incorporated into tandem devices (with multiple solar cells either in series or in parallel connection). Here, a tandem solar cell design that consists in a plurality of absorber cells stacked horizontally is implemented to absorb a larger portion of the solar spectrum and accordingly provide higher PCEs. For example, PSCs can be the top cell in a perovskite/Si tandem. A recent world record on the monolithic perovskite/Si tandem reached the efficiency of 29.5% PCE.[43]

Recently, the triple cation perovskite layer that consists of Cs^+ cation becomes a standard absorber, having higher PCE and longer stability while comparing with MAPI as mentioned in the previous section. Cs^+ is a large, non-radioactive, and stable monovalent cation. Notably, the CsFAMA layer has a black phase at room temperature without any additional annealing step. In other words, the perovskite crystallization starts with the photoactive black phase. Matsui and co-workers demonstrated unannealed CsFAMA triple cation perovskite cell PCE can reach PCE of 18%.[44]

1.1.1.2. Working Electrodes

Transparent conducting oxide materials are commonly used for developing various transparent devices in optoelectronic systems. Based

on the device architecture of perovskite solar cells, usually used TCO materials are indium-doped tin oxide (ITO) and fluorine-doped tin oxide (FTO). ITO and FTO are n-type degenerate semiconductors with a wide bandgap (≥ 3 eV).[45] These materials are highly transparent in the visible spectrum region, relatively stable under atmospheric conditions, chemically inert, provide low reflection and absorption in the visible region, and provide excellent electrical conductivity when it is coated on glass or plastic substrate.[46] FTO is especially preferred as a TCO in n-i-p architecture PSCs due to its high temperature resistance and affordable price than ITO.[47]

1.1.1.3. Back Metal Contacts

Metal-based contacts are a required layer to complete the photovoltaic device and an internal circuit. The metal contacts are mostly deposited by thermal evaporation and their process details are explained in Chapter 2. Universally, gold or silver are preferred as a back contact metal in n-i-p architecture PSCs due to their high work function and inertness. Nevertheless, gold is an extremely expensive metal when is compared to other alternative metals. Besides, it might interpenetrate through the HSL and interact with perovskite causing degradation in short-term studies.[48] In the section on the stability of perovskite devices, the effect of the metal selection on perovskite device stability will be explained.

1.1.1.4. Buffer Layer in inverted PSCs

Bathocuproine (BCP) has been usually applied as a buffer layer in inverted p-i-n configuration of the PSCs due to the formation of ohmic

contact between the electrode and the ESL and the reduction of interfacial charge recombination (**Figure 1.5**).[49]

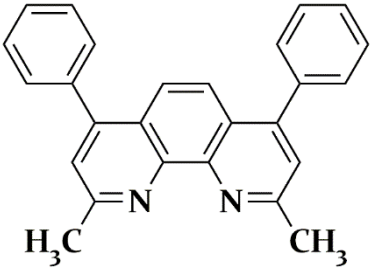

Figure 1.5. *Molecular Structure of BCP.*

Chen and co-workers have demonstrated that the thickness of the BCP buffer layer plays a critical role in charge accumulation, which leads to degradation of the perovskite device performance. Furthermore, they have shown that optimised thin BCP layer (5 nm) between PCBM and silver cathode cause to have smaller series resistance (R_S) owing to the formation of better ohmic contact and larger shunt resistance due to decrease of interfacial recombination.[50]

1.1.1.5. Charge Selective Materials

High-efficiency PSCs are typically designed with an organometal halide perovskite–infiltrated mesostructured as a light absorber and charge carrier, sandwiched between a p-type electron-blocking HSL and an n-type hole-blocking ESL (**Figure 1.2**). Both charge selective materials play a critical role in achieving the highest device performance for PSCs, and only these materials allow an efficient charge separation in the complete photovoltaic devices. These materials assist to (i) tune the work function

of the electrode to promote ohmic contact at the electrode interface and absorber layer; (ii) determine the polarity of the device; (iii) enhance the selectivity toward holes or electrons while blocking the other and minimizing charge carrier recombination at the interfaces; (iv) increase light-harvesting; (v) improve device stability. This section will explain which kind of commercial charge selective material is preferred to achieve highly efficient and stable perovskite devices.

Commercial Electron-Selective Hole-Blocking Materials

The electron-selective materials are mainly responsible for the selective extraction of electrons at the anode contact and block holes from recombination with injected electrons in the n-i-p architecture PSCs. For that reason, an ESL should have lower LUMO than the perovskite layer to satisfy band alignment with the perovskite layer (**Figure 1.3.**). Additionally, it must have high transmittance in the ultraviolet and visible radiation (UV-vis) region, allowing more photons to pass through, and be absorbed easily by the perovskite layer.

The ESL can be mainly categorised into three types: organic, inorganic, and composite ESLs. In a classic conventional perovskite device configuration, compact TiO_2 (c-TiO_2) and mesoporous TiO_2 (m-TiO_2) are the most commonly used inorganic ESLs. It is believed that the metal oxide scaffold provides an effective n-doping in this infiltered layer, resulting in a suitable n-type/intrinsic homogenization within the perovskite layer.[51] The c-TiO_2 blocking layer is usually deposited using a spray-pyrolysis method or spin-coating technique. The m-TiO_2 scaffold layer is always deposited by spin-coater nowadays. Optimum infiltration

of the perovskite layer into the pores of the m-TiO_2 is desirable to achieve a highly efficient perovskite device. In the meantime, the thickness of the ESL is critical for complete perovskite device performance. Kim and co-workers demonstrated that while the thickness of the TiO_2 increases, the fill factor (FF) and the V_{OC} decreases dramatically.[52]

Although being commonly used as ESL, TiO_2 also has some disadvantages that could possibly lead to ohmic losses or non-ideal space charge distribution with PSCs. Pathak and co-workers managed to improve electron conductivity and forthright V_{OC} of the TiO_2 by aluminium doping, reducing the number of sub-bandgap states of TiO_2. Recently, Giordano and co-workers used lithium salt to dope m-TiO_2, and they have demonstrated that the Li-doped TiO_2 electrodes exhibit superior electronic properties due to reducing electronic trap states enabling faster electron transport.[53] The lithium salt is generally used as a chemical dopant in the organic hole selective layer in the conventional structure of PSCs, and it has a positive influence on the hysteresis effect and the photovoltaic performance of the PSCs in a short time due to improved electronic properties.[54] The hysteresis effect is basically described as the difference between the PCE of forward scan (from short circuit current to forward bias, 0 V $\rightarrow$ V_{OC}) and reverse scan (from forward bias to short circuit, V_{OC} $\rightarrow$ 0 V) in current density-voltage (J-V) curves which are reported firstly by Snaith and co-workers in 2014.[55] Detailed information on the hysteresis effect will be given in the following chapter.

Unlike the inorganic ESL, the variety of the organic ESL are fewer in the literature for now. C60, indene-C60 bisadduct (ICBA), and phenyl-C61-butaric acid methyl ester (PCBM) are commonly employed in the inverted configuration as organic ESL. On the contrary to inorganic ESL, the LUMO energy level must be lower than the perovskite layer to satisfy energy alignment. While C60 passivates the grain boundaries and surfaces of the perovskite films, PCBM allows device structure on flexible substrates owing to solubility in a common solvent.[56]

Commercial Hole-Selective Electron-Blocking Materials

An ideal HSL needs to fulfil general requirements to work properly in PSCs, such as (i) good hole mobility (ideally higher than 10^{-3} cm^2/Vs), (ii) well-matched HOMO energy level, (iii) good solubility and film-forming properties, (iv) excellent thermal and photochemical stability.[57] Similar to its counterpart ESL, the HSL can be divided into two types: organic and inorganic HSLs. Most of the widely used electron-selective materials have a conduction band (or an electron affinity) energy around 4 eV. On the other hand, almost all hole-selective materials have an ionization potential, which varies considerably and has an effect on the open-circuit voltage (V_{OC}).[58,59] Additionally, hole selective layers lead to determine the crystal properties of the perovskite absorber layer by changing the wettability of the TCO in p-i-n type PSCs.[60]

In this thesis work, only commercial organic HSL are used as a reference. In a typical PSCs, the most widely used organic hole selective materials are polymers such as PTAA [(poly[bis(4-phenyl)(2,4,6-trimethyl-phenyl)amine],[24] PEDOT:PSS [poly(3,4-

ethylenedioxythiophene):poly(styrenesulfonate)][61] and/or low molecular weight molecules such as Spiro-OMeTAD (2,2',7,7'-Tetrakis[N,N-di(4-methoxyphenyl)amino]-9,9'-spirobifluorene) (**Figure 1.6**).[62] PTAA layer is widely used as a HSL in p-i-n PSCs, owing to its hydrophobic properties which increase perovskite grain size and directly affecting the performance of the perovskite devices.[24] Yet, the PTAA is a polymer-based hole selective material that means controlling its molecular weight will be a challenge. Additionally, it is high-priced, and not stable in ambient conditions.[63] PEDOT:PSS is one of the most common HSL in p-i-n PSCs and optoelectronic devices. Despite its superb optoelectronic properties, the acidity of PEDOT:PSS poses a fundamental threat to the long-term stability of the devices.[61] A huge number of inorganic alternatives to PEDOT:PSS are investigated, like nickel-based or copper-based semiconductors.[64]

To date, Spiro-OMeTAD has been the best molecule so far to make reproducible and highly efficient n-i-p PSCs. The molecular structure consists of two arylamine moieties linked in a 90° angle, with a Spiro central core in order to enhance its glass transition temperature (T_g) to improve its charge transport properties.[65] In addition, the oxidation potential is controlled by the inclusion of methoxy substituents ($-OCH_3$) in diphenylamine moieties. These methoxy substituents initially act as an electron-withdrawing group under an inductive effect but due to the resonance stabilization influence, methoxy substituents present an electron-donating characteristic.[66]

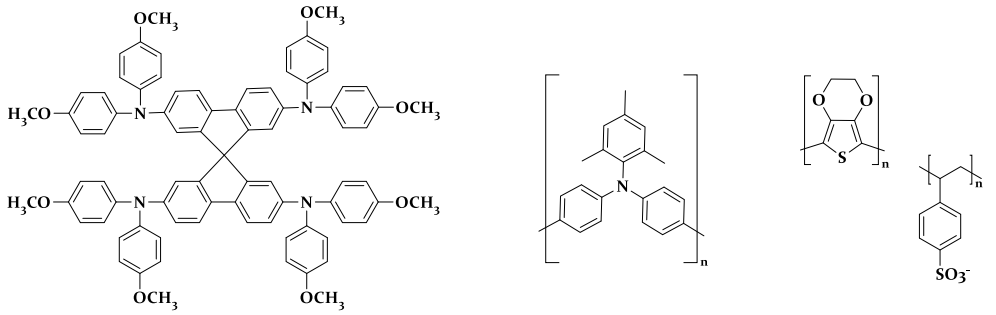

Figure 1.6. *Chemical structures of Spiro-OMeTAD, PTAA, and PEDOT:PSS.*

However, Spiro-OMeTAD has an expensive processing costs due to the complicated synthesis steps and required high purification methods.[67] A huge number of research studies have been done in the molecular design and synthesis route of new charge selective materials, to achieve high efficiency, low-cost fabrication, and long-term stability in the completed devices.

Chemical Doping

Chemical doping is a crucial method to achieve a high device efficiency by increasing the conductivity, controlling the energy levels, and reducing ohmic losses in HSLs and injection barriers at the interface with the electrodes in n-i-p architecture perovskite solar cells.[68,69] The basic principle of chemical doping is that additional mobile charge carriers are produced in organic semiconductors by electron donors or acceptors. There are two different kinds of doping materials used in the literature which are named n-type and p-type dopants. n-type dopant donates electrons to the LUMO of an intrinsic semiconductor and p-type dopant

removes electrons from the HOMO to generate holes of it.[70–72] This means that introducing additional charge carriers, holes, or electrons in an organic semiconductor results in higher conductivity. The basic requirement for an effective doping process is the proper electron affinity of the additive with respect to the energy levels of an organic semiconductor.

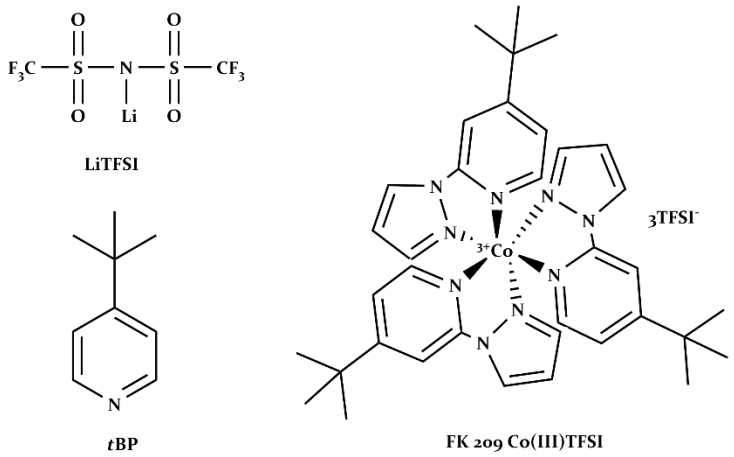

Figure 1.7. *Chemical structures of the LiFTSI, tBP, and FK209 Co(III)TFSI.*

The hole selective layer of PSCs is heavily doped with p-type dopants to provide the electrical conductivity required for commercially available Spiro-OMeTAD and other wide-bandgap HSLs. The most commonly used p-type dopants are 4-*tert*-butylpyridine (*t*BP),[73] Lithium bis(trifluoromethanesulfonyl)imide (LiTFSI),[74] and tris(2-(1*H*-pyrazol-1-yl)-4-*tert*-butylpyridine)cobalt(III) tri[bis (trifluoromethane) sulfonimide] (FK209 Co(III)TFSI)[75] in PSCs (**Figure 1.7**). Nevertheless, the use of dopants in HSLs has a negative effect on the stability of the entire device. The hygroscopic nature of the lithium salts causes to have

highly hydrophilic HSLs, and FK209 Co(III)TFSI shows a tendency towards chemical degradation.[54,76]

1.2. Non-commercial Organic Hole Selective Molecules

In this section, the synthesised organic hole selective materials will be discussed and compared with the most common commercially available hole selective material in terms of the optoelectronic properties and device performances.

1.2.1. Truxene Based Hole Selective Small Molecules

10,15-dihydro-5*H*-diindeno[1,2-a:1',2'-c]fluorene (truxene) is a planar heptacyclic polyarene structure that is obtained by trimerization of indan-1-one (**Figure 1.8**).[77] After its first reported synthesis in 1894, truxene and its derivatives have been utilized in many applications such as lasers,[78] liquid crystals,[79] organic light-emitting diodes,[80] and photovoltaics[81], due to the possibility and diversity of peripheral functionalization. The solubility of the molecule is a key factor in solution-processed PSCs. In 2003, Cao and co-workers synthesized the first hexa-alkylated and highly soluble truxene derivatives which received attention as a star shape core for synthesizing newly charge selective materials in PSCs.[82]

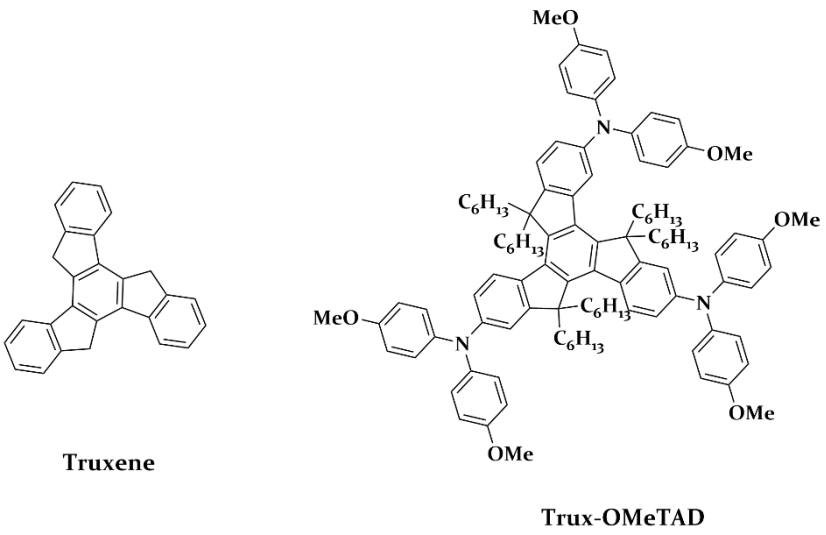

Figure 1.8. *Chemical structure of the truxene core and Trux-OMeTAD.*

After its first reported synthesis with alkyl chain for increasing solubility, Huang and co-workers designed a new truxene derivative with arylamine terminal moiety and hexyl side-chain.[81] They demonstrated that this new truxene based small molecule (Trux-OMeTAD) with planar, rigid, and fully conjugated molecular geometry, showed excellent hole mobility when it is compared with Spiro-OMeTAD in the p-i-n architecture perovskite solar cells (**Figure 1.8**). Trux-OMeTAD has shown the PCEs of around 18% due to its excellent hole mobility and proper surface energy. Moreover, truxene core ensures to show good thermal stability, with the decomposition temperatures (T_{des}) above 400 °C, at the 5% weight loss. The thermal behaviour of the charge selective layer is a crucial factor because of the annealing process of the intrinsic layer in p-i-n type perovskite solar cells. The hole selective layer's decomposition temperature should be higher than 100 °C to get rid of decomposed material under the perovskite layer during the annealing process, if not

it will cause a negative effect on the performance of the completed devices. Furthermore, truxene molecular structure and their molecular shape allow their deposition at the surface of the perovskite in face-to-surface configuration with strong interaction with the perovskite semiconductor surface. A similar approach has been observed for graphene oxide layers.[83]

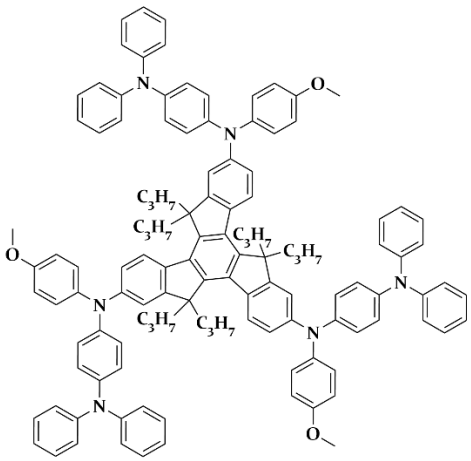

M115

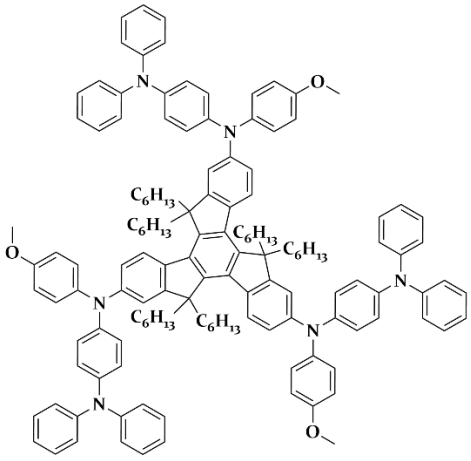

M116

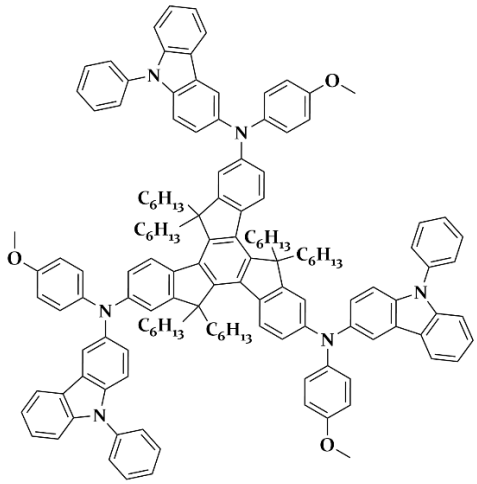

M117

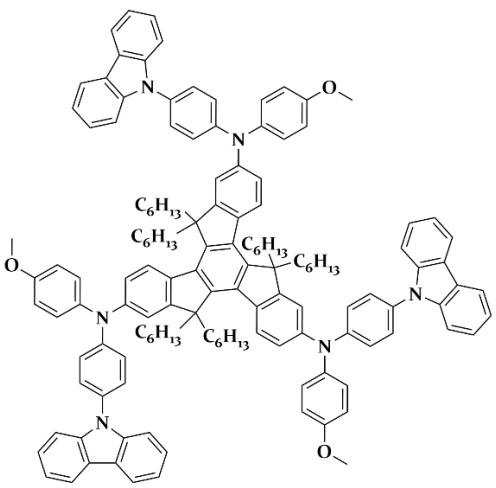

M118

Figure 1.9. *Chemical structures of M115, M116, M117, and M118.*

Wang and co-workers reported the application of four new truxene-based hole transporting materials in p-i-n architecture perovskite solar cells (**Figure 1.9**). These new hole selective materials had a higher photovoltaic performance with a PCE of 17.1% and better stability than PEDOT:PSS-based devices. They tested the devices with different hole selective layers under UV radiation (254 nm), which is one of the major reasons for the decomposition of the perovskite film in ambient air.[84] While the PEDOT:PSS-based device's PCE decreased dramatically, the truxene-based devices exhibited strong stability under UV radiation. The T_{80} (time until the cell reaches 80% of its initial efficiency) of the M118-based cell is 80 min. Compared to truxene-based cells, the PEDOT:PSS-based cell gradually decreases until they reach 80% of initial PCE at around 20 minutes. The p-type semiconductor plays a critical role in protecting the perovskite film from sunlight.[85]

1.2.2. Molecular Engineering of Self-Assembled Hole Selective Molecules

The application of self-assembled monolayers (SAMs) has gained tremendous attention lastly as a charge selective layer in photovoltaic devices, owing to advantages like a low price, stability, and additive-free.[61,86,87] The SAMs application, a smarter way of forming very thin and highly ordered layers, is to apply molecules that bind to a surface in the process of self-assembly due to a certain affinity to the surface of a functional group. The first publication of the preparation of a self-assembled monolayer on top of the metal surface was published by Zisman and co-workers in 1946.[88] SAMs ensure a new perspective to

increase fundamental understanding of self-organisation, structure-property relationships, and interfacial phenomena. Typically, SAMs are formed by three main moieties: an anchoring moiety that ensures the connection of the molecule to the surface via chemical bonding, a spacer moiety that determines the packing geometry, and a terminal moiety that alters the interfacial properties (**Figure 1.10**).[89] Besides, each part of SAMs provides unique properties, and the design of them is quite virtual to align their intended properties. In this section, each part of SAMs will be explained by giving examples from literature to make comprehensible the scope of this thesis.

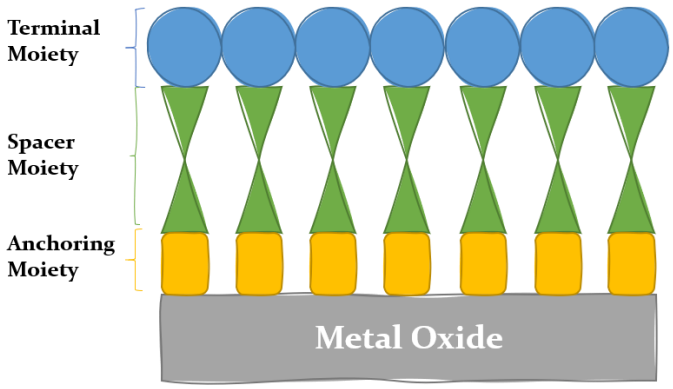

Figure 1.10. *Schematic representation of three main moieties of SAM.*

The Role of the Anchor Moieties in Self-Assembled Monolayers

The anchoring moiety is the part of the SAM that is responsible for its attachment to specific substrate's surface. An ideal molecular anchor moiety is required to provide the following characteristics: reproducible and well-defined binding, long stretching distance and suitable high junction formation probability, and small contact resistance.[90] There are several anchoring groups available that bind to specific substrates, giving

to the users the option to choose the type of electrode and molecule suitable for their purpose. The most widely researched class of SAMs has common anchor moieties such as thiols, silanes, phosphoric acid, and carboxylic acid, and boronic acid, which reacts with metal oxide surface and chemically bonds to this surface. The anchor moiety changes the electronic states and stabilizes the specific surface by chemically binding to the surface atoms. This type of interaction also determines the coverage rate of SAMs across the specific surface. Chemical reactions are usually dominated by reactions of Lewis acidic character, O^{2-} species (Lewis basic), and/or -OH groups at metal oxide surfaces, allowing for multiple reactivity forms. The -OH groups have an amphoteric character and a tendency to react via condensation and/or hydrogen-bonding mechanisms as illustrated in **Figure 1.11a.** However, different anchor moieties have different bonding strengths and contact geometries, which significantly affect the load-bearing properties of the molecular links.

Carboxylic acids are the most commonly used functional group owing to readily accessible and available precursors for attaching molecules to metal oxide surfaces in photovoltaic applications.[91] Yet, carboxylic acids tend to dissociate from the metal oxide surface under certain conditions, including exposure to aqueous and alkaline electrolytes.[92] However, silanes also have major drawbacks: they can be difficult to synthesize and isolate, they are sensitive to moisture, and can easily condense on their own (because of the favourable energy of formation for the Si-O-Si linkage). In addition, they present difficulties in experimental application and decomposition during storage.[93] To find an alternative solution to these troublesome situations, phosphoric acid is one of the

popular acid moieties among others, and it binds highly to the metal oxide surface as it has more -OH moieties than a carboxylic acid. The presence of the -OH group is the key factor in covalent bond formation and three oxygen atoms for covalent binding of the phosphoric acid to metal oxide surface in either monodentate, bidentate, or tridentate modes. Furthermore, the synthesis and purification of phosphoric acids are mostly easy, they can be stored in ambient conditions without undergoing self-condensation reactions unlike silanes.[94] **Figure 1.11b** shows the several types of bonding accepted for carboxylates, phosphonates and siloxyl groups on metal oxide surfaces.

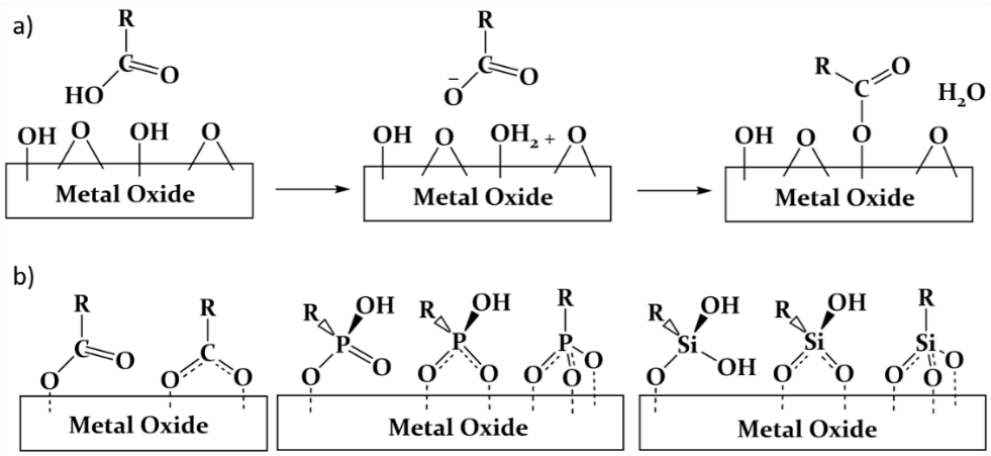

Figure 1.11. *Schematic representation of a) the reaction mechanism between a carboxylic acid binding group and metal oxide b) the different anchor moieties binding modes.*

In 2013, Brennan and co-workers systematically compared porphyrin derivatives with different anchor moieties to investigate their performance in photoelectrochemical cells. They functionalised a tetra-arylphorphyrin dye with silatrane (Zn-TTP-sil), phosphoric acid (Zn-TTP-PO_3H_2), and carboxylic acid (Zn-TTP-COOH) anchor moieties and

used them to attach the sensitizer on metal oxide surfaces in DSSCs (**Figure 1.12**). While all porphyrin derivatives with different anchor groups showed similar photophysical properties, the short-circuit current and the power conversion efficiency of the cell based on carboxylic acid had nearly twice compared to the phosphoric acid and silatrane linkers. They proposed that the carboxylic acid bearing sensitizer covers better the metal oxide surface and increases the light absorption which increases twice times the solar conversion efficiency.[91]

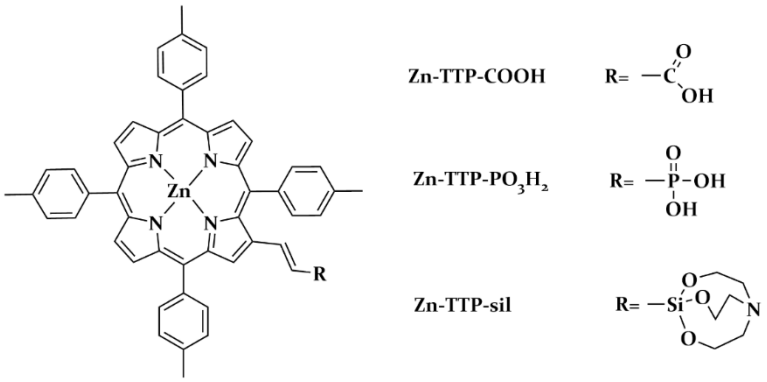

Figure 1.12. *Molecular structure of tetra-arylphorphyrin derivative with different anchor moieties.*[91]

In another study about anchor moieties of SAMs, Tao and co-workers comprehensively compared the conductance of aliphatic molecular wires with anchoring groups (-COOH, -SH, and -NH_2), showing a decrease in the following order: Au-SH > Au-NH_2 > Au-COOH.[95] They also demonstrated that the contact resistance is highly sensitive to the anchor moieties of SAMs, which varies in the order of Au-SH > Au-NH_2 > Au-COOH, however, the decay constant is weakly dependent on the anchor moieties. Moreover, they attributed their observations to the different electronic couplings between the molecules and the electrodes and the

alignment of the molecular energy levels relative to the Fermi energy level of the electrodes introduced by the different anchor moieties. Furthermore, they found that the binding strength information varies in the order of Au-SH > Au-NH_2 > Au-COOH by measuring the average length over which one can stretch each molecular junction until it breaks.[90]

The Role of the Spacer Moieties in Self-Assembled Monolayers

The spacer moiety is the backbone of the SAMs and forms a bridge between the anchor and terminal moieties. The length of the backbone plays a critical role to do electronically isolation from one contact to another. Moreover, spacer moiety affects the final packing of the structure by interacting laterally between molecules during the self-assembly process. The electronic structure of the spacer group controls the attenuation rate of the load transfer. For instance, the attenuation coefficient of the conjugated backbone is significantly lower than that of unconjugated backbones.[96] Furthermore, spacer moiety can be modified to align the energy levels of small molecules that will be used in PSCs as charge selective layers. In 2018, our group firstly demonstrated that triphenylamine-based SAMs can be used as a HSLs instead of PEDOT:PSS in p-i-n configuration PSCs. In this study, two new SAMs showed remarkable PCE due to having good hole extraction properties of triphenylamine (TPA) spacer. The best cell based on TPA showed remarkable PCE (15.9%) with a FF 77%, V_{OC} 1.06 V and J_{SC} of 19.4 mA/cm^2, and the best performing MC-43 based on cell show PCE (17.3%) with a FF of 80%, V_{OC} of 1.07 and J_{SC} of 20.3 mA/cm^2 (**Figure 1.13**).[61]

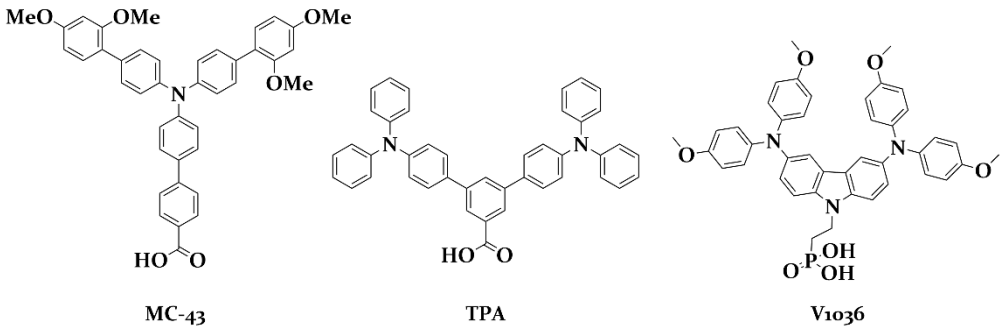

Figure 1.13. *The molecular structures of MC-43, TPA, and V1036.*

Simultaneously, Magomedov and co-workers reported a new molecule as a self-assembled HSL in p-i-n configuration PSCs. Carbazole and diphenylamine are selected as a spacer moieties to improve its hole transporting properties and phosphoric acid moiety is selected to attach the SAM on top of the ITO surface. They also demonstrated that the addition of a small molecule can have a positive impact on the overall performance of SAM based PSCs, reaching a PCE of 17.8% for a V1036-based device (**Figure 1.13**).[87]

On the other hand, the spacer can be also designed with electron transporting units such as fullerene, naphthalimide derivatives to improve the performance of PSCs. Fullerene is an excellent electron transporting unit and passivates the interface of n-type/perovskite layers. Consequently, fullerene boosts the charge extraction and decreases the electrical instability of the device. In the previous work, Wojciechowski and co-workers used fullerene derivatives (C60-SAM) on top of the TiO_2 to reduce the hysteresis of PSCs in 2014 (**Figure 1.13**). They observed slow electron transfer from perovskite to a TiO_2 that is the reason for the anomalous J-V hysteresis (see for details on hysteresis

section 1.1.1.5). The chemisorption of molecules onto the TiO_2 assisted the electron transfer, which made the interface with the perovskite during the photovoltaic process. The fullerene-based n-type SAM improved the PCE up to 17.3% with a considerably reduced hysteresis.[97] In subsequent studies, the fullerene derivatives are modified with -CN group (1 and 2, **Figure 1.14**) to increase their passivation effect on the interface of perovskite and improve the PCE of PSCs.[98]

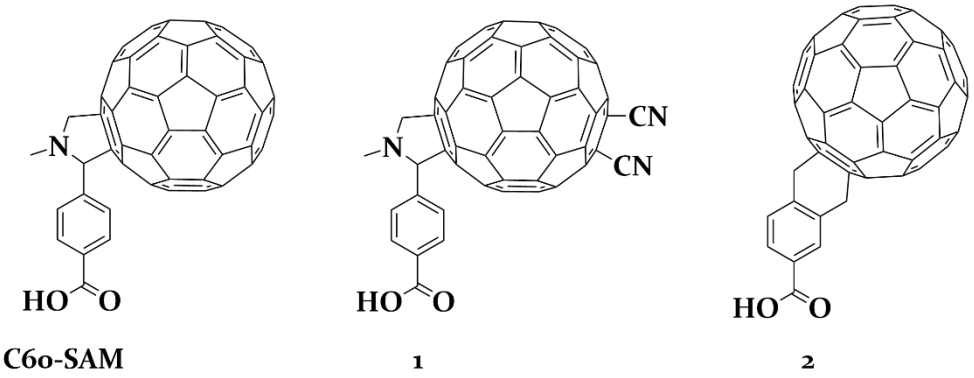

Figure 1.14. *The molecular structures of fullerene derivatives.*

Li and co-workers explored a series of naphthalimide derivatives (PN-P, TN-P, and NDI-P) to construct ESL via a chemical adsorption (**Figure 1.15**). The naphthalimide-based self-assembled n-type molecules remarkably increased the photovoltaic performance of PSCs, by having suitable LUMO energy levels as an ESL. They obtained the best result from NDI-P based devices reaches a PCE of 16%, that was the best result among non-fullerene ESL based n-i-p configuration PSCs.[99]

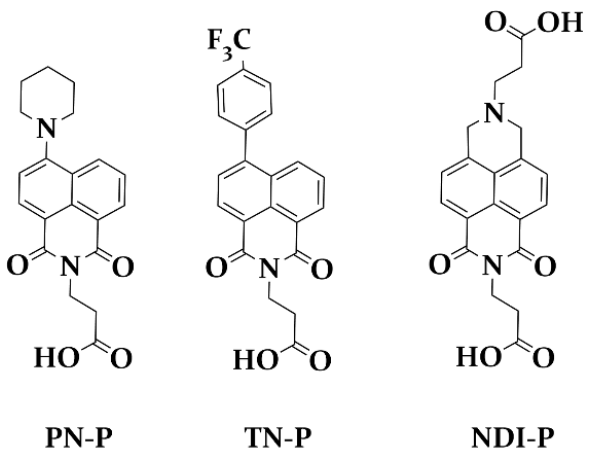

Figure 1.15. *The molecular structure of naphthalimide derivatives.*

Phthalocyanine Based Self-Assembled Hole Selective Small Molecule

Phthalocyanines (Pcs) are planar aromatic macrocycles and consist of four isoindole units. These units are presenting an 18 π-electron aromatic cloud delocalised over an arrangement of alternated nitrogen and carbon atoms (**Figure 1.16**). The physical properties of phthalocyanines can be tuned by putting more than 70 central metals with replacing the two hydrogen atoms and a variety of substituents can be integrated. Phthalocyanines mostly show a Q-bands (typically centred at 620-700 nm) in the visible region of the absorption spectra. For these reasons, phthalocyanines have been an important trade product for many years as dyestuffs for textiles and inks. Additionally, Pcs have excellent electronic and optical properties that arise from their electronic delocalization and make these compounds applicable in different fields of materials science and particularly promising as hole selective material in photovoltaic applications.

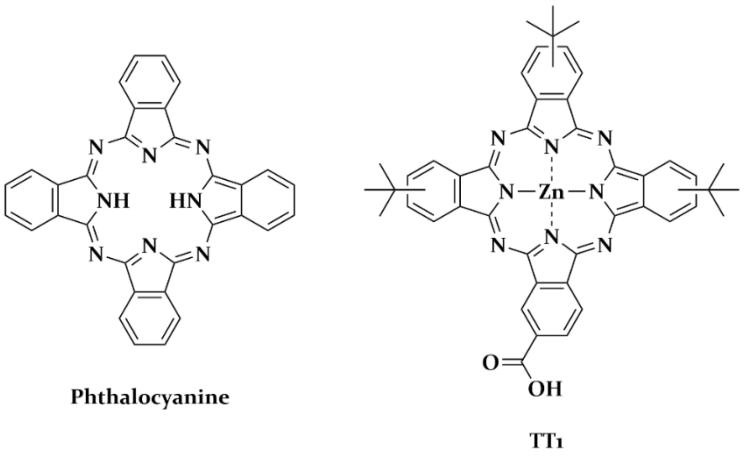

Figure 1.16. *Chemical structure of the phthalocyanine and TT1.*

Torres and co-workers focused on constructing multifunctional Pc-based donor-acceptor hybrids in which the complementary electroactive constituents are connected through a variety of covalent or supramolecular junctions.[100–102] In previous studies, zinc Pcs showed that the control over the formation of molecular aggregates onto the semiconductor nanoparticles which is crucial to have moderate efficiencies. However, Pcs have an excellent absorption in the near-IR region and their UV-vis spectra contain an optical window in the visible region that could allow their use in combination with a suitable dye to achieve panchromatic sensitization of the mesoporous photoelectrode. To avoid the formation of molecular aggregation onto semiconductor nanoparticles, they synthesised a tri-*tert*-butyl-substituted zinc Pc which adjusts the excited states to allow directionality of the charge transfer from the LUMO of the dye to the Titanium 3d orbital.[103] In 2007, Cid and co-workers synthesised a novel zinc carboxyphthalocynanine (TT1) which was substituted with *tert*-butyl group, to achieve increased power

conversion efficiency with its highly solubility in organic solvents, and its push-pull character that induces directionality in the excited state of the zinc Pc. They demonstrated the efficient electron injection of zinc Pc, which had a record efficiency for near-IR DSSCs under standard illumination conditions with yield 80% IPCE. Additionally, the combination of two dyes with complementary spectra achieved higher efficiency by taking advantage of the optical properties of the zinc Pc in DSSCs.[104]

The Role of the Terminal Moieties in Self-Assembled Monolayers

The terminal moieties play the most significant role in determining the perovskite solar cell performance, among other parts of SAMs. Due to the ionic nature of the perovskite layer, producing the various chemical interactions with different functional groups will be easier. For that reason, the suitable terminal group can provide a variety of functions through synthetic chemistry; wherein such functional groups can, in turn, significantly alter the wettability of the top layer, facilitating deposition of the forthcoming layer through both dipolar and dispersive interactions,[105] further affecting the crystallinity,[60] morphology and energy level offset.[106,107] Terminal groups currently under investigation include amino,[108] ammonium chloride,[109] ammonium iodide, thiol,[110] hydrogen,[111] hydrocarbons, benzene, pyridine,[112] bromo, chloro,[111] fluoro,[113] cyanide, and C60.[97]

To demonstrate the interfacial chemical interactions of terminal moieties with perovskite layer, Zuo and co-workers systematically investigated functionalised benzoic acid derivatives (BA-SAM, PA-SAM,

CBA-SAM, ABBA-SAM, and C3-SAM) on top of the SnO_2 (**Figure 1.17**). They observed that the chemical interactions are the predominant factor controlling the interfacial optoelectronic properties, due to the PSCs performance an opposite trend to that of the energy level alignment theory. Moreover, they demonstrated that the proper interfacial interactions can significantly reduce trap state density and assist interfacial transfer. With the use of 4-pyridinecarboxylic acid-based SAM (PA-SAM), the resulting perovskite solar cell exhibits remarkable improvements to reach the highest efficiency of 18.8%, resulting in a 10% increase compared to those without SAMs.[114]

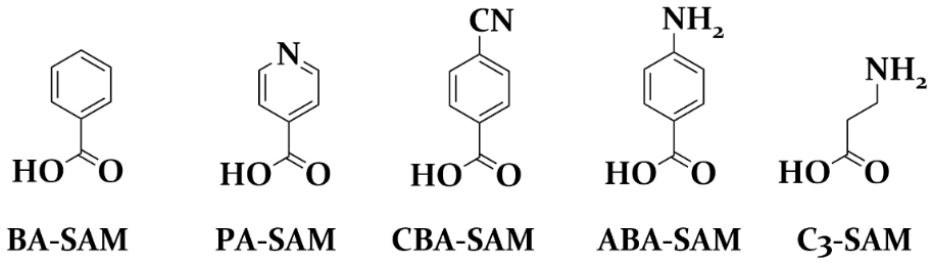

Figure 1.17. *The molecular structures of benzoic acid-based SAMs and C3-SAM.*

The SAMs are generally utilised to modify the inorganic charge selective materials such as TiO_2, SnO_2, and NiO_2 for improving their film quality and performance in PSCs. For instance, Wang and co-workers suppressed the drawbacks of NiO_2 in completed devices, they used a series of benzoic acid SAMs to passivate the surface defects of the NiO_x nanoparticles (**Figure 1.18**). They found that the 4-boromobenzoic acid-based (Br-BA) effectively passivate the surface between perovskite and NiO_x nanoparticles, reducing the trap-assisted recombination, minimizing the energy offset, and enhancing the perovskite

crystallisation by changing the HSL surface wettability. As a result of all these improvements, the PCE of PSCs is increased up to 18.4% with Br-BA-based SAMs, exceeding the control device PCE (15.5%).[111]

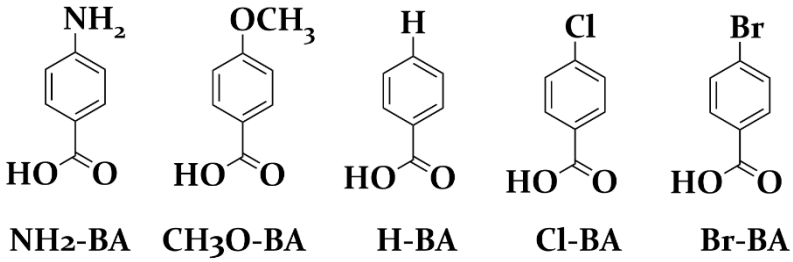

Figure 1.18. *The molecular structure of a series of benzoic acid SAMs.*

As we mentioned in the previous paragraph, the terminal group of SAMs also determines the wettability of the substrates that significantly enhance the crystalline properties of the perovskite layer. Han and co-workers demonstrated that when increase the ratio of methoxy group, the PCE of perovskite device is improved from 12.6% to 13.75% by effectively inducing dipole moment; in particular, TMBA gave a larger work function shift of ZnO ETL compared with MBA and DMBA.[115] TMBA effectively boosted the built-in voltage of PSCs, which resulted in an improved electron transfer from the active layer to the ETL and a higher open-circuit voltage (**Figure 1.19**).

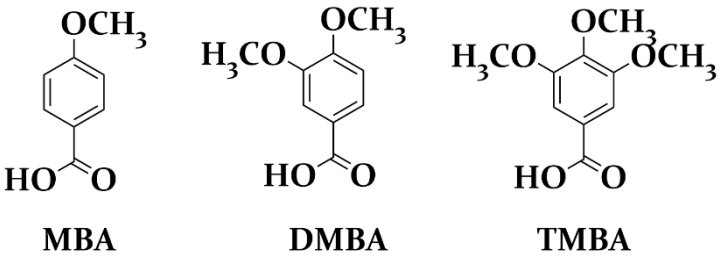

Figure 1.19. *The molecular structures of different positioned methoxy group based benzoic acid SAM derivatives.*

1.3. Stability of Perovskite Devices and Charge Selective Layers

Over the past few years, metal halide PSCs have quickly become the hottest topic in photovoltaics, and the fast development of device engineering has allowed the preparation of solar cells with PCE over 25%, surpassing commercial thin film PV technologies. Still, large-scale industrial application of PSCs faces the challenge of long-term stability as the initial efficiency of PSCs drops rapidly under operating conditions like biases, light, atmospheric exposure, etc. Some designs have been aimed at fabricating more stable PSCs, such as two-dimensional perovskite,[116] all-inorganic perovskite,[117] additives,[118] and interfacial engineering in recent times.[119] Nowadays, available technologies are relatively stable for more than 20 years, and they are feasible for large-scale energy production with similar performance.

The thin film PV technology can be assumed ready for large-scale industrial application after passing severe testing protocols. This procedure mainly includes an efficiency test under standard testing

control (STC) where cells are illuminated by 1000 W/m² with AM 1.5 G solar spectrum at 25 °C. Here, the initial efficiency of the PV cells is obtained from a current density-voltage (J-V) scan under STC. However, all the PV parameters of the PSCs depends on the scan rates, pre-bias, and device's temperature.[120–122] Therefore, it is significant to ensure detailed test conditions of J-V measurement for PSCs and complete device J-V characterisation with a stabilized power output achieved by the maximum power point (MPP) tracking.[123]

Initially, the power output is measured by the algorithm which applies the maximum power point voltage (V_{MMP}) from previous or initial J-V scan. Then, it increases/decreases the applied voltage and calculates the power difference, if the power output increases, it will continue to increase/decrease the applied voltage and reverse is true. Ultimately, the applied voltage alters around V_{MMP}. MPP curves of PSCs can reach a quasi-steady state that can be considered as the stabilized efficiency of the device, during a short time (usually between 2 and 5 minutes), assuming that the degradation is insignificant. [124–126] Consequently, MPP represents the real working conditions that ensure to estimate the energy output of a solar cell in operation by obtaining the accurate efficiency value from MPP.

On the other side, an outdoor test is an obligation for PV technology to start being sold commercially. In addition, it is necessary to estimate energy efficiency and payback time in this test. Therefore, one of the most important steps is to establish a standardized protocol for stability

testing of PSCs, including MPP tracking with defined day/night cycles, dark storage lifetime, damp heat testing and outdoor testing.[127]

It is well known that PSCs are highly susceptible to external stressors, which can be divided into five categories: atmospheric water and oxygen stability, thermal stability, light stability, electric field stability, and mechanical stability. First of all, oxygen and moisture resistances are a huge concern for PV technologies because of the oxidization of some components with water and O_2 in PV panels. They are also a threat for PSCs in most cases and the encapsulation technique can be used with PSCs, also commercialized PV technologies need proper encapsulation.[128] Moisture is known to degrade the perovskite layer even when it is encapsulated.[38,129] Additionally, encapsulation can be prone to cracking and edge leakage. When the MAPI layer is exposed to water, it decomposes into HI, CH_3NH_2 and PbI_2 and H_2O (Equation 1.2).[130] In contrast, small water addition into perovskite precursors or exposure to moisture during the crystallization process has been shown to be beneficial.[131,132] Wu and co-workers demonstrated that water molecules could promote homogenous nucleation and preferable crystallinity in the MAPI layer during annealing.[131] However, it is essential to prepare solar cells to have an inherent resistance to moisture ingress.

$$CH_3NH_3PbI_3 \overset{H_2O}{\longleftrightarrow} CH_3NH_2 + HI + PbI_2 \quad \text{Equation 1.2}$$

$$4HI + O_2 \leftrightarrow 2I_2 + 2H_2O$$

$$2HI \overset{h\upsilon}{\leftrightarrow} H_2 + I_2$$

Besides degradation caused by water, perovskite can also degrade when in contact with atmospheric condition. Specially, when oxygen is combined with light, it causes fast degradation in PSCs.[133] Aristidou and co-workers suggested an oxygen-induced degradation pathway of MAPI layer through the deprotonation of methylammonium (MA) where methylamine gas and PbI_2 are formed (Eq. 1.3).[134] Moreover, photo-excited electrons are accepted by oxygen molecules that are energetically favourable to light and possibly lead to the formation of superoxide species (O_2^-) found in iodide vacation sites. The superoxide anions then deprotonate the MA cations and decompose the material, moreover, this decomposition happens faster in the smaller crystal size.[134,135] Also, Alsari and co-workers showed that although the rate of degradation is lower compared to MAPI, defect-assisted oxygen and light-induced degradation are detected in mixed cations $[FA_{0.83}Cs_{0.17}Pb(I_{0.8}Br_{0.2})_3]$.[136]

$$CH_3NH_3PbI_3 + \frac{1}{4}O_2^- \xrightarrow{deprotonation} CH_3NH_2 + PbI_2 + \frac{1}{2}I_2 + \frac{1}{2}H_2O \quad \text{Eq. 1.3}$$

It is found that in the operating temperature range of -40 ° C to 85 ° C, a significant change in the PV performance of PSCs, depending on the operating temperature, occurred. Schwenzer and co-workers showed that the actual temperature cycle of the device (40 °C to 55 ° C) reduces the MAPI-based PSCs faster than keeping the device temperature at 25 ° C.[137] In 2016, it was proven that MAPI had lower chemical stability against external environmental factors and easily forms methylammonium iodide (MAI) and PbI_2.[138] The perovskite layer made up of only inorganic materials shows better thermal stability, comparing with the organohalide perovskite layer.[139]

MAPI degrades under illumination in the presence of oxygen as explained above. However, unlike the mechanism describe before, light induces degradation that may occur even in the absence of oxygen.[140,141] Jemli and co-workers highlighted that photons excite ′Pb^{+}···I^{0}′ complex which energetically tends to form the reactive I_2 and Pb^{2+} under illumination. Then, the oxygen and water diffused from the external environment into the perovskite layer can react with unstable lead species and this process will eventually produce PbI_2 and MA, causing damages to the perovskite crystals.[141]

Under the operation condition, perovskite absorber layer is subjected to an electric field. As all ionic species in the perovskite layer can potentially migrate in response to external electric fields.[142] For instance, cations can move quite easily through the cavity of the octahedral lattice of PbI_6^{4-} in the perovskite structure, leading to lattice distortions and contractions, and eventually degrading the material.[143]

As mentioned at the beginning of this Chapter, a perovskite layer is typically sandwiched between an electron selective layer and a hole selective layer to achieve high PCE from PSCs. Not only perovskite absorber can have intrinsic problem, but the charge selective layers can be the reason behind failure of the devices. A notable example is TiO_2, which is the first ESL implemented from DSSC to PSCs. Here, the surface of TiO_2 includes many oxygen vacancies that behave as electron donors that can react with atmospheric oxygen forming O_2^{-} anions and Ti^{4+} complexes. Under UV light exposure, the excited holes in TiO_2 can recombine with the adsorbed oxygen regions, leaving free electrons

which can eventually recombine with holes in the HSL and reduce charge extraction. Accordingly, TiO_2 is left with unfilled, immobile deep electron traps, quickly degrading the performance of PSCs over time, especially after several hours of full sunlight exposure.[144]

In the p-i-n configuration perovskite device, the degradation of PCBM has been observed under exposure to water and oxygen. To overcome this problem, ZnO has been deposited on top of the PCBM as a buffer layer for improving the stability of the device.[145] Even though inorganic charge selective layers are more stable than organic layers, the difference in the crystal structures and thermal expansion coefficients can create undesirable deep traps at the interfaces and also create cracks in the films during operating conditions.[146]

Organic hole selective layers such as PTAA, Spiro-OMeTAD and their derivatives are commonly utilized to achieve highly efficient PSCs. However, the solution-processed Spiro-OMeTAD layer is porous, which leads to the penetration of oxygen and water inside the perovskite layer. Additionally, the LiTFSI salt is one of the chemical dopants most commonly used in PTAA and Spiro-OMeTAD to improve their charge selective properties, as mentioned in previous section. However, the LiTFSI salt has a hygroscopic nature and accelerates the moisture degradation of PSCs.[146] Therefore, there have been many research effort to overwhelm this problem like improving organic charge selective layer's conductivity without the use of dopants and etc.[147,148] PEDOT:PSS is also another commonly used HSL and it has a hygroscopic character which can take up water in the atmosphere and reduces the stability of

PV device.[149] New organic and/or inorganic materials should be worked on to overcome these problems mentioned above.

It is particularly important to use top metal contacts for effective charge collection, and their good energy alignment with the contact layers and the perovskite absorbent layer for high efficiency. Aluminium is used in a variety of PV applications due to its affordability and accessibility. However, water and/or oxygen can diffuse within the pores of the aluminium layer in the ambient environment. Thereafter, aluminium will be oxidized, and a metal oxide layer will be formed with the organic layer in the interface because of its high reactivity. As a result of this, this metal oxide layer is an insulator and thus degrades the performance of solar cells.[150] Most of the common metal contact can interact with perovskite causing degradation such as silver, gold, etc.[48] In contrast, copper-based devices show better air stability, the copper layer retains its colour when stored for up to one month under atmospheric conditions.[151,152] The migration of the mobile iodine anions can be the main reason for metal contact degradation when considering the metal contact mechanism.[153] One way to solve the metal contact degradation can be to replace metal electrodes completely with carbon-based electrodes, nonetheless, so far the completed device efficiency is lower than metal contact employed PSCs.[154]

1.4. Motivation and Aim of the Thesis

In this section, the objective and motivation of this thesis will be explained briefly for each chapter.

The motivation of this thesis is to demonstrate the potential of low molecular weight small molecules as charge selective contacts or interfacial layers in perovskite solar cells and their influence on performance and stability. As described before, the application of these types of molecules in PSC has scarcely been reported, there are only a few examples and none of them are related to stability issues, as indicated in the bibliography of this thesis. Thus, we have selected and examined the activity of organic groups that are commonly used in photovoltaic applications like truxene, phthalocyanine, carbazoles, triphenyl, and diphenyl amines. In the following paragraphs, we describe the specific aims of each chapter that are related to the main objective of this thesis.

Chapter 1 presents fundamental knowledge of perovskite-based photovoltaic devices and a brief summary about each part that made the perovskite solar cells. The commercial and non-commercial charge selective layers which are used to achieve high efficiency and stable photovoltaic devices are compared by giving references from the literature.

Chapter 2 describes the experimental procedures, methods and techniques that are carried out to prove the synthesised molecule structures in this thesis. The general instrumentation and all the

characterisation techniques employed in this thesis are described in detail. Moreover, the fabrication process of different types of perovskite-based solar cells are explained and the advanced characterisation techniques which are used in these devices are given.

Chapter 3 gives the detailed synthesis and characterisation of the new Truxene-based Lewis based interfacial layer (Trux-FPy) (**Scheme 3.1** in Chapter 3) for PSC application. The interfacial layer properties of Trux-FPy are determined by UV-vis spectroscopy, to investigate its supramolecular interactions with the uncoordinated lead ions. Spiro-OMeTAD is used as an HSL in n-i-p configuration PSCs due to its energy level is suitable with interfacial layer. To understand carrier recombination and ion migration in perovskite solar cells, the advanced characterisation techniques (PI-CE, PI-TPV, and PI-TPC) are performed.

Chapter 4 introduces the novel synthetic pathway of TT1 (**Scheme 4.1** in Chapter 4), achieving high yield with ZnO catalyst. We utilised it as a self-assembled hole selective monolayer in p-i-n configuration PSCs to find an alternative material to PEDOT:PSS. The SAMs are characterised by contact angle measurement and UV-vis spectroscopy, showing their hole selective layer properties, and proving their existence on the metal surface before complete devices. After that, we used advanced optoelectronic transient techniques in completed PSCs to figure out the processes that govern the final open-circuit voltage.

Chapter 5 is focused on the long-term stability of PSCs based on SAMs. Two new carboxylic acid-based self-assembled small molecules are designed, synthesised, and characterised to achieve high PCE and stable

devices. Then, XPS and UPS measurements are performed to verify the ester bond on the metal oxide surface and determine the HOMO/E_F levels to figure out their charge selective properties. In the second part of this work, in collaboration with Prof. Antonio Abate and Dr. Nga Phung from HZB, as part of my short-term research stay, we fabricated CsFAMA-based PSCs with SAMs and monitored the long-term device stability by MPP tracking.

In the next chapter, **Chapter 6**, the terminal group of SAMs are investigated in a similar device structure (**Chapter 5**). Three triphenylamine-based SAMs are employed to understand their effect on the crystallinity and/or morphology of the perovskite layer, the device performance and stability. All the device fabrication and characterisations of the SAMs are done in collaboration with HZB.

Chapter 7 details the synthesis and characterisation of the three novels HSLs derived from truxene with electron donor properties named EADR01, EA01, and EA02 (**Scheme 7.2**). Based on their optical and electrochemical properties, they were suitable for use in PSCs. We employed HSL as a charge selective layer in n-i-p configuration devices and compared them with Spiro-OMeTAD. Their data are reported as preliminary results.

Chapter 8 describes the conclusions of the obtained results from the previous chapters.

Chapter 2

Experimental Procedures and Methods

2.1. Introduction

In this Chapter, the general experimental procedures, the characterisation techniques of new organic semiconductor molecules, the fabrication and photovoltaic characterisation of the perovskite solar cells will be explained.

In the first section, the general instrumentation and characterisation techniques (structural, thermal, optical, photoelectrical, etc.) are summarised, which are used for demonstrating that the newly synthesised organic small molecules are suitable candidates for this thesis scopes. Moreover, the device characterization techniques and stabilization procedures that are applied to the completed PSCs will be described.

In the second section, the deposition techniques are explained for each active layer used in the n-i-p and p-i-n configurations of the PSCs. Since critical points exist in every layer of the PSC structure, we reveal the experimental part we used in detail to get devices with very high performances and make them reproducible.

In the third section, there is a thorough description of the preferred commercial or synthesized inorganic and organic molecules as charge selective contacts or buffer layers and how they are deposited inside of the PSCs to achieve this thesis's goal.

In the last section of this chapter, the optoelectronic photo-induced transient techniques will be explained.

2.2. Organic Syntheses of Small Molecules

The specific synthesis of the molecules is described at the corresponding chapter. A general description of the reagents and characterisation is given in this chapter.

2.2.1. General Reagents and Solvents

All the chemical reagents used in this thesis are purchased from major commercial suppliers (TCI, Sigma Aldrich, Alfa Aesar, MERCK, Fluorochem, Dyenamo, Lumtec, and abcr gmbh). The chemical reagents are used directly without further purification unless otherwise mentioned. All oxygen and moisture sensitive reactions are performed under argon atmosphere using glassware flame-dried under high-vacuum (~10^{-2} mbar) backfilled with Argon. Tetrahydrofuran (THF) and toluene are dried over metallic sodium/benzophenone and freshly distilled prior to use, while common solvents are used without drying procedure. The course of the reactions is checked by thin layer chromatography (TLC) on Merck KGaA pre-coated TLC Silica gel 60 F_{254} aluminium sheets and visualised with a UV lamp (254 nm or 356 nm). All extracts are dried over powdered magnesium sulfate ($MgSO_4$) and sodium sulfate (Na_2SO_4) and solvents excess are removed by rotary evaporation under low pressure. The column chromatography is performed using Silicycle UltraPure SilicaFlash P60, 40-63 μm (230-400 mesh). Patterned ITO and FTO coated glass sheets are purchased from

Automatic Research GmbH and Xinyan Technology Ltd, with a resistance of 15 Ω per square.

2.3. General Instrumentation and Characterisation

In this part, the methods and techniques that are used in this thesis experiments are explained.

2.3.1. Structural Characterisation

^{1}H and ^{13}C Nuclear Magnetic Resonance Spectroscopy

^{1}H and ^{13}C Nuclear Magnetic Resonance (NMR) spectra are recorded on a Bruker Avance 400 (400 MHz for ^{1}H and 100 MHz for ^{13}C) and 500 (500 MHz for ^{1}H and 125 MHz for ^{13}C) spectrometer at room temperature. All the data are given as chemical shifts in δ, reported in ppm, measured using deuterated solvents, and referenced to the residual solvent signal. All NMR data is reported as the s (singlet), d (doublet), doublet of doublets (dd), t (triplet), doublet of triplets (dt), q (quartet), m (multiplet), brs (broad singlet); coupling constants, *J*, in Hz.

High-Resolution Mass Spectra

High-Resolution Mass Spectra (HR-MS) is recorded on a Waters LCT Premier liquid chromatography couple Time-of-Flight mass spectrometer (HPLC/MS-TOF) using electrospray ionization (ESI) as an ionization mode. Matrix-assisted laser desorption/ionization (MALDI),

and matrix-assisted laser desorption/ionization time-of-flight (MALDI-TOF) mass spectrometry are recorded on a Bruker Autoflex.

2.3.2. Thermal Measurements

Thermogravimetric analysis

Thermogravimetric analysis (TGA) gives information on the rate and the mass change of a sample as a function of temperature under programmed conditions. For instance, temperature conditions can affect changes in the sample mass. TGA is mostly used for knowing certain thermal events such as decomposition temperature (T_{des}), oxidation, and reduction, etc.[155] In this work, the decomposition temperature will be considered an important parameter for HSLs which are deposited before the perovskite layer and will resist to the annealing process of the perovskite layer in p-i-n type perovskite devices.

TGA data are collected in a TGA/SDTA851 Mettler Toledo equipment. The degradation temperatures are examined between 30 °C and 600 °C from 5% weight loss at 10 °C/min under N_2 atmosphere.

Differential Scanning Calorimetry

Differential Scanning Calorimetry (DSC) is the most often used thermal analysis method due to its speed, simplicity, and availability. Basically, the instrument measures the difference in the heat flow between the reference and the sample. DSC provides information about chemical and physical changes of material for determining the melting point (T_m), glass transition (T_g), and crystallization (T_c) values in **Figure 2.1**.[156] In

addition, this information consists of endothermic and exothermic processes, or changes in the heat capacity.[157]

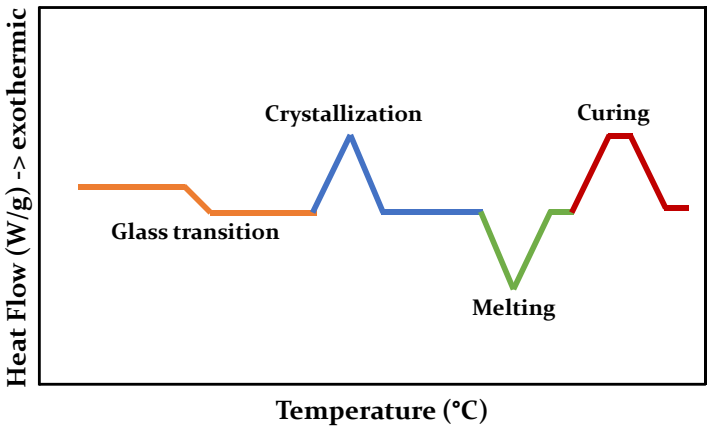

Figure 2.1. *Example of a differential thermogram showing the changes that can be encountered in semiconductor materials.*

DSC information is recorded using a DSC822e Mettler Toledo calorimeter at the following conditions: 10 °C/min, N_2 atmosphere. T_m, T_g, T_c temperatures of specimen are obtained from 30 °C to 450 °C performing three reversible cycles in N_2 atmosphere.

2.3.3. Optical Characterisations

Ultraviolet-visible spectroscopy

Ultraviolet-visible (UV-vis) spectroscopy is used to get the absorbance spectra of a compound in a solution or a solid-state film. Mainly, the electrons are excited from the ground state to the first singlet state of the material by the absorbance of light energy or electromagnetic radiation. The UV-vis region is comprised of a wavelength range from 200 nm to

800 nm.[158] UV-vis spectra are recorded on Shimadzu UV spectrometer 1700 with an optical range between 190 and 1100 nm.

All solution absorption measurements are performed in dichloromethane (DCM), chloroform (CF) and toluene with a 1 cm optical path length quartz cuvettes at room temperature in air.

Steady-State Fluorescence Emission

Steady-state fluorescence emission (PL) spectra are recorded on Horiba Jobin Yvon Lrd. with a PMT (UV-vis) and InGaAs (NIR) detectors that allow fluorescence measurements in the wavelengths range from 250 to 1600 nm at room temperature. In this thesis, the measured PL spectra has a peak around 760 nm for lead halide perovskite materials which can be shifted depending on the perovskite composition.

Estimation of the optical bandgap

The energy of the optical bandgap (E_g) is calculated accordingly to the Equation 2.1:

$$E_g = \frac{1242}{\lambda_{a.e.}} \qquad \text{Equation 2.1}$$

where $\lambda_{a.e.}$ is the absorption edge wavelength onset,[159] and its value is taken from the intersection of the normalized absorption and emission spectra recorded with a concentration of about 10^{-5} M.

2.3.4. Contact Angle Measurements

Contact angles can be used to characterise the surface properties of the transparent conductive oxide in its as-manufactured state. Therefore, it is important, in perovskite solar cell studies, to produce solid surfaces of sufficient quality. The contact angles precisely reflect the interaction between the liquid and the solid. Basically, the contact angle is defined by measuring the angle between the surface and the tangent of the drop surface at the contact.[160]

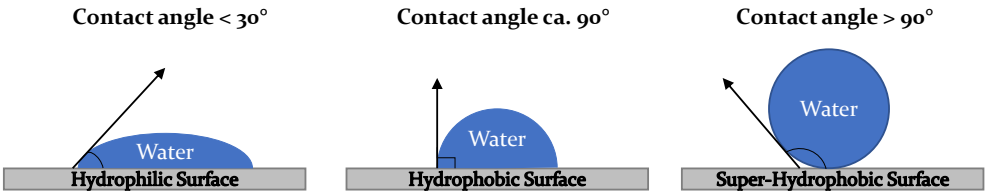

Figure 2.2. *Illustration of the measurement of the contact angle formed by a water droplet on top of surfaces with different properties.*

As it is shown in **Figure 2.2**, when the liquid is strongly attracted to the solid surface, the droplet will spread out on the solid surface (hydrophilic) and the contact angle will be lower than 30°. Less hydrophilic surfaces will have a contact angle up and about 90°. The super-hydrophobic surface will be larger than 90° and the droplet will not spread out at all.[161]

Contact angle measurements are carried out with a Kruss Drop Shape Analysis System DSA25 using deionised water as a solvent.

2.3.5. Electrochemical Characterisations

Cyclic voltammetry

Cyclic voltammetry (CV) measurements are carried out by a three-electrode assembly cell connected to a CH Instruments© 600c potentiostat/galvanostat. Three-electrode cells are the most used setup in electrochemical studies, particularly when the cell resistance is relatively high. In this design, the potential of the working electrode is monitored in relation to the reference potential, the current passes between a separate counter electrode and the working electrode. To minimize solution resistance in the cell, the reference electrode is placed as close as possible to the working electrode.[162,163] Three-electrode cell is equipped with a glassy carbon as working electrode, platinum as counter-electrode, and an Ag/AgCl as a reference electrode (non-aqua, in 3M potassium chloride) in acetonitrile (ACN) solution at a concentration of 0.5 mM. The supporting electrolyte is a 0.1 M solution of tetrabutylammonium hexafluorophosphate ($TBAPF_6$). All potentials are corrected against Fc/Fc^+ (E_{ferr}). The cyclic voltammograms are measured with a scan rate of 100 mV/s at room temperature.

Solution-based CV experiments are used to determine the relative molecular reduction potential ($^{1/2}E_{red}$) and oxidation potential ($^{1/2}E_{ox}$), $^{1/2}E_{ox}$ is ultimately related to the ionization energy; where $^{1/2}E_{ox}$= HOMO for organic semiconductor, VBM for inorganic semiconductor, $^{1/2}E_{red}$ = LUMO for organic semiconductor, conduction band maximum (CBM) for inorganic semiconductor. These levels are used to determine the electronic band gap (E_g^{el}) of semiconductors.

$$E_{HOMO} = -(4.8 - E_{ferr} + \tfrac{1}{2}\mathrm{E_{ox}}) \qquad \text{Equation 2.2}$$

$$E_{LUMO} = -(4.8 - E_{ferr} - \tfrac{1}{2}\mathrm{E_{red}}) \qquad \text{Equation 2.3}$$

$$E_g^{el} = E_{HOMO} - E_{LUMO} \qquad \text{Equation 2.4}$$

Empirical equations are used for calculating HOMO/VBM, LUMO/CBM energy levels and the electronic band which is dependent on the used cell such as the electrodes, solvents, etc.[163,164] For this reason, the estimated values in this thesis have been referenced to standard materials.

Ultraviolet Photoelectron Spectroscopy

Ultraviolet Photoelectron spectroscopy (UPS) is one of the conventional methods to determine the ionization energy, which is equal to the HOMO level of the organic semiconductor. In UPS, the ultraviolet light impacts a thin film of the sample that ejects electron from its surface. The electron's kinetic energy varies according to its molecular orbital (MO), and the sum of the absolute value of the electron kinetic energy and its orbital potential energy is equal to the photon energy.[165] The highest kinetic energy belongs to the electron from the HOMO:

$$E_k = h\nu - E_{HOMO} \qquad \text{Equation 2.5}$$

where E_k is the highest kinetic energy of the electron, $h\nu$ is the energy of the ultraviolet photon.[166] If we compare UPS with CV, the estimation of the HOMO level of the molecule is more confident in UPS than solution-based CV experiments. In CV measurements, due to certain solvent-

solute interactions in solutions, affecting dissolving energy, it can alter the nature (and hence energy) of the low-lying excited states of dissolved molecules.[167]

UPS measurements are done, employing He I radiation ($h\nu$ = 21.22 eV) from a He discharge lamp yielding the energy offset of the HOMO from the Fermi energy level (E_F). For the UPS measurements the samples are biased with -15 V *versus* ground to facilitate the emission of the secondary electrons.

2.3.6. X-ray Measurements

X-ray Diffraction

When X-rays interact with a crystalline material, consistent elastic scattering, also called diffracted light, can be emitted. Elastic X-ray scattering can be accurately described in terms of classical electromagnetic theory. An electron in an alternating electromagnetic field oscillates with the same frequency as the field. When an X-ray beam hits an atom, the electrons in the atom begin to oscillate at the same frequency as the incident beam and emit electromagnetic radiation. The sum of these radiations is described as the scattering power of an atom.[168]

The atoms are formed in a well-ordered structure in a crystalline material and repeated through the material. The X-ray Diffraction (XRD) pattern can be used to identify the material due to its uniqueness and it is mostly collected using grazing incidence XRD (GIXRD). The GIXRD uses a quite small incidence angle which is fixed during the measurement so that the

probing volume is mainly within the thin film. Additionally, the total diffraction volume is larger due to a long pathway of X-ray in the specimen at a small incidence angle which improves the statistic of the measurements.[169]

XRD measurements are performed in air with the PANalytical X'Pert Pro MPD (multi-purpose diffractometer) using grazing incidence geometry. GIXRD patterns are collected with a step size of 0.02 degree, for 6 seconds each step.

X-ray Photoelectron Spectroscopy

Surface analysis by X-ray photoelectron spectroscopy (XPS) is achieved by irradiating a specimen with monoenergetic soft X-rays and analysing the energy of the detected electrons. Mg Kα (1253.6 eV) or Al Kα (1486.6 eV) X-rays are commonly applied in the literature. These photons have limited penetrating power in a solid on the order of 1-10 nm. The X-rays interact with atoms and cause electrons to be emitted by the photoelectric effect in the surface region. The photoelectric effect can be described as the electrons that can be ejected from the surface of the metal when light shines on a metal. The emitted photoelectron is the result of complete transfer of the X-ray energy to a core level electron. The kinetic energy of the emitted electrons can be estimated by:

$$E_{kin} = h\vartheta - BE - \Phi_s \qquad \text{Equation 2.6}$$

where $h\vartheta$ is the energy of the photon, BE is the binding energy of the electron, and Φ_s is the work function of the material.

The spectrum is acquired as a plot of the number of detected electrons per energy interval *versus* their kinetic energy. Each element has a unique spectrum, and the binding energy of photoelectrons will not change when different X-ray sources are applied. The spectrum derived from a mixture of elements is roughly the sum of the peaks of the individual components. Since the mean free path of electrons in solids is exceedingly small, the detected electrons originated from only the top few atomic layers, making XPS a unique surface-sensitive technique for chemical analysis.[170,171]

To study the chemical state of the atoms of the compounds XPS measurements are performed using Mg Kα radiation ($h\nu$ = 1253.6 eV, P = 150 W) to excite the photoelectrons with a XR50 (SPECS) X-ray source. It houses a CLAM 4 (VG) electron analyser for photoemission (PES) spectroscopy. The measurements are carried out in the CISSY ultra-high vacuum apparatus ($p < 2\times10^{-8}$ mbar). The X-ray source and the analyser are arranged under a fixed 54° "magic" angle. More details on the setup are available elsewhere.[172]

The XPS spectra are corrected for charging by referencing the 4f transition of a gold reference to 84.0 eV. The spectra are then analysed by subtracting a Shirley-type background approximation and fitting Voigt-type peaks[173] to the remaining signal. The Lorentzian FWHM is constrained to 0.6 eV while the Gaussian FWHM is allowed to float within a range of 0.7-1.2 eV. The peak centres are constrained to value ranges to prevent overlapping or peaks exchanging positions, but care is

taken not to allow values to run into the constraining limits. Peak areas are constrained to only assume values ≥ 0.

2.3.7. Photoelectrical Measurements

Space-Charge Limited Current Method

The charge carrier mobility of HSLs is measured by the space-charge limited current (SCLC) method. SCLC method is applied to only p-type materials sandwiched between the contacts. The device structure is basically ITO/PEDOT:PSS/HSL/Au. The current density-voltage curve is measured and the concentration of charge carriers and the electric field in the device estimated by the mobility of the holes, instead of by the recombination of the holes. The measured data is fitted in the SCLS regime using Mott-Gurney law shown in **Figure 2.3** and Equation 2.7.[174,175]

$$J_{SCLC} = \frac{9}{8}\varepsilon_0\varepsilon_r\mu\frac{V_{eff}}{d^3} \qquad \text{Equation 2.7}$$

Here, μ is the mobility of HSL, d is the thickness of HSL, V_{eff} is the applied voltage (from 1 to 5 V) and $\varepsilon_0\varepsilon_r$ is the dielectric constant which has a value of 3 for organic semiconductors, according to the literature.[176] The HSL thickness is usually fixed around 100 nm and the films are deposited via spin-coating. The PEDOT:PSS layers are deposited onto cleaned and treated ITO substrates via spin coating as described in the section 2.5.2. of this Chapter. The data are recorded with a Keithley 2612A by sweeping from 1 to 5 V at a scan rate of 40 mV/s.

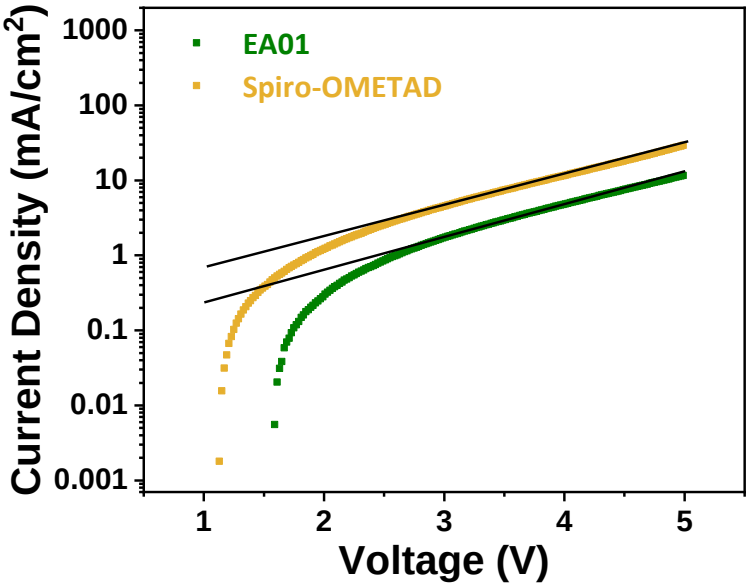

Figure 2.3. *SCLC measurement of the HSLs used in Chapter 7. The data is fitted to the Equation 2.7 which is shown as a black line for each HSLs.*

2.3.8. Scanning Electron Microscopy

The morphology of the perovskite layer and completed perovskite device layers are viewed by using Scanning Electron Microscope (SEM) and Environmental Scanning Electron Microscopy (ESEM), respectively. The SEM principally detects a secondary electron between the electron beam and the electrons of the sample with high acceleration voltage as shown in **Figure 2.4**. The secondary electrons are expelled from the material's atom and are recorded as an image due to the high primary electron beam hitting the sample under vacuum. The different topologies of the sample cause various contrast colours for the final image. For instance, heavy atoms can deflect electrons strongly and they appear much brighter in the image. Additionally, the backscattered electron detector can deliver the crystal orientation of the sample obeying Bragg's law

giving Kikuchi patterns. Finally, SEM detectors use a semiconductor or a scintillation to detect the electrons from the specimen which are converted to photons then to an electric signal.[177]

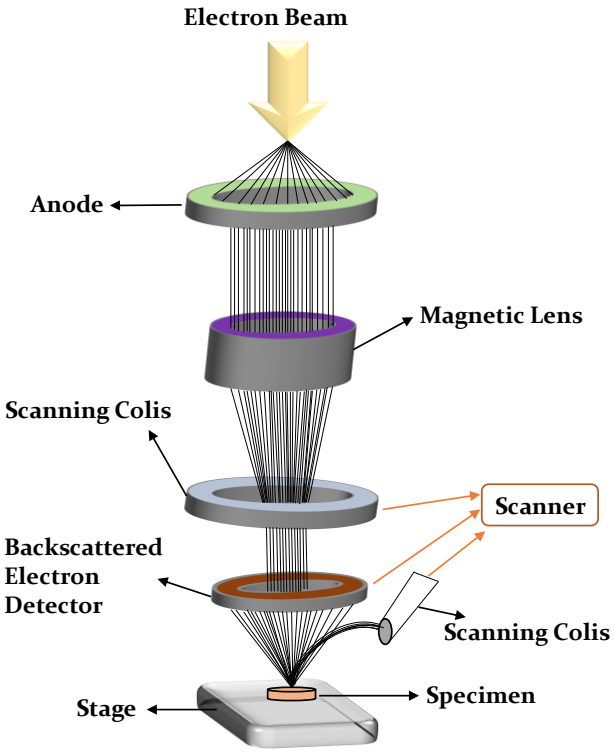

Figure 2.4. *Schematic representation of the basic SEM*

The SEM images are acquired with Hitachi S4100 at 30k magnification. The voltages used for SEM is 5 keV.

2.3.9. Atomic Force Microscope

Atomic Force Microscopy (AFM), which is used to get images of the surface of the films, is based on van der Waals interaction between the surface of the material and tip junction, capillary forces, covalent forces, electrostatic forces, common repulsive interaction forces, the van der

Waals, etc. interaction triggers a force gradient that adjusts the oscillation. While the tip scans across the surface of the specimen, the surface topography can be mapped by continually altering the mean level position in order to maintain a fixed tip-sample interaction. The force regimes can be categorized into three imaging modes: contact AFM (the tip uses a continuous force ~ 1-1000 nN normal to the surface of the specimen); intermittent contact AFM (an oscillating tip-cantilever is carried close to the specimen so that it more aggressively strikes or gently taps); and noncontact AFM (a tip oscillates with a much smaller magnitude and never *contacts* the surface of the specimen, certainly interacting via Van der Waals forces instead).[177]

AFM images are obtained with a Pico SPM II instrument and the tip is in the noncontact mode. The images are processed with the WSxM software.

2.3.10. Photophysical Measurements

Time-Correlated Single Photon Counting Measurements

Time-correlated single-photon counting (TCSPC) is a common technique for fluorescence lifetime measurements which is based on the detection of single emitted photons over the time of the luminescence decay.[178] The technique provides information about the possible paths of the radiative recombination of a semiconductor. If the semiconductor absorbs a photon, the electron will be excited from its ground state (HOMO/VBM) to higher excited states (LUMO/CBM). In the end, this electron will be recombined radiatively to its ground state by the

emission of photons that depend on the band-gap energy of the semiconductors.[179]

Lifetime measurements are performed on an Edinburgh Instruments LifeSpec-II based on the TCSPC technique, equipped with a PMT detector, double subtractive monochromator, and 470 nm picosecond pulsed diode laser source. All perovskite films are protected with poly(methyl methacrylate) PMMA (~30 nm) to do measurements in the ambient condition. In this thesis, all time resolved photoluminescence (TRPL) decays have been fitted to a biexponential decay with following equation:

$$y = A_1 \exp\left(-\frac{t}{\tau_1}\right) + A_2 \exp\left(-\frac{t}{\tau_2}\right) \qquad \text{Equation 2.8}$$

where A_i is an amplitude, τ_i is characteristic decay lifetime.[180]

2.3.11. Characterisation Techniques of Perovskite Devices

In this section, the employed characterisation techniques for completed perovskite devices will be explained. The evaluation of the photovoltaic parameters and the calculation of the power conversion efficiency of the perovskite devices will be defined.

Calculation of the Power Conversion Efficiency by Current Density-Voltage Scan

The Current Density-Voltage measurement is the most important technique for determining power conversion efficiency (PCE) of the

perovskite devices. The PCE is the ratio between the incident light power density and the maximum electrical power output under standard test conditions (STC) (1000 W/cm², AM 1.5 G and at 25 °C) as described in IEC 60904-3.[181] The PCE of solar cells is determined with measurement of the photocurrent by scanning the bias potential. It is mainly calculated from the current density-voltage (J-V) curve under 1 Sun STC, using a solar simulator (ABET 11000 Sun 2000) calibrated with a Fraunhofer ISE Si photodiode. These STCs correlate to the solar radiation spectrum at mid-latitudes, corresponding to the solar spectrum at a solar zenith angle of 48.2°.[182] The results are expressed as a current density – voltage (J-V) curve and the ratio of the maximum output power (P_{Max}) to the irradiation intensity is described as the power conversion efficiency (η) (Equation 2.9).

$$\eta = \frac{P_{out}}{P_{in}} = \frac{J_{SC}V_{OC}FF}{P_{in}} \qquad \text{Equation 2.9}$$

The photovoltaic parameters for both reverse and forward scan conditions short-circuit current density (J_{SC}), open-circuit voltage (V_{OC}), fill factor (FF), power conversion efficiency (η) can be extracted from the J-V curves (**Figure 2.5**). The J_{SC} value can be determined when the voltage is zero in the cell, and it depends on directly the active area of the cell. In the opposite situation, while the current density is zero in the cell, the V_{OC} value can be determined. The FF value is the ratio between the maximum power output (J_{MP} x V_{MP}) and the outcome of J_{SC} and V_{OC} (Equation 2.10).

$$FF = \frac{J_{MP}V_{MP}}{J_{SC}V_{OC}} \qquad \text{Equation 2.10}$$

The J-V curves can be obtained with two different scan sweeps; forward is called when scan sweep is from J_{SC} to V_{OC}, the reverse is called when scan sweep is from V_{OC} to J_{SC}. Generally, in n-i-p configuration perovskite devices, to perform the J-V measurement in both scan sweep showed characteristic difference which is called hysteresis. This will be explained in the following section.

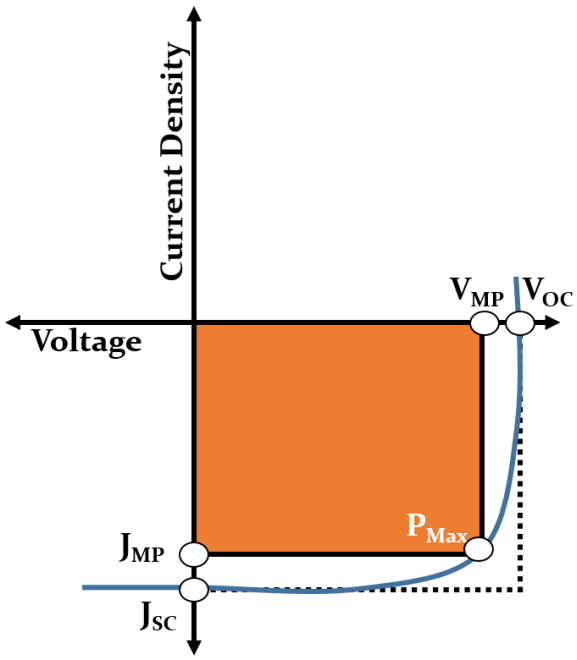

Figure 2.5. *Example of a typical J-V curve of a perovskite solar cell highlighting the J_{SC}, V_{OC}, current and voltage at maximum power (J_{MP} and V_{MP}, respectively), and FF.*

The scan rate is 100 mV/s starting from forward scan using Keithley Model 2612A as a voltage source. The opposite scan sweep of forward is defined as reverse.

The Open-Circuit Voltage and Short-Circuit Current Density Stabilization

The short-circuit current density (J_{SC}) and the open-circuit voltage (V_{OC}) stabilisation time are especially useful because the n-i-p configuration has high hysteresis. Hysteresis is described as slow rise in V_{OC} that is associated with the ionic movements within the perovskite. The detailed description of the hysteresis is mentioned in the following section.

The stabilization measurements are employed while the cell is in open-circuit and dark conditions. The cell is illuminated after a few seconds from dark to one sun condition and the evolution of the J_{SC} or the V_{OC} growth is recorded.

External Quantum Efficiency Measurement

The external quantum efficiency (EQE), alternatively called the incident-photon-to-current-efficiency (IPCE), is described as the ratio between the number of electrons generated and the number of incident photons, considering one photon generates one electron-hole pair (this means that up and down-conversion absorber can have, theoretically, and EQE of greater than 100%). The essential requirement of any good solar cell is that light with energy above the bandgap can be absorbed and photogenerated carriers can be extracted. Experimentally, the light from a broadband light source, often a Xenon lamp, is chopped and selected through a monochromator to generate single wavelength light source. The number of generated electrons is recorded per each wavelength. EQE can be calculated by following equation:

$$EQE = \frac{hvJsc}{I_{in}e} \qquad \text{Equation 2.11}$$

where J_{SC} is the short circuit current density, hv is the photon energy, I_{in} is the incident light intensity and e is the absolute value of electron charge. The cell is kept at short-circuit condition, and the current through the cell is measured with a source meter for each wavelength. Since the EQE is the spectral response of the cell, it can be used to calculate the integrated $J_{SC,EQE}$ of the cell under illumination and with following equation 2.12:

$$J_{SC,EQE} = \int qEQE(\lambda)S(\lambda)d\lambda \qquad \text{Equation 2.12}$$

where $S(\lambda)$ is photons per seconds. The short-circuit current density is generally measured from the J-V curve, which is defined as $J_{SC,JV}$ under the solar simulator (**Figure 2.6**). The integrated short-circuit current density, is defined as $J_{SC,EQE}$, is calculated by setup uses a Xe lamp in combination with a monochromator as light source. Typically, the $J_{SC,EQE}$ is relatively lower (10-20%) than the $J_{SC,JV}$ for PSCs.

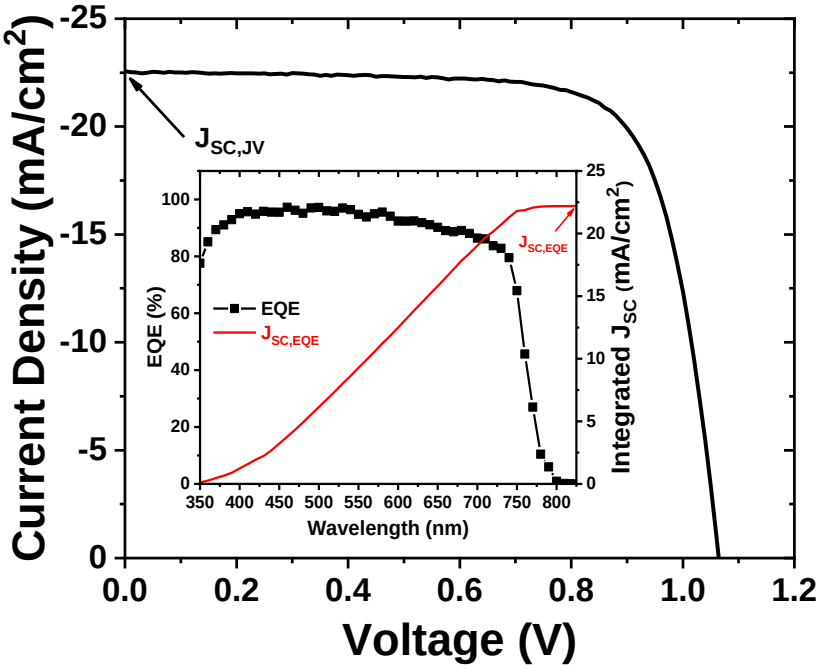

Figure 2.6. *Example of the J-V curve and EQE spectrum of a PSC.*

EQE measurement is recorded by an Oriel Instruments QEPVSI-b system with a Xenon lamp (Newport 300 W). The white light is chopped at a frequency of 78 Hz by a Newport Cornerstone 260 monochromator. Before each measurement, a Si diode with a known spectrum is used as reference. The response from the solar cells is measured with a Stanford Research SR830 Lock-In amplifier and evaluated by a commercial software named TracQ.

Open-Circuit Voltage and Short-Circuit Current Dependency on Light Intensity

The different light intensities are employed to determine the V_{OC} and J_{SC} dependence with light intensity (Φ) using different optical filters. These filters fix the intensity of the light that will pass through to the device

from the light source. The different J-V curves are obtained from same device under different light intensities as shown in **Figure 2.7**.

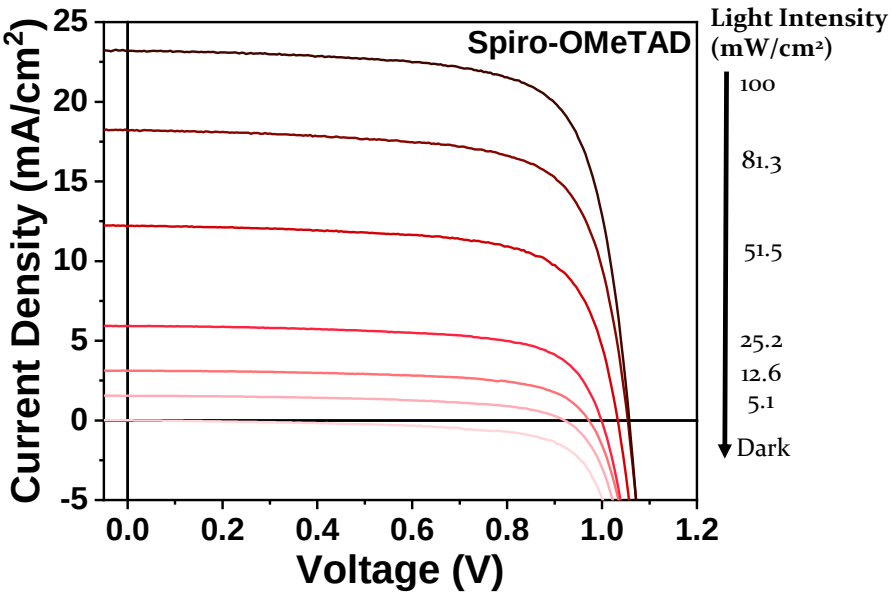

Figure 2.7. *The J-V curves of the device with Spiro-OMETAD under different light intensities on reverse condition.*

The V_{OC} and J_{SC} values are extracted at each light intensity from the JV curves of the device. For the case of the J_{SC} dependence with light intensity, the J_{SC} is fitted to a power law dependence ($J_{SC}\alpha\Phi^{\alpha}$), and it is possible to estimate if there are photocurrent losses under short circuit conditions. Ideally, there are no photocurrent losses under short circuit conditions, if α is equal to 1 (**Figure 2.8b**). On the other side, for the case of the V_{OC} dependence with light intensity, the ideality factor (n_{id}) can be calculated which shows how much the device differs from the ideal diode behaviour. The ideal factor value can be between 1 and 2; when the ideal factor is equal to 1, it means band-to-band recombination and if the n_{id} is equal to 2 which is means the SRH recombination or trap mediated

is predominant (**Figure 2.8a**). The non-ideal diode equation including the net current (J) is in Equation 2.13.

$$J = J_{SC} - J_0\left(e^{\frac{qV}{n_{id}K_BT}} - 1\right) \qquad \text{Equation 2.13}$$

where J_0 is a constant, K_B is the Boltzmann constant, q is the elementary charge, and T is the device temperature. J value will be equal to zero while the device at open-circuit condition, so Equation 2.8. can be converted to Equation 2.14.

$$J_{SC} = J_0\left(e^{\frac{qV_{OC}}{n_{id}K_BT}} - 1\right) \qquad \text{Equation 2.14}$$

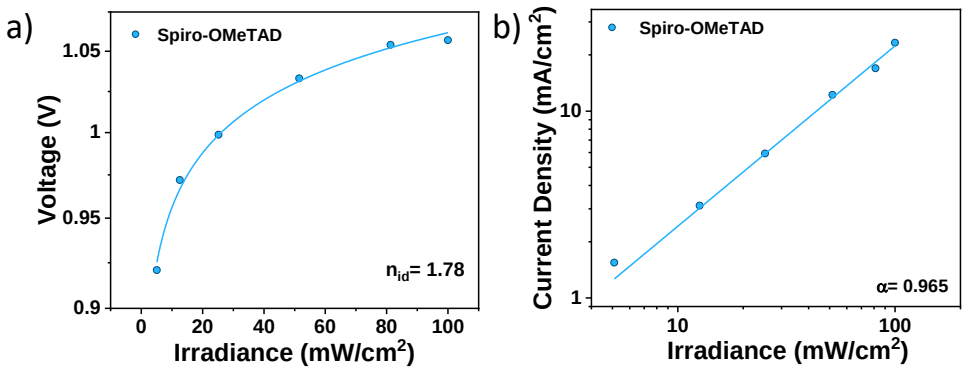

Figure 2.8. *Estimation of the a) The ideal factor and b) The J_{SC} dependence with light intensity obtained from the reverse JV curves on* ***Figure 2.7****.*

In addition, the ideality factor (n_{id}) can be derived from the J_{SC} linear increment linearly with the light intensity through Equation 2.15.

$$V_{OC} = \frac{K_BT}{n_{id}q} In\Phi \qquad \text{Equation 2.15}$$

Hysteresis Index

Hysteresis Index (HI) is fundamentally described as the discrepancy between the two scanned efficiencies, which in turn are derived from the J_{SC}, V_{OC}, and FF of the forward scan ($V \leq 0$ to $V \geq V_{OC}$) and the reverse scan ($V \geq V_{OC}$ to $V \leq 0$) (**Figure 2.9**).[55,183,184] HI value can be calculated by the following formula:

$$Hysteresis\ Index = \frac{PCE\ (reverse) - PCE\ (forward)}{PCE\ (reverse)} \qquad \text{Equation 2.16}$$

Hysteresis in PSCs is an epiphenomenon caused by the presence of both surface charge recombination and/or mobile ionic species.[185,186] From early studies, it has been assumed that ion migration is a possible cause of the slow response; others are ferroelectricity and charge carrier trapping.[55] Afterward, several studies have proven the ion migration hypothesis by modelling and microscopic simulations.[187,188]

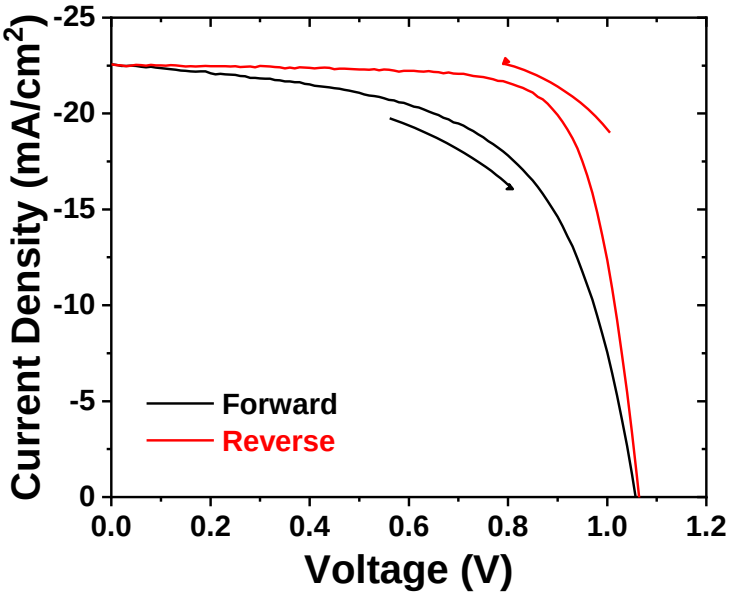

Figure 2.9. *Example of the hysteresis index having the difference at scan direction of the n-i-p architecture perovskite solar cell.*

Hysteresis is one of the obstacles to determine the actual power conversion efficiency of perovskite solar cells. For that reason, many papers assert to increase the device performance by reducing the HI. However, the perovskite solar cell is a dynamic system in nature that is responsive to illumination and external field. In other words, in response to an external field, the mobile ions will react slowly than the voltage sweep, i.e., the changes in the internal field, which adjusts the ion distribution in the absorber. Remarkably, the p-i-n structured device of PSCs have generally a negligible HI when compared to the n-i-p structured device. The most popular explanation for this is associated with ion movement stabilization. The commonly used fullerene in p-i-n structure has been hypothesised to passivate perovskite film's pinholes and grain boundaries.[189] Mobile ions in the perovskite film interact with

fullerene small molecules to form a fullerene halide radical, which is supposed to stabilize electrostatic properties, suppress the electric field prompted anion migration that could possibly cause hysteresis, and thus ensure no hysteresis.[189,190] Hence, it is consensual to report not only the J-V scans of PSCs, but also the quasi-steady state efficiency, i.e., holding the device at approximately the maximum power point voltage and letting the photocurrent stabilise to determine a steady-state efficiency.[183]

2.3.12. Maximum Power Point Tracking of Perovskite Solar Cells

A custom-built high-throughput Ageing Setup is used for the ageing test of perovskite solar cells (**Figure 2.10**).[126] Each cell is individually maximum power point (MPP) tracked by the use of special electronics. A perturb and observe[191] algorithm with a voltage step-width of 0.01 V and a delay time of 1 s is applied to track the MPP. PCE_{MPP} tracking values are automatically recorded for all cells every 2 minutes and normalised to the starting value. During the tracking, the active area is touching a heat pad to ensure direct thermal coupling and Peltier-elements are used for cooling and keep the cells at 25 °C continuously.

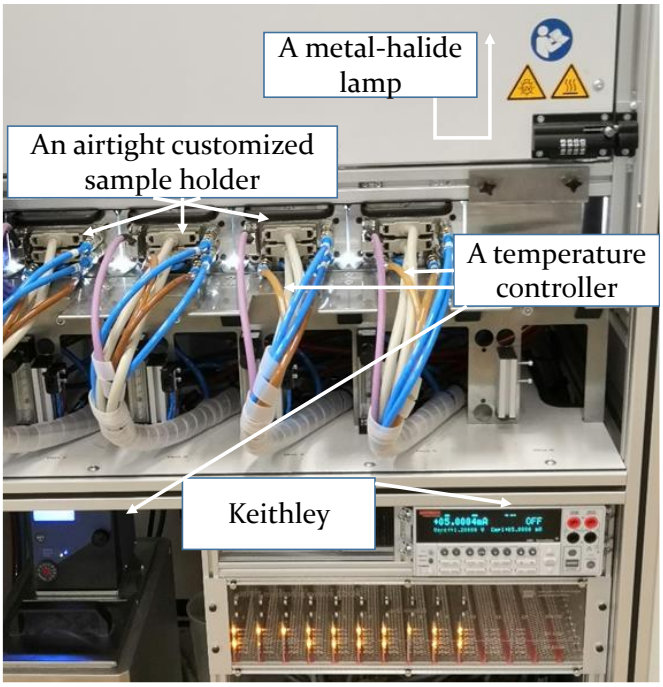

Figure 2.10. *Picture of the custom-built high-throughput Ageing Setup*

MPP tracking of devices is performed without encapsulation and under a continuous flow of nitrogen in a closed box. A metal-halide lamp with H2 filter is used as a light source with 100 mW/cm² intensity. A comparison of the spectrum of the light source with H2 filter to AM 1.5 G is shown in **Figure 2.11a**.

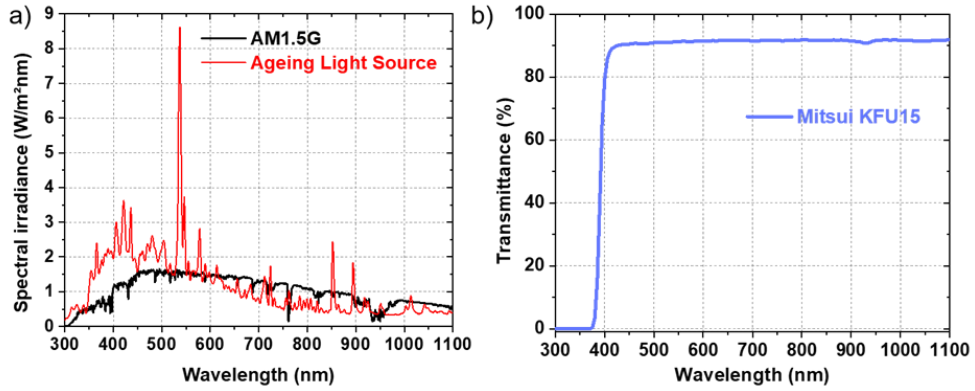

Figure 2.11. *a) Spectrum distribution of the lamp used for MPP tracking ageing test of perovskite solar cells. b) Transmittance spectra of the UV-blocking foil as named Mitsui KFU15.*

The light source intensity is actively controlled using a silicon irradiation-sensor which is itself calibrated using a Silicon reference. For experiments with UV-filter, the UV-blocking foil "KFU15" by Mitsui is used to block UV light with wavelengths below 380 nm. The transmittance of the UV-blocking foil (in text named UV filter) is shown in **Figure 2.11b**. The light source intensity reaching the solar cells tested with UV-filter is measured to be approximately 80 mW/cm² due to the filter and its diffusing properties. The ageing test is in accordance with the ISOS-L-1l protocol. The UV-induced degradation is carried out with a Vilber Lourmat VL-6.L lamp. The power of the UV tube is 6 Watt. All HSLs deposited ITO substrates have been exposed to 365 nm for 30 minutes before perovskite deposition.

2.4. Deposition Techniques of Active Layers

In this section, the experiment procedure of the deposition techniques will be described for each active layer in PSCs.

2.4.1. Spin-coating

The spin-coating has been used for the deposition of thin films for several decades in organic and inorganic photovoltaic devices. A classic process involves depositing a small amount of a fluid solution onto the centre of the substrate and then spinning the substrate at high speed. Centripetal acceleration will cause the solution to spread to, and eventually off, the edge of the substrate leaving a thin film of the solution on the surface of the substrate. In the end, the final thickness of the film will depend on the nature of the solution (viscosity, surface tension, drying rate, etc.). The speed unit of this process is revolutions per minute (rpm) which means the number of turns in one minute. The coated film properties can be affected by the acceleration of the substrate towards the final speed. Particularly, it is important to precisely control acceleration since the solution begins to dry during the first part of the spin cycle. In the first few seconds of the spin-coating process, 50% of the solvents in the solution will be lost to evaporation in some processes.[192]

Spin-coating deposition (**Figure 2.12**) produces uniform SAMs by a simple process where the SAM molecules are first spread over the surface at a certain speed and then rinsed by spin-coater to remove the

remaining extra molecules. The spin-coating method is the most used one to prepare planar PSCs due to its convenient and fast deposition feature.

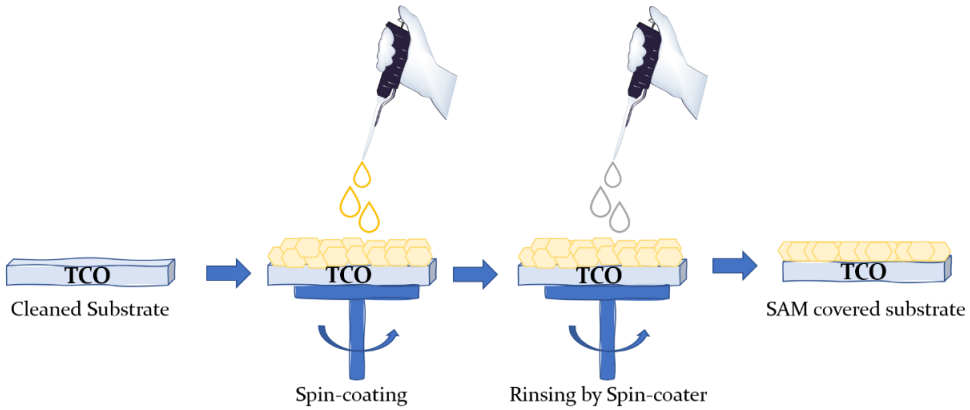

Figure 2.12. *Illustration of the spin-coating method for SAMs.*

The optimised spin-coating process is used for all type of the perovskite layer, some of HSLs and ESLs are reported later in this Chapter (**Figure 2.13**).

Figure 2.13. *Picture of the spin coater which is used for depositing active layers in PSCs*

2.4.2. Dip-coating

Dip-coating is the most widely used technique for laboratory applications which is fundamentally based on simple processing, low cost, and high coating quality between the available deposition techniques. Dip-coating indicates the deposition of a wet liquid film by the withdrawal of a substrate from a liquid coating medium. The wet chemical sol-gel processing paves the way for all kinds of coating materials due to the versatility and ease of liquid film deposition techniques. Liquid film deposition techniques involve the application of a liquid precursor film on a substrate which then is converted to the desired coating material in the following post-treatment step.[193]

Dip-coating method (**Figure 2.14**) is usually applied to mesoporous surfaces and refers to the immersion of the surface in a solution of SAMs where the molecule absorbs chemically. Absorption can be controlled by adjusting solvent, concentration, immersion time, and speed. The extra molecules are later rinsed with solvent by spin coating.

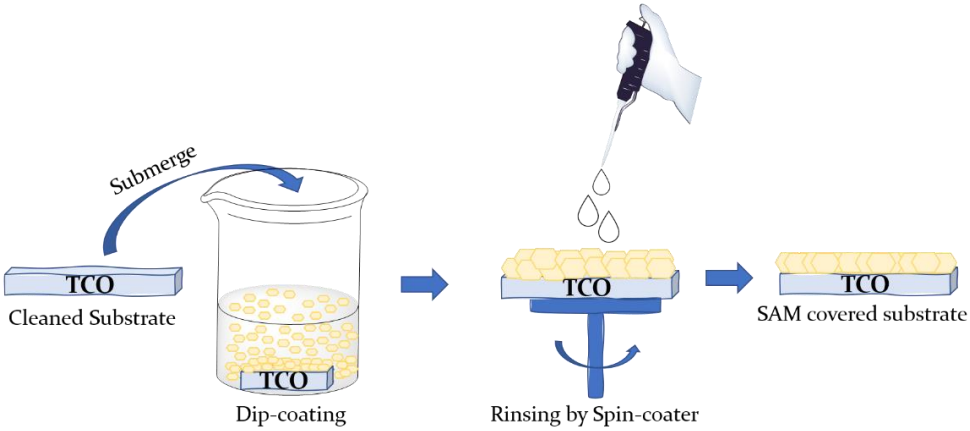

Figure 2.14. *Illustration of the dip-coating method for SAMs.*

In this thesis work, we have used the designed glass beaker which is resized for our substrate's sizes (**Figure 2.15**). This designed beaker ensures the cleaned substrates are immersed vertically in the precursor solution that has a cap to protect the concentration of the solution during the dip-coating process. The UV-O_3 treated ITO covered substrates are immersed in the solution of the SASM during optimised time at room temperature. After the dip-coating process, the substrates are rinsed with the same solvent to get rid of the non-attached molecules or excess molecules from SAM covered surface and they are dried via spin-coating at 3000 rpm for 30 sec. All dip-coating and post-treatment processes are done in a glovebox for protecting the monolayer surface before depositing the perovskite layer. The self-assembled monolayers are stable on the ITO surface in the nitrogen filled glovebox for one week.

Figure 2.15. *Picture of the dip-coating beaker.*

2.4.3. Aerosol Spray Pyrolysis

In the aerosol spray pyrolysis (ASP), usually a series of liquid droplets splash onto the substrates dragged by a gas flow from a beaker containing the source solution, the temperature evaporates the residual solvents, leaving a dry precipitate where a chemical reaction occurs. Yet, the thermodynamic properties of the source solution which contains the intended material will determine whether the initial droplets certainly splash the substrates.[194,195] ASP has a number of positive features. For instance, relatively pure particles in the submicron range and a wide range of chemical compositions can be produced including complex, multi-component systems. Additionally, each droplet performs as a microreactor in which the constituents are mixed on the atomic level thus particle homogeneity is expected. The method has the potential for the continuous creation of particles in one step.[196] ASP method is only applied for having a homogeneous c-TiO_2 layer on top of the FTO substrates (**Figure 2.16**). Its detailed procedure is explained in the section 2.5.4 of this Chapter.

Figure 2.16. *Picture of the aerosol spray method*

2.4.4. Vacuum Thermal Evaporation

The deposition technique of the vacuum thermal evaporation involves heating until evaporation of the material to be deposited is achieved. The material vapour eventually condenses in form of the thin film on the cold substrate surface. The ultra-high vacuum is usually around $9x10^{-7}$ mbar and $2x10^{-6}$ mbar. During the metal or organic material evaporation, a high voltage is passing through a tungsten metal boat or a high temperature crucible, respectively that is filled with the material to be deposited. The substrates are placed upside down (looking at the direction of evaporation) in a substrate holder and protected by a deposition shutter that is in the open position during evaporation process as shown in **Figure 2.17a**. The metals can be evaporated by deposition controller with manual or automatic program and the model of the metal evaporator is INFICON SQC-310C (**Figure 2.17b**). The organic materials are evaporated by deposition controller with only

manual program and the model of the controller is CreaPhys GmbH CU 103 (**Figure 2.17c**).

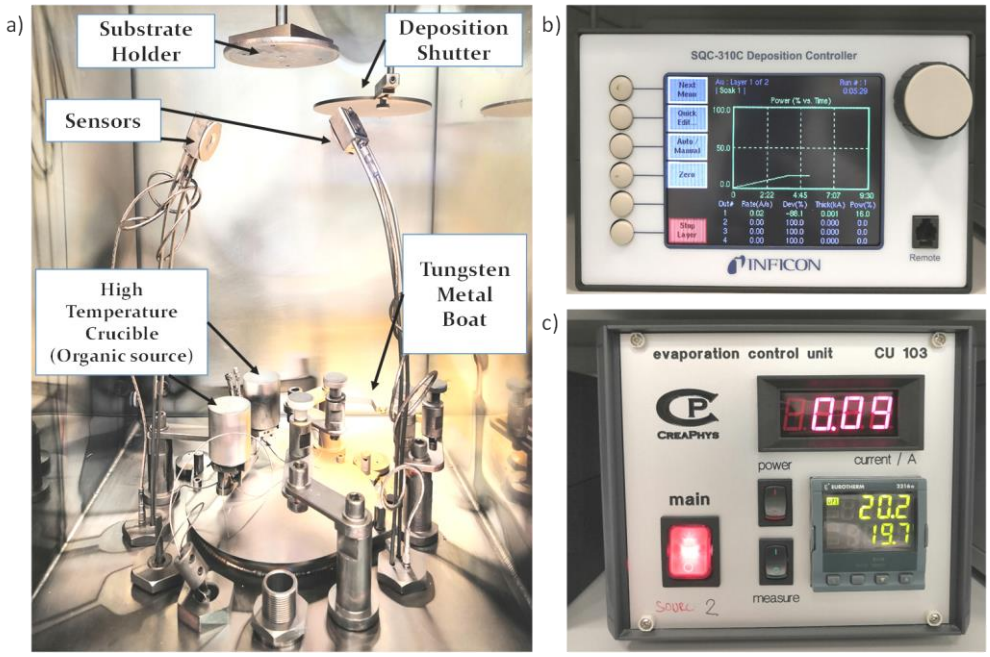

Figure 2.17. *Picture of a) the different parts of evaporator b) the metal deposition controller and c) the organic deposition controller*

2.5. Fabrication of Perovskite Solar Cells

In this section, two different kinds of PSC structures will be described as two of the most employed architectures for achieving high and stable devices. The architecture designs are illustrated in **Figure 2.18**. In this thesis, the novel hole selective layers are employed for both architectures. The deposition procedures of each layer for both types of device structures are mentioned in detail.

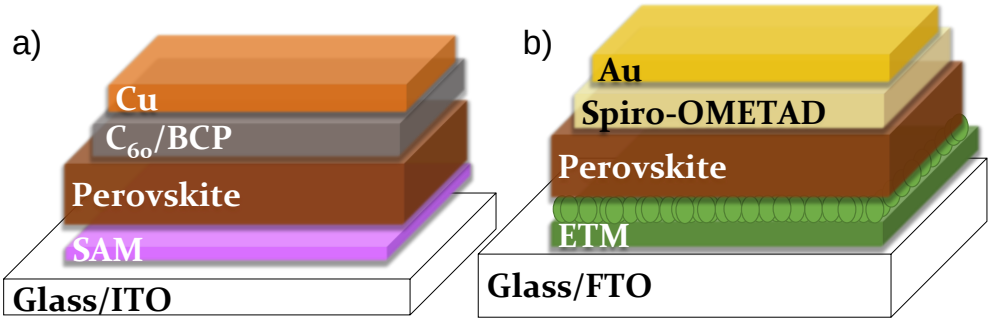

Figure 2.18. *Schematic illustration of the layers involved in the two most typical PSCs structures a) p-i-n planar and b) n-i-p mesoscopic*

2.5.1. Cleaning of the Transparent Conducting Oxides Covered Glass Substrates

For both type of PSCs, we have used general cleaning method for all ITO and FTO covered glass substrates. The cleaning of the substrates is crucial to avoid oily impurities and dusts which can cause unfavourable consequences for the final performance of the perovskite solar cells.

The patterned ITO/FTO glass substrates are cleaned for 15 minutes with Mucasol 2% solution in deionised water, acetone, and isopropanol in an ultrasonic bath, respectively at 50 °C. After physical cleaning, the cleaned layers are dried well before treated in a UV-O_3 cleaner for 15 min. After UV-O_3 treatment, the ITO/FTO substrates are immediately used in the next step or transferred to N_2 filled glovebox if the next step should be done in an inert atmosphere.

2.5.2. Hole Selective Layers

We have used just organic commercially available HSLs for comparing with our synthesised small molecules in this thesis. Spiro-OMeTAD, PEDOT:PSS and PTAA are used as a reference HSL in Chapter 3 & Chapter 7, Chapter 4 and Chapter 5 & Chapter 6, respectively.

The PEDOT:PSS is a well-known HSL for organic and lead halide perovskite photovoltaic devices. The drawbacks and the advantages of it are explained in Chapter 1. The PEDOT:PSS layer is coated via spin-coating onto the UV-O_3 treated ITO by using a two-step method (1st step; 4500 rpm. 30 seconds and 2nd step; 3500 rpm. 30 seconds). The final thickness of PEDOT:PSS is around 35 nm after the annealing process at 130 °C for 30 min. The deposition and annealing steps of PEDOT:PSS are employed in the clean room to remove residual water from surface. After this step, the substrates are directly transferred to a glovebox for depositing the perovskite layer.

In recent years, PTAA is the most common HSL in the p-i-n configuration of PSCs because it gives higher PCE compared to PEDOT:PSS. PTAA's HSL properties are mentioned with instances from literature in Chapter 1. To make PTAA layers, PTAA is dissolved at a concentration of 2 mg/mL in dry toluene. The deposition of PTAA layer is performed by spin-coating at 5000 rpm for 30 seconds and then annealed at 100 °C for 10 minutes. The solution preparation and deposition steps of PTAA are done in the N2-filled glovebox due to its oxygen and humidity sensitivity. The thickness of PTAA layer (10 nm) is an important parameter for having favourable wettability in order to

achieve the perovskite layer without pinholes onto the PTAA layers. Additionally, PTAA can be used as a HSL in n-i-p configuration of the PSCs instead of Spiro-OMETAD.

Spiro-OMeTAD is the most celebrated HSL in n-i-p configuration of the PSCs which is deposited on top of the perovskite layer as mentioned in Chapter 1. A 60 mM Spiro-OMeTAD solution in chlorobenzene is doped with dopants such as *t*BP, LiTFSI, and FK 209 Co(III)TFSI to enhance its HSL properties. The molar ratio of the solution is 1 Spiro-OMeTAD: 3.3 *t*BP:0.5 LiTFSI (from a 1.8 M stock solution in ACN): 0.05 FK 209 Co(III)TFSI (from a 0.25 M stock solution in ACN). After added all the dopants to the Spiro-OMeTAD solution, a PTFE (0.2 μm) filter is used for eliminating aggregations or not solved materials before spin-coating process. After deposition of the Spiro-OMeTAD layer, all substrates are transferred to the dry box with a 10% relative humidity, and they are stored there overnight. The FTO side of the substrates is cleaned to avoid a short circuit after metal deposition. A sharp razor and a cotton swap with DMF are used just before metal contact deposition.

Deposition Methods of Self-Assembled Small Molecules

Most of the self-assembled small molecules (SASM) are usually easily soluble in non-halogenated organic solvents for using dip-coating and spin-coating deposition methods. In addition, SASM solution temperature is raised up to 60 ˚C for increasing solubility in non-halogenated organic solvents before the dip-coating or spin-coating processes.

Deposition of Self-Assembled Small Molecules by Dip-Coating

The general molarity of SASM is approximately 0.1 mM for dip-coating method. The treated ITO substrates are fully submerged in the solutions for dip-coating method. After 4 hours of dipping, the SASM-HSL films onto ITO substrates are dried from excess solution. Afterwards, 500 µL of fresh anhydrous solvent, the same one used for preparing SASM solution, are poured onto SASM-HSL covered ITO, followed by spin coating at 3000 rpm for 30 s. This washing step is a necessary and easy way for removing non-bonded SASMs from metal oxide surfaces.

Self-Assembled Small Molecules Deposition by Spin-Coating

The general molarity of SASM is around 1 mM in solvents for spin-coating. EADR04 did not show good results with the spin-coating method due to its low solubility. The precursor solution is filtered with the PTFE (0.2 µm) filter to eliminate aggregates or insoluble materials before spin-coating.

For the spin-coating method, 100 µL of the SAM solution is homogeneously poured onto the UV-O_3 treated ITO and deposited by spin-coating at 3000 rpm for 30 seconds. The washing step or any post-treatment as thermal annealing is not applied after deposition of SASM by spin-coating.

2.5.3. Perovskite Layers

One-Step MAPI Deposition for n-i-p Structure

All perovskite solutions are prepared in a N_2-filled glovebox. The n-i-p configuration PSCs based on MAPI perovskite and prepared with one-step deposition technique in Chapter 3. The concentration of the MAPI solution is 1.25 M. To prepare the solution, first, the required amount of PbI_2 is weighed and dissolved in DMSO. To increase the solubility of the lead salt, we heat the solution up at 150 °C for 10 minutes. Then, the solution is cooled down to room temperature and the methylammonium iodide (MAI) is added.

It is especially important to control the atmosphere and the solvent vapours inside the glovebox. Hence, the work is carried out with a continuous N_2 flow that removes the dimethyl sulfoxide (DMSO) vapours.

The deposition of the perovskite solution is carried out using the antisolvent treatment. First, 40 µl of the perovskite solution is spin-coated with a two-step program. First, 1000 rpm for 10 s using an acceleration of 500 rpm, and then 4000 rpm for 30 s with an acceleration of 500 rpm. 10 seconds before the spinning process ends, 100 µl of chlorobenzene is spin-coated right on the centre of the spinning substrate. The films are annealed for 45 minutes at 100 °C.

Two-Step MAPI Deposition for p-i-n Structure

The p-i-n configuration PSCs are based on MAPI composition and prepared with a two-step deposition technique in Chapter 4. In the first step, 80 µl of 1M filtered PbI_2 in a mixture of anhydrous DMF:DMSO (9:1; v:v) is deposited on top of HTMs for 90 seconds. In the second step, 100 µL of 0.32 M filtered MAI in anhydrous isopropanol is statically dripped onto the PbI_2 coated substrate during the last 30 seconds of the spinning. PbI_2 solution is stirred at 50 ˚C for 1 hour. All the solutions are filtered with a PTFE filter (0.22 µm). When the coated process is over, the substrates are directly moved onto a hotplate and are annealed for 10 min at 100 ˚C. The perovskite layer thickness is around 350 nm.

CsFAMA Perovskite Deposition for p-i-n Structure

The triple cation perovskite [$(Cs_{0.05}FA_{0.79}MA_{0.16}Pb(I_{0.84}Br_{0.16})_3$] onwards labelled as CsFAMA, is prepared according to M. Saliba et al.[15] procedure, what refers to using an anti-solvent deposition technique for p-i-n configuration (see Chapter 5 and 6). Briefly, $PbBr_2$ (1.5 M) and PbI_2 (1.5 M) are dissolved in a mixture of anhydrous dimethylformamide (DMF): dimethyl sulfoxide (DMSO) (4:1 volume ratio) and added to formamidinium iodide (1.09:1 molar ratio) and methylammonium bromide (1.09:1 molar ratio) powders respectively, to obtain $MAPbBr_3$ and $FAPbI_3$ solutions with a final concentration of 1.24 M. These two solutions are then mixed in a 17:83 volume ratio. Finally, the cesium cation is added from a 1.5 M CsI solution in DMSO in a 5:95 volume ratio. The perovskite solution is spin-coated on top of the HTM layer using the following program: 4000 rpm (5 s acceleration) for 35 s (program's total

time is 40 s). After 25 s, 250 µl of anisole is dropped on the spinning substrate to promote fast solvent-removal forming a smooth and compact layer. After the spin-coating program, the perovskite-coated sample is annealed at 100 °C for 60 min.

CsFAMA Perovskite Deposition for n-i-p Structure

The CsFAMA [$(Cs_{0.05}FA_{0.79}MA_{0.16}Pb(I_{0.84}Br_{0.16})_3$] layer is prepared with an anti-solvent deposition technique for n-i-p configuration (Chapter 7). Firstly, PbBr2 (1.5 M) and PbI2 (1.5 M) are dissolved in a mixture of anhydrous DMF:DMSO (4:1 volume ratio) and added to formamidinium iodide (1.09:1 molar ratio) and methylammonium bromide (1.09:1 molar ratio) powders respectively, to obtain $MAPbBr_3$ and $FAPbI_3$ solutions with a final concentration of 1.24 M. These two solutions are then mixed in a 17:83 volume ratio. Secondly, the cesium cation is added from a 1.5 M CsI solution in DMSO in a 5:95 volume ratio. The perovskite solution is spin-coated on top of the HSL using the following 2 step program: first is at 2000 rpm/s with 2000 rpm/s acceleration for 12 seconds, the second one is 6000 rpm/s with 2000 rpm/s acceleration for 23 seconds (program's total time is 35 s). After 30 s, 300 µl of anisole is dropped on the spinning substrate to promote fast solvent-removal forming a smooth and compact layer. After the spin-coating program, the perovskite-coated sample is annealed at 100 °C for 60 minutes.

2.5.4. Electron Selective Layers

The Compact TiO_2 Layer Prepared by Spin-Coating

The compact TiO2 layer is deposited by spin-coating on top of the UV-O_3 treated FTO. A 0.3 M titanium diisopropoxide bis(acetylacetonate) (75 wt.% in isopropanol) ($Ti(iPrO)_2(acac)_2$) solution is prepared in dry isopropanol. The solution is deposited onto the FTO substrates and the compact TiO_2 layer is formed on it by spin-coating at 4000 rpm for 25 seconds with an acceleration of 1000 rpm/s. The coated substrates are pre-annealed at 125 °C for 5 minutes right after the spin-coating process. Then, the pre-annealed substrates are transferred into a hot plate and sintered at 450 °C for 30 minutes.

The Compact TiO_2 Layer Prepared by Spray Pyrolysis

A compact TiO_2 layer is deposited by aerosol spray pyrolysis using oxygen as a carrier gas as mentioned in the section of deposition techniques of active layers. The precursor solution of the compact TiO_2 film is prepared using 0.480 mL of acetylacetone, 0.720 mL of ($Ti(iPrO)_2(acac)_2$) (75 wt.% in isopropanol) and 10.8 mL of absolute ethanol (EtOH). The total amount (12 mL) of the precursor solution is sufficient for 24 substrates. After UV-O_3 treatment, the substrates are heated to 450 °C and kept at this temperature for 15 min. Once the deposition of the compact TiO_2 by aerosol spray pyrolysis is over, the substrates are sintered at the same temperature for 30 minutes. The whole precursor solution is sprayed from the substrates at a distance of

20 cm with an inclination of 45 degrees, with at least 20 seconds of delay between each spray cycle.

The Mesoporous TiO_2 Layer Deposited by Spin-Coating

The mesoporous TiO_2 is deposited on top of the compact TiO_2 by spin-coating at 4000 rpm for 10 second and 2000 rpm acceleration. The solution of the TiO_2 paste (30 nrd) is prepared using 0.3 g per 2 mL of absolute ethanol (125 mg/mL) and the paste is well dissolved under stirring. The dispersed solution of the mesoporous TiO_2 should be prepared at least one day before use and can be kept under stirring all the time. The coated substrates are pre-annealed at 125 °C for 5 minutes right after the spin-coating process. Then, the pre-annealed substrates are transferred into a hot plate and sintered at 450 °C for 30 minutes. The final thickness of the mesoporous TiO_2 is around 150-200 nm.

Lithium Surface Treatment by Spin-Coating

Lithium bis(trifluoromethanesulfonyl)imide (LiTFSI) is deposited onto the TiO_2 covered substrates just before the deposition of the perovskite layer for the studies in Chapter 7. Its positive effect on the hysteresis and the photovoltaic performance of the PSCs are explicated in Chapter 1. The concentration of the LiFTSI solution is 3 mM. The required amount of LiFTSI salt is dissolved in acetonitrile. The LiFTSI layers are prepared by spin-coating at 3000 rpm/s for 10 sec and 1000 rpm/s acceleration. The coated substrates are pre-annealed at 100 °C for 5 minutes right after the spin-coating process. Later, the pre-annealed substrates are transferred into a hot plate and sintered at 450 °C for 30 minutes.

The $TiCl_4$ Post Treatment Achieved by Chemical Bath Deposition

This treatment is applied right after the deposition of the compact TiO_2 which is deposited by spin-coating for the studies in Chapter 3. Once the compact TiO_2 covered substrates are cold down to room temperature, they are dipped into a 40 mM $TiCI_4$ solution at 70 °C for 30 minutes. Then, the immersed substrates are rinsed with DI water and ethanol and dried with a compressed air. If the mesoporous TiO_2 is deposited right after this step, the calcination is not needed. If the substrates will be stored for the following step, the sintering step will be repeated at 450 °C for 30 minutes.

The Carbon 60 and Bathocuproine Layer by Thermal Evaporation

Carbon 60 (C_{60}) is preferred as an ESL in the p-i-n configuration of the PSCs as described in Chapters 4, 5 and 6. 23 nm of C60 are evaporated on top of perovskite layer with rate of 0.5-0.2 Å/s. The BCP is evaporated on top of the C60 layer as a buffer layer with an optimised thickness of 9 nm.

2.5.5. Metal Electrodes

The metal electrode is deposited onto the different active layers for completing the perovskite solar cells. Gold (80 nm), silver (100 nm) or copper (100 nm) are deposited using thermal evaporation under ultra-high vacuum ($1x10^{-6}$ mbar). To define the active area of the cells, a pattern mask is used during metal evaporation. The active area of the cell is 0.09 cm^2 in Chapters 3, 4 and 7. The active area of the cell is 0.16 cm^2 in

Chapters 5 and 6. All the metal electrodes are evaporated with rate lower than 1 Å/s.

2.6. Optoelectronic Transient Techniques

In this section, the optoelectronic transient techniques, such as photo-induced charge extraction (PI-CE), photo-induced transient photovoltage (PI-TPV), and photo-induced transient photocurrent (PI-TPC) will be described. These techniques give useful information about carrier transport, accumulation, and recombination kinetics in completed devices. Doing measurements with completed devices offers the advantage of having comparable results of devices operating under practical conditions which is of outmost importance to understand the behaviour of PSCs. The photovoltaic performance of the PSCs can be affected by light soaking and the application of a voltage bias is mentioned in Chapter 1.

2.6.1. Photo-Induced Charge Extraction

Photo-induced charge extraction (PI-CE) is one of the techniques that is carried out under operational conditions and it is designed to measure the stored charge in the solar cell.[197] Here, the solar cell's V_{OC} is stabilised in the J-V curve at one point under illumination and the stabilization of V_{OC} can take time due to the presence of mobile ions in the completed PSCs, as explained in Chapter 1. Then, the solar cell is switched to the short circuit through a small and known resistance (50 Ω) and the light

source is simultaneously switched off after V_{OC} is balanced. After stabilisation, there is a current transient owing to the solar cell discharged through the contacts .[198,199]

Schematic diagram of charge extraction measurement is illustrated in **Figure 2.14a**. To be examined, the solar cell is positioned ahead of a white LED (LED from LUXEON Lumileds and powered by an Aim-TTi PLH120-P power supply) and the intensity of the white LED can be regulated to determine the V_{OC} of the solar cell. In the first microseconds, most of the free charges flow through the resistor to create a current, and a voltage drops within it. An oscilloscope (Yokogawa DLM2052 with an internal resistance of 1 MΩ) is connected to the solar cell to measure the transient voltage over time.

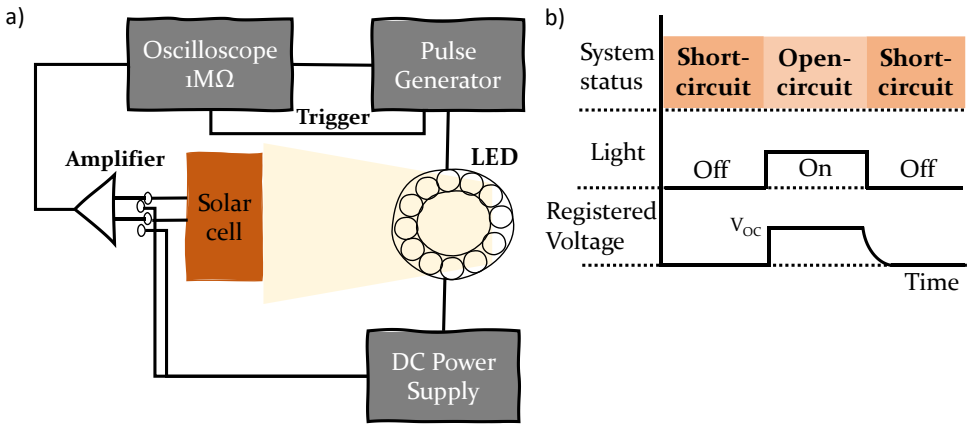

Figure 2.19. *Schematic diagram of a) PI-CE measurement b) PI-CE measurement process.*

An important issue to be addressed here is that CE extracts all the kinds of charges like ionic, carriers, and geometrical charges which are present at the device at a given voltage. For that reason, charge extraction must

be faster than the carrier recombination to prevent charge losses before the solar cell is short-circuited.[200]

Ohm's law can be used to estimate the charge in the solar cell integrating the transient voltage over time as shown in **Figure 2.19b** and Equation 2.17:

$$Q = \frac{1}{R}\int_{t=0}^{t=t} V(\mathrm{t})dt \qquad \text{Equation 2.17}$$

Where Q is the charge, R is the small resistance (50 Ω), and V (t) is the voltage at a given time. The example reported in **Figure 2.20** has two different regions; the linear part that belongs to the linear dependence which is already defined in perovskite solar cells as geometrical capacitance (C_{geo}), and the exponential part that is related with the chemical capacitance in the solar cell.[201,202]

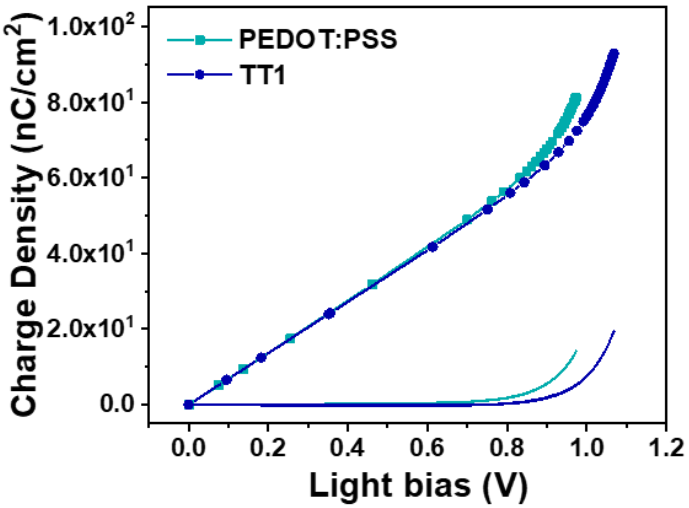

Figure 2.20. *Total charge density (symbolised line) at different V_{OC} which includes carriers in the contacts and bulk. Charge density (solid line) at different light bias without C_{geo} represents only the experimental part of the fits: $y = Be^{Cx}$ (chemical capacitance).*

In solar cells, the accumulation of charges within the electrodes and the selective contacts is defined as C_{geo}. Geometrical capacitance follows a parallel plate capacitor model:

$$Q = C_{geo}V = \frac{\varepsilon_0 \varepsilon_r A}{d} V \qquad \text{Equation 2.18}$$

where A is the active area of the plate of the capacitor, ε_0 is the electric constant, ε_r is the relative permittivity, and d is the distance between the two plates.

On the contrary, the selective contact is drained at higher illumination and the charges start accumulating in the perovskite bulk giving rise to the chemical capacitance. The charge extracted follows the Maxwell-Boltzmann distribution:

$$Q = Q_0 \left[\exp\left(\frac{qV}{mK_BT}\right) - 1\right] \qquad \text{Equation 2.19}$$

where K_BT/q is the thermal voltage, Q_0 is the charge density and m is a factor related with the deviation from the thermal voltage.[203] We obtain zero charge for zero voltage with the subtraction of 1 to the exponential factor.[204,205] Finally, we obtain an expression for the charge extraction as a function of the voltage when Equation 2.18 and Equation 2.19 are combined (Equation 2.20):

$$Q = C_{geo}V + Q_0 \left[\exp\left(\frac{qV}{mK_BT}\right) - 1\right] \qquad \text{Equation 2.20}$$

2.6.2. Photo-Induced Transient Photovoltage

Photo-induced transient photovoltage (PI-TPV) is a time-resolved technique that has been applied in photovoltaic devices to study carrier recombination processes.[206,207] In this technique, the photovoltaic device, which is in open-circuit, is excited by a fast and small perturbation of incoming light that can be directly associated to a small perturbation of the quasi-Fermi level.[208] To perform PI-TPV, the photovoltaic device is held at an open-circuit under a continuous light source to probe the recombination lifetime under working conditions which also promotes a constant and stabilised V_{OC}. The device is kept at an open circuit, the current could not flow through the contacts while it is connected to an oscilloscope that can register the changes in voltage in overtime as shown in **Figure 2.21a**. When the V_{OC} is stabilised, the device is excited with a short-lived laser pulse which causes the generation of a small perturbation of the V_{OC}, as represented in **Figure 2.21b**.

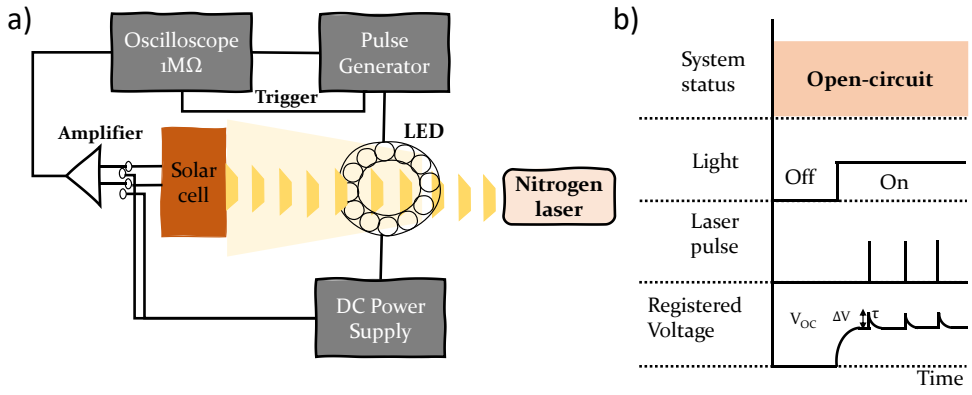

Figure 2.21. *Schematic diagram of a) photo-induced transient photovoltage (PI-TPV) measurement b) PI-TPV measurement process.*

A nanosecond nitrogen laser (PTI GL-3300) has been used to allow us to control excitation wavelength using different organic dyes. For this thesis studies, the emission of Rhodamine 6G (R6G) at 590 nm is employed as an excitation wavelength. An analogue function generator (Aim-TTi TG330) has been used to trigger the pulse that generates a square wave pulse with a duration of 1.5 ns. A semi-transparent optical filter has been used to adjust the intensity of the laser pulse to validate a small perturbation regime. The extra carriers produced by the laser pulse are forced to recombine since the device is in open circuit conditions and cannot be extracted, this leads to the registration of the transient respect to the initial V_{OC}. It is possible to compare a small perturbation lifetime ($\tau_{\Delta n}$) with V_{OC} (**Figure 2.21b**):

$$\tau_{\Delta n} = \tau_{\Delta n0} exp\left(-\frac{qV_{OC}}{\theta K_B T}\right) \qquad \text{Equation 2.21}$$

where $\tau_{\Delta n0}$ is the equilibrium carrier lifetime, θ is the deviation from the thermal voltage (K_BT/q). In **Figure 2.22a**, the $\tau_{\Delta n}$ is obtained from the monoexponentially fitting of the photo-induced transient decay which is directly associated with the recombination rate.

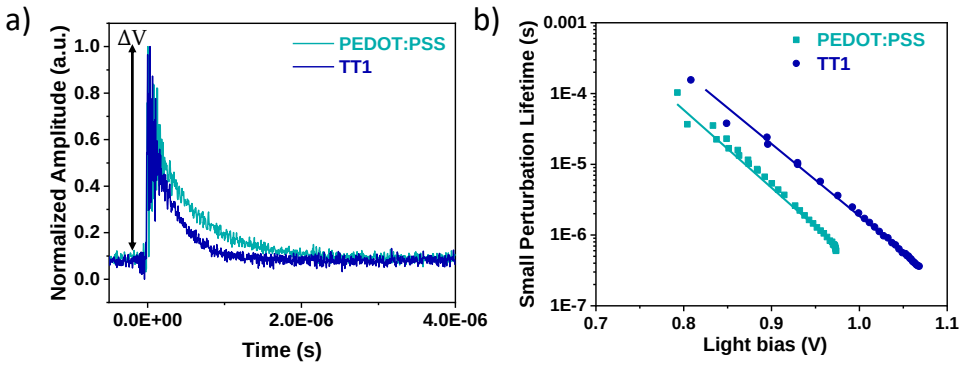

Figure 2.22. *Example of a) the intensity of the small perturbation (ΔV) and the small perturbation lifetime ($\tau_{\Delta n}$) decay extracted from PI-TPV b) plot of the $\tau_{\Delta n}$ as a function of the different light bias applied (symbolised line) and the exponential fit to Equation 2.21 (solid line).*

2.6.3. Photo-Induced Transient Photocurrent and Differential Capacitance

The photo-induced transient photocurrent (PI-TPC) measurement setup is quite similar to the PI-TPV measurement setup, except that the device is kept in short-circuit conditions and is connected to a small resistance (50 Ω). In principle, this technique allows us to predict the extra carriers generated by the small perturbation induced via the laser pulse (ΔQ).[198,209] The laser pulse creates a small perturbation in the device current measured in the oscilloscope as a voltage drop across the resistor that is easily converted into a transient current using Ohm's law. The amount of the charges generated by the nitrogen laser pulse are measured and integrated over time with this transient current as shown in **Figure 2.23**.

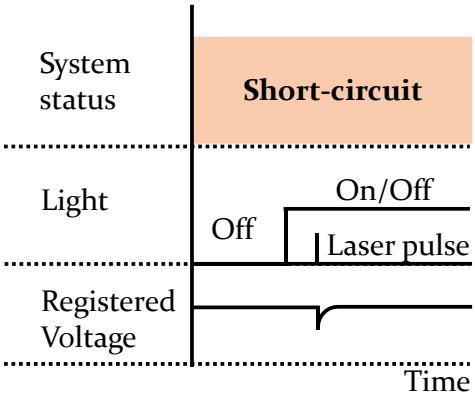

Figure 2.23. *PI-TPC measurement processes*

On the other hand, the PI-TPC technique has limitations since it is only valid when charge carrier losses are insignificant under short circuit conditions, hence the charge collection process is not affected by carrier recombination. Three different measurements need to be checked to prove it:

Firstly, the J_{SC} dependence of the device with the light intensity which is defined in this Chapter's section 2.3.11 must fit a power law. This means that there is no significant carrier loss in a short circuit. Secondly, the PI-TPC decays must be similar under different light irradiation conditions; this means the charges generated by the laser pulse must be independent of the background light intensity. Lastly, carrier collection must be faster than carrier recombination; this means the PI-TPC decay is faster than the PI-TPV decay. The PI-TPC technique can be used to estimate the charge density in the device via the differential capacitance (DiffCap) method, if all these requirements are fulfilled. DiffCap method is used to estimate the charge density in the device and mainly combines the data acquired from PI-TPV and PI-TPC measurements.[209] From PI-TPV

technique we obtain the intensity of the perturbation generated by the laser pulse at every light intensity (ΔV). From PI-TPC technique we estimate the created charges by the laser pulse (ΔQ), which should be the same at different light intensities, as we have already mentioned. Then, DiffCap permits us to calculate the capacitance of the device at different light biases through Equation 2.22.

$$C(V_{OC}) = \frac{\Delta Q}{\Delta V} \qquad \text{Equation 2.22}$$

In DiffCap method, two different regimes are noticed which are described in the PI-CE (see section 2.6.1.). When the contacts are drained with charges, they start accumulating in the perovskite bulk, giving rise to a chemical capacitance resulting in an exponential trend.[210] After all, when we take an integration of DiffCap at every voltage by using Equation 2.17., it gives us an estimation of the stored charges in the device. The stored charges in the device can be correlated with the increasing voltage using Equation 2.20.

$$Q(V_{OC}) = \int_0^{V_{OC}} C(V_{OC}) dV_{OC} \qquad \text{Equation 2.23}$$

In addition, if we compare the obtained small perturbation lifetime from the PI-TPV experiments with the obtained charge density from the CE or DiffCap tests, this comparison allows us to make a fair assessment between different devices. Moreover, from this experiment, the recombination order (δ) can be acquired allowing us to calculate the total carrier lifetime (τ).[211,212] Initially, to acquire the recombination order, the values of a small perturbation lifetime around 1 sun should be compared and fitted with a power law dependence:

$$\tau_{\Delta n} = \tau_{\Delta n0} \left(\frac{Q}{Q_0}\right)^{-\lambda} \qquad \text{Equation 2.24}$$

where $\tau_{\Delta n0}$ is the equilibrium small perturbation lifetime, Q_0 is the charge density, λ is a parameter which describes the slope of the power law and is correlated with the recombination order as $\delta=\lambda+1$.[211] We have subtracted the value of C_{geo} while using the charge density to study the processes in the bulk of the perovskite.

Ultimately, the recombination order ($\tau=\tau_{\Delta n}\cdot\delta$) can be used for converting the small perturbation lifetime ($\tau_{\Delta n}$) to the total carrier lifetime (δ).[211] Herewith, it is possible to acquire a significant comparison of the recombination rates between different devices from the total carrier lifetime values.

Experimental Procedures and Methods

Chapter 3

Truxene Derivatives as Lewis Base Interlayers in Perovskite Solar Cells

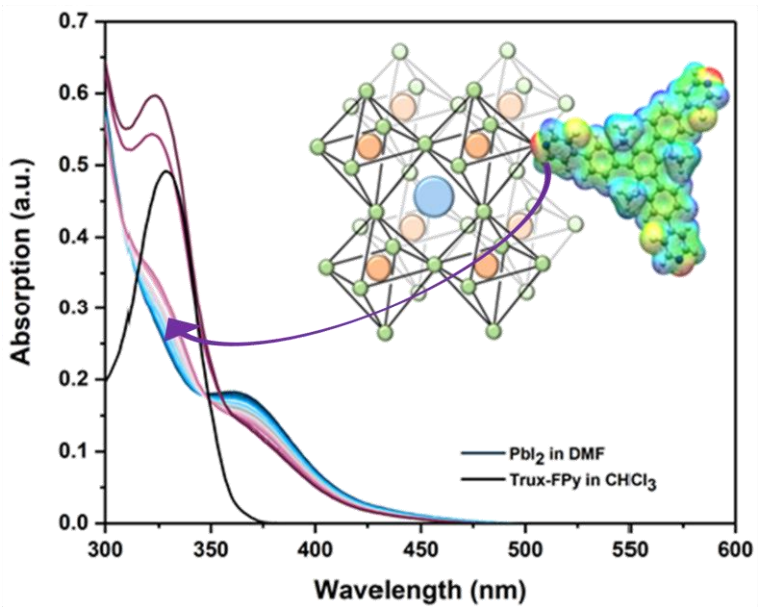

This chapter is based on the published work: Aktas, E. et al. Supramolecular Coordination of Pb^{2+} Defects in Hybrid Lead Halide Perovskite Films Using Truxene Derivatives as Lewis Base Interlayers. ***ChemPhysChem*** 20, 2702–2711 (2019).[213]

3.1. Abstract

Truxene derivatives are good candidates for the passivation of defects when deposited onto hybrid lead halide perovskite thin films owing to their molecular structure and properties. Moreover, their semiconductor characteristics can be tailored through the modification of their chemical structure, which allows -upon light irradiation- the interfacial charge transfer between the perovskite film and the truxene molecules. In this chapter, we investigated the use of the molecules as surface passivation agents and their effect in completed solar cells. We observed that these molecules reduce the nonradiative carrier recombination dynamics in the perovskite thin film through the supramolecular complex formation between the truxene molecule and the Pb^{2+} defects at the perovskite surface. Interestingly, this supramolecular complexation neither affect the carrier recombination kinetics nor the carriers collection but induced noticeable hysteresis on the photocurrent *versus* voltage curves of the solar cells under 1 sun illumination.

3.2. Introduction

The passivation of defects is one of the keys to increase the solar cell efficiency in inorganic or hybrid photoactive thin films. The defects induce a change in the solar cell voltage reducing the energetic difference between the quasi-Fermi levels because of an increase of the carrier recombination and the solar cell photocurrent, because less photo-generated carriers are extracted. Lately, in hybrid lead halide perovskite

Truxene Derivatives as Lewis Base Interlayers in Perovskite Solar Cells

materials, many research groups have started to study the effect of molecules, as additives, to reduce the presence of surface defects.

The truxene scaffold has an excellent thermal stability; a must when incorporated into organic electronic devices.[214,215] Their molecular structure allows their deposition at the surface of the perovskite in face-to-surface configuration with strong interaction with the perovskite semiconductor surface. A similar approach has been observed for graphene oxide layers.[83] Moreover, the introduction of 3-fluoropyridine substituents will act as a Lewis base to passivate the non-coordinated Pb^{2+} ions present at the surface of the perovskite.

In this work, we synthesised a new truxene derivative, 4,4',4''-(5,5,10,10,15,15-hexahexyl-10,15-dihydro-5*H*-diindeno[1,2-a:1',2'2-c]fluorine-2,7,12-triyl)tris(3-fluoripyridine) (Trux-FPy). We evaluated its optical and electronic properties for PSCs. Furthermore, we do have deposited a thin film of Trux-FPy on top of the MAPI hybrid perovskite and studied its role as a Lewis base to passivate perovskite defects. Finally, we measured the performance of completed perovskite solar cells and the effect of the Trux-FPy thin film as interfacial layer between the perovskite and the hole selective material.

3.3. Results and Discussions

3.3.1. Design and synthesis

The syntheses of 1a, 1b, and 1 is carried out following the scientific literature. Our ^{1}H and ^{13}C NMR data were in good agreement with those values previously reported.[81,216,217] The truxene core (1a) is first synthesised through the condensation of 1-indanone in acetic acid (AcOH) and concentrated hydrochloric acid (HCI). Then, alkylation reaction is carried out with 1-bromohexane ($CH_3(CH_2)_5Br$) and $^{t}BuOK$ in THF to increase truxene core (1b) solubility. The bromination reaction of truxene core is performed with dibromine (Br_2), iron(III) chloride ($FeCl_3$) in CF, resulting in 1 in 93% yield. The 3-fluoro-4-pyridine is then introduced by the Suzuki cross coupling reaction with sodium carbonate (Na_2CO_3) and tetrakis(triphenylphosphine)palladium(0) [$Pd(PPh_3)_4$] in dry THF, resulting in Trux-FPy in 46% yield. The detailed syntheses procedure is described in section 3.5 and the syntheses pathway is shown in **Scheme 3.1**.

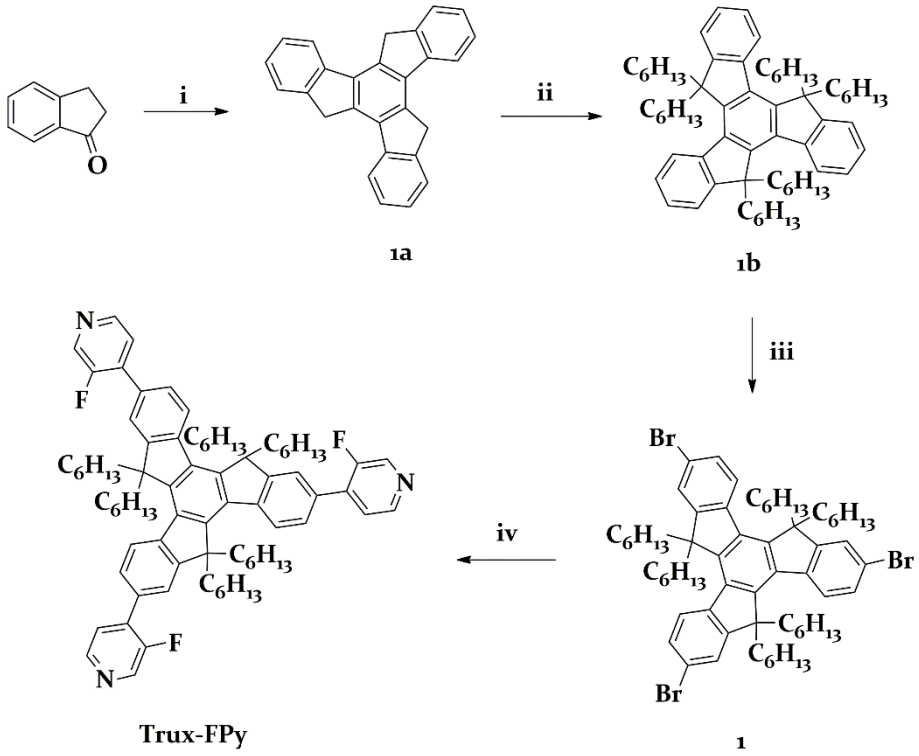

Scheme 3.1. *Synthetic route for the Trux-FPy. (i) AcOH, HCI (ii) ^{t}BuOK, $CH_3(CH_2)_5Br$, THF (iii) $FeCl_3$, Br_2, $CHCl_3$ (iv) 3-fluoro-4-pyridine boronic acid pinacol ester, Na_2CO_3, $Pd(PPh_3)_4$, dry THF.*

3.3.2. Thermal, Optical, and Electrochemical Properties

In this section, the main properties of Trux-FPy as an interlayer material will be discussed to understand whether they are good candidates for use in perovskite solar cells.

The thermal behaviour of Trux-FPy is analysed by TGA and DSC measurements. All the recorded data are shown in **Table 3.1**. The decomposition temperature (T_{des}) is determined around 404 °C for Trux-

FPy which is slightly lower than the employed hole selective layer that is Spiro-OMeTAD (424 °C).[218] High decomposition temperature is required for charge selective and/or interfaces layers when the photovoltaic device needs a high-temperature fabrication process. The TGA curve for Trux-FPy is shown in **Figure 3.1a**.

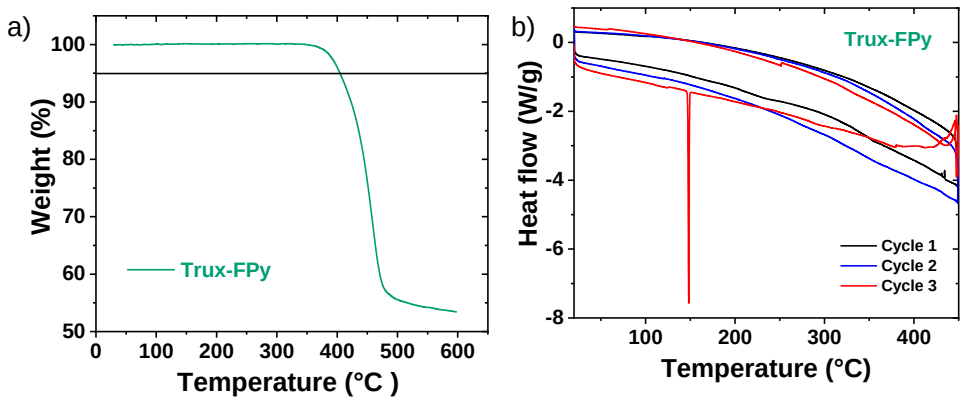

Figure 3.1. *The analysis of a) TGA and b) DSC for Trux-FPy.*

The chemical and physical changes of Trux-FPy under high temperature is determined by DSC. The melting and/or crystallisation peak is not observed during the first and second heating cycles. In the third heating cycle, the T_g value is determined for Trux-FPy around 150 °C as shown in **Figure 3.1b**.

Table 3.1. *Thermal properties of Trux-FPy.*

Small Molecule	T_{des} *(°C)* [a]	T_g *(°C)* [b]
Trux-FPy	404	150

[a] Decomposition temperature determined from TGA (5 % weight loss). [b] Glass transition temperature determined from the third cycle of DSC. All experiments are carried out under N_2 atmosphere, scan rate of 10 °C/min.

Truxene Derivatives as Lewis Base Interlayers in Perovskite Solar Cells

The Trux-FPy showed reversible oxidation and reduction processes (**Figure 3.2**) in solution. The oxidation waves of Trux-FPy are determined at +1.20 V and +0.95 V vs Ag/Ag^+ reference electrode in the oxidation process (**Figure 3.2a**). Likewise, the Trux-FPy showed reversible reduction waves at -1.92 V and -1.85 V *versus* Ag/Ag^+ reference electrode (**Figure 3.2b**). We have estimated the energies for the HOMO and the LUMO energy levels using Fc/Fc^+ as an internal reference electrode.[164] The results are -5.37 eV and -2.42 eV, respectively. All the relevant electrochemical parameters are listed in **Table 3.2**.

Attending to the energy values given for the MAPI CB and VB of -5.43 eV and -3.90 eV[219] the Trux-FPy has a very low energy offset (E_{offset}) for the hole transfer, E_{offset}=0.07 eV. Such E_{offset} will suffice, as shown later, to allow carrier transport to the HSL, the Spiro-OMeTAD.

Once the electrochemical characteristics of the Trux-FPy are measured, we turned onto the optical measurements. **Figure 3.2c** illustrates the UV-visible absorption spectra for the Trux-FPy in solution and in thin film.

Truxene Derivatives as Lewis Base Interlayers in Perovskite Solar Cells

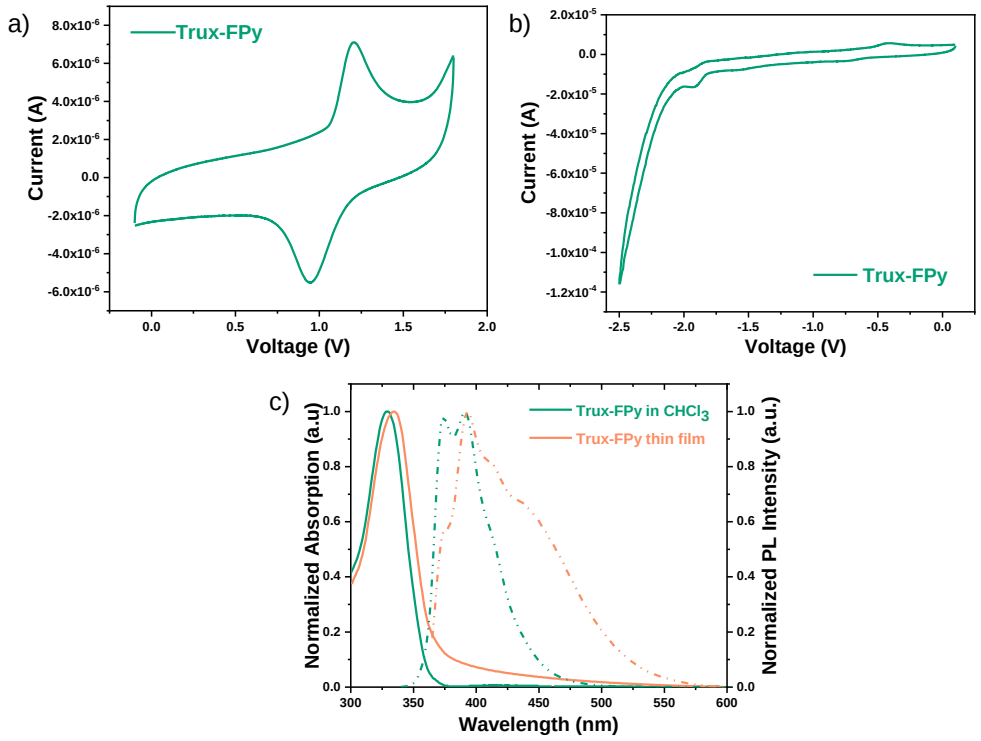

Figure 3.2. *a) The oxidation waves b) The reduction waves. Single scan cyclic voltammogram of Trux-FPy on glassy-carbon electrode in 0.1 M $TBAPF_6$/ACN solution. Absorption (solid lines) and emission (dashed lines) spectra of Trux-FPy in $CHCl_3$ and thin film.*

The Trux-FPy film does not show a noticeable new absorption band that may correspond to intermolecular interactions as shown in **Figure 3.2c.** Nonetheless, the main band in the UV region (λ_{max}= 340 nm) is slightly red shifted, which indicates the formation of molecular aggregates. Notwithstanding the featureless UV-visible spectra, the fluorescence emission spectra, on the contrary, shows remarkable fine structure with a visible shoulder centred λ_{em}= 460 nm, which agrees with the presence of intermolecular interactions accounting for the existence of molecular aggregates.

Table 3.2. *Optical and energetic properties of the Trux-FPy in solution.*

Small Molecule	$\lambda_{abs.}$ ***(nm)***	$\lambda_{em.}$ ***(nm)***	$\lambda_{a.e.}$ ***(nm)***	$E_g^{opt.}$ ***(eV)***	$^{1/2}E_{Ox}$ ***(V)***	$^{1/2}E_{Red}$ ***(V)***	***HOMO (eV)***	***LUMO (eV)***
Trux-FPy	335	395/415/ 440	365	3.40	1.20/ 0.95	1.92/ 1.85	-5.37	-2.42

3.3.3. Photophysical and Photovoltaic Properties of Perovskite-Based Devices

The deposition of Trux-FPy, using the spin-coating technique, on top of a MAPI perovskite thin film shows modest quenching of the fluorescence emission (**Figure 3.3a**), which indicates that due to the rather small E_{offset} between MAPI and Trux-FPy the interfacial hole transfer process is not efficient. Importantly, when Trux-FPy is used as an interfacial layer between MAPI and the Spiro-OMeTAD, the quenching process approaches unit yield, which implies outstanding interfacial charge transfer between the MAPI film and the Spiro-OMeTAD through the interfacial layer of Trux-FPy. It is important to highlight that the interfacial layer of Trux-FPy between MAPI and the Spiro-OMeTAD has a thickness of 5 nm approximately, which is thin enough to allow charge transport through it.

Truxene Derivatives as Lewis Base Interlayers in Perovskite Solar Cells

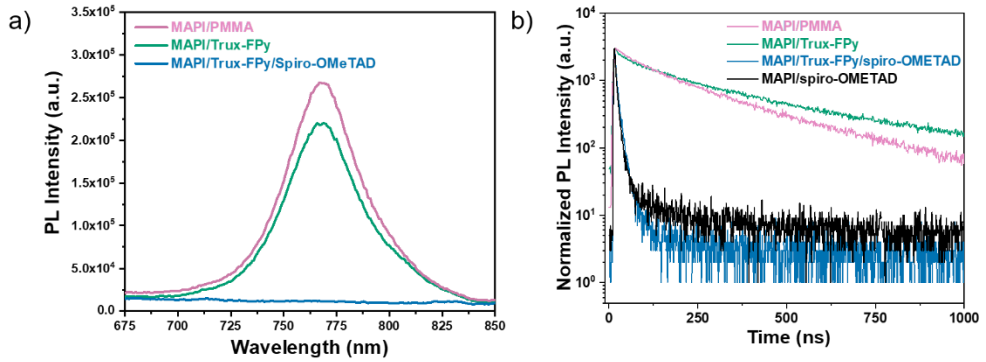

Figure 3.3. *a) Luminescence emission band upon excitation at λ_{ex}=435 nm at room temperature for the MAPI/PMMA (total thickness of 450–500 nm), the MAPI/Trux-FPy (thickness of Trux-FPy ≈5 nm) and MAPI/Trux-FPy/Spiro-OMeTAD (total thickness of Trux-FPy/Spiro-OMeTAD= 150–200 nm) b) Normalized luminescence emission decays (λ_{ex}=470 nm) measured at room temperature for MAPI/PMMA, MAPI/Spiro-OMETAD, MAPI/Trux-FPy, and MAPI/Trux-FPy/Spiro-OMETAD on glass substrate.*

Also, we focus on the role of Trux-FPy in the passivation of the Lewis acid sites that act as traps for free carriers at the MAPI film surface, as we have previously hypothesised. **Figure 3.3b** shows the luminescence emission decays recorded at room temperature, using the time correlated single photon-counting technique, using the same films as in **Figure 3.3a** Moreover, we have also added the MAPI/Spiro-OMeTAD thin film for comparison purposes. The MAPI films are coated with PMMA with encapsulating purposes.[220]

TRPL decays show two different decay profiles. The faster decay is being assigned to trap filling whereas the slower decay corresponds to the bimolecular recombination. TRPL decays are fitted to a biexponential decay as mentioned in Chapter 2. The results of the fitting are shown in **Table 3.3**, obtaining a lifetime τ_1=69 ns and τ_1=53 ns for MAPI/PMMA

and MAPI/Trux-FPy samples, respectively. This kinetics, associated with trap filling, shows us the role of Trux-FPy, passivating traps on the perovskite surface, as it takes shorter times to be filled. It is also interesting the analysis of the lifetime τ_2, which we already have assigned to bimolecular recombination in the perovskite. With values of 268 ns and 346 ns for MAPI/PMMA and MAPI/Trux-FPy respectively, it represents a direct evidence of the passivation effect of Trux-FPy layer, indeed.

***Table 3.3**. Fitting values obtained from the de-convolution of the luminescence decays in **Figure 3.3b**.*

Films	τ_1 *(ns)*	τ_2 *(ns)*
MAPI/PMMA	69	268
MAPI/Spiro-OMETAD	5	21
MAPI/Trux-FPy	53	346
MAPI/Trux-FPy/Spiro-OMETAD	5	16

The passivation of Lewis acid sites at the surface of the MAPI perovskite leads to an improvement of the carrier's lifetime. This improvement is not seen, however, in the steady state luminescence emission represented in **Figure 3.3a** as an increase in the perovskite emission quantum yield due to the effective but not efficient interfacial charge transfer between the MAPI film and the Trux-FPy film. Moreover, in good agreement with **Figure 3.3a**, the luminescence decay for the sample

MAPI/Trux-FPy/spiro-OMeTAD shows efficient quenching and much faster decay kinetics.

We moved one-step further and fabricated solar cells to proof if the passivation of the surface defects using the Trux-FPy interfacial layer results also beneficial in a complete device.

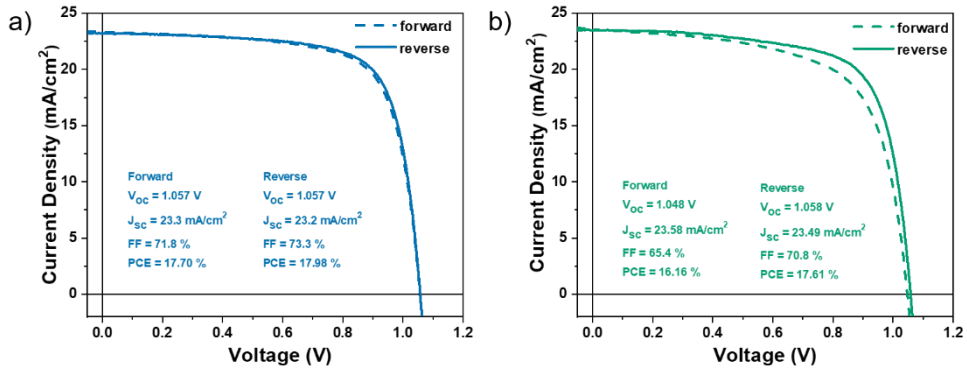

Figure 3.4. *J-V curves a) the MAPI/Spiro-OMeTAD b) the MAPI/Trux-FPy/Spiro-OMeTAD solar cells when illuminated under sun simulated 1 sun conditions (100 mW/cm² 1.5 AM G).*

Figure 3.4 illustrates the measured J-V curves for the best MAPI/Trux-FPy/spiro-OMeTAD and the MAPI/spiro-OMeTAD used as a reference. At first glance, the use of Trux-FPy as interfacial layer, although achieved the passivation of the MAPI surface as shown in **Figure 3.4a**, does not improve noticeably the solar cell efficiency. A more detailed statistical study also supports this observation (**Figure 3.5**).

Truxene Derivatives as Lewis Base Interlayers in Perovskite Solar Cells

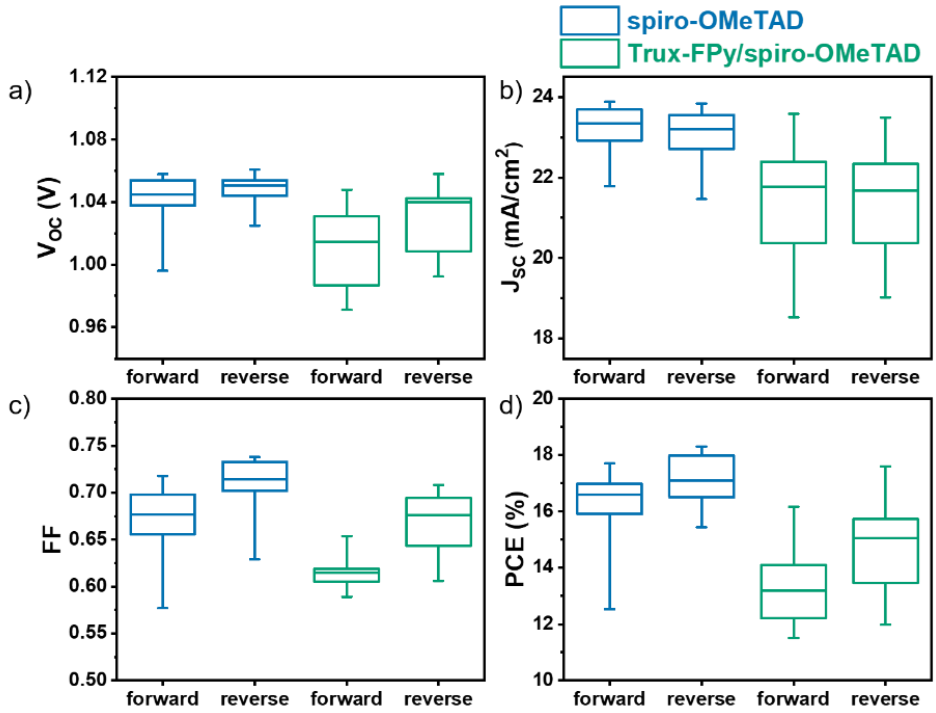

Figure 3.5. *Device performance statistic for different sets of devices employing MAPI/Trux-FPy/Spiro-OMETAD and MAPI/Spiro-OMETAD sun simulated irradiated conditions at 1 sun a) V_{OC}, b) J_{SC}, c) FF, and d) PCE.*

We would like to highlight that even in the best case for the MAPI/Trux-FPy/Spiro-OMeTAD solar cells there are minor differences between the forward and the reverse J-V curve. This difference accounts for the hysteresis process that has been largely discussed in Chapter 2 for hybrid lead halide perovskites.

In this case the reference sample, measured under identical conditions, shows negligible hysteresis, which leads us to think that the observed differences are due to the presence of the Trux-FPy interlayer. A first hypothesis is that due to the low E_{offset} between the MAPI film and the Trux-FPy film, the latter results in a practical barrier that hampers the

efficient transport of charges and will result in the accumulation of electronic holes and ionic species at the interface between the MAPI film and the Trux-FPy film. Hence, further studies, in complete devices under *operando* conditions, are carried out to analyse if the losses in efficiency are related to carrier losses due to interfacial recombination processes. **Figure 3.6** illustrates the changes in open circuit voltage (V_{OC}) and short-circuit current upon illumination.

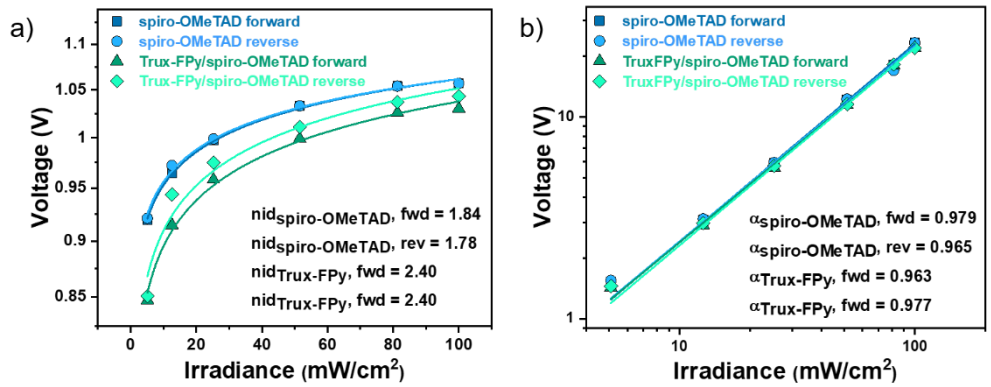

Figure 3.6. *Light Intensity vs a) V_{OC}, and b) J_{SC}.*

As can be seen in **Figure 3.6**, there is a substantial difference between the values for the MAPI/Trux-FPy/spiro-OMeTAD and the MAPI/spiro-OMeTAD. Those values correspond to the fitting as shown in section 2.3.11.

In non-ionic solar cells, values close to unity (kT/q) indicate that the bimolecular recombination is the dominant process. However, for values higher than 1 (1.7–1.8 for the MAPI/Spiro-OMeTAD and 2.4 for MAPI/Trux-FPy/Spiro-OMeTAD) it indicates that there are other parallel processes that occur during illumination. One of these is the

reorganisation of ions at the perovskite solar cell, which has been demonstrated to play a role in the final V_{OC} of the solar cell.[120,221]

The major dependence of V_{OC} on irradiance and the higher slope value for MAPI/Trux-FPy/Spiro-OMeTAD based perovskite solar cells implies that these processes have a greater impact when the Trux-FPy layer is present, which agrees with the greater hysteresis observed in **Figure 3.4**. Moreover, the analysis of the slope of the J_{SC} versus light illumination intensity gives similar values close to unity, which implies that carrier recombination at short circuit is negligible. The J-V curves measured to obtain these values at different light intensities are shown in **Figures 3.7**.

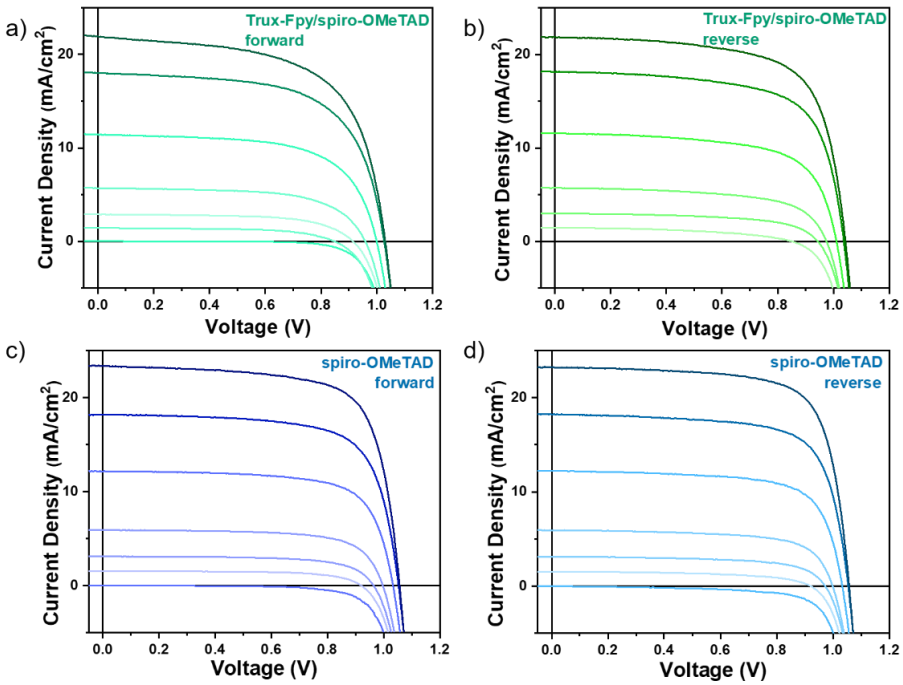

Figure 3.7. *J-V curves of a) Trux-FPy/Spiro-OMeTAD forward, b) Trux-FPy/Spiro-OMeTAD reverse, c) Spiro-OMeTAD forward and d) Spiro-OMeTAD reverse based devices at different light intensities. From these J-V curves, it is derived the values for J_{SC} and V_{OC} dependence with the light intensity.*

Truxene Derivatives as Lewis Base Interlayers in Perovskite Solar Cells

We decided to focus more in depth on the Lewis base properties of the Trux-FPy and carried out a titration experiment using PbI_2 and the Trux-FPy molecule in solution. As can be seen in **Figure 3.8a**, upon addition of increasing amounts of Trux-FPy an isosbestic point appears at λ=350 nm, which is indicative of a supramolecular interaction between the Trux-FPy and the Pb^{2+} ions. Moreover, the new supramolecular complex has a maximum absorption band at 325 nm, which is 10 nm blue shifted with respect to the Trux-FPy main absorption band in the UV. **Figure 3.8b** shows the electrostatic potential (ESP) surface calculated at DFT level for a methyl derivative of Trux-FPy.

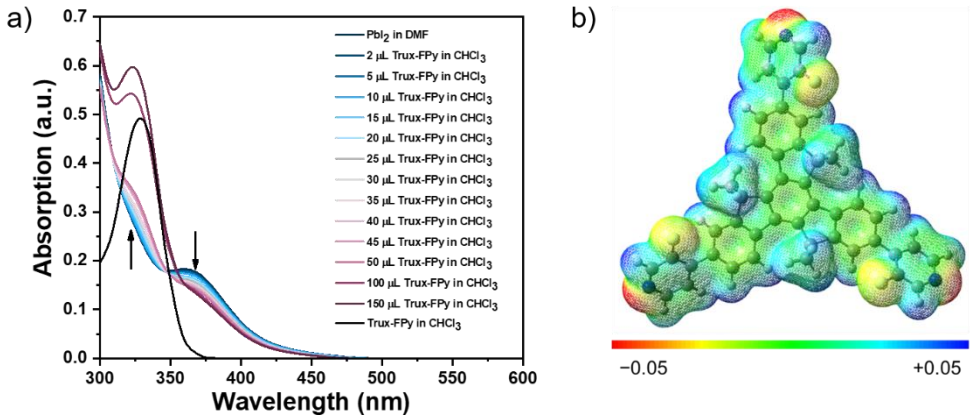

Figure 3.8. *a) UV-visible spectra of the titration experiment using 3 mL of a 0.1 mM solution of PbI_2 in dimethylformamide in a quartz cuvette and increasing concentration of Trux-FPy from a stock solution of 0.05 mM in chloroform. b) Electrostatic potential surface of a methylated model of the Trux-FPy molecule.*

The molecule shows a planar π-conjugated core where the largest negative charges are localised on the pyridinic N atoms (density in red) and the F atoms (density in yellow). Hence, those N atoms are expected to coordinate the Pb^{2+} uncoordinated atoms at the perovskite surface

through Lewis acid-Lewis base supramolecular interactions, which is in good agreement with the experiment shown in **Figure 3.8a**.

3.3.4. Charge storage and recombination using optoelectronic transient techniques

We have discussed that techniques such as PI-CE and PI-TPV, developed to study DSSC and OSC (organic solar cells), can be particularly useful to understand carrier recombination and ion migration in perovskite solar cells in Chapter 2. In this work, we do have used PI-CE and PI-TPV to measure the above-mentioned solar cell properties. **Figure 3.9** shows the PI-CE and PI-TPV decays obtained under 1 sun illumination conditions for two of the best solar cells fabricated in this work.

As can be observed in **Figure 3.9**, the photo-induced carrier recombination at 1 sun measured using PI-TPV and the PI-CE decays are similar in both perovskite solar cells. Hence, we can conclude that the differences in the device performance are not due to the carrier recombination or the carrier extraction.

Truxene Derivatives as Lewis Base Interlayers in Perovskite Solar Cells

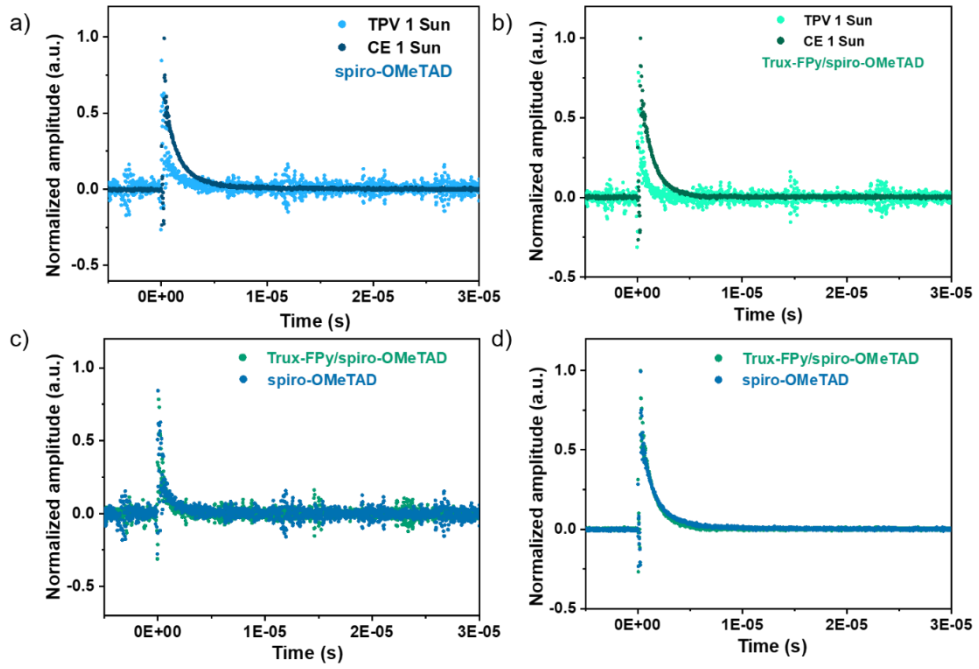

Figure 3.9. *The decays at 1 sun for the PI-CE and the PI-TPV a) Spiro-OMETAD, and b) Trux-FPy/Spiro-OMETAD. c) the normalized PI-TPV decays comparison for both solar cells. d) the normalized PI-CE decays comparison for both solar cells.*

To further confirm this experimental observation, we measured the interfacial carrier recombination kinetics at different charge obtained at different light bias (different V_{OC} because of different light irradiation intensities) in **Figure 3.10**. In **Figure 3.11**, we show the dependence of carrier lifetime at different light bias and the carrier density at different light bias.

Truxene Derivatives as Lewis Base Interlayers in Perovskite Solar Cells

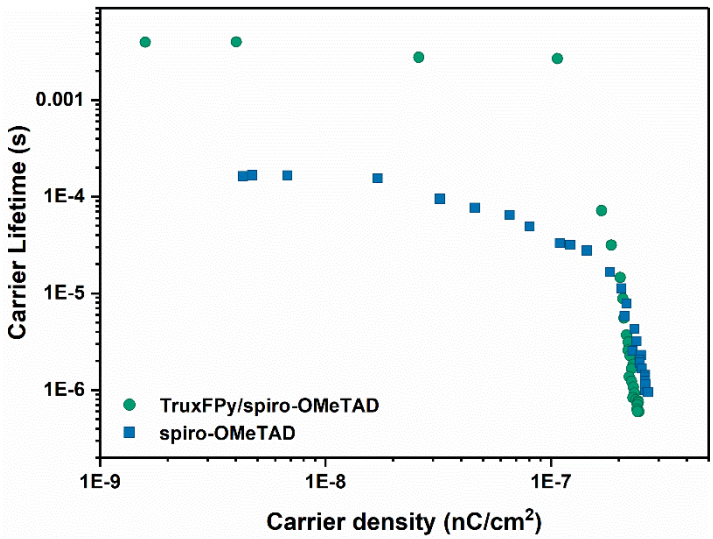

Figure 3.10. *Carrier lifetime vs charge obtained for different light bias for MAPI/Trux-FPy/Spiro-OMeTAD (green) and MAPI/Spiro-OMeTAD (blue).*

As illustrated in **Figure 3.10**, for charge values corresponding to light irradiation intensity close to 1 sun the carrier lifetime is alike and, moreover, the slope of the curves is also close in units, which implies that the interfacial carrier recombination order is very much close. Thus, our first hypothesis that the possible accumulation of ions is responsible for the observed hysteresis is not accurate. Nonetheless, considering the spectroscopic data, it results evident that the Trux-FPy do passivate the defects in the perovskite thin film.

Truxene Derivatives as Lewis Base Interlayers in Perovskite Solar Cells

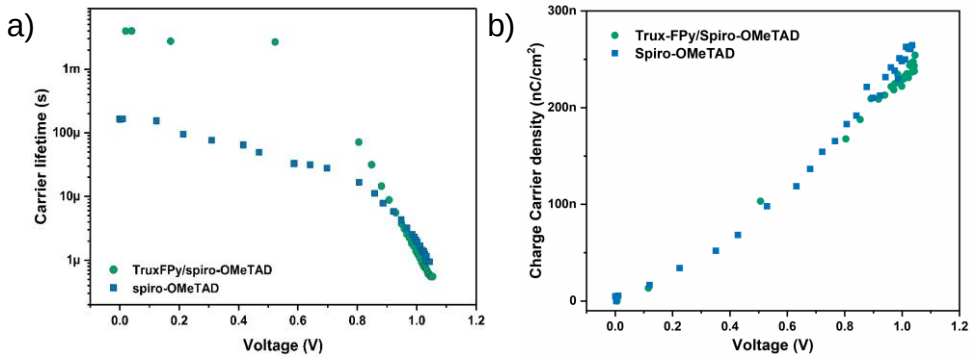

Figure 3.11. *a) The Carrier lifetime as a function of the photovoltage generated in the devices. b) Carrier density obtained at different photovoltage using the PI-CE technique.*

3.4. Conclusions

We have designed and synthesised an organic semiconducting molecule with truxene core. The molecule, Trux-FPy, is intended to contain peripheral moieties that can work as Lewis bases to passivate surface defects in lead halide perovskite originated by the non-coordinated lead. Those surface defects act as traps for carriers and increase the carrier recombination, which, in overall, limits the solar cell efficiency. The Trux-FPy is fully electrochemically and optically characterised, and it is found that, upon deposition on top of the MAPI thin film, the Trux-FPy thin film decreases the number of defects at the MAPI surface increasing its luminescence lifetime. Moreover, the Trux-FPy thin film is capable of carrying out interfacial charge transfer processes with the MAPI thin film upon illumination, which leads us to incorporate the Trux-FPy as interfacial layer.

Once incorporated as an interfacial layer between the MAPI film and the HTM spiro-OMeTAD film, the best solar cells matched the efficiency of those standards prepared using only Spiro-OMeTAD. Nonetheless, the presence of hysteresis in the J-V curves for the Trux-FPy containing solar cells is noticed.

An analysis in depth of the MAPI/Trux-FPy/spiro-OMeTAD solar cells using PI-CE and PI-TPV techniques determines that the interfacial carrier recombination processes in these devices are not affected by the presence of the Trux-FPy interfacial layer. Nevertheless, the Trux-FPy interfacial layer does have supramolecular interactions with the

uncoordinated lead ions. Our results show the potential of surface supramolecular interactions between the perovskite semiconductor and intermediate layers to decrease the uncoordinated site defects, which are the cause negative effects in the perovskite solar cells performance.

3.5. Synthetic Methods and Procedures

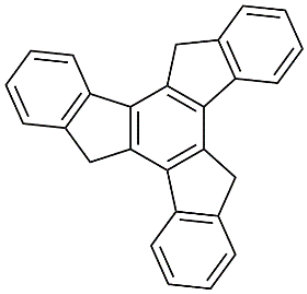

1a

10,15-Dihydro-5H-diindeno(1,2-a;1',2'-c)fluorene (1a)

1-Indanone (0.5 g, 10.6 mmol) is dissolved in acetic acid (10.0 mL), and then concentrated hydrochloric acid (5.0 mL) is added. The solution is heated to 120 °C and refluxed overnight. The hot mixture is poured into saturated sodium carbonate aqueous solution (100.0 mL) with ice and stirred for 1 h. The yellow precipitate is filtered and washed with acetone (50.0 mL) and ethanol (50.0 mL) to give an off-white powder 1a. (0.8 g, 64 % isolated yield).

^{1}H NMR (500 MHz, $CDCl_3$) δ (ppm) 7.97 (d, J=7.6 Hz, 3H), 7.71 (d, J=7.4 Hz, 3H), 7.50 (t, J=6.8, 3H), 7.40 (t, J=7.4, 3H), 4.29 (s, 6H).

^{13}C NMR (101 MHz, CDCl3) δ (ppm) 143.8, 141.7, 137.1, 135.3, 126.9, 126.3, 125.1, 121.9, 36.6.

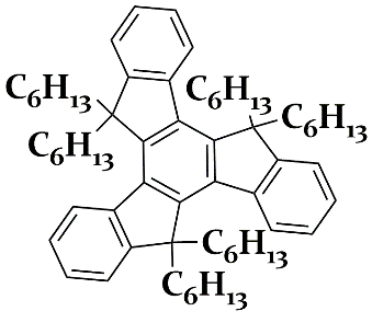

1b

5,5,10,10,15,15-Hex(1-hexyl) 10,15-Dihydro-5H-diindeno(1,2-a;1',2' c)fluorene (1b)

To a suspension of 1a (0.5 g, 1.5 mmol) and ^{t}BuOK (5.7 g, 51.0 mmol) in dry THF (50.0 mL) 1-bromohexane (3.2 mL, 22.5 mmol) is added at room temperature under argon atmosphere. The resulting suspension is heated at 70 °C and stirred overnight. The solid material in the reaction mixture is removed through

filtration and washed with hexane (100.0 mL). The filtrate part is concentrated down under reduced pressure and the resulting oil is dissolved in hexane (50.0 mL). The mixture is washed with 0.2 M HCl (25.0 mL) and saturated $NaHCO_3$ (50.0 mL). The organic layer is dried over $MgSO_4$ and concentrated in vacuo. Then, the residue is purified by silica column chromatography using hexane as eluent to afford the target compound 1b as off-white powder (0.85 g, 67% isolated yield).

^{1}H NMR (400 MHz, $CDCl_3$) δ (ppm) 8.42 (d, J=7.5 Hz, 3H), 7.54–7.48 (m, 3H), 7.46–7.35 (m, 6H), 3.19–2.89 (m, 6H), 2.27–1.98 (m, 6H), 1.09–0.78 (m, 36H), 0.64 (t, J=7.1 Hz, 18H), 0.61–0.50 (m, 12H).

^{13}C NMR (101 MHz, $CDCl_3$) δ (ppm) 153.6, 144.8, 140.3, 138.4, 126.3, 125.9, 124.6, 122.1, 55.6, 37.0, 31.5, 29.5, 23.9, 22.3, 13.9.

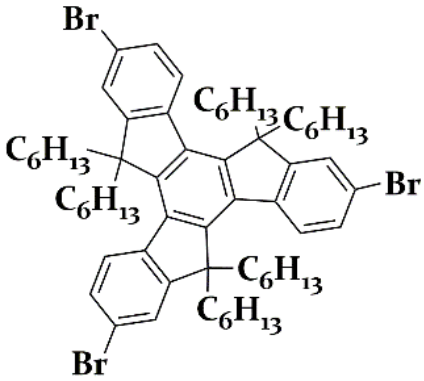

1

2,7,12-Tribromo-5,5,10,10,15,15-hexahexyl-10,15-dihydro-5-H-diindeno[1,2-a:1',2'-c]fluorene (1)

To a solution of compound 1b (0.83 g, 0.98 mmol) in chloroform (8.0 mL) $FeCl_3$ (2.0 mg, 0.012 mmol) is added as catalyst. A solution of bromine (0.2 mL, 3.43 mmol) in chloroform (2.0 mL) is added dropwise under stirring at 0 °C. The mixture is allowed to warm to room temperature and stirred overnight. Then, a saturated Na_2SO_3 aqueous solution (20.0 mL) is added to remove excess bromine. The mixture is extracted with chloroform (3x50.0 mL), and the combined organic phases are dried over $MgSO_4$.

After the solvent is removed, the yellow residue is recrystallised from ethanol to yield the compound 1 as an off-white powder (0.99 g, 93 % isolated yield).

^{1}H NMR (400 MHz, $CDCl_3$) δ (ppm) 8.17 (d, J=8.5 Hz, 3H), 7.56 (d, J=2.0 Hz, 3H), 7.51 (dd, J=8.4, 2.0 Hz, 3H), 2.93–2.72 (m, 6H), 2.10–1.92 (m, 6H), 0.99–0.77 (m, 36H), 0.62 (t, J=7.1 Hz, 18H), 0.51–0.36 (m, 12H).

^{13}C NMR (101 MHz, $CDCl_3$) δ (ppm) 155.9, 144.9, 138.9, 137.6, 129.4, 125.9, 125.5, 121.0, 56.0, 36.8, 31.4, 29.4, 23.9, 22.2, 13.9.

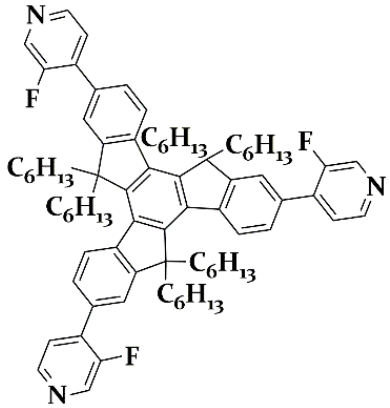

Trux-FPy

4,4',4"-(5,5,10,10,15,15-Hexahexyl-10,15-dihydro-5H-diindeno [1,2-a:1',2'-c]fluorene-2,7,12-triyl)tris(3-fluoropyridine) (Trux-FPy)

In a 50 mL two-neck round bottom flask 1 (0.25 g, 0.23 mmol), 3- fluoro-4-pyridine boronic acid pinacol ester (0.30 g, 1.38 mmol) is added and the system is purged with argon for 30 minutes. Then, freshly dried THF (15.0 mL) and Na_2CO_3 solution (2 M, 2.0 mL) are added to the medium. Finally, $Pd(PPh_3)_4$ (20.0%, 53.0 mg) is added as catalyst and the reaction temperature is set to 80 °C and stirred overnight. After the solvent is removed in vacuo, chloroform (50.0 mL) is added to the crude product and the mixture is washed with brine (2×50.0 mL) and water (2×50.0 mL) until a clear solution is obtained. The organic layer is dried over anhydrous $MgSO_4$, filtered and concentrated in vacuo. Finally, the residue is purified by

silica column chromatography using Hexane: Ethyl acetate (2:1) as elution solvents. Precipitation from methanol yielded Trux-FPy as off-white powder (0.12 g, 46% isolated yield).

^{1}H NMR (400 MHz, $CDCl_3$) δ (ppm) 8.61 (d, *J*=2.6 Hz, 3H), 8.54 (dd, *J*=4.9, 0.8 Hz, 3H), 8.49 (d, *J*=8.3 Hz, 3H), 7.76 (d, *J*= 1.7 Hz, 3H), 7.72 (d, *J*=8.2 Hz, 3H), 7.58 (dd, *J*=6.8, 5.0 Hz, 3H), 3.06–2.93 (m, 6H), 2.25–2.11 (m, 6H), 1.02–0.80 (m, 36H), 0.68–0.51 (m, 30H).

^{13}C NMR (101 MHz, $CDCl_3$) δ (ppm) 154.1, 146.4, 146.0, 141.2, 139.3, 139.0, 137.9, 136.2, 131.0, 127.0, 124.9, 124.1, 122.7, 56.0, 37.0, 31.4, 29.4, 24.0, 22.2, 13.8.

Calcd. for $C_{78}H_{96}F_3N_3^+$, (M^+): 1131.7551; found: 1131.7544 (0.6 ppm).

Anal. Calcd. for $C_{78}H_{96}F_3N_3$: C, 82.71; H, 8.54; N, 3.71. Found: C, 82.62; H, 9.00; N, 3.65.

Chapter 4

Phthalocyanine as a Hole Transporting Material in Perovskite Solar Cells

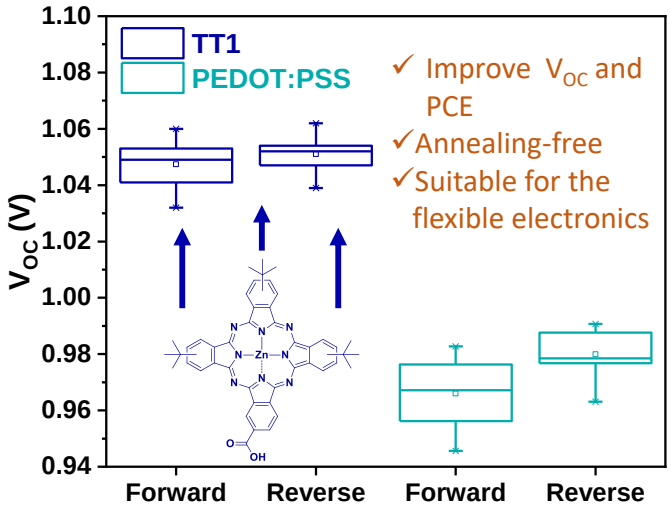

This chapter is based on the published work: Aktas, E. et al. Self-assembled Zn Phthalocyanine as a robust p-type selective contact in Hybrid Lead Halide Perovskite Solar Cells. **Nanoscale Horizons** 2020,5, 1415-1419.[222]

Phthalocyanine as a Hole Transporting Material in Perovskite Solar Cells

4.1. Abstract

The use of self-assembled monolayers as selective charge extracting layers in perovskite solar cells is a great approach to replace the commonly used charge selective contacts, as they can easily modify the interface to enhance the final solar cell performance. Here, we report a novel synthetic approach of the commonly known zinc phthalocyanine (ZnPc) molecule TT1, widely employed in DSSCs and previously used in perovskite solar cells. TT1 is used as a p-type selective contact, and it demonstrates its ability to form SAM on top of the ITO transparent electrode, obtaining higher efficiencies compared to PEDOT:PSS based perovskite solar cells.

4.2. Introduction

In this work, we employ zinc phthalocyanine with carboxylic acid TT1 as p-type selective contact deposited as a SAM in inverted perovskite solar cells. TT1 is a well-known phthalocyanine, widely used in DSSC and that has demonstrated its facility to attach to metallic oxides,[223] such as ITO. Additionally, it has also been employed in perovskite solar cells as a thin film on top of the mixed-ion perovskite layer. Zhang and co-workers reported that the optimised concentration of TT1 and chemical dopant showed reproducible efficiency of up to 13.7%.[224] Here, using a novel synthetic route, we use for the first time TT1 as a p-type contact using the SAM approach. TT1 already provides tri-*tert*-butyl groups at the periphery of the moieties, which prevents the formation of molecular aggregates. We obtain efficient perovskite solar cells, and we investigate

the origin of such differences, which accounts for differences in energetics rather than recombination kinetics.

4.3. Results and Discussions

4.3.1. Design and Synthesis

In this study, we developed the first direct transformation of hydroxyl methyl phthalocyanine into its corresponding carboxyl derivative (TT1) catalysed by ZnO in high yield (**Scheme 4.1**). The dehydrogenation of hydroxy methyl phthalocyanine is performed in zinc oxide (ZnO) and potassium hydroxide (KOH) solution in mesitylene to yield TT1 in 96% yield and hydrogen gas as the only by-product. The final compound (TT1) is fully characterised by ^{1}H NMR, LC/Mass, and MALDI-TOF-MS.

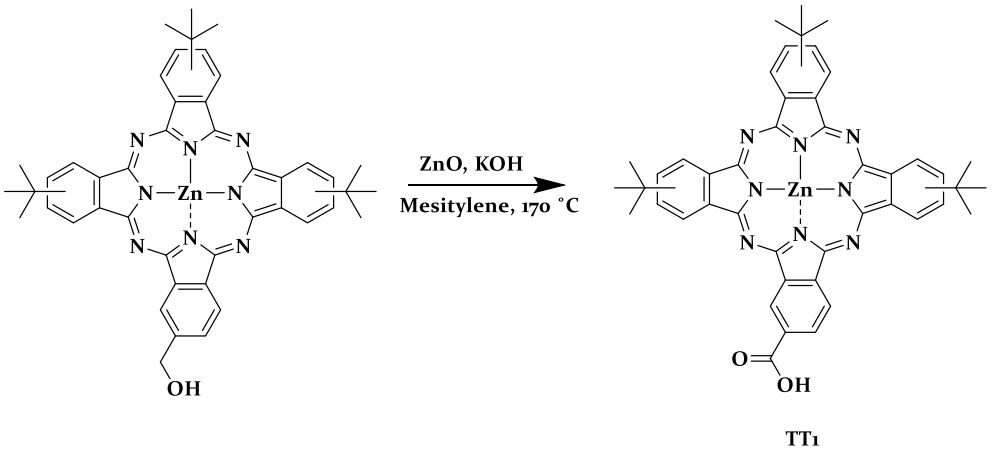

Scheme 4.1. *Synthetic pathway of TT1*

The catalytically active species in the solution is believed to be the corresponding zinc alkoxide from the reaction of alcohol with ZnO and KOH. Degradation of alkoxide resulted in Zinc hydride and the corresponding aldehyde. The aldehyde can transfer to the carboxylate and the starting alcohol by either a Cannizzaro reaction or a Tishchenko reaction in the presence of KOH.[225]

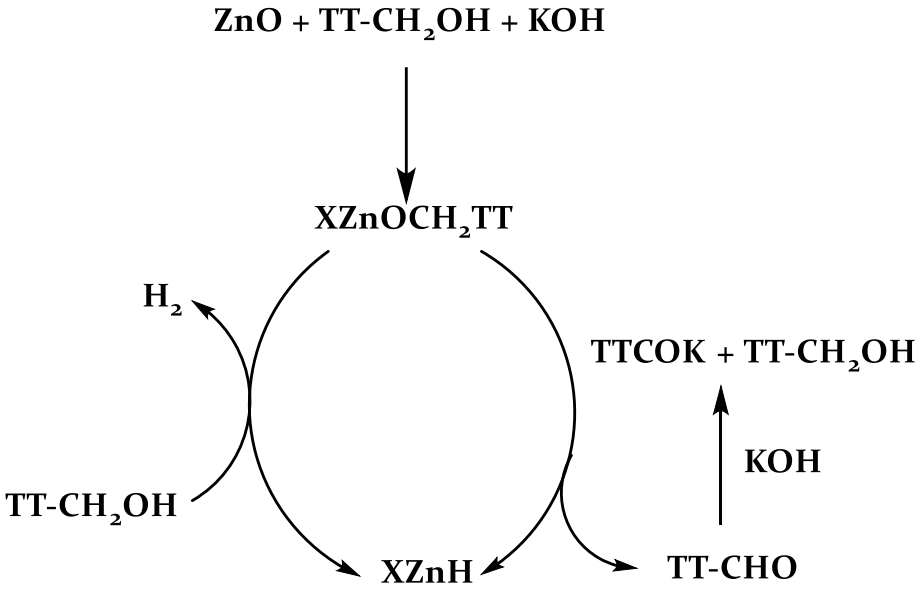

Figure 4.1. *Reaction mechanism of TT1*

4.3.2. Optical and Electrochemical Properties

Figure 4.2 illustrates the energy levels of the different materials used in the device and compares the differences between the p-type selective contacts. All energy values have been previously reported in the scientific literature.[223]

Phthalocyanine as a Hole Transporting Material in Perovskite Solar Cells

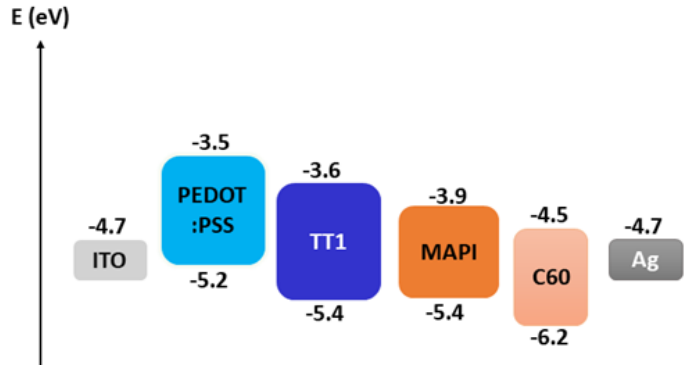

Figure 4.2. *Energy level diagram of the different materials used in the fabrication of the MAPI.*

At first sight, the deeper HOMO energy value for TT1 would be responsible for the gain in V_{OC} registered in the solar cells. Thus, the differences in V_{OC} could be explained by the differences in energetics between the PEDOT:PSS and the TT1 molecule in section 4.3.4. The optical absorption spectra of TT1 in IPA and thin film are exhibited in **Figure 4.3**. To demonstrate the existence of TT1 after dip-coating deposition on top of the ITO surface, we recorded the optical absorption spectra of bare ITO and TT1 deposited ITO. We have observed the characteristic absorption peak of TT1 at 620 nm and 700 nm. The existence of SAMs is generally proven by UPS measurements (for details see section 2.3.6), unfortunately, we could not access this equipment during this thesis. UV-vis is more easily accessible and gives information about the metal surface in short time.

Phthalocyanine as a Hole Transporting Material in Perovskite Solar Cells

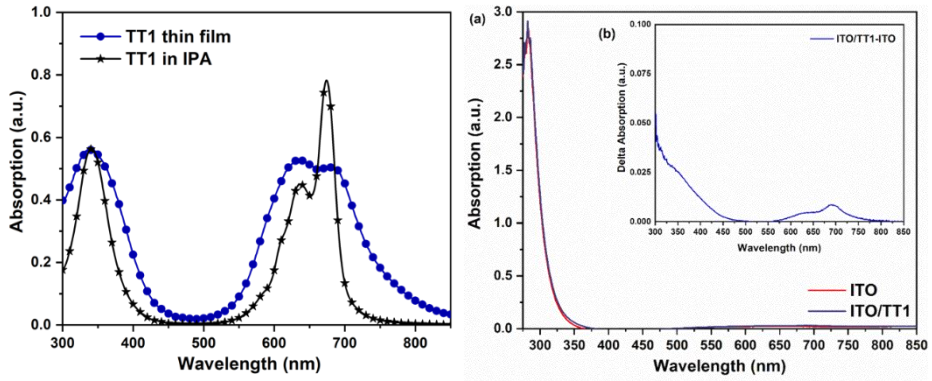

Figure 4.3. *Left, UV-visible spectrum of TT1 in IPA (TT1=0.01 mM) and deposited in a cover slide glass as thin film (film thickness of ~30 nm). Right, UV-vis absorbance (a) and difference (b) spectra of ITO and ITO/TT1 as thin film (TT1 is deposited as a self-assembled monolayer on ITO).*

After proving the existence of the TT1 on the ITO surface, we investigated the wettability of the ITO surface after dip-coating deposition TT1. We used applicatory contact angle measurement for determining the TT1-covered surface wettability which is applied with water (see for details section 2.3.4). The water contact angle of TT1 on ITO is 76 ° that ensures a miscible interface for the MAPI perovskite two-step solution process. In other words, TT1 provides a hydrophilic surface that means the droplet will spread out at all and the perovskite layer will be pinhole-free.[60]

Phthalocyanine as a Hole Transporting Material in Perovskite Solar Cells

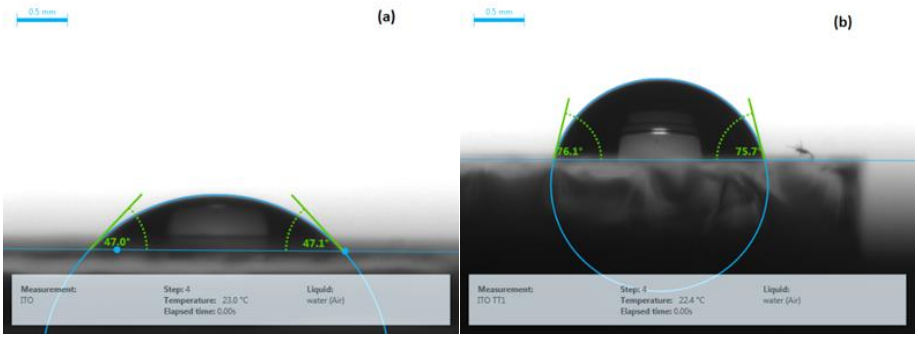

Figure 4.4. *Contact angle measurements on the (a) bare ITO surface, (b) ITO/TT1 surface.*

To examine the effect of the hole selective layer's wettability on perovskite films, perovskite layers grown on HSLs, and bare ITO are characterised by SEM and AFM. As can be seen in **Figure 4.5** and **Figure 4.7**, a closer look to the hybrid lead halide perovskite thin film grown onto the TT1 SAM or the PEDOT:PSS polymer layer did not show any relevant difference, resulting in high quality perovskite films.

Figure 4.6 shows the cross-sectional full device, where the perovskite thin films are uniform with a thickness of approximately 350 nm. Additionally, it is possible to identify the PEDOT:PSS layer and its thickness of around 35 nm.

Phthalocyanine as a Hole Transporting Material in Perovskite Solar Cells

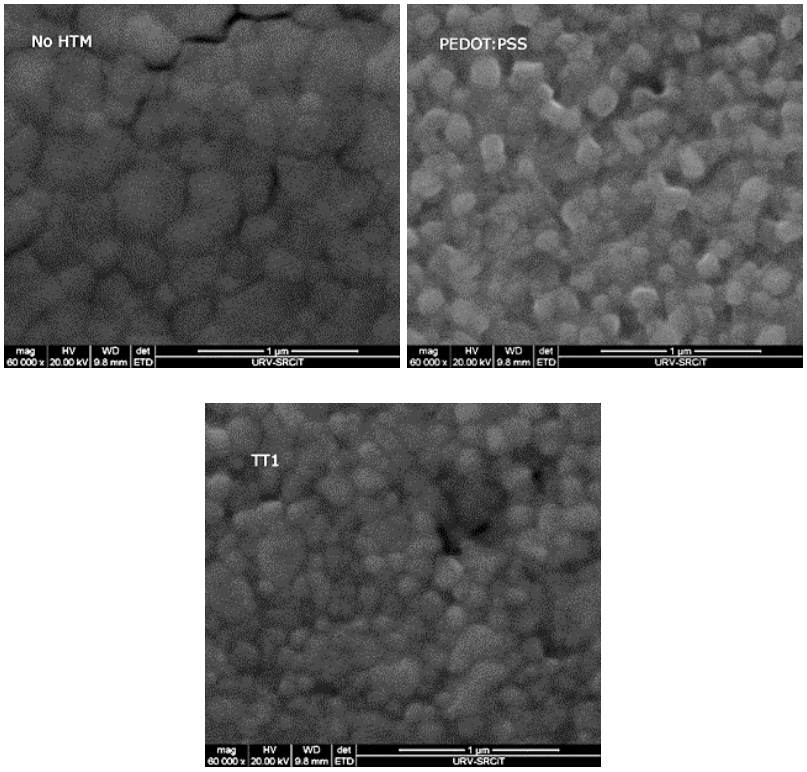

Figure 4.5. *Top view ESEM pictures of (a) ITO/MAPI, (b) ITO/PEDOT:PSS/MAPI and (c) ITO/TT1/MAPI.*

Phthalocyanine as a Hole Transporting Material in Perovskite Solar Cells

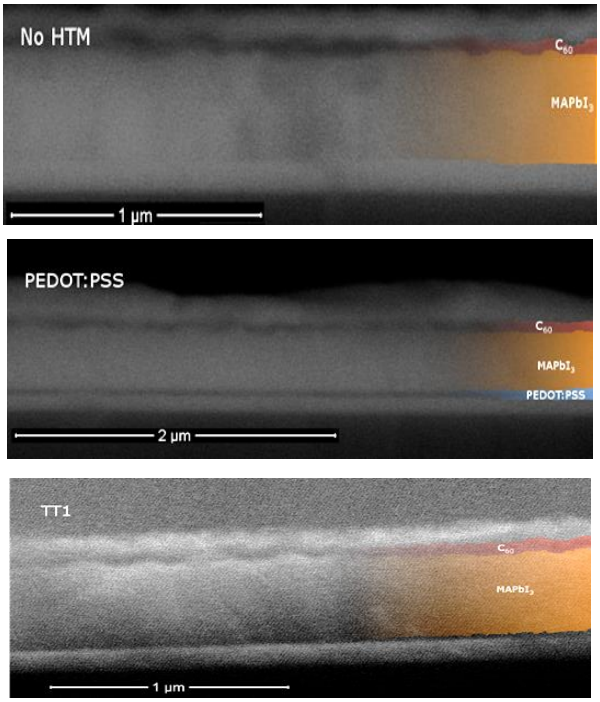

Figure 4.6. *Cross-section ESEM pictures of different architectures employed in this study with (a) ITO/MAPI/C60/Ag, (b) ITO/PEDOT:PSS/MAPI/C60/Ag and (c) ITO/TT1/MAPI/C60/Ag.*

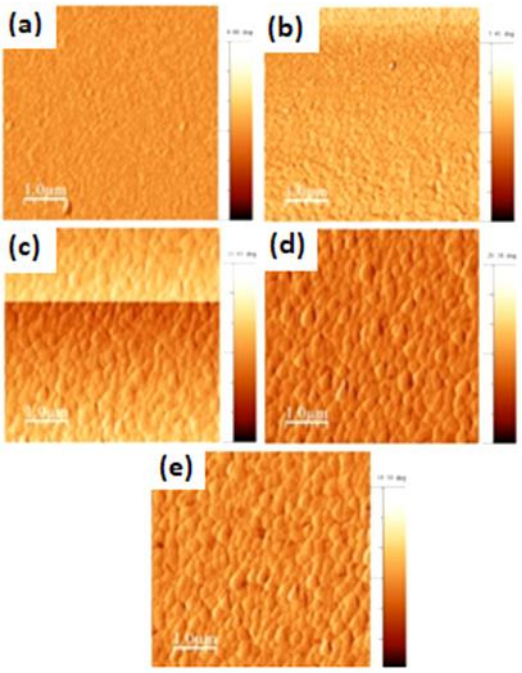

Figure 4.7. *Topographical atomic force microscopy (AFM) pictures of (a) TT1/ITO, (b) PEDOT:PSS/ITO, (c) MAPI/ITO, (d) MAPI/PEDOT:PSS/ITO and (e) MAPI/TT1/ITO electrodes. The scale bar is 1 μm.*

4.3.3. Photovoltaic Properties of Perovskite-Based Devices

The state-of-the-art device structure with ITO/HTMs/MAPI/C_{60}/Ag sandwich architecture is used in this study.[61] PEDOT:PSS is deposited on top of the UV-O_3 treated ITO substrates using spin-coating deposition method and after the annealing process is applied to these layers at 130 °C for 30 min. to get rid of residual solvent (see for details section 2.5.2). TT1 is easily soluble in nonhalogenated solvents, and the substrates are dipped in the 0.3 mM TT1 solution in IPA for 4 h at room temperature. After that, the TT1 deposited substrates are rinsed with IPA (100 μl) by spin-coater (see for details section 2.4.2). Then, the perovskite (MAPI or

CsFAMA) layer is placed on top of the HTMs (see for details section 2.5.3), and the substrates are annealed at 100 °C for 10 min. By following perovskite layer deposition, C_{60} (30 nm) is thermally evaporated as an electron selective layer in order to passivate the grain boundaries and surfaces of perovskite films.[56] Finally, to complete the devices, silver (100 nm) is thermally evaporated under high vacuum ($9x10^{-7}$ mbar).

The photovoltaic performance of the devices is measured under AM 1.5 G conditions, J-V curves are recorded by applying a forward and reverse bias with a scan rate of 40 mV/s. **Figure 4.8** shows the J–V curves for perovskite solar cells made using PEDOT:PSS, an ionic polymer, used as our reference, and TT1 SAMs. As can be seen, both devices show negligible hysteresis and TT1 based solar cells show larger V_{OC}. In fact, the measured voltage is substantially larger than the V_{OC} measured for perovskite solar cells using a thin film of TT1 as the HTM.

Phthalocyanine as a Hole Transporting Material in Perovskite Solar Cells

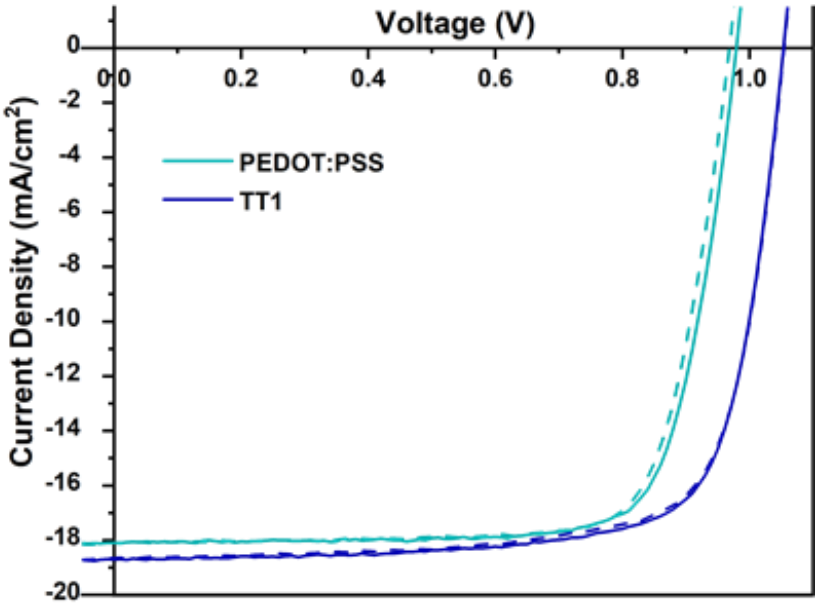

Figure 4.8. *J-V curves of the champion devices using TT1 (Blue) and Pedot:PSS (Cyan) as p-type selective contacts measured under 1 Sun conditions (100 mW/cm², AM 1.5G) with a scan rate of 0.04 V/s. Both forward (forward, from 0 V to 1.2 V, dashed lines) and reverse (reverse, from 1.2 V to 0 V, solid lines) measurements are shown.*

Of utmost importance is the fact that, on average, TT1 based perovskite solar cells always show better device performance than PEDOT:PSS due to having higher V_{OC} (**Figure 4.9**). The statistical distribution of the cell parameters is achieved from more than 20 devices (**Table 4.1**).

Phthalocyanine as a Hole Transporting Material in Perovskite Solar Cells

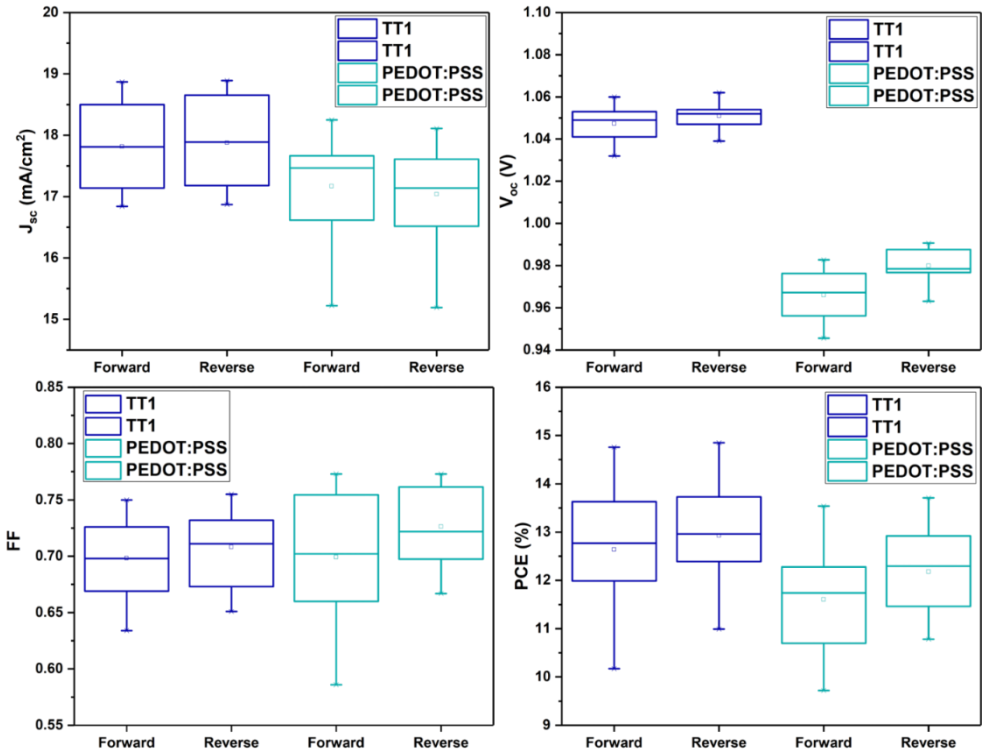

Figure 4.9. *Statistical distribution of the photovoltaic parameters with different p-type materials, TT1 (blue) and PEDOT:PSS (cyan) @1 sun (100 mW/cm², AM 1.5 G) conditions with a scan rate of 0.04 V/s.*

Phthalocyanine as a Hole Transporting Material in Perovskite Solar Cells

Table 4.1. *Photovoltaic parameters with the standard deviation from the devices using PEDOT:PSS and TT1 as HTMs.*

HTMs	***Scan Direction***	***J_{SC} (mA/cm²)***	***V_{OC} (V)***	***FF (%)***	***PCE (%)***
PEDOT: PSS	forward	17.17 ±1.5	0.967 ±0.05	69.9 ±1.0	11.62 ±2.09 (13.71)
	reverse	17.04 ±1.7	0.984 ±0.04	72.6 ±0.8	12.18 ±1.5 (13.68)
TT1	forward	17.85 ±1.0	1.045 ±0.01	68.7 ±0.6	12.89 ±1.96 (14.85)
	reverse	17.92 ±1.0	1.049 ±0.01	69.7 ±0.5	13.11 ±1.0 (14.11)

In this thesis, we also have employed triple cation perovskite (onwards labelled as CsFAMA) absorbers with TT1 in p-i-n type perovskite devices. CsFAMA is preferred as an absorber, owing to giving higher device performance.[15] However, TT1 showed underperformance in comparison to MAPI due to having lower V_{OC} while having better FF as shown in **Figure 4.10**.

Phthalocyanine as a Hole Transporting Material in Perovskite Solar Cells

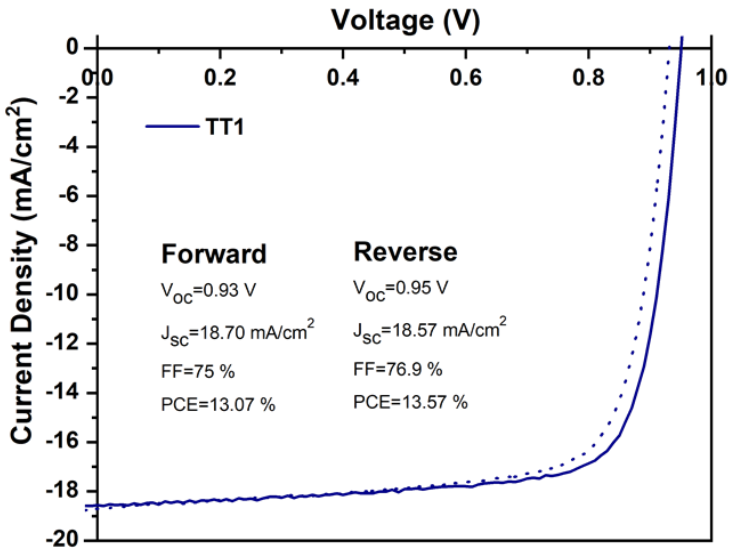

Figure 4.10. *J-V curves for the ITO/TT1/CsFAMA/C_{60}/BCP/Ag solar cells when illuminated under sun simulated 1 sun conditions (100 mW/cm², 1.5 AM G).*

Charge selective layers play a vital role on power conversion efficiency and stability of the perovskite devices (see for details 1.1.1.5). After having sufficient power conversion efficiency from TT1 and PEDOT:PSS without dopant, to investigate the role of charge selective layer on short-term perovskite device stability, the maximum V_{OC} and J_{SC} point tracking to the best devices is performed for 2 min. We could not observe any significant decrease in V_{OC} and J_{SC} values of the completed device over time.

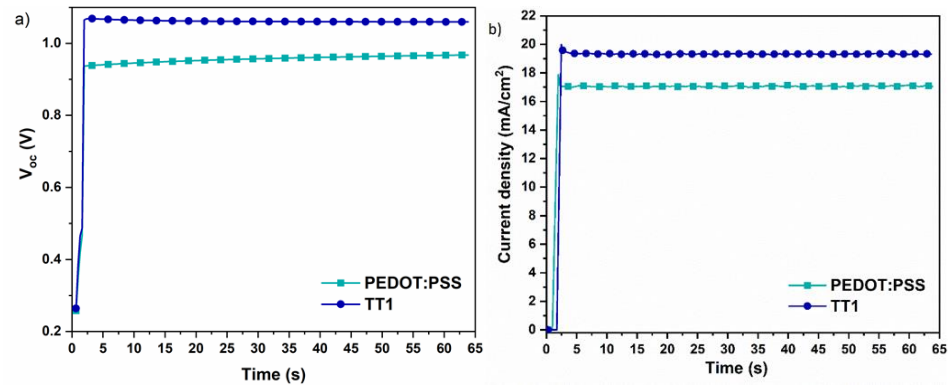

Figure 4.11. *a) V_{OC} and b) J_{SC} stability of the best devices when illuminated under sun simulated 1 sun conditions (100 mW/cm2, 1.5 AM G) for 1 minute.*

4.3.4. Charge storage and recombination using optoelectronic transient techniques

We carried out transient optoelectronic techniques under *operando* conditions in order to study the origin of the differences observed in the V_{OC} between both p-type contacts when used in complete devices. The use of transient optoelectronic techniques, such as photo-induced transient photovoltage (PI-TPV), photo-induced transient photocurrent (PI-TPC), or differential capacitance (DiffCap) has been demonstrated as a useful approach to study charge recombination and charge storage on operating devices. In this case, we will use these techniques to study what is the origin of the differences observed on the V_{OC}, if they are related to changes in the energetics, or, if this is associated with different carrier kinetics[25,198,226] The description of the techniques and data treatment can be found in section 2.6.

The DiffCap measurements agree with the differences in energy between the PEDOT:PSS film and the TT1 SAM with a shift of the exponential curves registered for different voltages close to the $^{max}V_{OC}$ corresponding to 1 sun irradiation. Two different regimes are observed in **Figure 4.12**. First, a constant part, related to the geometric capacitance in the device, related to the charges stored in the contacts and electrodes.[201,202] The second regime, the exponential part, is related to the chemical capacitance. Once the contacts are depleted with charges, they start accumulating in the bulk of the perovskite.[201] The difference between both exponential curves is ~100 mV, in good agreement with the experimental values recorded for the devices at 1 sun (^{TT1}Voc = 1.05 V and $^{PEDOT:PSS}$Voc = 0.98 V). In this case, the differences in the exponential tail are what we expected. The V_{OC} will increment with the quasi-Fermi level splitting (QFLS) with the light bias until the contacts are depleted with charges, therefore we expect that the QFLS will be also correlated with the HOMO values of the p-type selective contacts. A higher QFLS is expected for TT1, which is confirmed by the differences observed in **Figure 4.12**.

Phthalocyanine as a Hole Transporting Material in Perovskite Solar Cells

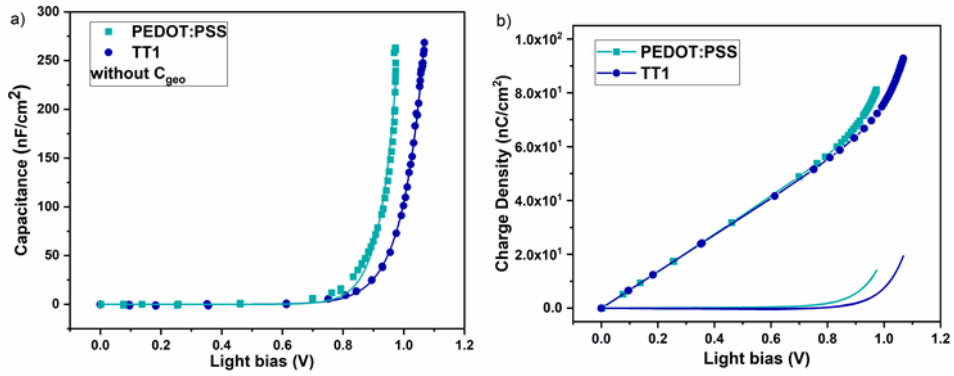

Figure 4.12. *(a) The $Diff_{Cap}$ measurements after the subtraction of the solar cells C_{geo} and (b) Total charge density (symbolised) at different V_{OC} which includes carriers in the contacts and bulk. Charge density (solid) at different light bias without C_{geo} represent only the experimental part of the fits: $y=Be^{Cx}$ (chemical capacitance).*

Once the differences in the DiffCap measurements are registered we turned on the analysis of the carrier recombination dynamics in these devices. The TPV decays are registered under the same illumination conditions used for the DiffCap. **Figure 4.13** illustrates the differences in carrier recombination kinetics for both types of solar cells studied in this work. The measured kinetics are fitted to Equation 2.24 in the section 2.6.

Phthalocyanine as a Hole Transporting Material in Perovskite Solar Cells

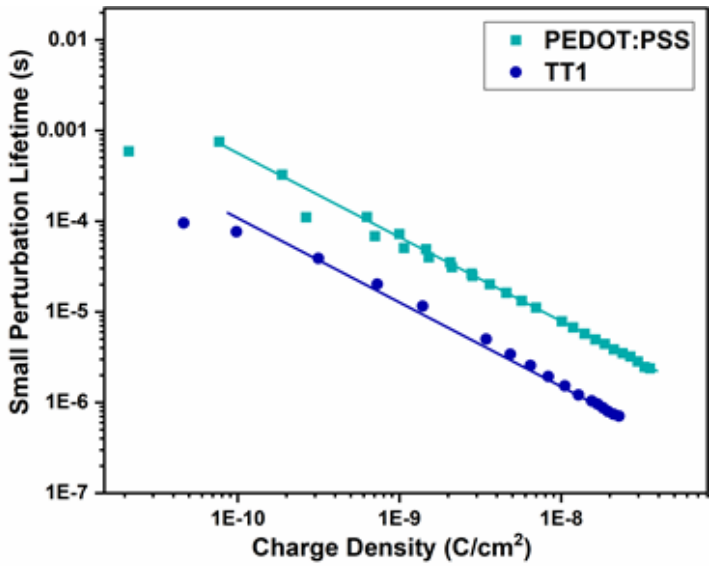

Figure 4.13. *Carrier lifetime at the different charge measured from the exponential part of the measurements shown in* ***Figure 4.12****. The solid lines correspond to the fittings to Equation 2.24.*

From the fitting to Equation 2.24, described in the section 2.6, we obtained a carrier recombination order δ of 1.90 and 1.94 for PEDOT:PSS and for the TT1 based devices, respectively. Although we found that PEDOT:PSS presents slower recombination dynamics compared to TT1, the δ values confirm our hypothesis; the differences in V_{OC} observed between inverted MAPI solar cells, using fullerene as an n-type selective contact and PEDOT:PSS or TT1 SAMs as a p-type selective contact, are due to the difference in energetics and not due to different carrier recombination kinetics.

4.4. Conclusions

We developed a highly efficient synthesis of benchmark phthalocyanine TT1, and we have demonstrated that TT1 SAMs can be used as efficient p-type selective contacts without annealing treatment in MAPI perovskite solar cells achieving efficiencies close to 15% at 1 sun under sun-simulated light (1.5 AM G spectra). The devices show voltages over 1 V due to the correct alignment of the HOMO energy level with the MAPI perovskite VB. In contrast, PEDOT:PSS devices, used as a control, show lower V_{OC} due to higher HOMO energy values. The measured device capacitance, as well as the evaluation of the carrier recombination order under operando conditions, supported the observation that the V_{OC} differences are due to the differences in HOMO energy value and not due to faster or slower carrier recombination dynamics at the solar cells. These results shown herein open new avenues for the use of robust molecules such as phthalocyanines and porphyrins as efficient p-type SAM contacts in thin film solar cells.

4.5. Synthetic Method and Procedure

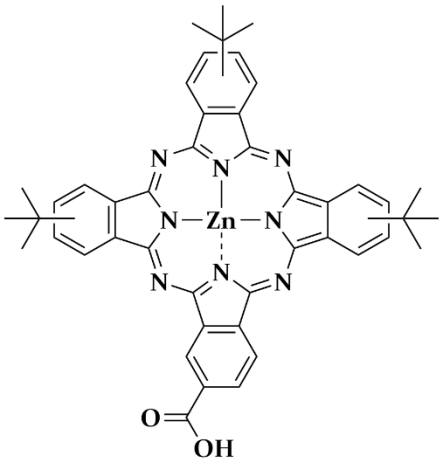

TT1

Zinc oxide (0.4 mg, 0.005 mmol) and potassium hydroxide (2.8 mg, 0.05 mmol) are placed in an oven-dried tube, which is placed in a Radley carousel. The tube is three times subjected to vacuum and then nitrogen gas. Vacuum is applied again, and the carousel heated to 170 °C for 1 h. Then the tube is refilled with nitrogen gas. Anhydrous and degassed mesitylene (1 mL) is added by syringe and the mixture heated to reflux. Hydroxyl derivative phthalocyanine 1 (0.05 mmol, 40 mg) that previously is dissolved in degassed mesitylene (1 mL) is added dropwise by syringe, and the reaction is stirring under a flow of nitrogen for 24 h at 170 °C. The mixture is cooled down to room temperature and the mesitylene is evaporated under vacuum. The precipitate is acidified with (2 mL) 16% aqueous hydrochloric acid. The aqueous layer is extracted with ethyl acetate (3x5 mL). The combined organic layers are dried over sodium sulfate and concentrated in vacuum to give the TT1 as a pure compound in 96 % yield (38 mg).

^{1}H NMR (400 MHz, DMSO) δ = 9.48- 9.28 (m, 8H), 8.33-8.25 (m, 4H), 1.83 – 1.76 (brs, 27H) ppm.

MALDI-TOF m/z calc. for $C_{45}H_{40}N_8O_2Zn^+(M^+)$: 790.24; found: 789.60.

Phthalocyanine as a Hole Transporting Material in Perovskite Solar Cells

Chapter 5

Carbazole Based Self-Assembled Hole-Selective Monolayer for Ultra-Stable and Highly Efficient Perovskite Solar Cells

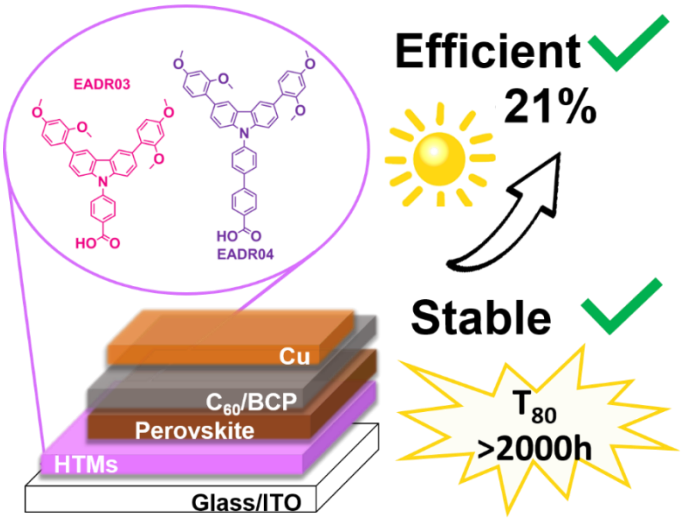

This chapter is based on the published work: Aktas, E. et al. Understanding the perovskite/self-assembled selective contact interface for ultra-stable and highly efficient p–i–n perovskite solar cells. **Energy & Environmental Science** 2021[227]

Carbazole Based Self-Assembled Hole-Selective Monolayer for Ultra-Stable and Highly Efficient Perovskite Solar Cells

5.1. Abstract

The current perovskite solar cell efficiency is close to silicon PV record values. Yet, the roadblock for industrialization of this technology is its stability. The stability of the solar cell not only depends on the stability of the perovskite material itself, but also notably on its contact layers and their interface with the perovskite, which plays a paramount role. This study rationalizes the design of new molecules to form self-assembled monolayers as hole-selective contacts. The new molecules increased the stability of perovskite solar cells to maintain 80% of its initial PCE of 21% for 250 h at 85 °C under 1 sun. The excellent charge collection property as well as a perovskite passivation effect enable the highly stable and efficient devices demonstrating the vast potential of this new type of contacts in photovoltaic application.

5.2. Introduction

In a short 10 years learning curve, perovskite solar cell (PSCs) efficiency reached over 25% from an initial 3.8%. Yet, despite having extraordinary progress on the device's efficiency, halide perovskite's long-term stability is one of the main roadblocks towards its industrialization. To improve the device's stability, not only the intrinsic stability enhancement of halide perovskite is essential, but also the stability of the device contact layers plays a crucial role. Highly priced organic charge selective materials drive the research to look for new organic conjugated molecules like self-assembled monolayers (SAMs), which have been applied before in organic-based optoelectronic devices.[228] Recently,

SAMs have been used as charge selective contacts for PSCs and the power conversion efficiency has rapidly achieved to 21% under standard measurement conditions.[113]

In this study, we designed and synthesized two new carbazole based self-assembled molecules for HSLs in p-i-n solar cells. We demonstrated stable efficiency above 21% delivering a solar cell open-circuit voltage (V_{OC}) of 1.19 V for a perovskite bandgap of 1.63 eV using these two SAMs. Remarkably, solar cells retain 80% of its initial conversion efficiency after 250 h maximum power point tracking under one sun AM 1.5 G illumination at 85 °C. These results are a new milestone for the development of a new class of hole selective materials in PSCs, which exhibits at the same time high efficiency and stability, which is paramount for the necessary transfer to industrial applications.

5.3. Results and Discussions

5.3.1. Design and Syntheses

The synthesis of *3,6-bis(2,4-dimethoxyphenyl)-9H-carbazole* is performed as our previously reported study.[229] *4-(3,6-bis(2,4-dimethoxyphenyl)-9H-carbazol-9-yl)benzoate* (EADR03-COOEt) and *4'-(3,6-bis(2,4-dimethoxyphenyl)-9H-carbazol-9-yl)-[1,1'-biphenyl]-4-carboxylate* (EADR04-COOMe) are synthesized through palladium-catalyzed Buchwald-Hartwig cross-coupling reaction using tris(dibenzylideneacetone)dipalladium(0) [$Pd_2(dba)_3$], tri-*tert*-butylphosphine tetrafluoroborate [(*tert*-Bu)$_3$P], sodium *tert*-butoxide

Carbazole Based Self-Assembled Hole-Selective Monolayer for Ultra-Stable and Highly Efficient Perovskite Solar Cells

(*tert*-BuO-Na^+). The pure compound of EADR03 and EADR04 are hydrolysed by potassium hydroxide in solvent mixture of methanol:tetrahydrofuran under reflux condition. The molecule structures of synthesized compound are confirmed by means of ^1H and ^{13}C NMR, HR-MS and Elemental Analysis. Structures of the synthesized compounds are confirmed by means of ^1H and ^{13}C NMR spectroscopy.

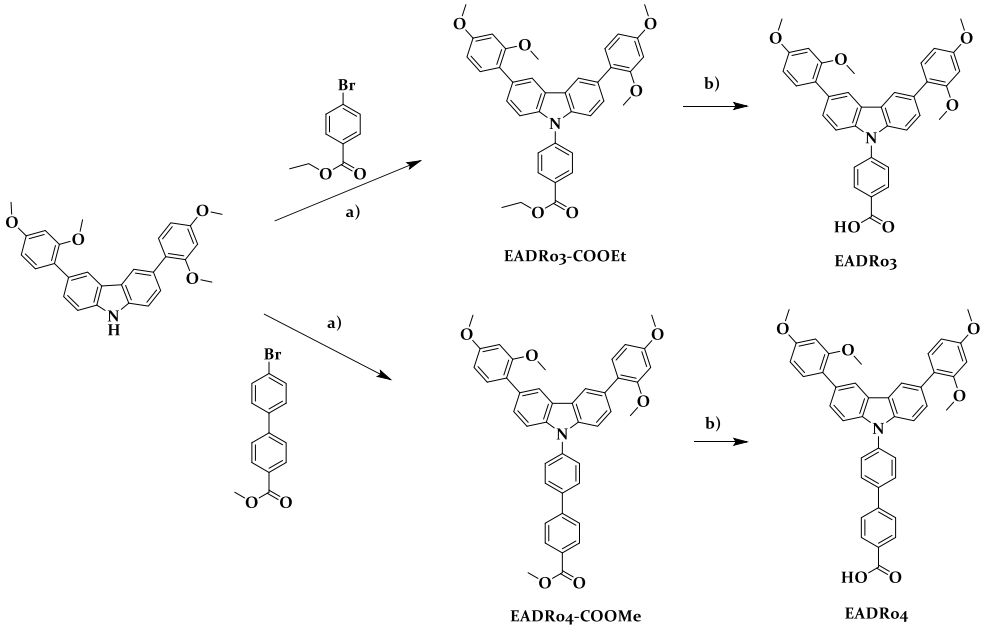

Scheme 5.1. *Synthesis pathway of SAMs; a) Tris(dibenzylideneacetone)dipalladium(0) (0.10 equiv.), tri-tert-butylphosphine tetrafluoroborate (0.20 equiv.), sodium tert-butoxide (1.1 equiv.), dry Toluene (10.0 mL), Argon, 115 °C, 24 h b) potassium hydroxide (10 equiv.), solvent mixture of methanol: tetrahydrofuran (1:1, v:v), 85 °C, 24 h.*

Scheme 5.1. shows the synthesis pathway of the new SAMs, where *4-(3,6-bis(2,4-dimethoxyphenyl)-9H-carbazol-9-yl)benzoic acid* (EADR03) and *4'-(3,6-bis(2,4-dimethoxyphenyl)-9H-carbazol-9-yl)-[1,1'-biphenyl]-4-carboxylic acid* (EADR04) have a carbazole moiety as electron donor unit.[230] On the one hand, such a carbazole chemical group has electron-rich block properties, which leads to increase PCE up to 18% in PSCs.[231–233] Subsequent electron-rich groups are mainly added as substituents in the carbazole moiety to align the energy levels with the perovskite material and increase its solubility in common organic solvents. On the other hand, the substituted position for the photo-active conjugated phenyl benzene plays a critical role in the electron-donating effect. For instance, if the methoxy groups are only located at the meta-position, it will have an electron-withdrawing effect.[234] Nevertheless, if it is only positioned at the ortho-position, it will twist the phenyl ring out of the plane, causing the undesired steric effect.[235] For these reasons, the 1,3-dimethoxybenzene is chosen as a substituent for carbazole moiety. The synthetic details are given in the synthetic methods and procedures part of this chapter.

5.3.2. Thermal, Optical, Electrochemical, And Photophysical Properties of SAMs and Perovskite Layer

The thermal behaviour of EADR03 and EADR04 is analysed by DSC and TGA (**Figure 5.1** and **Table 5.1**). The TGA showed remarkably high thermal stability with decomposition temperature (T_{des}) (5% weight loss)

for EADR04 (354 °C) than EADR03 (180 °C). Likewise, DSC confirmed that the glass transition temperature (T_g) during the first cycle for EADR03 and the second cycle for EAD04 is 173 °C and 354 °C, respectively. Both of SAMs might exist in both amorphous and semi-crystalline state that consisted uniform films of them while annealing perovskite layer. In the following section, the effect of thermal behaviours of SAMs on the stability of completed device will be discussed.

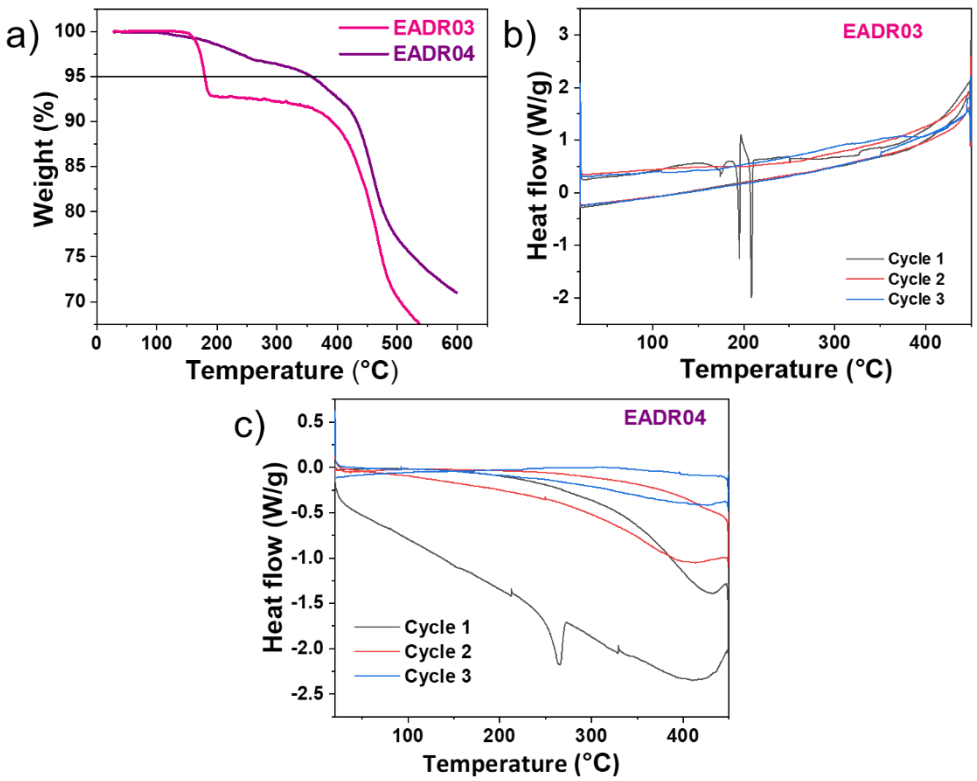

Figure 5.1. *a) TGA analysis of EADR03 and EADR04. DSC analysis of b) EADR03, and c) EADR04.*

Table 5.1. *Thermal properties of EADR03 and EADR04.*

HTMs	T_{des} *(°C)* [a]	T_g *(°C)* [b]
EADR03	180	173
EADR04	354	354

[a] Decomposition temperature determined from TGA (5 % weight loss). [b] Glass transition temperature determined from the first and second cycle of DSC. All experiments are carried out under N2 atmosphere, scan rate of 10 °C/min.

We examined the atomic bonds of SAMs onto the metal oxide surface using XPS. The spectra are analysed as described in the appendix (**Table A.1**). The C1s spectra, are decomposed into 4 peaks assigned to C-C or C-H at 284.6 eV (284.7 eV), to C-O at 286.0 eV (285.9 eV), COOCH bonds at 287.0 eV (287.0 eV), and to O-C=O bonds at 288.5 eV (289.1 eV) for EADR03 (EADR04) (**Figure 5.2a** and **c** respectively).[236,237] The [C-O] / [C-C + C-O] area ratios amount to 25% for EADR03 and 30% for EADR04. From the structure formulae, one would expect 15% for EADR03 and 12% for EADR04 ignoring attenuation due to inelastic electron scattering. The evident excess in C-O bonds is likely caused by solvent residues. It is worth noting that the bare ITO surface also exhibits C1s peaks situated at 284.9 eV, 285.8 eV, 287.0 eV, and 289.1 eV (**Figure A.60a**). These carbon contributions are presumably largely residues from the cleaning procedure. The O1s region, **Figure 5.2d** and **f** exhibit peaks belonging to In-O at 530.1 eV, to surface hydroxides at 530.9 eV (530.8 eV), to C=O at 532.8 eV (532.8 eV) and to C-O at 533.1 eV (533.2 eV) for EADR03 (EADR04) in the O1s spectra.[238,239] The bare ITO substrate also showed four components: 530.3 eV (InSnO), 530.8 eV, 531.8 eV, and 532.9 eV (see

Figure A.60b), where the carbon compounds are again presumably cleaning residues.

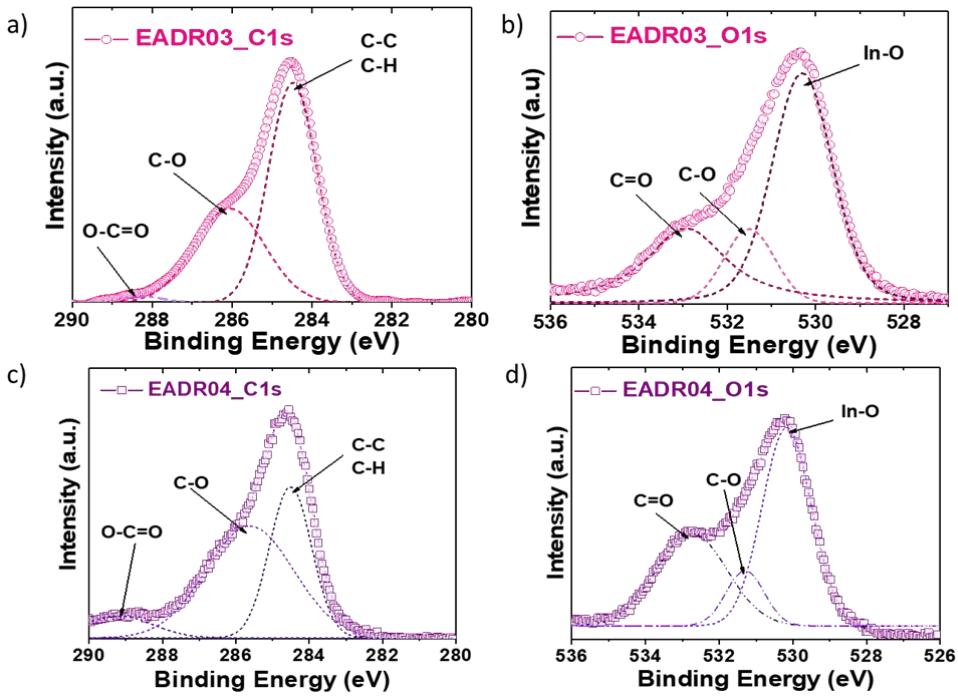

Figure 5.2. *The XPS high-resolution survey spectra of a) C1s b) O1s for ITO/EADR03 and c) C1s, d) O1s for ITO/EADR04.*

The formation of ester bonds demonstrates bonding between the carbon atom of carboxylic acid and the oxygen atom of the hydroxyl group on ITO or to solvent residues.[240] Moreover, we observe a much weaker signal of this characteristic ester bond in C1s and O1s spectra of a bare ITO in these regions, which further points to the presence of SAMs on ITO (**Figure A.61**). The N1s spectra show the same peak position of *ca.* 400 eV for both SAMs, indicating the presence of the C-N bond in the structure (**Figure A.61c**). These are a strong hint to the presence of SAMs on the ITO substrate.

To prove the suitable energetic properties as hole selective material for PSCs, we performed UPS on SAM layer attached to ITO substrate similar to what is used in the device. Here, ITO coated glasses are homogenously covered with SAMs by dipping method. The condensation reaction occurs between the carboxylic acid (-COOH) anchor group of SAMs and the surface hydroxyl group (-OH) of metal oxide to give ester (O-C=O) type linkages,[91,241] which result in the formation of a monolayer of SAM on the ITO. The optical bandgap of SAMs is estimated from the absorption edge wavelength ($\lambda_{a.e.}$) using UV-vis measurement[242] (**Figure 5.3** and **Table 5.2**). From UPS measurement and optical bandgap we calculate the position of the SAM' LUMO. The valence band onset and the E_F value EADR03 and EADR04 are schematically displayed in **Figure 5.7**. In this study, we employed the triple cation perovskite ($Cs_{0.05}FA_{0.79}MA_{0.16}Pb(I_{0.84}Br_{0.16})_3$ onwards labelled as CsFAMA) as the absorber layer adapted from Saliba *et al.*[243] The energetic properties of PTAA, used as a reference, and CsFAMA are obtained from the literature and all values reference to the vacuum level.[244] SAMs exhibits better electron blocking character than PTAA due to the carbazole unit in small molecule backbone that increases the LUMO level while works as efficient hole extraction layers.

Carbazole Based Self-Assembled Hole-Selective Monolayer for Ultra-Stable and Highly Efficient Perovskite Solar Cells

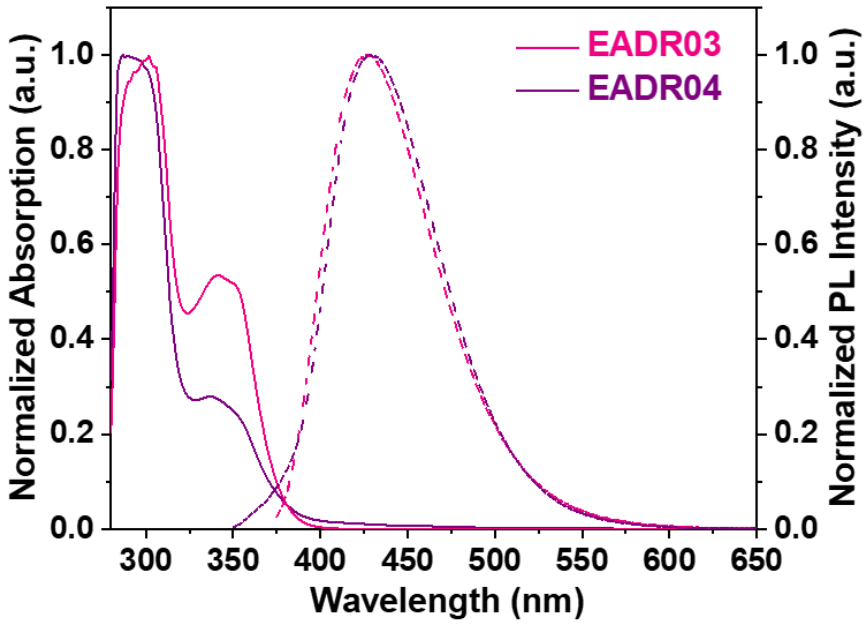

Figure 5.3. *Absorption (solid lines) and emission (dashed lines) spectra of EADR03 and EADR04.*

Table 5.2. *Optical and energetic properties of small molecules.*

SAMs	$\lambda_{abs.}$ *(nm)*	$\lambda_{em.}$ *(nm)*	$\lambda_{a.e.}$ *(nm)*	$E_g^{opt.}$ *(eV)*	*LUMO (eV)*
EADR03	300/345	425	378	3.28	**1.77**
EADR04	290/335	430	374	3.31	**1.74**

Carbazole Based Self-Assembled Hole-Selective Monolayer for Ultra-Stable and Highly Efficient Perovskite Solar Cells

Additionally, we designed the SAM molecules with 1,3-dimethoxybenzene moiety acting as a terminal group that provides a miscible interface for the perovskite one-step solution process. A miscible interface ensures a homogenous and compact perovskite film.[245] To determine the surface wettability, contact angle measurements are performed on bare ITO and p-type materials deposited on ITO. The contacting angles of the water on bare ITO, PTAA, EADR03 and EADR04 are 8.13˚, 88.15, 50.19˚ and 51.63, respectively (**Figure 5.4**). PTAA layer shows a higher hydrophobicity than the SAMs in agreement with the previous report,[246] leading to a poor wetting for perovskite solution on PTAA.

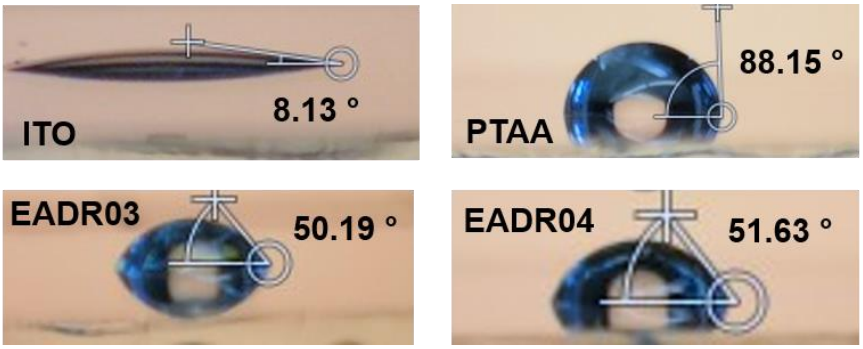

Figure 5.4. *Contact angle measurements on the bare ITO, ITO/PTAA, ITO/EADR03 and ITO/EADR04 surfaces.*

We note that in the XRD patterns (**Figure 5.5**), though there is no detectable peak shift or peak broadening in the perovskite phase, however, there is a noticeable more pronounced PbI_2 phase in the perovskite on PTAA than on SAMs. This higher PbI_2 content is also visible in the SEM images as bright small grain on the surface (**Figure 5.6**). Although it has been reported that excess PbI_2 in the perovskite can improve the device performance, a recent report has shown that higher PbI_2 consisted perovskite can lead to lower stability in devices due to the formation of metallic Pb, which can be the origin of non-radiative recombination centers,[247] which will be discussed in details in the following section.

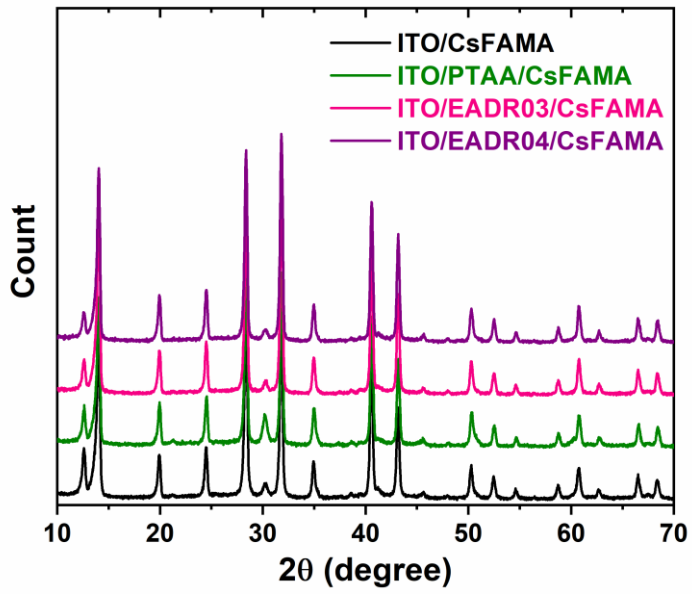

Figure 5.5. *X-ray diffraction patterns of perovskite layers grown on bare ITO, ITO/PTAA, ITO/EADR03 and ITO/ EADR04. The patterns are well in agreement with literature containing similar perovskite compounds.*

Carbazole Based Self-Assembled Hole-Selective Monolayer for Ultra-Stable and Highly Efficient Perovskite Solar Cells

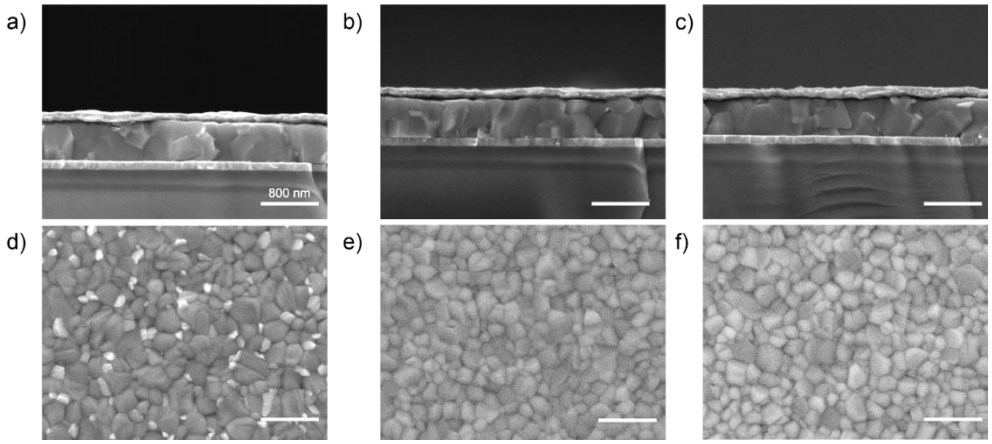

Figure 5.6. *Scanning electron microscopic images of cross-sectional full device of a) PTAA, b) EADR03 and c) EADR04 employed planar PiN perovskite solar cells; and top view of perovskite layers grown on d) ITO/PTAA, e) ITO/EADR03 and f) ITO/EADR04. All scale bars are 800 nm.*

5.3.3. Spectroscopy, Photovoltaic Properties and Device Stability Investigation of Perovskite-Based Devices

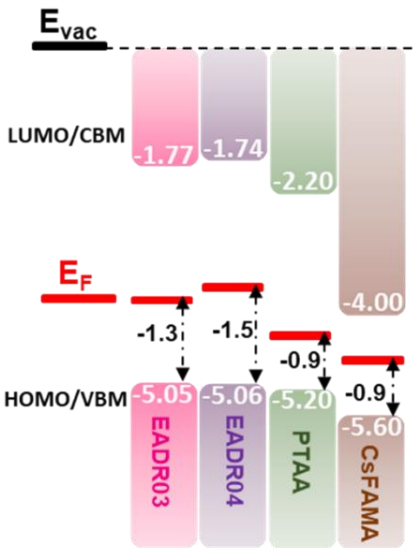

Figure 5.7. *Energy alignment of different layers. The band edge positions of SAMs, PTAA and CsFAMA layer's from UPS measurements in the schematic representation. Note that the SAM layer's values (EADR03 and EADR04) are measured with UPS (**Figure A.66** showed UPS spectra) (see for details section 2.3). Before UPS measurement, the ITO substrate is treated with UV-Ozone to ensure similarity with used substrates in devices.*

To understand the charge transfer property of these new SAMs as HSLs for PSCs, we performed TRPL using λ=470nm as excitation wavelength as shown in **Figure 5.8**. The traces exhibit two different decay profiles fitted to a bi-exponential function as previously reported.[213,248,249] SAM-based perovskite films show initial fast decay that can be assigned to trap

filling, while the slower decay most likely corresponds to the bimolecular recombination. The lifetimes τ_1 of EADR03, EADR04, PTAA and the perovskite are 15 ns, 9 ns, 2 ns and 7 ns, respectively, and the lifetimes τ_2 calculated are 158 ns, 106 ns, 12 ns and 83 ns for EADR03, EADR04, PTAA and the perovskite, respectively (**Table 5.3**). Interestingly, in **Figure 5.8b**, the luminescence decay of perovskite layers on SAMs shows efficient quenching that supports their efficient hole transporting character compared to PTAA. Not only that we have evidence of a faster charge extraction using SAM compared to PTAA, but the increased PL yield can also indicate interfacial passivation effect[250] compared to PTAA sample shown in **Figure 5.8c** similar to reported carbazole based polymer.[251]

Carbazole Based Self-Assembled Hole-Selective Monolayer for Ultra-Stable and Highly Efficient Perovskite Solar Cells

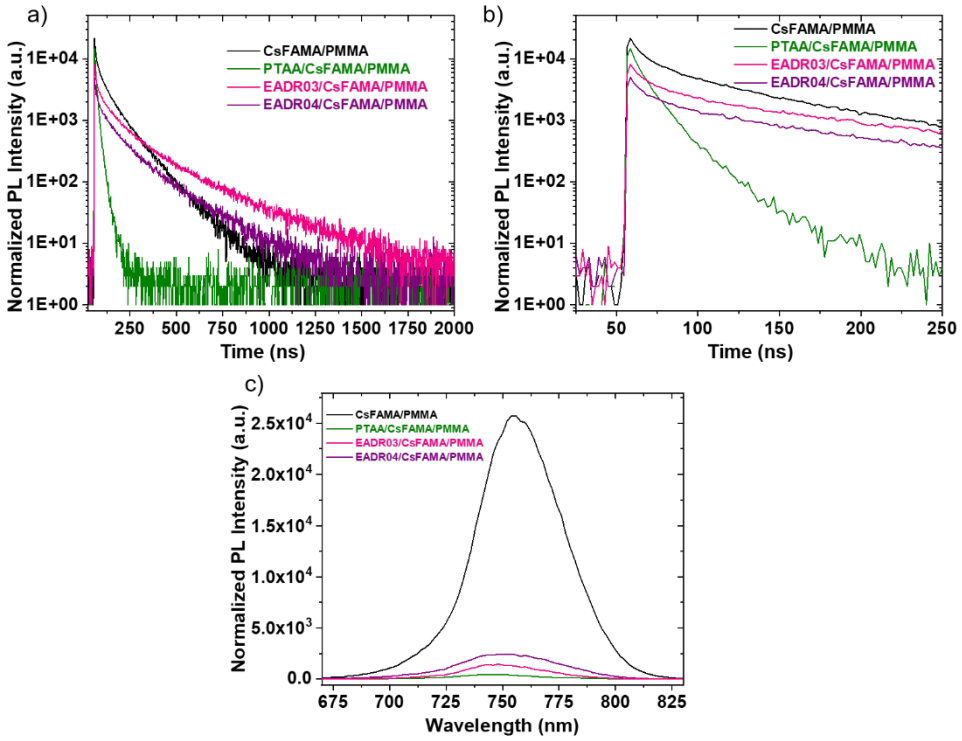

Figure 5.8. *Luminescence emission decays (λ_{ex}=470 nm) measured for a) 2000 ns and b) 250 ns for CsFAMA/PMMA, the PTAA/CsFAMA/PMMA, EADR03/CsFAMA and EADR04/CsFAMA/PMMA on ITO coated glass substrate at room temperature. c)Luminescence emission band upon excitation at λ_{ex}=470 nm for the CsFAMA/PMMA, the PTAA/CsFAMA/PMMA, EADR03/CsFAMA and EADR04/CsFAMA/PMMA (total thickness of 550-600 nm) at room temperature.*

Table 5.3. *Fitting values are obtained from the de-convolution of the luminescence decays in* ***Figure 5.8b****.*

Films	τ_1 ***(ns)***	τ_2 ***(ns)***
CsFAMA/PMMA	7	83
PTAA/CsFAMA/PMMA	2	12
EADR03/CsFAMA/PMMA	15	158
EADR04/CsFAMA/PMMA	9	106

We employed in this study the state-of-the-art device architecture with ITO/ SAM or PTAA/CsFAMA/C_{60}/BCP/Cu sandwich architecture in **Figure 2.18**.[252] Cesium-containing triple cation perovskite (CsFAMA) is deposited on top of the HSLs using the one-step method. Afterwards, C_{60}, an electron selective layer, is thermally evaporated on top of the perovskite layer. The fullerene C_{60} has excellent electron-extraction properties in photovoltaic devices. Thus, it is preferred for the electron transport layer.[253] Lastly, a BCP buffer layer and copper (Cu) electrode are evaporated to complete the device. SAMs are generally deposited on metal oxide surface as a monolayer through a variety of methods like solution assisted self-assembly (dip-coating), vapour deposition and spin-coating method.[239] Here, we used the paradigmatic PTAA as our baseline to determine the performance of cells with SAMs. PTAA is not only widely used in p-i-n PSCs as polymeric HSL, which can be coated into a thin homogenous layer from solution and show higher than 18%

PCEs.[24,254,255] Detailed fabrication process of perovskite solar cells is presented in the Chapter 2.

The choice of solvent is the first step and critical step for SAMs to have a well-organised interface between SAMs and perovskite absorber. Here, the design of EADR03 and EADR04 consists of carboxylic acid moiety on the molecule backbone, which makes the molecules soluble in non-halogenated solvents as EtOH and IPA. The devices with SAMs as HSLs show statistically better performance with IPA using the dipping method compared to ethanol (**Figure 5.9** and **Figure 5.10**). The best PV parameters of solvent optimisation are summarised in **Table 5.4**. Consequently, we achieve more than 20% PCE with dipping method with EADR03 as the HSL, whereas spin coating method only has a maximum of 17% (**Figure 5.11** and **Figure 5.12**). The best device parameters of EADR03 with different deposition methods are shown in **Table 5.5**. On the other hand, EADR04 is not suitable for spin-coating methods because of solubility problems.

Carbazole Based Self-Assembled Hole-Selective Monolayer for Ultra-Stable and Highly Efficient Perovskite Solar Cells

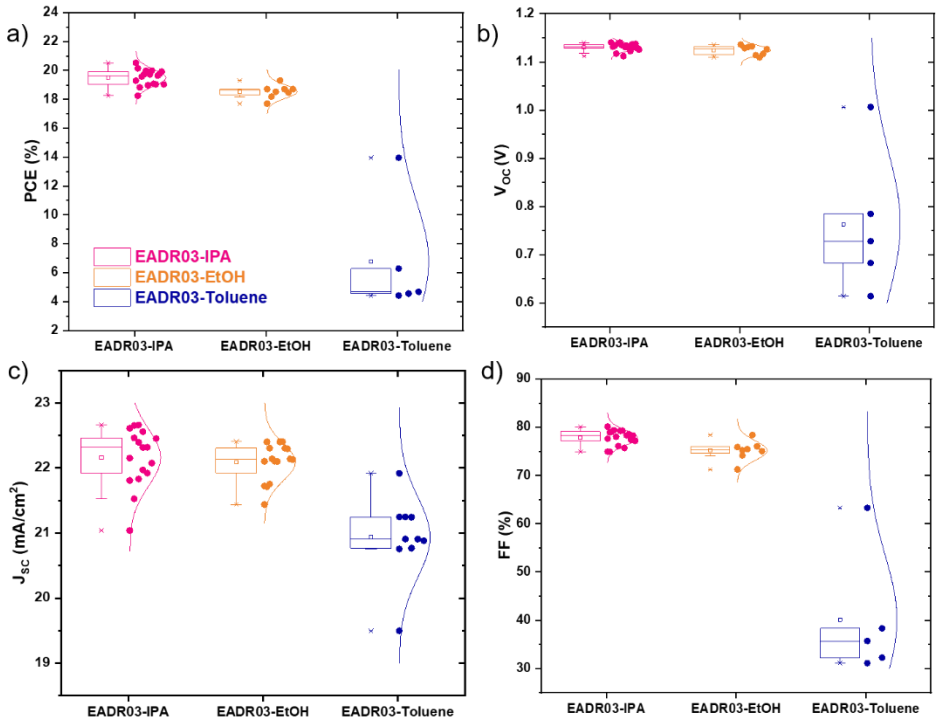

Figure 5. 9. *Device performance statistic total 30 devices from EADR03 in different solvents in the devices a) PCE, b) V_{OC}, c) J_{SC}, d) FF.*

We note that here the dipping method is preferable due to lower solubility of the molecules in alcohol. Nonetheless, the solubility is not the only deciding factor for device performance. The molecules have excellent solubility in toluene, yet the devices using this solvent exhibit unsatisfactory performance (**Table 5.4**). The reason behind the different behaviour is beyond the scope of this study and will require further research.

Carbazole Based Self-Assembled Hole-Selective Monolayer for Ultra-Stable and Highly Efficient Perovskite Solar Cells

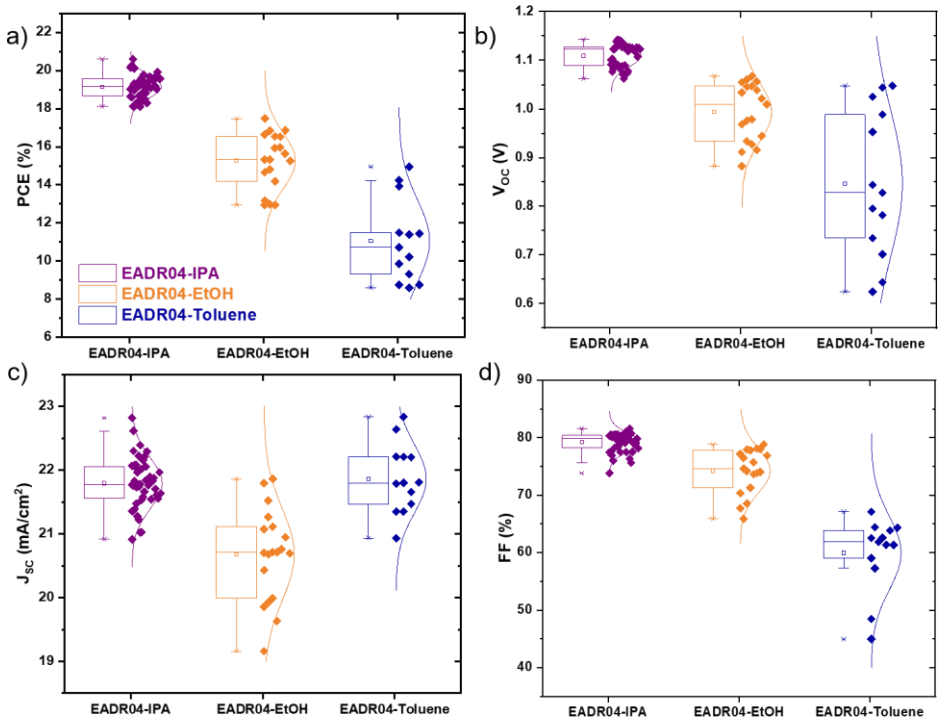

Figure 5.10. *Device performance statistic over 10 devices per conditions from EADR04 in different solvents in the devices a) PCE, b) V_{OC}, c) J_{SC}, d) FF.*

Carbazole Based Self-Assembled Hole-Selective Monolayer for Ultra-Stable and Highly Efficient Perovskite Solar Cells

Table 5.4. *Best photovoltaic parameters from EADR03 and EADR04 in different solvents.*

SAMs	Solvents	Scan Direction	PCE (%)	V_{OC} (mV)	J_{SC} (mA/cm^2)	FF (%)
EADR03	IPA	forward	20.4	1127	22.6	80
		reverse	20.5	1132	22.6	80
EADR03	EtOH	forward	19.4	1130	21.7	79
		reverse	19.2	1132	21.7	78
EADR03	Toluene	forward	13.3	993	21.9	61
		reverse	13.9	1006	21.9	63
EADR04	IPA	forward	20.6	1140	22.6	80
		reverse	20.4	1143	22.6	79
EADR04	EtOH	forward	15.9	1038	20.7	74
		reverse	17.6	1083	21.1	77
EADR04	Toluene	forward	14.1	1025	22.2	62
		reverse	14.3	1037	22.2	62

Carbazole Based Self-Assembled Hole-Selective Monolayer for Ultra-Stable and Highly Efficient Perovskite Solar Cells

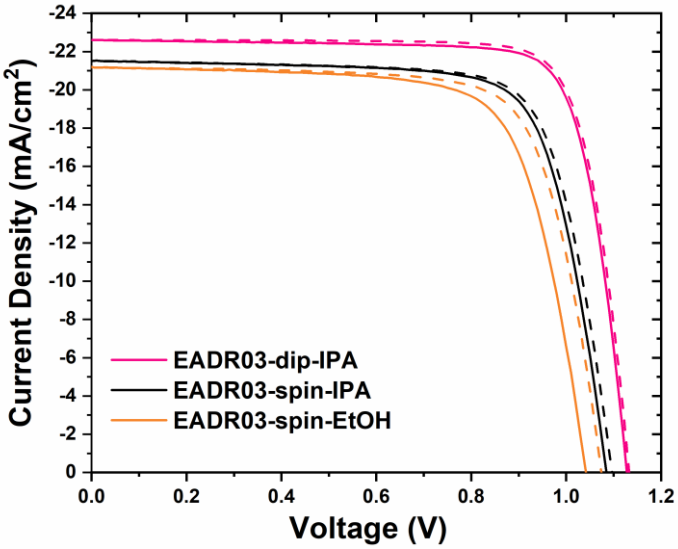

Figure 5.11. *Best J-V curves from EADR03 with different deposition methods.*

Carbazole Based Self-Assembled Hole-Selective Monolayer for Ultra-Stable and Highly Efficient Perovskite Solar Cells

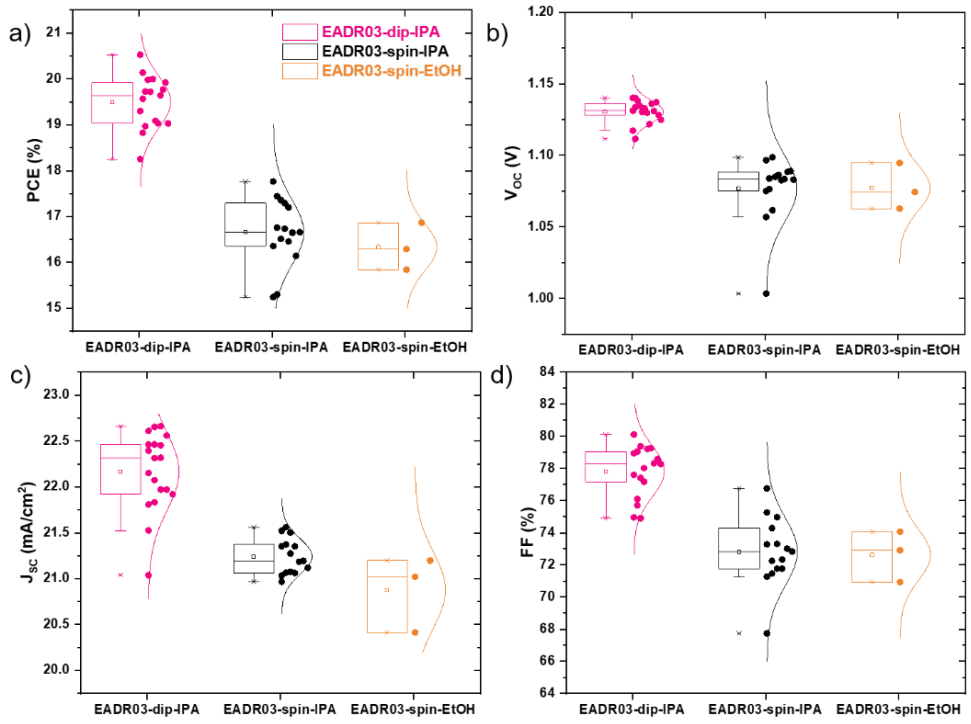

Figure 5.12. *Device performance statistic total 30 devices using different deposition methods of EADR03 in the devices a) PCE, b) V_{OC}, c) J_{SC}, d) FF. Forward and reverse scan value plotting together.*

Table 5.5. *Photovoltaic parameters from EADR03 with different deposition methods.*

SAM	Deposition Method	Solvents	Scan Direction	PCE (%)	V_{OC} (mV)	J_{SC} (mA/cm^2)	FF (%)
EADR03	Dip-coating	IPA	forward	20.4	1127	22.6	80
			reverse	20.5	1132	22.6	80
EADR03	Spin-Coating	IPA	forward	17.5	1084	21.5	75
			reverse	17.7	1096	21.5	75
EADR03	Spin-Coating	EtOH	forward	15.9	1041	21.2	72
			reverse	16.9	1074	21.2	74

Figure 5.13 shows the J-V scans of the best devices with PTAA, EADR03 and EADR04 measured at a scan rate of 100 mV/s from forward to reverse bias. MPP tracks of the best devices are placed in **Figure 5.13b**. MPP-tracked efficiencies are comparable with the respective J-V values, which is expected from the negligible hysteresis. A statistical distribution of the cell parameters is achieved from more than 15 devices for each HSLs in **Figure 5.13a** showing systematically higher performance of SAM based cells compared to PTAA. The best PCE of EADR03 and EADR04 is 20.5% and 20.6% surpassing PTAA cells' best value of 18.9%. Remarkably, the V_{OC} values of SAM-based devices demonstrate more than 1.1 V and the FF values >80 %. The superior electron blocking of SAM compared to PTAA is attributed to the higher V_{OC} and FF values of EADR03 and EADR04 compared to PTAA. Specifically, the voltage of SAM-based

devices is approximately 150 mV larger than that of PTAA. This device performance improvement is not directly correlated to the HOMO level of the material as PTAA has a deeper HOMO level compared to SAMs (**Figure 5.7**): instead, SAM as a material, which can have both efficient charge transport and passivation effect, results in this improvement. We emphasize that we achieve this desirable property of a contact layer without the use of dopants, which has been shown to degrade the perovskite layer.[256] Our result resonates with the conclusion of Al-Ashouri et al.[244] on phosphonic anchor SAMs. These results establish the tremendous promising benefit of SAM as an attractive class of material for selective layers realized in both perovskite and organic PV.[61,222,257]

Carbazole Based Self-Assembled Hole-Selective Monolayer for Ultra-Stable and Highly Efficient Perovskite Solar Cells

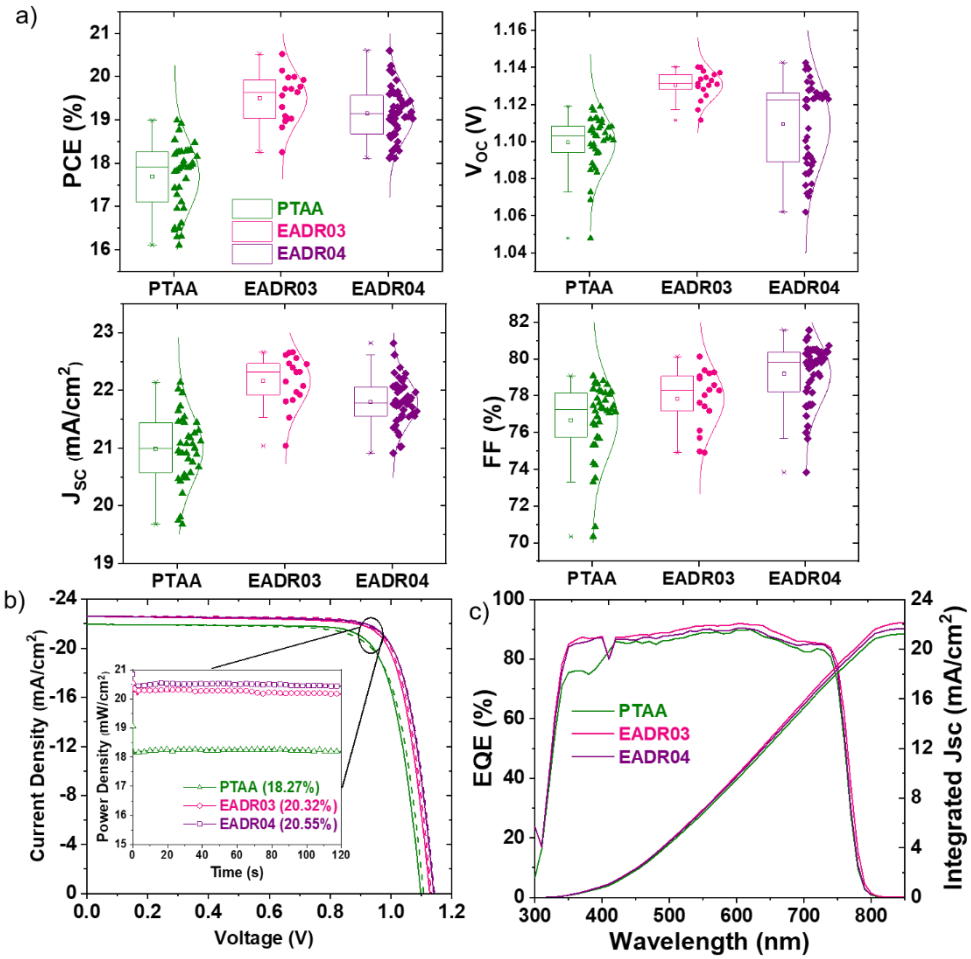

Figure 5.13. *a) Device performance statistic with different hole selective layers. b) Best J-V curves from PTAA, EADR03 and EADR04 with quasi-steady state efficiency. c) Corresponding external quantum efficiency curves which show integrated current density in agreement with values from J-V measurement.*

In addition, the J-V scan of SAM-HSL based full device showed a lower leakage current in place of PTAA under dark conditions in **Figure 5.15**. Low dark current also indicates a high density of SAM on ITO. The integrated J_{SC} of the best devices from EQE integration is shown in **Figure 5.13c**. A higher current density is also achieved thanks to less parasitic absorption of SAM compared to PTAA in the short wavelength range similar to phosphonic SAMs developed for the same device architecture.[87] Integrated J_{SC} values have a negligible difference (~1 mA/cm^2) with the J_{SC} values gained from the J-V scans for the best device. The devices with the SAMs as HSLs show minor HI[55,183] between reverse and forward J-V scans. All photovoltaic parameters of the best devices are provided in **Table 5.6**.

Carbazole Based Self-Assembled Hole-Selective Monolayer for Ultra-Stable and Highly Efficient Perovskite Solar Cells

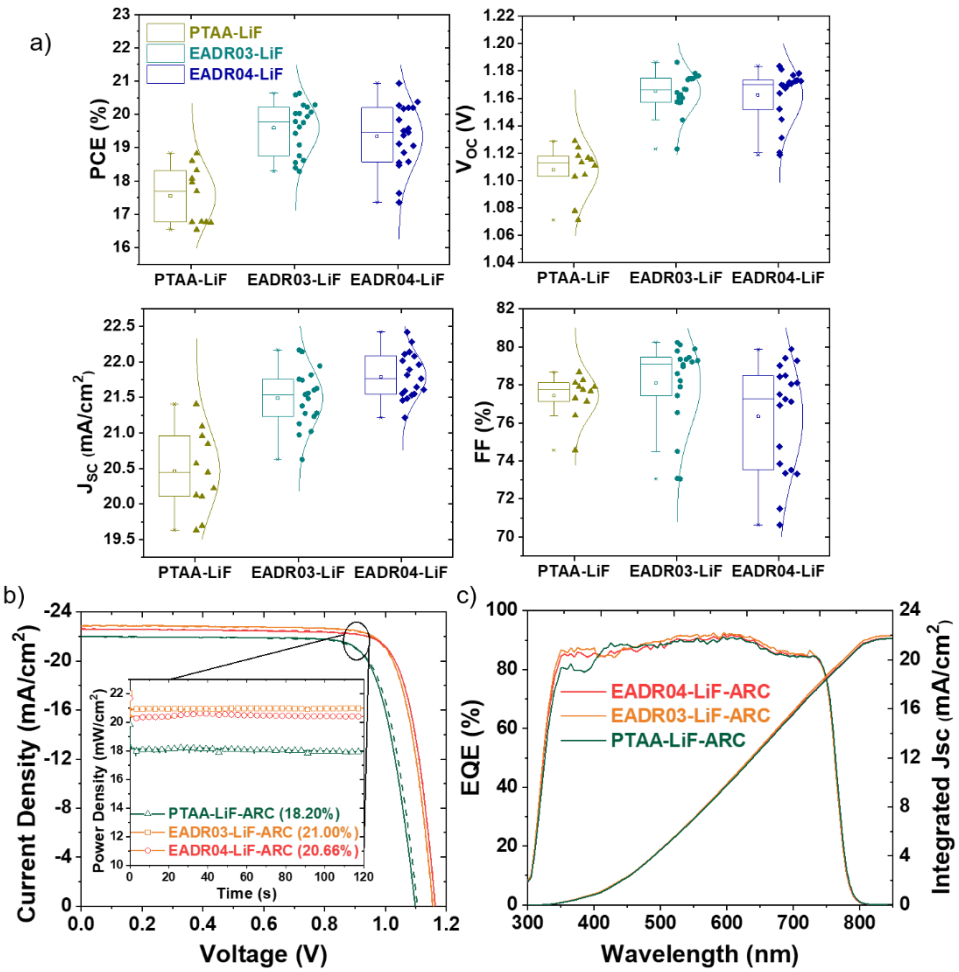

Figure 5.14. *a) Device performance statistic total of 50 devices from PTAA, EADR03 and EADR04 with LiF. b) Best J-V curves from PTAA, EADR03 and EADR04 with LiF and anti-reflection coating in the devices with quasi-steady state efficiency. c) Corresponding external quantum efficiency curves which show integrated current density in agreement with values from J-V measurement with anti-reflection coating.*

Carbazole Based Self-Assembled Hole-Selective Monolayer for Ultra-Stable and Highly Efficient Perovskite Solar Cells

As we have demonstrated the good passivation effect of SAM on the interface between perovskite and the HSLs compared to the commonly used polymer PTAA, the other interface with electron selective layer is equally important. It has been reported that the interfacial recombination at perovskite/C_{60} dominates the losses in voltage of this device architecture and it can be improved by an ultrathin passivation layer of LiF (~1 nm).[252] In this study, we used the same approached to enhance further the final V_{OC} of the device, reaching 1.19 V with 1.63 eV bandgap perovskite with EADR03 based cells. **Table 5.6** summarizes the champion devices in this study. As shown in **Table 5.6**, the improvement brought from LiF is higher in SAM-based devices compared to PTAA-based ones (**Figure 5.16**). This can be attributed to slightly higher PbI_2 content on the surface of the perovskite grown on PTAA than SAM (shown as bright grain in SEM images – **Figure 5.6**). The presence of PbI_2 on the surface can partially reduce the interfacial recombination at perovskite/C_{60} because of its wide bandgap.[258] With the improvement from LiF (the V_{OC} increases for more than 50 mV) and an anti-reflection coating, the SAM-based device reached more than quasi-steady-state 21% for the EADR03 cell and 20.7% for EADR04 after 2 minutes of MPP tracking (**Figure 5.14b**).

Carbazole Based Self-Assembled Hole-Selective Monolayer for Ultra-Stable and Highly Efficient Perovskite Solar Cells

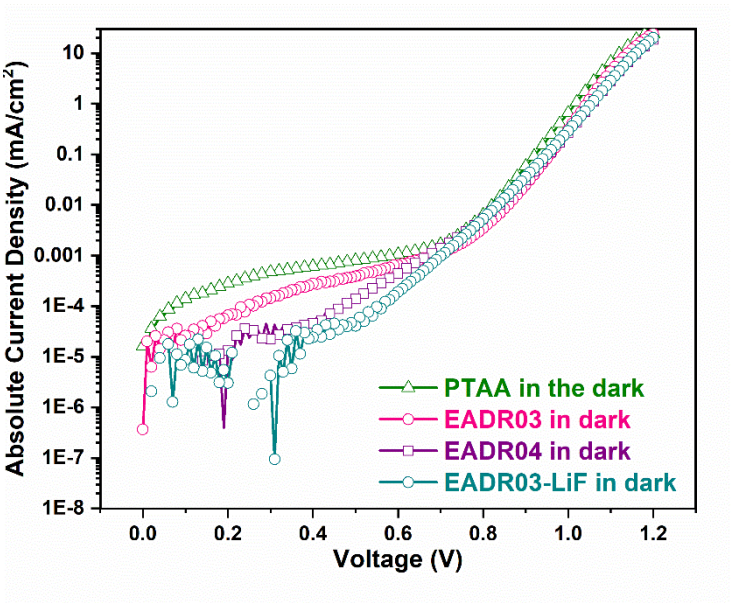

Figure 5.15. *Dark J-V curves of the hole selective contacts.*

Carbazole Based Self-Assembled Hole-Selective Monolayer for Ultra-Stable and Highly Efficient Perovskite Solar Cells

Table 5.6. *Photovoltaic parameters of the best performing devices based on different HSLs with and without LiF and anti-reflection coating with a scan speed of 100 mV/s.*

HSLs	*LiF*	*ARC*	*Integrated J_{SC} (mA/cm²)*	*J_{SC} (mA/cm²)*	*V_{OC} (mV)*	*FF (%)*	*PCE (%)*	*HI (%)*
PTAA	No	No	21.2	21.9	1098	79	18.9	-0.01
PTAA	Yes	No	21.0	21.4	1124	78	18.8	0.06
PTAA	Yes	Yes	21.7	22.0	1105	78	18.9	0.00
EADR03	No	No	22.1	22.6	1132	80	20.5	0.00
EADR03	Yes	No	21.2	21.9	1186	79	20.5	0.03
EADR03	Yes	Yes	21.9	22.9	1156	80	21.2	0.00
EADR04	No	No	21.6	22.6	1140	80	20.6	-0.01
EADR04	Yes	No	21.0	22.2	1177	80	20.9	0.03
EADR04	Yes	Yes	21.8	22.6	1164	80	21.0	0.00

Carbazole Based Self-Assembled Hole-Selective Monolayer for Ultra-Stable and Highly Efficient Perovskite Solar Cells

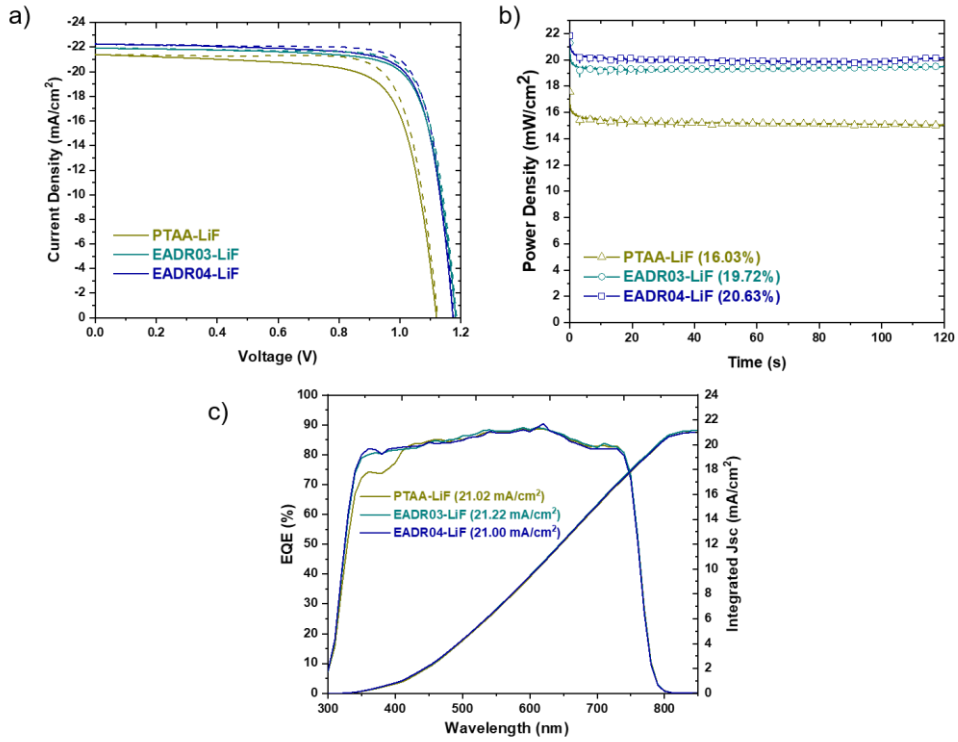

Figure 5.16. *a) Best J-V curves from PTAA, EADR03 and EADR04 with LiF. b) Quasi-steady state efficiency of charge selective contacts with LiF employed perovskite solar cells. c) Corresponding external quantum efficiency curves which shows integrated current density in agreement with values from J-V measurement with LiF.*

Carbazole Based Self-Assembled Hole-Selective Monolayer for Ultra-Stable and Highly Efficient Perovskite Solar Cells

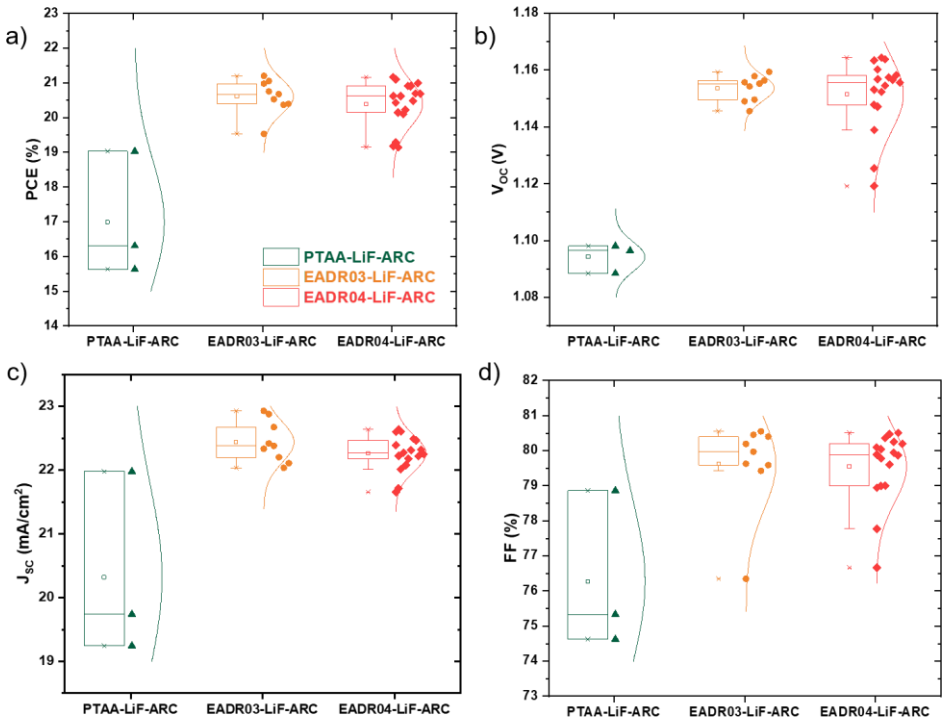

Figure 5.17. *Device performance statistic total 25 devices from PTAA, EADR03 and EADR04 with LiF and antireflection coating in the devices a) PCE, b) V_{OC}, c) J_{SC}, d) FF.*

Perovskite-based PV has reached 25.5% certified PCE and surpassed the conventional PV thin-film technologies and approaching the state-of-the-art silicon single-junction solar cell.[12] However, to integrate into the PV industry, perovskite's lack of stability is the main problem to tackle in the field.[259] Here, we use a high through-put ageing setup, which can track hundreds of devices at once. We compared the stability of PTAA with EADR03 and EADR04 cells in the continuous MPP in one sun illumination. As can be seen in **Figure 5.18a**, the PTAA cells rapidly lost more than 15% of its initial PCE after 24 hours of MPP tracking. Meanwhile, the SAMs based devices exhibit excellent higher stability

(note that the curves are averaged from different devices and show statistical values rather than only best device).

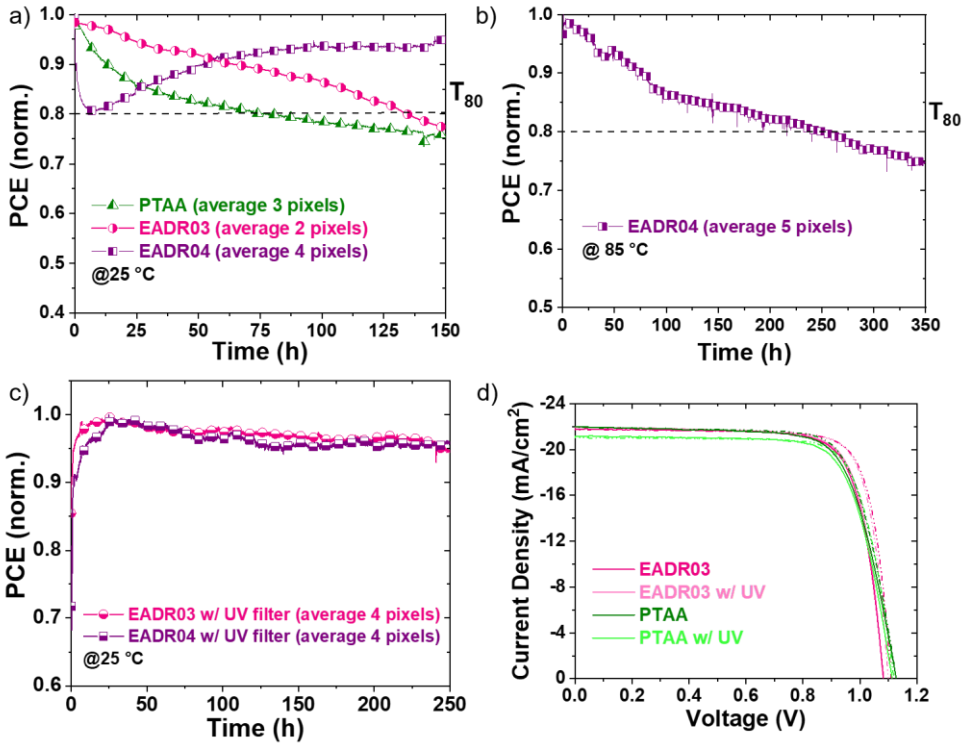

Figure 5.18. *Long-term continuous maximum power point tracking a) EADR03, EADR04 and PTAA based devices with BCP at 25 degree Celsius. b) EADR04 with BCP at 85 degree Celsius. c) EADR03 and EADR04 based devices with UV filter (cut-off at 350 nm at 25 degree Celsius. Note that the values are averaged from different devices from different batches. All the measurements are done in an N_2 atmosphere without encapsulation. d) Best J-V curves from PTAA and EADR03 with and without UV light exposition (365 nm) for 30 minutes, prior to perovskite layer fabrication.*

The EADR04 cells, though showing a fast drop in the first few hours, regain its initial efficiency and retain 95% of the initial efficiency after 150 h of continuous MPP tracking before they have a declining trend. We extrapolate this trend and estimate the T_{80} (time until the cell reaches 80% of its initial efficiency) to result in a more than 800 hours T_{80} for

EADR04 cells. Compared to EADR04 cells, the EADR03 cells gradually decrease until they reach 80% of initial PCE at around 180 h (as can also be seen in **Table 5.7**). This trend is more evident when the EADR04 cells are aged at an elevated temperature of 85 °C (**Figure 5.18b**) where the cells retain 80% of its initial efficiency for approximately 250 h continuous MPP tracking. This difference between the two SAMs can be attributed to the structure of the molecules. As can be seen in **Figure 5.1**, EADR04 has higher decomposition temperature compared to EADR03 thanks to the extra phenyl in the linkage group (chain) between anchoring group and functional group. Note that the thermogravimetry indicates the decomposition temperatures (180 °C for EADR03 and 354 °C for EADR04), which is indeed not the same temperature as the operational conditions. However, thermogravimetry can still indicate the resiliency of the molecules at high temperature and long-time operation conditions. Similar to our observation, Li et al. has reported that different conjugated side-chain polymers have higher thermal stability.[260]

Table 5.7. *Estimated T_{80} of the p-i-n perovskite solar cell with different HSLs from the MPP traces with and without UV filter.*

HSLs	*Initial PCE (%)*	*Ageing Temperature and Illumination*	*Tracking Time (h)*	*Estimated T_{80} (h)*
PTAA	18.5	25 °C, metal-halide lamp, 100 mW/cm²	250	81
EADR03	19.3	25 °C, metal-halide lamp, 100 mW/cm²	250	183
EADR03	19.9	25 °C, metal-halide lamp with UV filter, 100 mW/cm²	250	1574
EADR04	17.9	25 °C, metal-halide lamp, 100 mW/cm²	250	872
EADR04	19.9	25 °C, metal-halide lamp with UV filter, 100 mW/cm²	250	2086
EADR04	20.1	85 °C, metal-halide lamp, 100 mW/cm²	350	242
PTAA*	16	25 °C, White LED, 100 mW/cm²	170	9,000

*The selected report has similar device architecture in inert gas conditions and room temperature.

We attribute this encouraging improvement in the stability of SAMs as HSLs compared to PTAA to the excellent stability of SAMs in UV light. Indeed, when we expose PTAA layers to the UV light for 30 minutes prior to perovskite deposition, the device exhibits lower J_{SC} whereas UV light has negligible effect on EADR03 (as can be seen in **Figure 5.18d** and **Table 5.8**). This is more evidenced in the device statistic shown in **Figure 5.19** where PTAA cells loss on average more than 1 mA/cm² after UV exposure. We emphasize that even without any UV light stress on the

perovskite absorber layer, the UV light has a detrimental effect on PTAA in contrast to the SAMs whose devices did not show this behaviour. The UV-induced degradation in PTAA is very likely due to the breaking of carbon bonds in the aromatic rings into smaller fragments.[261] In addition, polymers have been reported to undergo the photochemical pathway in which the polymer hydrocarbon chain can break down into free radicals in the presence of oxygen. This UV-photochemical can severely deteriorate polymeric material properties.[262] This also indicates a potential degradation pathway of polymer HSLs in ambient air that is undesirable for PSCs application. Notably, a bulk of PTAA (~ 10 nm) and a single molecular layer (1-3 nm) might not be directly comparable in this study. The UV absorption of the SAM layer is negligible compared to the PTTA layer. We do expect that absorption of PTAA layer about 1 order of magnitude higher than SAM layer if we only consider the thicknesses of the two layers.

Carbazole Based Self-Assembled Hole-Selective Monolayer for Ultra-Stable and Highly Efficient Perovskite Solar Cells

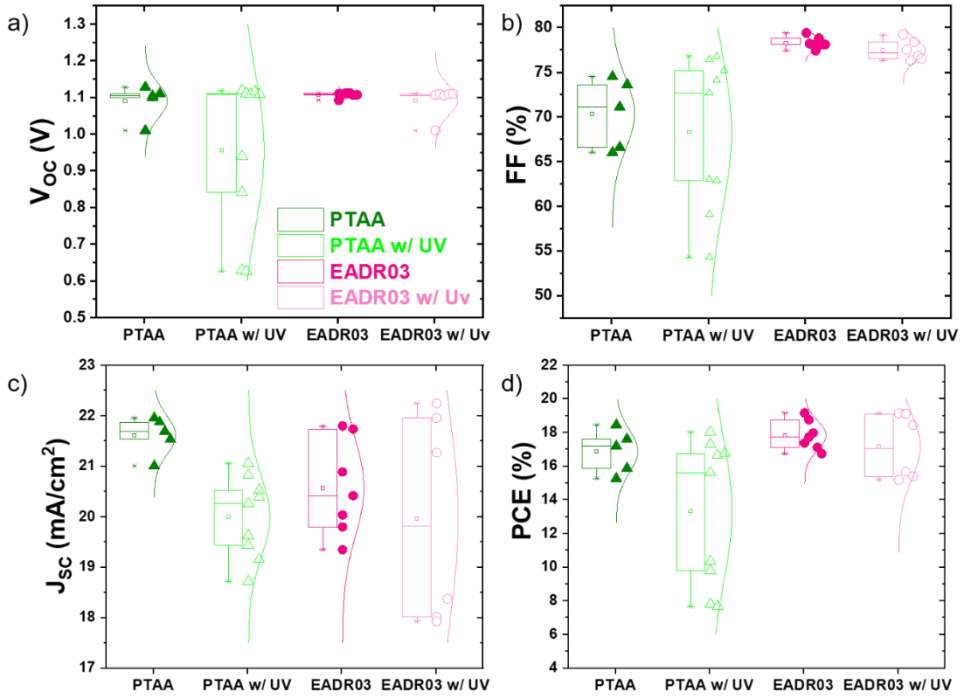

Figure 5.19. *Device performance statistic total of 25 devices from PTAA and EADR03 with and without UV light exposition.*

Therefore, the defects that the UV absorption may create are more likely to impact the PTAA layer than the SAM layer. However, the PTAA layer thickness directly affects the FF and V_{OC} parameters of PSCs which are discussed earlier by Stolterfoht and co-workers in 2017. They have demonstrated that diluted PTAA solution leads to having an incomplete coverage of ITO, decreasing the selectivity of the PTAA layer under the perovskite layer.[24] We note that high stability of PTAA in n-i-p cells has been reported,[263] nonetheless, in n-i-p structure, the UV photons are absorbed in the n-type and perovskite absorber layers before reaching PTAA.

In this work, we have significantly higher intensity in the range of 300-500 nm with the used lamp for ageing measurements compared to global AM 1.5 spectrum (**Figure 2.11a** in Chapter 2). Hence, the measurement condition accelerates the UV-induced PTAA degradation, which can be the reason behind the lower stability of our PTAA p-i-n cells compared to reported values in the literature (**Table 5.7**). Moreover, this is also an accelerating ageing measurement for perovskite. The instability of perovskite under UV light has been widely reported,[264,265] mostly because of the photochemical degradation of PbI_2 into metallic lead Pb^0 forming non-radiative recombination centers, reducing the cells' efficiency.[266] We used a UV filter (cut-off at 350 nm) to improve the lifetime of the devices (**Figure 5.18c**). Although we still have a significantly higher intensity of the simulated spectrum in 350-500 nm region compared to global AM 1.5 (**Figure 2.11b** in Chapter 2), we do see a considerable enhancement of the cells' lifetimes as can be seen in **Table 5.7** (we note that the light intensity is lower than one sun illumination). The EADR04 cells' T_{80} reaches more than 2000 h. Therefore, the reported values in **Table 5.7** are an underestimation of the cells' potential in this study.

Table 5.8. *Photovoltaic parameters of the best performing devices based on different HSLs with and without UV light exposition with a scan speed of 100 mV/s.*

HSLs	*UV light*	J_{SC} *(mA/cm²)*	V_{OC} *(mV)*	*FF (%)*	*PCE (%)*	*HI (%)*
PTAA	No	21.9	1128	74	18.3	0.02
PTAA	Yes	21.0	1119	76	17.8	0.03
EADR03	No	21.7	1110	79	19.0	0.05
EADR03	Yes	21.9	1100	79	19.0	0.04

We acknowledge that at elevated temperatures, the metal electrode such as gold can interact with perovskite causing degradation.[48] However, copper has been shown to be stable when used in combination with perovskite, and the degradation using copper is due to presence of moisture and oxygen and the potential oxidation products (*e.g.* $Cu(OH)_2$ or CuO_X).[152] Our study on device stability has been done on inert atmosphere to avoid this particular degradation pathway.

Carbazole Based Self-Assembled Hole-Selective Monolayer for Ultra-Stable and Highly Efficient Perovskite Solar Cells

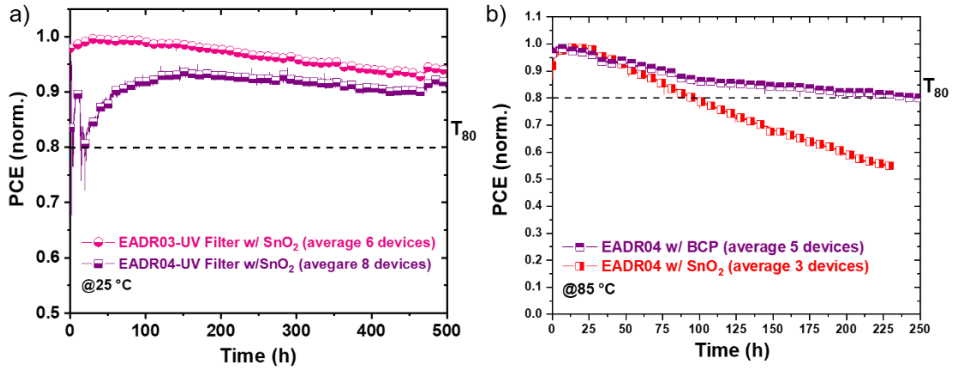

Figure 5.20. *Long-term continuous maximum power point tracking a) EADR03 and EADR04 based devices with UV Filter and SnO_2 at 25 °C. b) EADR04 based devices with BCP and SnO_2 at 85 °C. Note that the values are averaged from different devices from different batches. All the measurements are done in an N_2 atmosphere without encapsulation.*

Recent report by Zheng et al. showed that BCP can have low thermal stability due to its crystallisation at high temperature (>80 °C).[267] Here, to test whether changing buffer layer to an inorganic material can avoid the further degradation, we used SnO_2 instead of BCP. This enhanced the stability of the device at 25 °C, but not at higher temperature as can be seen in **Figure 5.20** and **Table 9**. This excludes the degradation pathway due to thermal instability of BCP.

Table 5.9. *Estimated T_{80} of the p-i-n perovskite solar cell with EADR03 and EADR04, BCP and SnO_2 from the MPP traces with and without UV filter at different temperatures.*

SAMs	*UV Filter*	*BCP*	*SnO_2*	*Initial PCE (%)*	*Ageing Temperature and Illumination*	*Tracking Time (h)*	*Estimated T_{80} (h)*
EADR03	Yes	No	Yes	18.9	25 °C, metal-halide lamp, 100 mW/cm²	500	1383
EADR04	Yes	No	Yes	19.4	25 °C, metal-halide lamp, 100 mW/cm²	500	3582
EADR04	No	Yes	No	20.1	85 °C, metal-halide lamp, 100 mW/cm²	250	242
EADR04	No	No	Yes	19.9	85 °C, metal-halide lamp, 100 mW/cm²	225	106

5.4. Conclusions

This study demonstrates the importance of the molecular design when using SAMs as selective contacts in perovskite solar cells. The SAMs have become the approach to achieve high solar-to-energy conversion efficiencies and, herein, we show that SAMs can lead to remarkable stable solar cells. In our study, we use both carbazole and methoxy moieties as electron donors for efficient charge selection, good electron blocking properties and surface passivation of the perovskite. Moreover, the 1,3-dimethoxybenzene terminal group of the molecule is compatible with perovskite formation resulting in a smooth and compact perovskite film. This design enables the perovskite cells reaching more than 21% stabilized efficiency and, most importantly, the monolayer-based devices exhibit superior stability compared to PTAA based cells, which are the current standard for perovskite solar cells approaching silicon PV values. We demonstrated that stabilizing the perovskite/SAMs interface is the way to commercialize perovskite solar cells.

5.5. Synthetic Methods and Procedures

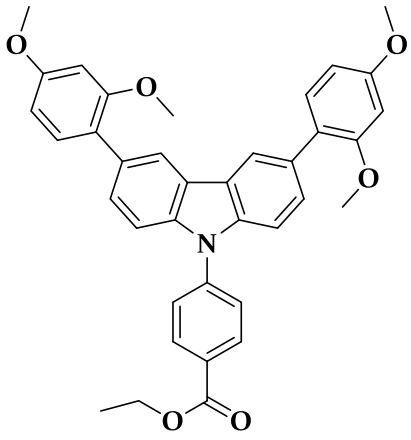

EADR03-COOEt

Ethyl 4-(3,6-bis(2,4-dimethoxyphenyl)-9H-carbazol-9-yl)benzoate (EADR03-COOEt)

A mixture of ethyl 4-bromobenzoate (0.25 mg, 1.09 mmol), 3,6-bis(2,4-dimethoxyphenyl)-9H-carbazole (0.53 mg, 1.20 mmol), $Pd_2(dba)_3$ (0.10 mg 0.11 mmol), tri-*tert*-butylphosphine tetrafluoroborate (0.063 mg, 0.22 mmol), sodium *tert*-butoxide (0.11 mg, 1.2 mmol) are dissolved in 10.0 mL freshly dried toluene in a 25.0 mL two-neck flask under argon atmosphere. The system is purged with argon for 30 minutes. Then, the mixture is refluxed at 115 °C overnight. The reaction is gradually cooled to room temperature and the solution is concentrated under vacuum. A brine solution (200.0 mL) is added and the solution is extracted with ethyl acetate (EtOAc) (2x100.0 mL). The combined extracts are dried over anhydrous magnesium sulphate, filtered and concentrated under vacuum. The compound is purified by column chromatography (Hexane:EtOAc, 5:1, v:v) and obtained yellow liquid (430 mg, 68% yield).

^{1}H NMR (400 MHz, $CDCl_3$) δ 8.30 (ppm) (d, J = 8.5 Hz, 2H), 8.23 (dd, J = 1.7, 0.7 Hz, 2H), 7.72 (d, J = 8.6 Hz, 2H), 7.57 (dd, J = 8.5, 1.7 Hz, 2H), 7.49 (dd, J = 8.5, 0.7 Hz, 2H), 7.36 (d, J = 8.9 Hz, 2H), 6.64 – 6.58 (m, 4H), 4.46 (q, J = 7.1 Hz, 2H), 3.88 (s, 6H), 3.82 (s, 6H), 1.45 (t, J = 7.1 Hz, 3H).

Carbazole Based Self-Assembled Hole-Selective Monolayer for Ultra-Stable and Highly Efficient Perovskite Solar Cells

^{13}C NMR (101 MHz, $CDCl_3$) δ (ppm) 166.00, 160.05, 157.54, 142.22, 139.44, 131.54, 131.32, 130.87, 128.78, 127.93, 126.15, 124.17, 124.02, 121.27, 109.22, 104.67, 99.11, 61.22, 55.67, 55.48, 14.21.

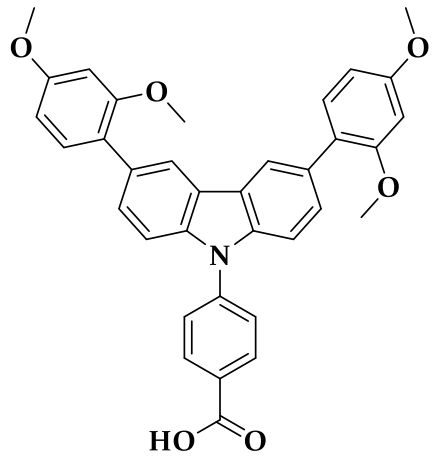

EADR03

4-(3,6-bis(2,4-dimethoxyphenyl)-9H-carbazol-9-yl)benzoic acid (EADR03)

An aqueous solution of KOH (382 mg, 6.80 mmol) is added to 4-(3,6-bis(2,4-dimethoxyphenyl)-9*H*-carbazol-9-yl)benzoate (400 mg, 0.68 mmol). Then, to this aqueous phase, a methanol and tetrahydrofuran (1:1) mixture is added to maintain complete dissolution at 85 °C. The mixture is refluxed at 85 °C overnight. The reaction is gradually cooled to room temperature and the solution is concentrated under vacuum. 200.0 mL of water is added, and the resulting aqua layer is treated with 2M HCl to obtain an off-white colour, which is filtered and dried under vacuum, to afford 4-(3,6-bis(2,4-dimethoxyphenyl)-9H-carbazol-9-yl)benzoic acid (340 mg, 89% yield).

^{1}H NMR (400 MHz, DMSO) δ (ppm) 8.28 (d, J = 1.7 Hz, 2H), 8.25 (d, J = 8.6 Hz, 2H), 7.84 (d, J = 8.5 Hz, 2H), 7.54 (dd, J = 8.6, 1.6 Hz, 2H), 7.50 (d, J = 8.5 Hz, 2H), 7.33 (d, J = 8.3 Hz, 2H), 6.70 (d, J = 2.4 Hz, 2H), 6.66 (dd, J = 8.4, 2.4 Hz, 2H), 3.83 (s, 6H), 3.79 (s, 6H).

^{13}C NMR (101 MHz, DMSO) δ (ppm) 167.24, 160.26, 157.64, 141.52, 139.08, 131.79, 131.69, 131.25, 129.70, 128.51, 126.55, 123.67, 123.49, 121.42, 109.70, 105.77, 99.43, 56.05, 55.75.

ESI-MS m/z calc. for $C_{35}H_{28}NO_6^-$ (M^-): 558.1922; found: 558.1912.

Elemental Anal. calcd. for $C_{35}H_{29}NO_6$: C, 75.12; H, 5.22; N, 2.50. Found: C, 70.21; H, 4.90; N, 2.2

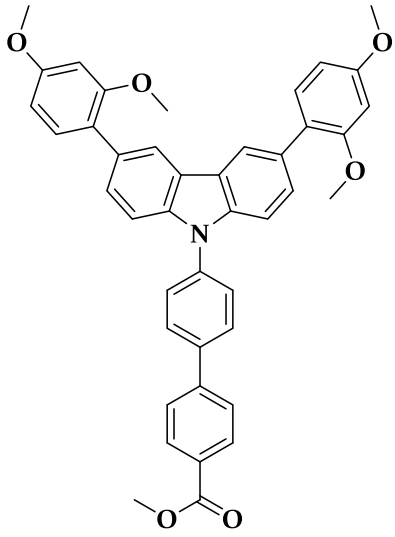

EADR04-COOMe

Methyl 4'-(3,6-bis(2,4-dimethoxyphenyl)-9H-carbazol-9-yl)-[1,1'-biphenyl]-4-carboxylate (EADR04-COOMe)

A mixture of methyl 4'-bromo-[1,1'-biphenyl]-4-carboxylate (0.25 mg, 0.85 mmol), 3,6-bis(2,4-dimethoxyphenyl)-9H-carbazole (0.45 mg, 1.03 mmol), $Pd_2(dba)_3$ (0.16 mg 0.17 mmol), tri-*tert*-butylphosphine tetrafluoroborate (0.10 mg, 0.34 mmol), sodium *tert*-butoxide (0.09 mg, 0.94 mmol) are dissolved in 15.0 mL freshly dried toluene in a 50.0 mL two-neck flask under argon atmosphere. The system is purged with argon for 30 minutes. Then, the mixture is refluxed at 115 °C overnight. The reaction is gradually cooled to room temperature and the solution is concentrated under vacuum. A brine solution (200.0 mL) is added, and the solution is extracted with ethyl acetate (EtOAc) (2x100.0 mL). The combined extracts are dried over anhydrous magnesium sulphate, filtered, and

concentrated under vacuum. The compound is purified by column chromatography (Hexane:EtOAc, 2:1, v:v) and recrystallised is performed in EtOH to give light yellow colour crystals (300 mg, 53%).

^{1}H NMR (400 MHz, $CDCl_3$) δ (ppm) 8.26 (dd, J = 1.7, 0.7 Hz, 2H), 8.20 – 8.17 (m, 2H), 7.87 (d, J = 8.5 Hz, 2H), 7.80 – 7.76 (m, 2H), 7.73 (d, J = 8.5 Hz, 2H), 7.58 (dd, J = 8.5, 1.7 Hz, 2H), 7.50 (dd, J = 8.5, 0.7 Hz, 2H), 7.38 (d, J = 9.0 Hz, 2H), 6.65 – 6.60 (m, 4H), 3.98 (s, 3H), 3.88 (s, 6H), 3.83 (s, 6H).

^{13}C NMR (101 MHz, $CDCl_3$) δ (ppm) 166.96, 160.01, 157.56, 144.71, 139.92, 138.74, 138.04, 131.57, 130.47, 130.30, 129.21, 128.69, 127.82, 127.24, 127.04, 124.35, 123.76, 121.24, 109.24, 104.69, 99.14, 55.68, 55.66, 55.48, 55.46, 52.20.

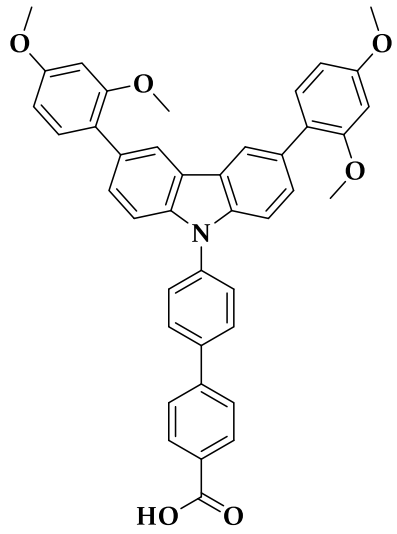

EADR04

4'-(3,6-bis(2,4-dimethoxyphenyl)-9H-carbazol-9-yl)-[1,1'-biphenyl]-4-carboxylic acid (EADR04)

An aqueous solution of KOH (0.30 mg, 4.60 mmol) is added to methyl 4'-(3,6-bis(2,4-dimethoxyphenyl)-9*H*-carbazol-9-yl)-[1,1'-biphenyl]-4-carboxylate (EADR04-COOMe) (0.30 mg, 0.46 mmol). Then, to this aqueous phase, a methanol and tetrahydrofuran (1:1) mixture is added to maintain complete dissolution at 85 °C. The mixture is refluxed at 85 °C overnight. The reaction is gradually cooled to room temperature and the solution is concentrated under vacuum. 200.0 mL of water is added,

and the resulting aqua layer is acidified with 2M HCl. Then, the crude product is purified with flash chromatography (140 mg, 48% yield).

^{1}H NMR (400 MHz, DMSO) δ (ppm) 13.04 (s, 1H), 8.29 (d, J = 1.7 Hz, 2H), 8.09 (dd, J = 10.8, 8.5 Hz, 4H), 7.96 (d, J = 8.4 Hz, 2H), 7.82 (d, J = 8.6 Hz, 2H), 7.54 (dd, J = 8.6, 1.7 Hz, 2H), 7.51 – 7.46 (m, 2H), 7.38 – 7.29 (m, 2H), 6.74 – 6.64 (m, 4H), 3.83 (s, 6H), 3.80 (s, 6H).

^{13}C NMR (101 MHz, DMSO) δ (ppm) 167.57, 160.23, 157.66, 143.86, 139.52, 138.36, 137.63, 137.61, 131.69, 130.91, 130.57, 129.17, 128.42, 127.45, 127.38, 123.64, 123.45, 121.43, 109.61, 105.76, 99.47, 56.07, 56.02, 55.76, 55.72, 40.64, 40.43, 40.22, 40.01, 39.80, 39.59, 39.38.

ESI-MS m/z calc. for $C_{41}H_{32}NO_6^-$ (M^-):634.2235; found: 634.2246.

Elemental Anal. calcd. for $C_{41}H_{33}NO_6$: C, 77.46; H, 5.23; N, 2.20. Found: C, 74.22; H, 5.38; N, 2.23.

Chapter 6

Triphenylamine Based Self-Assembled Hole Selective Monolayers with Different Positioned Terminal Group in Perovskite Solar Cells

Triphenylamine Based Self-Assembled Hole Selective Monolayers with Different Positioned Terminal Group in Perovskite Solar Cells

6.1. Abstract

Recent application of self-assembled monolayers as a charge selective layers in perovskite solar cells has gained tremendous attention. Highly efficient and stable devices have been released with stand-alone SAMs binding on ITO substrates, however, further understanding about the effect of the structure of SAM on PSCs is required. Herein, three triphenylamine-based self-assembled hole selective small molecules have been synthesized by placing different positioned dimethoxy phenyl substituents. They have been effectively employed in p-i-n configuration PSCs and the highest power conversion efficiency of 19.8% is comparable with commercially available materials due to their cost-effectiveness and reproducibility. This study gives an insight into the fundamental understanding of self-organisation, structure-property relationships, and interfacial phenomena. The *para-&ortho-* positioned substituents induce larger perovskite grain size that permit to obtain higher power conversion efficiency.

6.2. Introduction

SAMs are typically made of an anchoring group that connects the small molecules to the conductive oxide surface via chemical bonding, a spacer that controls the packing geometry, and a terminal group that adjusts the surface and interface properties.[113,268,269] The control of interface properties has drawn attention due to improving the charge extraction with better energy alignment and reduced trap density in recent

times.[112,270] Moreover, the terminal group determines the wettability of the SAMs which directly affects the grain size and grain boundaries of the perovskite layer. The most ordinarily used terminal groups are pyridines, thiols, or cyano groups for adjusting the work function and passivating the perovskite layer.[271,272] Furthermore, the presence of methoxy groups in SAMs makes wetting surfaces that ensure excellent covering and reproducibility of the perovskite layer, while PTAA is hydrophobic.

The main purpose of our previous study (Chapter 5) was to investigate the effect of the spacer moiety of SAMs on the thermal stability of the PSCs. We demonstrated that the PTAA layer-based devices exhibited inferior stability compared to SAMs.[227] In this study, triphenylamine (TPA) moiety is selected as a spacer, which are drawn attention due to their good thermal and morphological stabile properties in PSCs.[273] When the T_g of HSLs are higher than the operating temperature, higher molecular motion and transition to the crystalline state are minimized. In the opposite case, this leads to the formation of grain boundaries between the crystal, which might trap charge carriers and eventually result in degradation of device performance.[274,275] Besides, TPA exhibits a good electron donor unit property with two key properties: easy oxidizability of the amine nitrogen atom and the ability to carry positive charge efficiently.[276] Having high T_g and low ionization potentials are important for HSL-based extremely stable and efficient PSCs.[277]

Herein, we investigate how the methoxy (-OMe) group positions in TPA-based SAMs affect the electronic properties, the perovskite solar cell

performance, and stability. According to the literature, the methoxy group presents electron-withdrawing properties due to its inductive effect. Hammett demonstrated that the substitution position can introduce electron-donating or electron-withdrawing properties in the *para-&meta*-positions, respectively, while the ortho-position causes a more steric hindrance.[278] Also, Seok and co-workers revealed that the different arrangement of the methoxy groups affects the energy of the highest occupied molecular orbital (HOMO) and the lowest unoccupied molecular orbital (LUMO). The lower LUMO energy behaviours as an electron blocking layer increases fill factor (FF) while causing high shunt resistance and low series resistance.[234]

In this work, the -OMe substituents are positioned in TPA-based small molecule structure on *para-&ortho*- (RC24), *ortho-&meta*- (RC25), and *para-&meta*- (RC34) and their structure-activity relationships as the HSL are explored in PSCs. We aim to prove which substitution positions could give a suitable energy level to ensure high PSCs performance, likewise, changing the wettability of the HSLs and increasing the grain size of perovskite. The three SAMs have provided highly reproducible PCE above 19.5% at one sun AM 1.5 G illumination. This study demonstrates that the -OMe groups' position affects the PSCs performance and quasi-steady-state efficiency, and the *para-&ortho*- positions ensure the best performance within the other positions.

6.3. Results and Discussion

6.3.1. Synthesise of Self-Assembled Monolayers

Scheme 6.1 shows the syntheses pathway of the new TPA-based SAMs, where *4-(bis(2',4'-dimethoxy-[1,1'-biphenyl]-4-yl)amino)benzoic acid* (**RC24**), *4-(bis(2',5'-dimethoxy-[1,1'-biphenyl]-4-yl)amino)benzoic acid* (**RC25**) and *4-(bis(3',4'-dimethoxy-[1,1'-biphenyl]-4-yl)amino)benzoic acid* (**RC34**) have a TPA moiety as an electron donor unit. TPA based self-assembled moieties are modified with dimethoxyphenyl substituents due to assisting in lowering the oxidation potential and increasing the solubility of the molecules.[273] The dimethoxyphenyl substituents are placed in *para-&ortho-*, *ortho-&meta-*, and *para-&meta-* positions as a terminal group. The methoxy substituent position's alignment mainly affects the work function, photophysical and surface properties of the molecule, which are crucially important for the perovskite device performance. The carboxylic acid is preferred as anchoring to increase the coverage ratio of SAMs along the ITO surface and stabilise this surface by chemically attaching to the -OH group.[61] The synthetic details of the TPA-based SAMs are presented in the section 6.5.

Triphenylamine Based Self-Assembled Hole Selective Monolayers with Different Positioned Terminal Group in Perovskite Solar Cells

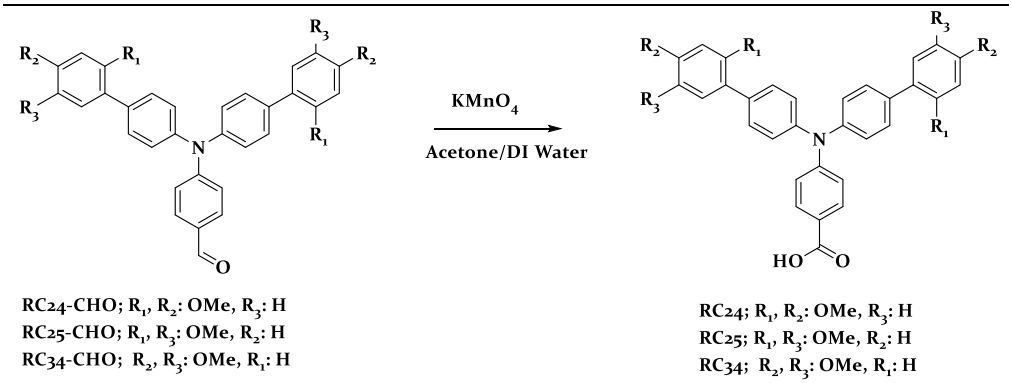

RC24-CHO; R_1, R_2: OMe, R_3: H
RC25-CHO; R_1, R_3: OMe, R_2: H
RC34-CHO; R_2, R_3: OMe, R_1: H

RC24; R_1, R_2: OMe, R_3: H
RC25; R_1, R_3: OMe, R_2: H
RC34; R_2, R_3: OMe, R_1: H

Scheme 6.1. *Synthetic pathway of RC24, RC25, and RC34*

6.3.2. Thermal, Optical, Electrochemical, And Photophysical Properties of SAMs and Perovskite layers

TPA-based SAMs exhibit good thermal and morphological stability under device fabricating and operating conditions. The thermal behaviour of RC24, RC25 and RC34 is analysed by DSC and TGA (see **Table 6.1**, **Figure 6.1**). TGA showed remarkably high thermal stability with decomposition temperatures (5% weight loss) at 347 °C, 383 °C, and 386 °C for RC24, RC25 and RC34, respectively. Likewise, DSC confirmed elevated T_g during the third heating cycle for RC24, RC25 and RC34 at 115 °C, 224°C, 193 °C, respectively. The fact that TPA-based SAMs exist in both amorphous and semi-crystalline state may explain their uniform coating when annealing the perovskite films at 100 °C.[233]

Triphenylamine Based Self-Assembled Hole Selective Monolayers with Different Positioned Terminal Group in Perovskite Solar Cells

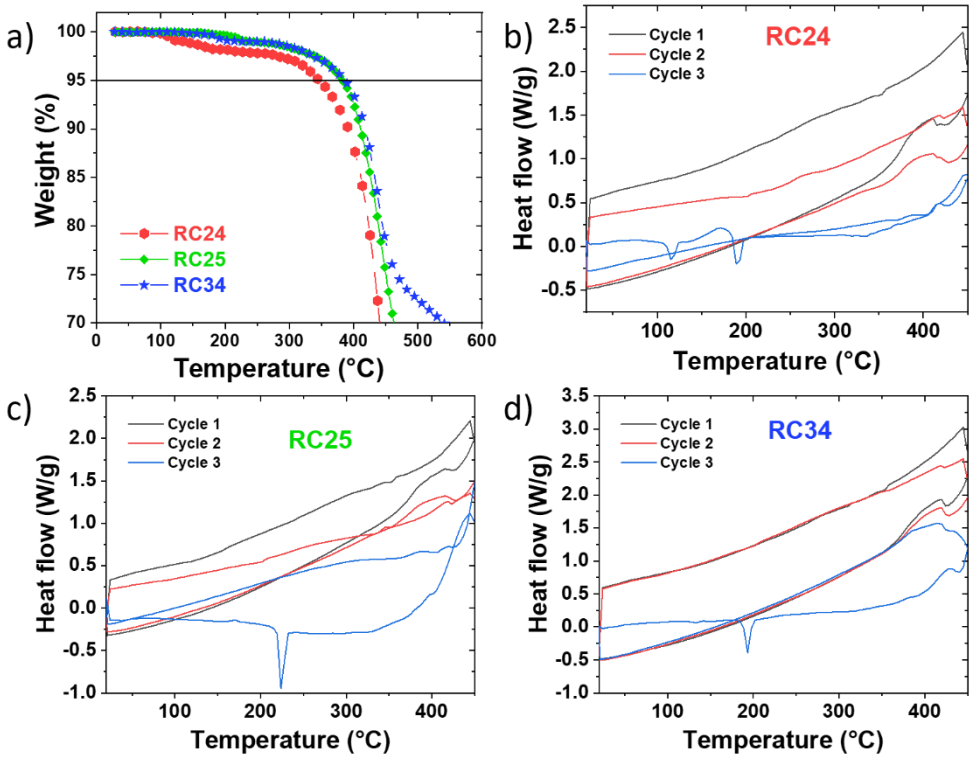

Figure 6.1. *a) TGA analysis of RC24, RC25, and RC34. DSC analysis of b) RC24, c) RC25, and d) RC34.*

Table 6.1. *Thermal properties of RC24, RC25, and RC34.*

HTMs	T_{des} (°C) [a]	T_g (°C) [b]
RC24	115	347
RC25	224	383
RC34	193	386

[a] Decomposition temperature determined from TGA (5 % weight loss). [b] Glass transition temperature determined from the third cycle of DSC. All experiments are carried out under N_2 atmosphere, scan rate of 10 °C/min.

Triphenylamine Based Self-Assembled Hole Selective Monolayers with Different Positioned Terminal Group in Perovskite Solar Cells

Initially, we have demonstrated that the TPA-based SAMs are well attached to the -OH group of the ITO by chemically attaching to the surface atom using XPS (see for details section 2.3.6). The chemical reaction between the anchor group (carboxylic acid, phosphoric acid, etc.) and the surface group (-OH) of the metal oxide can be defined as a condensation reaction that produces ester-type linkages (O-C=O).[89,91,222] In the case of the TPA derivatives, the C1s spectra of the surface are decomposed into four peaks assigned to C-H and C-C bonds at 284.7 eV, 284.8 eV and 284.5 eV, to C-O bonds at 285.7 eV, 285.8 eV and 285.6 eV, to O-C=O att. bonds at 286.7 eV, 286.8 eV and 286.6 eV, and to O-C=O bonds at 288.9 eV, 289.1 eV and 289.0 eV for RC24, RC25 and RC34, respectively (**Figure 6.2**).[171,236] The O1s spectra decomposed into four peaks are assigned to In-O bond at 530.0 eV, to surface hydroxides at 530.9 eV, to the C=O bond at 531.8 eV for all SAMs and to the C-O bond at 533.1 eV for RC24 and 533.0 eV for RC25 and RC34.[239] The bare ITO surface exhibits common C1s and O1s peaks while comparing with SAM deposited ITO surface, which is shown in **Figure A63** and **Figure A64** that can be caused by solvent residues from the cleaning procedure as observed in the previous study. The summarised fitting data of the C1s and O1s spectrum are given in **Table A.2**.

Triphenylamine Based Self-Assembled Hole Selective Monolayers with Different Positioned Terminal Group in Perovskite Solar Cells

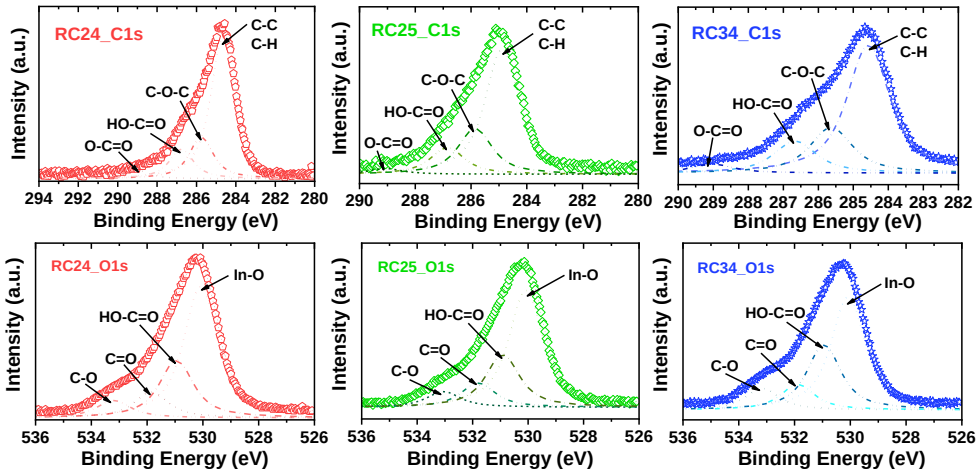

Figure 6.2. *The XPS high-resolution survey spectra of C1s and O1s for RC24, RC25 and RC34.*

After assigning the chemical bonds of the SAMs on the ITO surface, we have investigated the energetic properties of them to demonstrate their hole selective properties for PSCs. Herein, we have chosen the $Cs_{0.05}FA_{0.79}MA_{0.16}Pb(I_{0.84}Br_{0.16})_3$ (onwards labelled as CsFAMA) perovskite as an absorber layer, owing to having higher device performance and stability, inducing highly uniform perovskite grains and increasing device reproducibility.[15] TPA-based SAM's LUMO energy levels are calculated by utilising the optical bandgap which is estimated from the $\lambda_{a.e.}$ using UV-vis measurement (**Figure 6.3** and **Table 6.2**).[242] The VBM and the E_F values of RC24, RC25, RC34, and CsFAMA perovskite are determined by UPS (Figure A65) and schematically displayed in **Figure 6.8** and all values refer to the vacuum level.[279] The RC34 with *para-&meta-* positioned -OMe substituents exhibits slightly lower oxidation potential as a result of inductive effect of substituent

position and it has better electron blocking character than RC24 and RC25, owing to higher LUMO energy level (**Figure 6.8**).

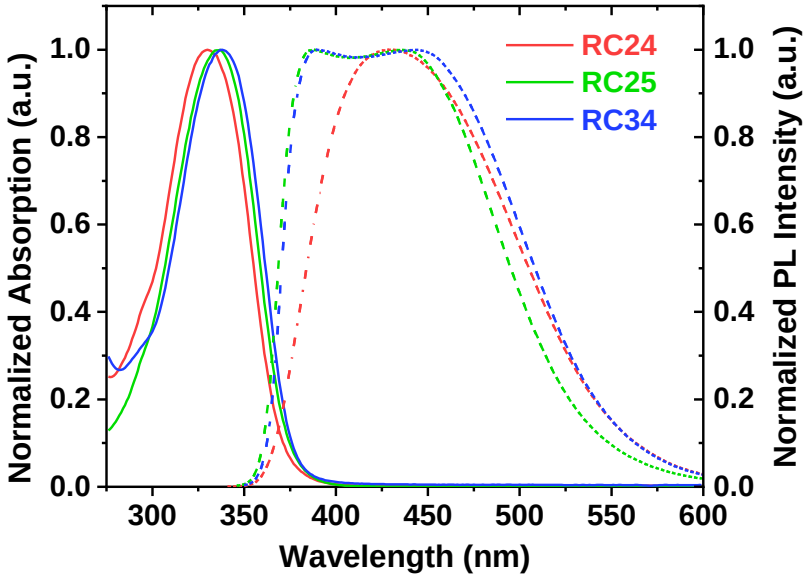

Figure 6.3. *Absorption (solid lines) and emission (dashed lines) spectra of RC24,RC25 and RC34.*

Table 6.2. *Optical and energetic properties of RC24, RC25 and RC34.*

SAMs	$\lambda_{abs.}$ *(nm)*	$\lambda_{em.}$ *(nm)*	$\lambda_{a.e.}$ *(nm)*	$E_g^{opt.}$ *(eV)*	*LUMO (eV)*
RC24	330	430	377	3.29	1.84
RC25	335	390/345	370	3.35	1.88
RC34	338	385/335	372	3.34	1.74

Triphenylamine Based Self-Assembled Hole Selective Monolayers with Different Positioned Terminal Group in Perovskite Solar Cells

To understand the role of different positioned terminal groups on top of the ITO surface, we focused on surface's wettability after the deposition SAMs. We used contact angle measurement for determining the SAMs-covered ITO surface wettability, performed with water (see for details section 2.3.4). The -OMe group's position influence the hydrophobicity of SAMs being as follows: RC34 < RC25 < RC24. The *para-&ortho-* positions gives a contact angle of 42.0°, the *ortho-&meta-* positions of 38.3° and the *para-&meta-* positions of 32.3° (**Figure 6.4**). In this work, the terminal group of the SAMs 1,3-dimethoxybenzene ensures a miscible interface for the CsFAMA perovskite one-step solution process. A miscible interface provides a compact and homogenous film and reproducibility of devices. On the other hand, the differently positioned dimethoxyphenyl substituents in TPA-based SAMs strongly affect the morphology of the obtained perovskite films.

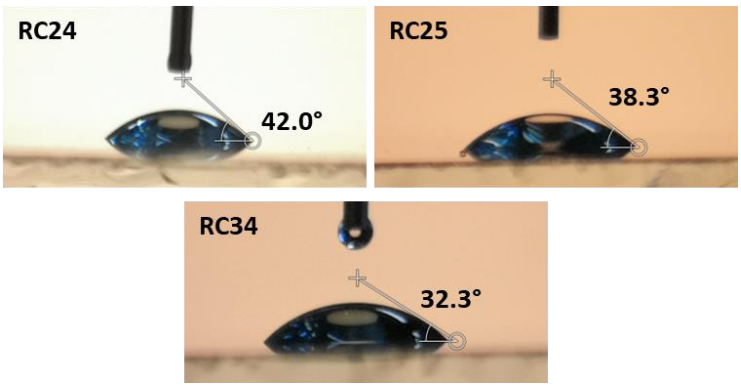

Figure 6.4. *Contact angle measurements on the RC24, RC25, and RC34 surfaces.*

Triphenylamine Based Self-Assembled Hole Selective Monolayers with Different Positioned Terminal Group in Perovskite Solar Cells

To examine the effect of the substitution position on perovskite films, perovskite layers grown on SAMs are characterised by SEM, and the related grain size distributions are estimated as listed in **Table 6.5**. **Figure 6.5** shows the full cross-sectional device, the surface morphology, and grain size distribution of the perovskite thin film grown on SAMs. Initially, the perovskite thin films are uniform, covering the entire substrates, and pinhole-free. Therefore, the bright small grains can be assigned as PbI_2 due to excess content in the perovskite thin film that can improve the device performance as reported in previous studies.[247,280] The perovskite thin layer grown on RC24, with the *para-&ortho-* positioned dimethoxyphenyl substituents, produced larger crystal grains and fewer grain boundaries, while the average grain size was estimated to be around 385±106 nm for RC24, 357±185 nm for RC25, and 301±85 nm for RC34.

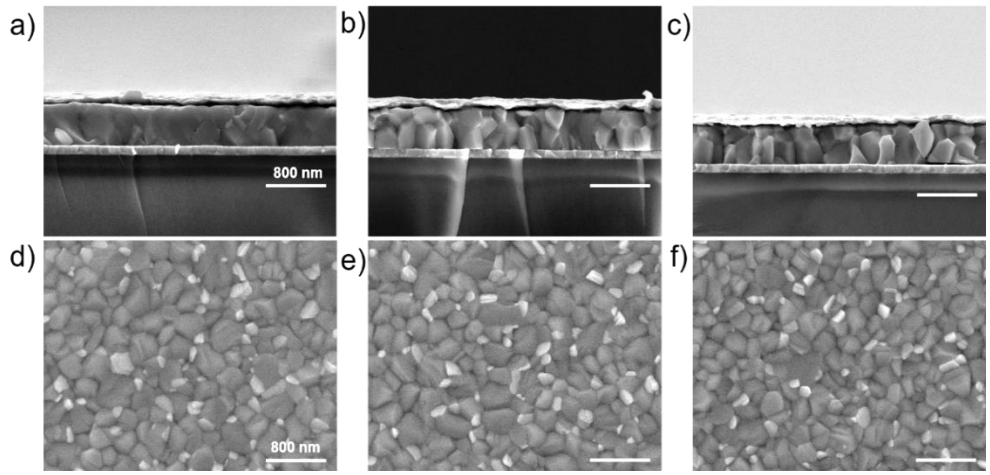

Figure 6.5. *Scanning electron microscopic images of cross-sectional full device of a)RC24, b)RC25 and c) RC34 employed planar PiN perovskite solar cells; and top view of perovskite layers grown on d)ITO/RC24, e)ITO/RC25 and f) ITO/RC34. All scale bars are 800 nm.*

However, we acknowledge that SEM images are inadequate to identify the perovskite grain,[281] thus, to further confirm the crystal size of the perovskite layers on different SAMs, we performed Le Bail analysis on the XRD patterns of perovskite layers (fitted patterns can be found in **Figure A67**).[282] The domain size of the perovskite can be quantified by the Lorentzian contribution to the peak broadening of the perovskite diffracted peaks in the XRD patterns (**Figure 6.7**). Le Bail analysis demonstrates that RC24-based perovskite exhibits the largest domain size (approximately 100 nm), whereas RC35 domain size is 70 nm in agreement with SEM images. We note that the domain is the largest unit of the same orientation of perovskite unit cells and grain can consist of multiple domains of perovskite. More importantly, the SEM cross-sectional images of RC25 and RC34 in **Figure 6.5** indicate small grains at the interface of SAM/perovskite and grain boundaries in the vertical direction whereas the perovskite layer grown on RC24 has monolithic grain. This can affect the charge transport and device's performance in a quasi-steady-state condition, as discussed in the later section.

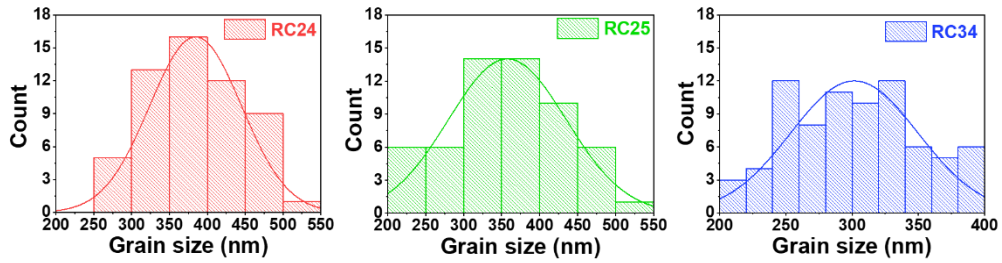

Figure 6.6. *The grain size distribution of the perovskite thin films based on RC24, RC25, and RC34.*

Triphenylamine Based Self-Assembled Hole Selective Monolayers with Different Positioned Terminal Group in Perovskite Solar Cells

By combining the average grain size with the hydrophobicity discussed previously (RC34 < RC25 < RC24), it is becoming evident that these two parameters correlate. Concisely, the position of a suitable substituent is critical to the formation of uniform perovskite films with large grain sizes, what do directly affect the perovskite device performance. Additionally, the large grain size is vital for perovskite solar cells due to transporting/collecting charge carriers efficiently and reducing charge recombination.[60]

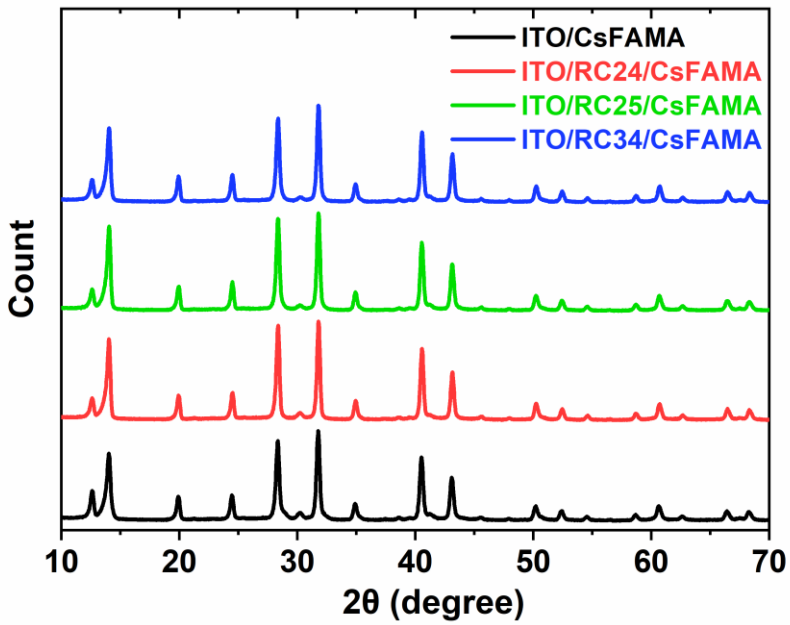

Figure 6.7. *X-ray diffraction patterns of perovskite layers grown on bare ITO, ITO/RC24, ITO/RC25, and ITO/RC34. The patterns are well in agreement with literature containing similar perovskite compounds.*

Triphenylamine Based Self-Assembled Hole Selective Monolayers with Different Positioned Terminal Group in Perovskite Solar Cells

6.3.3. Spectroscopy, Photovoltaic Properties and Device Stability Investigation of Perovskite-Based Devices

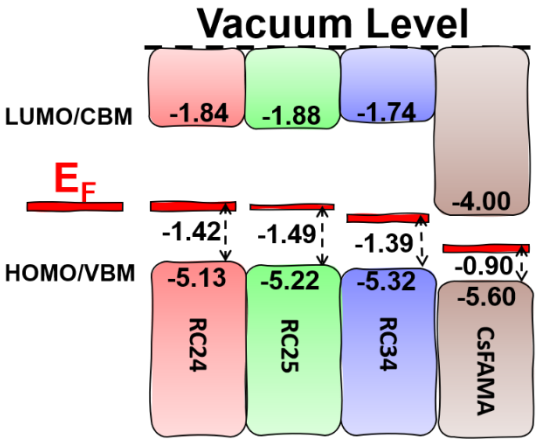

Figure 6.8. *Energy alignment of different layers. The band edge positions of SAMs, PTAA and CsFAMA layers are estimated from UPS measurements in the schematic representation. Note that the SAM layers' values (RC24, RC25 and RC34) are measured with UPS (**Figure A.65** shows UPS spectra). Before UPS measurement, the ITO substrate is treated with UV-Ozone to ensure similarity with used substrates in devices.*

Figure 6.9a shows the photoluminescence spectrum of the CsFAMA film in a variety of bilayer configurations, including ITO/CsFAMA, ITO/RC24/CsFAMA, ITO/RC25/CsFAMA, and ITO/RC34/CsFAMA. The photoluminescence peak at 750 nm is entirely reliable with previous reports of emission from CsFAMA,[283] and the spectral position of the emission is stable among all the samples. Moreover, there is a substantial quenching effect when the CsFAMA perovskite is placed in contact with SAMs. The different positions methoxy-substituted SAMs have similar

efficient quenching showing their efficient hole transporting character. Additionally, we used TRPL to investigate the radiative recombination dynamics using λ_{ex}= 470 nm as excitation wavelength as shown in **Figure 6.9b**, which is acquired with TCSPC technique. Here, two different decay profiles for RC24 and one decay profile for RC25 and RC34 which are fitted to a bi-exponential function (see for details section 2.3.10) as earlier studies. The slower decay can be corresponded to the bimolecular recombination, while the fast decay likely corresponds to trap filling for SAM-based perovskite films. The lifetimes τ_1 obtained are 21 ns, 20 ns, 17 ns, and 19 ns for the CsFAMA perovskite, RC24, RC25, and RC34, respectively, while the lifetimes τ_2 of the CsFAMA perovskite, RC24, RC25, and RC34 are 122 ns, 130 ns, 115 ns, and 107 ns, respectively (**Table 6.3**). The lifetime τ_1 is assigned to trap filling that shows us the passivating trap role of SAMs in contact with the perovskite surface to take shorter times to be filled. Excitingly, RC24 possessed an interfacial passivation effect[250] due to the increased PL yield related to the Lewis base molecule TPA[284], while RC25 and RC34 do not. The presence of the Lewis acid-base interactions between amino groups in TPA and the positively charged defects, as under-coordinated Pb^{2+} in the perovskite, passivate surface defects and significantly decrease the nonradiative recombination in perovskite films.[213,285,286] We fabricated perovskite solar cells to move one step further and to investigate the influence of differently positioned dimethoxy substituents in SAMs on the power conversion efficiency and stability.

Triphenylamine Based Self-Assembled Hole Selective Monolayers with Different Positioned Terminal Group in Perovskite Solar Cells

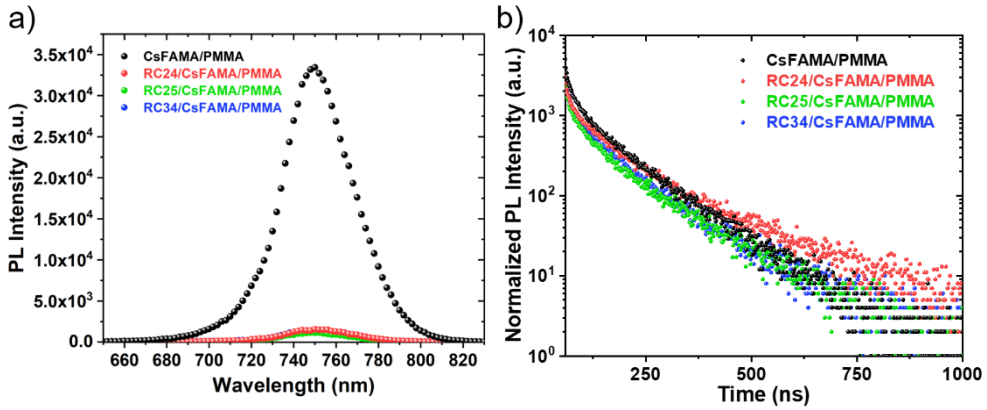

Figure 6.9. *a) Luminescence emission band upon excitation at λ_{ex}=470 nm for the CsFAMA/PMMA, RC24/CsFAMA/PMMA, RC25/CsFAMA/PMMA and RC34/CsFAMA/PMMA (total thickness of 550-600 nm) at room temperature. b) Luminescence emission decays (λ_{ex}=470 nm) measured for 1000 ns for CsFAMA/PMMA, RC24/CsFAMA/PMMA, RC25/CsFAMA/PMMA and RC34/CsFAMA/PMMA on ITO coated glass substrate at room temperature.*

Table 6.3. *Fitting values are obtained from the de-convolution of the luminescence decays in* ***Figure 6.9b****.*

Films	τ_1 (ns)	τ_2 (ns)
CsFAMA/PMMA	21	112
RC24/CsFAMA/PMMA	20	130
RC25/CsFAMA/PMMA	17	115
RC34/CsFAMA/PMMA	19	107

The state-of-the-art device structure with ITO/SAM/CsFAMA/C60/BCP/Cu sandwich architecture is used in this study, shown in **Figure 2.18**.[15] TPA-based SAMs are deposited on top of

the UV-O_3 treated ITO substrates using the dip-coating deposition process. Then, the perovskite (CsFAMA) layer is placed on top of the SAMs using the one-step method. By following perovskite layer deposition, C_{60} is thermally evaporated as an electron selective layer to passivate the grain boundaries and surfaces of perovskite films.[56,287] Afterwards, a thin layer of BCP is evaporated on top of the electron selective layer as a buffer layer for eliminating charge accumulation at the C_{60}/BCP/Cu interfaces.[288] A 100 nm Cu electrode is evaporated to complete the device. The section 2.5 gives all the fabrication processes of the perovskite solar cells.

All SAMs are deposited on top of the ITO substrates using a dip-coating method which is the most applied method for having a well-organised interface under the perovskite absorber. The non-attached molecules could be eliminated with the used solvent by rinsing or an ultrasonic cleaning bath. A dip-coating method could be optimised by using non-halogenated solvents thanks to the anchor group of SAMs. In this study, the most commonly non-halogenated solvents are used for optimising the effect of SAM layers on the performance of the perovskite solar cells. The statically better performance of the perovskite devices with higher FF and J_{SC} are showed with EtOH (**Figure 6.10**). The best photovoltaic parameters of the solvent optimisation for each SAMs are summed up in **Table 6.4**, where the FF values of the RC24 have a significantly narrower distribution comparing to RC25 and RC34.

Triphenylamine Based Self-Assembled Hole Selective Monolayers with Different Positioned Terminal Group in Perovskite Solar Cells

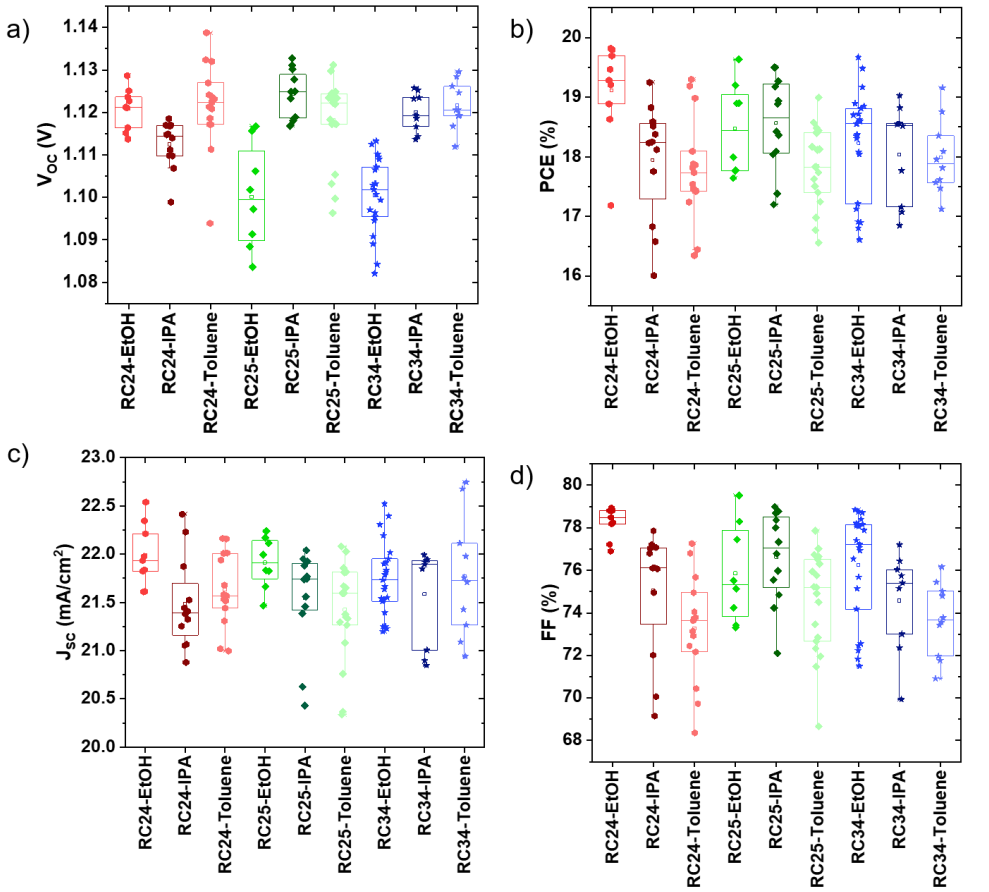

Figure 6.10. *Device performance statistic total 50 devices from RC24, RC25 and RC34 in different solvents in the devices a) V_{OC}, b) PCE, c) J_{SC}, d) FF.*

Triphenylamine Based Self-Assembled Hole Selective Monolayers with Different Positioned Terminal Group in Perovskite Solar Cells

Table 6.4. *Photovoltaic parameters of the best performing devices based on different hole selective layers in different solvents and with a scan speed of 100 mV/s.*

SAMs	*Solvents*	*Scan Direction*	*J_{SC} (mA/cm^2)*	*V_{OC} (mV)*	*FF (%)*	*PCE (%)*
RC-24	EtOH	forward	-22.3	1118	79	19.7
		reverse	-22.3	1123	79	19.8
RC-24	IPA	forward	-22.4	1108	77	19.1
		reverse	-22.4	1115	77	19.2
RC-24	Toluene	forward	22.2	1102	76	18.6
		reverse	-22.2	1127	77	19.3
RC-25	EtOH	forward	-22.1	1101	79	19.2
		reverse	-22.1	1116	79	19.6
RC-25	IPA	forward	-21.9	1127	79	19.4
		reverse	-21.9	1132	79	19.5
RC-25	Toluene	forward	-22.0	1102	75	18.3
		reverse	-22.0	1125	77	18.9
RC-34	EtOH	forward	-22.5	1101	79	19.6
		reverse	-22.5	1109	79	19.7
RC-34	IPA	forward	-21.9	1124	77	19.1
		reverse	-21.9	1123	76	18.8
RC-34	Toluene	forward	-22.7	1121	73	18.7
		reverse	-22.7	1126	75	19.1

Triphenylamine Based Self-Assembled Hole Selective Monolayers with Different Positioned Terminal Group in Perovskite Solar Cells

The best device's J-V with RC24, RC25, and RC34 measured at a scan rate of 100 mV/s are shown in **Figure 6.11a**. Specifically, the V_{OC} of the RC24 SAM-based device is approximately 17 mV larger than RC25 and RC34 SAM-based devices while the scan direction is from V_{OC} to J_{SC}. An and co-workers demonstrated that with increasing average grain size, the V_{OC} could be significantly enhanced by over 200 mV with a slight increase in FF.[289] The best PCE of RC24, RC25 and RC34 is 19.8%, 19.6%, and 19.7%, surpassing the commercially available HSLs from literature.

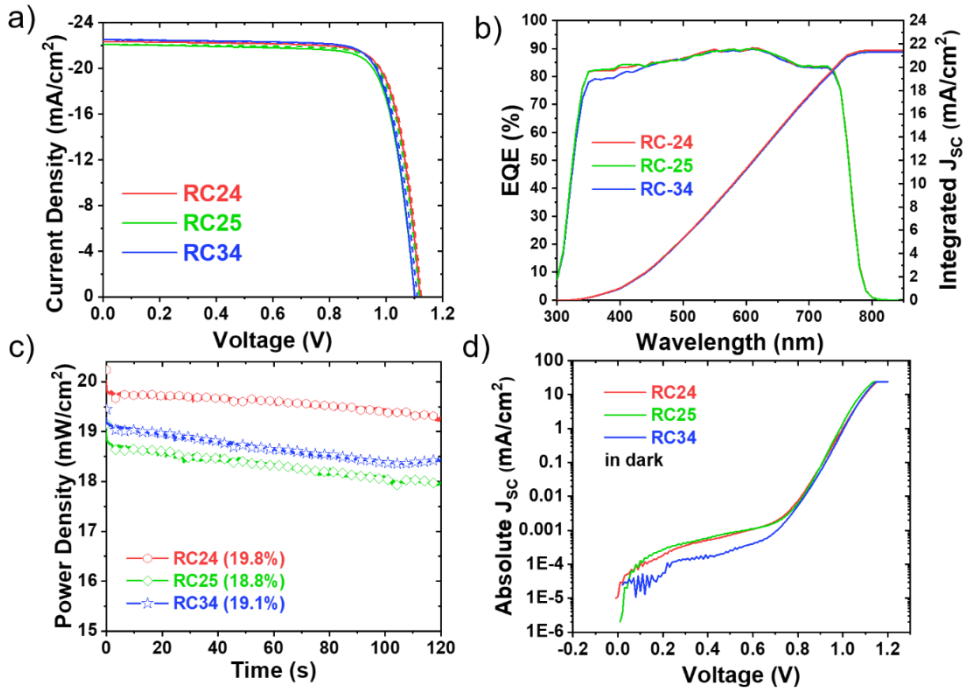

Figure 6.11. *a) Best J-V curves from RC24, RC25, and RC34 in EtOH. b) Corresponding external quantum efficiency curves which shows integrated current density in agreement with values from J-V measurement. c) Quasi-steady state efficiency of best RC24, RC25, and RC34. d) Dark J-V curves of the hole selective contact.*

In **Figure 6.11d**, the J-V scan of SAMs-HSL based full device indicated a similar lower leakage current under dark conditions. A low dark current is one of the proofs to show a high density of SAMs on ITO surfaces. EQE is done to understand how efficiently a perovskite layer transforms light into the current.[290] The integrated $J_{SC,EQE}$ of the best devices is close to the $J_{SC,J-V}$, as shown in in **Figure 6.11b**, and the devices show insignificant HI between reverse and forward J-V scans. The best devices photovoltaic parameters are listed in **Table 6.5**.

To understand the effect of a differently positioned methoxy substituent in SAMs with short-term perovskite device stability, maximum power point (MPP) tracks of the best devices are performed. After the first J-V scan, MPP tracks are made where RC25 and RC34 display a significantly lower performance than RC24. Expectedly, RC24, RC25, and RC34 based perovskite cells lost around 3%, 4%, and 5% of their initial PCE after 120 seconds of MPP tracking, respectively as can be seen in **Figure 6.11c**. In addition, RC25 and RC34 devices exhibit a significant burn-in loss in the first few seconds in MPP and continue to decrease afterwards. On the contrary, the *ortho-&para*-position substituted RC24 devices show a more stable MPP output. This can be attributed to its higher hydrophobicity (water contact angle 42.0°).[291] Moreover, previous report shows that mobile ions in the perovskite layers can be trapped at the grain boundaries, resulting in a longer transient in device response.[292,293] Thus, lower grain boundary densities in perovskite grown on RC24 could contribute as well to a slower decay slope seen in MPP tracking (**Figure 6.11c**).

Triphenylamine Based Self-Assembled Hole Selective Monolayers with Different Positioned Terminal Group in Perovskite Solar Cells

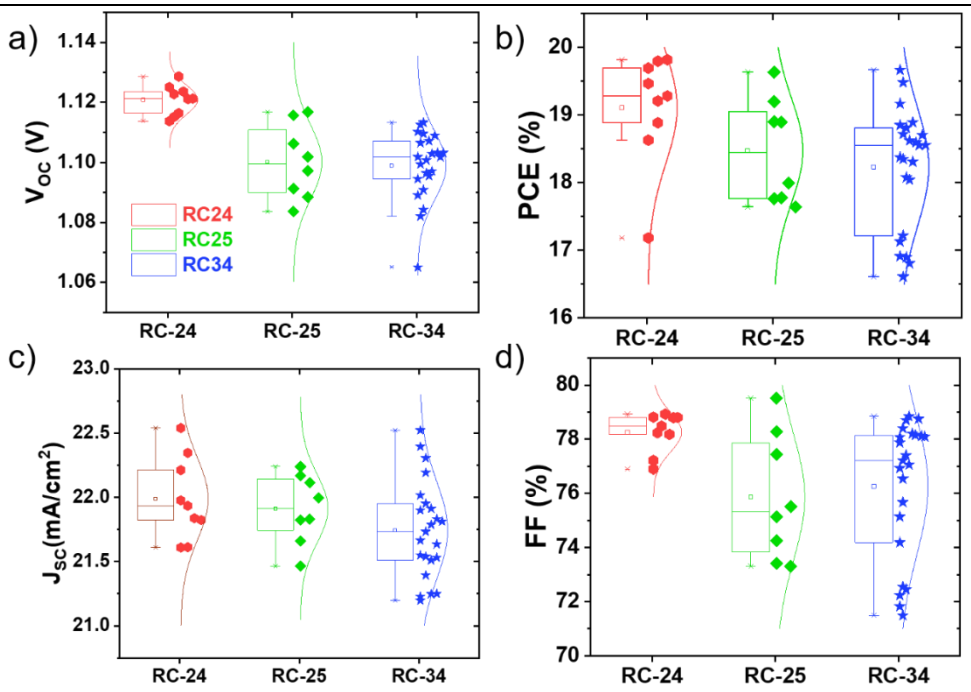

Figure 6.12. *Device performance statistic total 40 devices from in EtOH in the devices a) PCE, b) V_{OC}, c) J_{SC}, d) FF.*

Table 6.5. *Photovoltaic parameters of the best performing devices based on TPA-base self-assembled hole selective monolayers with a scan speed of 100 mV/s.*

SAMs	*Average Grain Size (nm)*	*$J_{SC,EQE}$ (mA/cm²)*	*$J_{SC,J-V}$ (mA/cm^2)*	*V_{OC} (mV)*	*FF (%)*	*PC (%)*	*HI (%)*
RC-24	385±106	21.5	-22.3	1123	79	19.8	0.00
RC-25	357±185	21.4	-22.1	1116	79	19.6	0.02
RC-34	301±85	21.3	-22.5	1109	79	19.7	0.00

6.4. Conclusions

In conclusion, we synthesised and characterised three new self-assembled hole selective monolayers for application in p-i-n perovskite devices. TPA based SAMs are demonstrated to be effective in enhancing the efficiency of perovskite devices to 19.8%. Our results provide a simple molecule design strategy for achieving the reduced hysteresis and the highly efficient perovskite devices. As we mentioned earlier, the -OMe group's existence increases the wettability of the metal oxide substrates, although their position as a terminal group directly might affect the device performance by increasing grain size and decreasing the grain boundary density in the perovskite layer. The reduced grain boundaries improve the crystal quality of the perovskite, furthermore, it decreases the hysteresis and increases the PCE of the perovskite device. This study provides new guidelines to understand the importance of the molecule design of the charge selective contact and their role in the efficiency and stability of the PSCs.

6.5. Synthetic Methods and Procedures

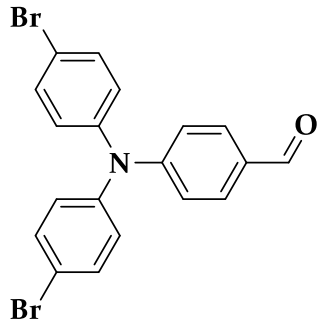

2

4-[Bis(4-bromophenyl)amino]benzaldehyde (2)

4,4′-Dibromotri-phenylamine (3 g, 7.44 mmol) is dissolved in anhydrous DMF (15 mL) at 0 °C. To this mixture, $POCl_3$ (17.39 mL, 186 mmol) was slowly added. The mixture is heated to 90 °C for 1 h under argon atmosphere. After cooling to room temperature, the mixture was poured into ice water and aqueous NaOH is then added to the mixture. The mixture is stirred for 1 h and then filtered. The yellow precipitate is washed with excess cold water and dried under vacuum. The crude product is purified by column chromatography on SiO_2 with dichloromethane (DCM) as the eluent to give 2 (3.05 g, 7.07 mmol, 95 %) as a yellow solid.

^{1}H NMR (500 MHz, CD_2Cl_2, 25°C) δ (ppm) 9.82 (s, 1 H), 7.71 (d, J = 8.56 Hz, 2 H), 7.46 (d, J = 8.64 Hz, 4 H), 7.04 (m, 6 H).

^{13}C NMR (126 MHz, $CDCl_3$,25 °C) δ (ppm) 190.17, 152.30, 145.14, 132.82, 131.12, 130.25, 127.49,120.41, 117.82.

Triphenylamine Based Self-Assembled Hole Selective Monolayers with Different Positioned Terminal Group in Perovskite Solar Cells

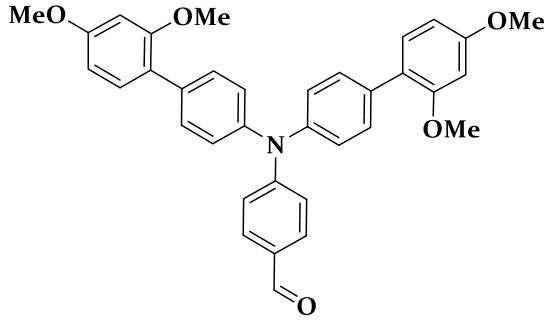

RC24-CHO

4-[Bis(2',4'-dimethoxy-[1,1'-biphenyl]-4-yl)amino]benzaldehyde (RC24-CHO)

In a Schlenk flask charged with Ar atmosphere, compound 2(3 g, 6.96 mmol), 2-(2,4- dimethoxyphenyl)-4,4,5,5-tetramethyl-1,3,2-dioxaborolane (5.50 g, 20.84 mmol) and $Pd(PPh_3)_4$ (0.86 g,0.744 mmol) are dissolved in freshly dried THF (50 mL). To this mixture, K_3PO_4 (59.5 mL, 0.5 M in H_2O) is added. The reaction mixture is degassed three times using freezethaw cycles and then the reaction mixture is stirred at 50 °C for 14 h. After cooling to room temperature, distilled water is added and the mixture is extracted with DCM three times. The combined organic extracts are dried withanhydrous $MgSO_4$, and the solvent is evaporated under vacuum.The crude product is purified by column chromatography over silica gel with DCM as the eluent and subsequent recrystallisation in ethanol to give RC24-CHO (3.42 g, 6.27 mmol, 90 %) as a yellow solid.

^{1}HNMR (500 MHz, $CDCl_3$, 25°C) δ (ppm) 9.84 (s, 1 H), 7.70 (d, J = 8.51 Hz,2 H), 7.49 (d, J = 8.40 Hz, 4 H), 7.27 (d, J = 8.50 Hz, 2 H), 7.20 (d, J =8.35 Hz, 4 H), 7.10 (d, J = 8.55 Hz, 2 H), 6.60 (m, 4 H), 3.85 (s, 6 H),3.83 (s, 6 H).

^{13}C NMR (126 MHz, $CDCl_3$, 25°C) δ (ppm) 190.44, 160.37, 157.44, 153.47, 144.31, 135.13, 131.30, 131.14, 130.57, 128.96,125.82, 122.62, 119.43, 104.73, 99.03, 55.53, 55.44.

MS (ESI):m/z calculated for $C_{35}H_{31}NNaO_5^+$: 568.2094; found: 568.2096.

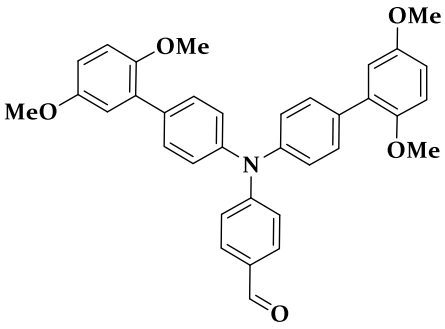

RC25-CHO

4-(bis(2',5'-dimethoxy-[1,1'-biphenyl]-4-yl)amino)benzaldehyde (RC25-CHO)

The desired product is yellow in colour. The yield of the product is 85 %.

^{1}H NMR (500 MHz, CD_2Cl_2, 25°C) δ (ppm) 9.85 (s, 1H), 7.75 (d, J = 8.78 Hz, 2H), 7.59 (d, J = 8.83 Hz, 4H), 7.29 (d, J = 8.81 Hz, 4H), 7.17 (d, J = 8.82 Hz, 2H), 6.99-6.96 (m, 4H), 6.91-6.88 (m, 2H), 3.83 (s, 6H), 3.82 (s, 6H).

^{13}C NMR (126 MHz, CD_2Cl_2, 25°C) δ (ppm) 190.13, 153.84, 153.17, 150.74, 144.94, 135.27, 131.06, 130.75, 130.50, 129.34, 125.73, 119.52, 116.41, 113.07, 112.53, 56.03, and 55.67.

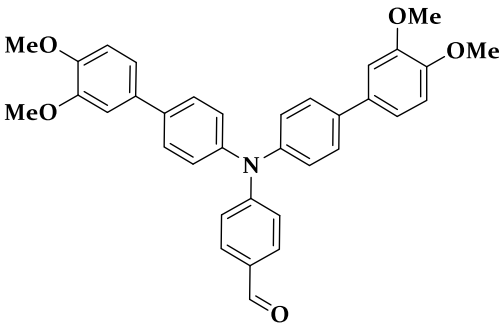

RC34-CHO

4-(bis(3',4'-dimethoxy-[1,1'-biphenyl]-4-yl)amino)benzaldehyde (RC34-CHO)

The desired product is yellow in colour. The yield of the product is 85 %.

^{1}H NMR (500 MHz, CD_2Cl_2, 25°C) δ (ppm) 9.85 (s, 1H), 7.74 (d, J = 8.60 Hz, 2H), 7.61 (d, J = 8.40 Hz, 4H), 7.30 (d, J = 8.40 Hz, 4H), 7.20 (dd, J =

8.20 Hz, *J* = 1.83 Hz, 2H), 7.16-7.14 (m, 4H), 6.99(d, *J* = 8.30 Hz, 2H), 3.84 (s, 6H), 3.82 (s, 6H).

^{13}C NMR (126 MHz, CD_2Cl_2, 25°C) δ (ppm) 190.41, 153.08, 149.47, 148.96, 144.91, 137.70, 133.07, 131.08, 129.40, 127.87, 126.43, 119.54, 119.03, 111.83, 110.38, and 55.86.

General procedure for the preparation of SAM's

The corresponding aldehyde (0.275 mmol) is dissolved in an acetone and DI water (v/v 6/0.3 mL) mixture and heated to 50 °C. To this reaction mixture, potassium permanganate (0.412 mmol) is added, and the resulting reaction mixture is heated to reflux for 10 min (consumption of starting material is monitored by thin layer chromatography). Acetone is then evaporated, and water (10 mL) is added to the mixture. The crude mixture is centrifuged, and aqueous layer is then acidified with 2 M HCl until precipitation. The precipitate is filtered, washed with water followed by diethyl ether. Recrystallisation of the precipitate in DCM/Cyclohexane gave the desired product.

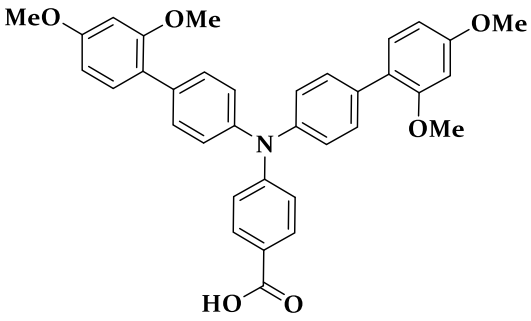

RC24

4-(bis(2',4'-dimethoxy-[1,1'-biphenyl]-4-yl)amino)benzoic acid (RC24)

The desired product is white in colour. The yield of the product is 60 %.

^{1}H NMR (500 MHz, DMSO, 25°C) δ (ppm) 12.44 (s, 1 H), 7.80 (d, J = 8.65 Hz, 2H), 7.47 (d, J = 8.35 Hz, 4H), 7.25 (d, J = 8.35 Hz, 2H), 7.16 (d, J = 8.35 Hz, 4H), 6.94 (d, J = 8.65 Hz, 2H), 6.66 (d, J = 1.75 Hz, 2H), 6.61 (dd, J = 8.40 Hz, J = 1.90, 2H), 3.80 (s, 6H), 3.78 (s, 6H).

^{13}C NMR (126 MHz, DMSO, 25°C) δ (ppm) 167.45, 160.51, 157.56, 151.75, 144.68, 134.91, 131.37, 131.28, 130.92, 125.82, 122.01, 119.42, 105.82, 99.38, 55.99, 55.73.

Mass (ESI), (m/z) calculated for $C_{35}H_{30}NO_6^-$: 560.2079; found: 560.2087.

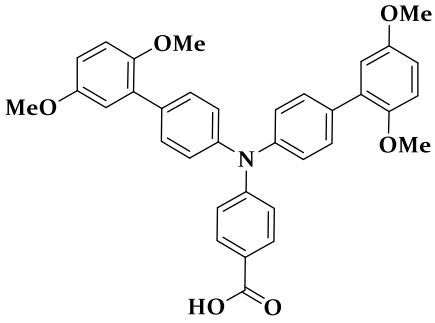

RC25

4-(bis(2',5'-dimethoxy-[1,1'-biphenyl]-4-yl)amino)benzoic acid (RC25)

The desired product is pale yellow in colour. The yield of the product is 65 %.

^{1}H NMR (500 MHz, DMSO, 25°C) δ (ppm): 12.49 (s, 1 H), 7.79 (d, J = 8.75 Hz, 2H), 7.51 (d, J = 8.55 Hz, 4H), 7.15 (d, J = 8.55 Hz, 4H), 7.01 (d, J = 7.75 Hz, 2H), 6.94 (d, J = 8.80 Hz, 2H), 6.87-6.85 (m, 4H), 3.71 (s, 6H), 3.69 (s, 6H).

^{13}C NMR (126 MHz, DMSO, 25°C) δ (ppm): 167.78, 154.18, 152.01, 151.08, 145.66, 135.09, 131.77, 131.52, 130.54, 126.02, 123.55, 120.32, 116.60, 114.29, 113.87, 56.85, and 56.26.

Mass (ESI), (m/z) calculated for $C_{35}H_{30}NO_6^-$: 560.2079; found: 560.2068.

Triphenylamine Based Self-Assembled Hole Selective Monolayers with Different Positioned Terminal Group in Perovskite Solar Cells

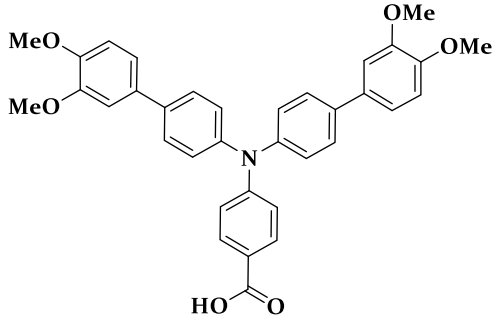

RC34

4-(bis(3',4'-dimethoxy-[1,1'-biphenyl]-4-yl)amino)benzoic acid (RC34)

The desired product is pale yellow in colour. The yield of the product is 58 %.

^{1}H NMR (500 MHz, DMSO, 25°C) δ (ppm): 12.51 (s, 1 H), 7.79 (d, J = 8.85 Hz, 2H), 7.63 (d, J = 8.70 Hz, 4H), 7.19-7.15 (m, 8H), 6.99 (d, J = 7.75 Hz, 2H), 6.95 (d, J = 8.85 Hz, 2H), 3.80 (s, 6H), 3.75 (s, 6H).

^{13}C NMR (126 MHz, DMSO, 25°C) δ (ppm): 167.77, 151.90, 149.90, 149.26, 145.63, 137.24, 133.06, 131.75, 128.58, 126.72, 123.53, 120.29, 119.43, 113.05, 111.09, and 56.39.

Mass (ESI), (m/z) calculated for $C_{35}H_{30}NO_6^-$: 560.2079; found: 560.2072.

Chapter 7

Truxene Derivatives as Hole Transporting Materials in Perovskite Solar Cells

7.1. Abstract

Herein we present a new structural design of hole selective molecules, named EADR01, EA01, and EA02, which consists of truxene core with carbazole diamine terminal groups and hexyl sidechains. These small molecules exhibit good thermal stability and appropriated oxidation properties. Perovskite solar cells fabricated using the n-i-p configuration with EA01 as HSL, show a maximum PCE of 16.7%.

7.2. Introduction

In this study, truxene core is preferred due to its exceptional solubility, the ease with which it may be modified, and high thermal stability.[215] It can be coupled with carbazole and diphenylamine derivatives to tune the HOMO energy levels of small molecules for extracting charges efficiently from perovskite absorber layer. Carbazole and triphenylamine are selected as donor strength moieties, the logical trend is the following carbazole < triphenylamine, due to possibility of compensating for the photogenerated charge with phenyl rings surrounding the nitrogen atom.[294] The electron-rich group is attached to carbazole and triphenylamine derivatives for improving their electron donor ability.[232,273] Dimethoxy and methyl units are positioned at *para-&ortho*-positions on the phenyl group owing to enhance electron-donating effect. Moreover, methoxy moieties enhance the solubility of small molecules in organic solvents. In the previous Chapter, we investigated the role of the substituent group position on the PSCs performance. In this chapter, we followed the same strategy when we decided about the

substituent position in the small molecule structures, to have a suitable electron donor moiety in HSLs.

We designed and synthesised new three truxene-based hole selective molecules and characterised their thermal, optical, electrochemical and photophysical properties. Furthermore, we employed them as a hole selective molecules in n-i-p configuration PSCs for achieving highly efficient and stable devices.

7.3. Results and Discussion

7.3.1. Design and Syntheses

Three new truxene and carbazole-based small molecules are synthesised to achieve highly thermal stable hole selective molecules to have durable PSCs. The syntheses of carbazole substituent moieties are shown in **Scheme 7.1.** The synthesis of 1 is detailed in section 3.5 of Chapter 3. The moieties named Carbazole-DMP,[62] Carbazole-DAMP, and Carbazole-DAP are synthesised by Stille cross coupling reaction with tri-*tert*-butylphosphine tetrafluoroborate [$(t\text{-}Bu)_3PH{\cdot}BF_4$], tris(dibenzylideneacetone)dipalladium(0) [$Pd_2(dba)_3$], and sodium-*tert*-butoxide in dry toluene, resulting in EADR01, EA01, and EA02 in 47%, 74% and 74% yield, respectively. The detailed syntheses procedure is described in section 7.5 and the syntheses pathway is shown in **Scheme 7.2.**

Truxene Derivatives as Hole Transporting Materials in Perovskite Solar Cells

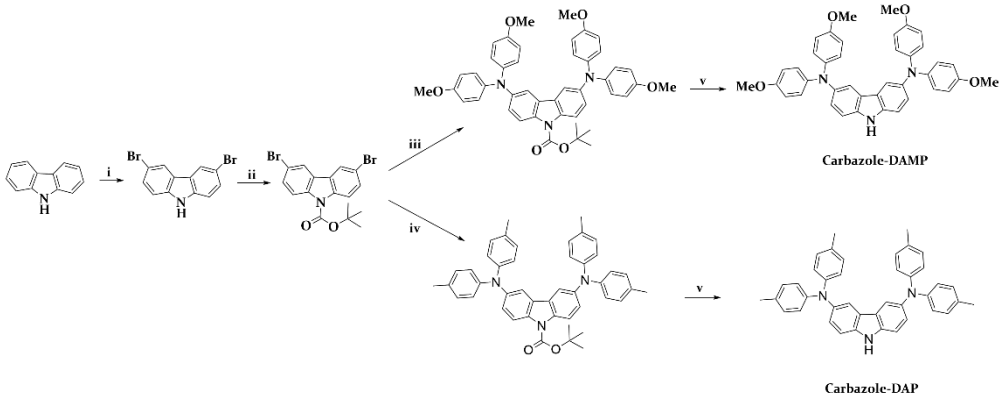

Scheme 7. 1. *Syntheses pathway of Carbazole-DAMP and Carbazole-DAP i) NBS (2 equiv.), DMF, 0 °C, 3h; ii) 4-(dimethylamino)pyridine (0.2 equiv.), di-tert-butyl decarbonate (1.5 equiv.), dry THF, 85 °C, 3h; iii) bis(4-methoxyphenyl)amine (2.1 equiv.), sodium-tert-butoxide, tri-tert-butylphosphonium tetrafluoroborate (20%), tris(dibenzylideneacetone)dipalladium(0) (10%), dry toluene, overnight; iv) di-p-tolylamine (2.1 equiv.), sodium tert-butoxide (3 equiv.), sodium-tert-butoxide, tri-tert-butylphosphonium tetrafluoroborate (20%), tris(dibenzylideneacetone)dipalladium(0) (10%), dry toluene, overnight; v) potassium tert-butoxide (3 equiv.), toluene:EtOH (3:1 v:v), overnight.*

Truxene Derivatives as Hole Transporting Materials in Perovskite Solar Cells

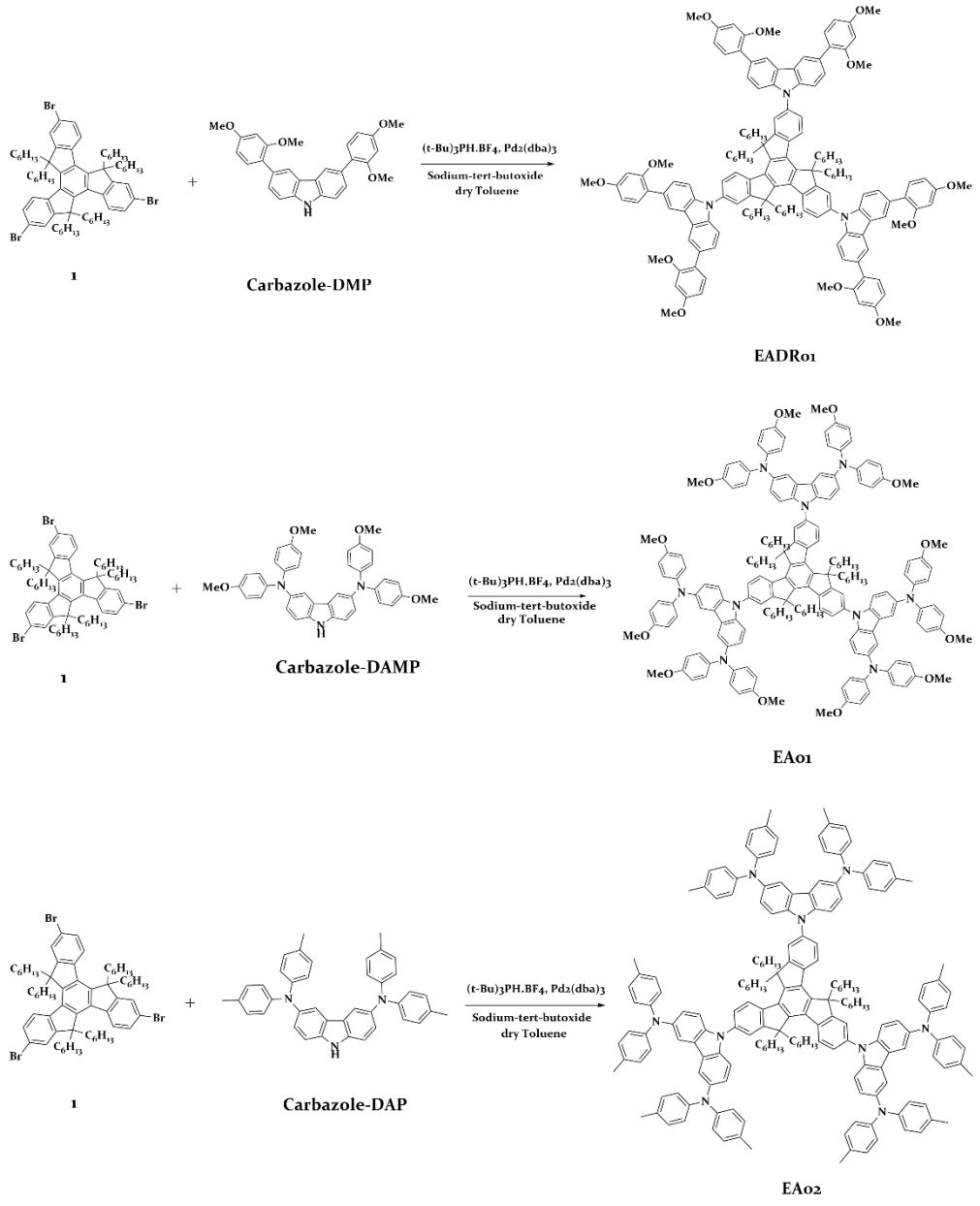

Scheme 7.2. *Syntheses pathway of EADR01, EA01 and EA02.*

7.3.2. Thermal, Optical, Electrochemical, and Photophysical Properties

The thermal behaviour of truxene-based small molecules are determined by TGA and DSC measurements. The summarised recorded data are given in **Table 7.1**. The T_{des} is observed around 428 °C, 414 °C, and 416 °C for EADR01, EA01, and EA02, respectively. The TGA curves of truxene-based small molecules are shown in **Figure 7.1**. Generally, truxene-based small molecules exhibit good thermal stability, starting to decompose (5% weight loss under N_2 atmosphere) at temperatures above 400 °C.

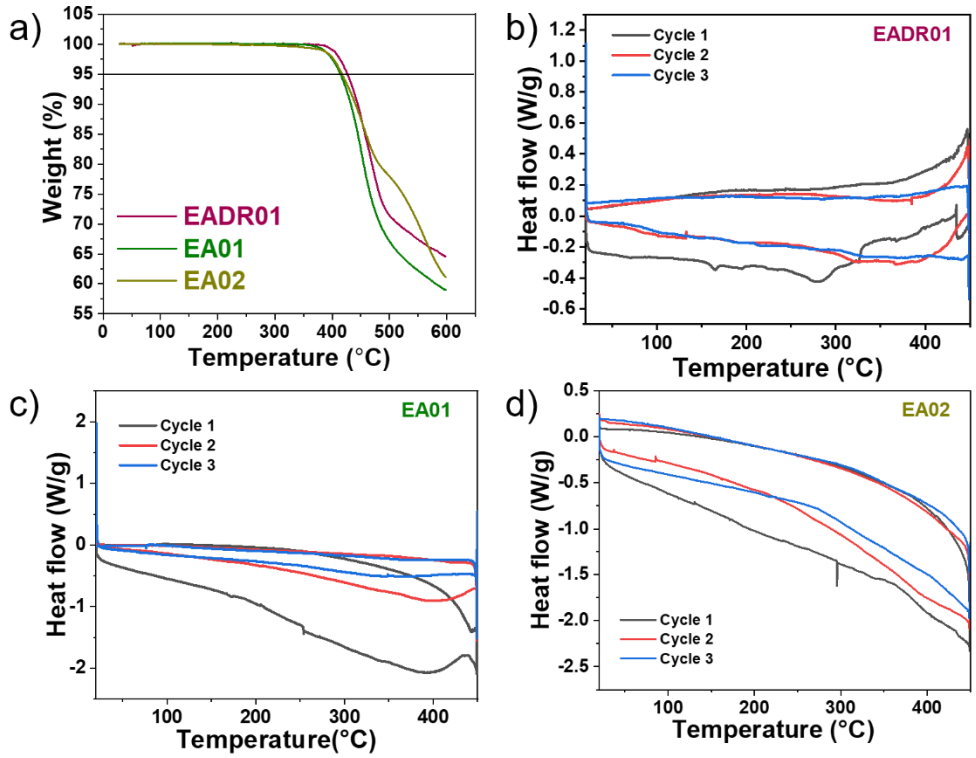

Figure 7.1. *a) TGA analysis of EADR01, EA01, and EA02. DSC analysis of b) EADR01, c) EA01, and d) EA02.*

Truxene Derivatives as Hole Transporting Materials in Perovskite Solar Cells

To determine the chemical and physical changes of truxene-based small molecules, the DSC measurement is performed. The melting and/or crystallisation peak is noted from the first heating cycle, where the T_g values determined for EADR01, EA01, and EA02 are 165 °C, 160 °C, and 125 °C, respectively, as shown in **Figure 7.1** and **Table 7.1**. The sharp endothermic peak that indicates the melting point is not observed, however, a small amount of truxene-based small molecule melts during first cycle. These small molecules can be good candidates as charge selective molecule in PSCs, having stable thermal character at high temperature.

As mentioned in Chapter 6, the thermal behaviour of HSL plays a critical role in PSCs since their molecular motion and transition to the crystalline state are affected by operating temperatures (>85 °C).[295] Having high resistance to elevated temperatures, these HSL-based PSCs should be highly stable and efficient.

Table 7.1. *Thermal properties of EADR01, EA01 and EA02.*

HTMs	T_{des} **(°C)** [a]	T_g **(°C)** [b]
EADR01	428	165
EA01	414	160
EA02	416	125

[a] *Decomposition temperature determined from TGA (5 % weight loss).* [b] *Glass transition temperature determined from the first cycle of DSC. All experiments are carried out under* N_2 *atmosphere, scan rate of 10 °C/min.*

Truxene Derivatives as Hole Transporting Materials in Perovskite Solar Cells

The UV-vis absorption spectra of truxene-based small molecules show two absorption peaks positioned at 306/350 nm, 310/375 nm, and 330/360 nm for EADr01, EA01 and EA02, respectively. These peaks are observed in the UV region and correspond to π-π* transitions and extended π-conjugated system, that in the case of EA01 and EA02 showed a red shift due to having diphenylamine moiety.[296]

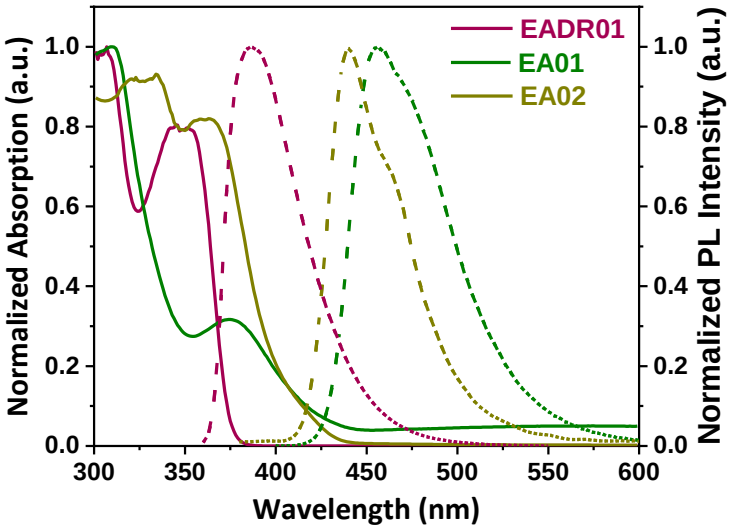

Figure 7.2. *Absorption (solid lines) and emission (dashed lines) spectra of EADR01, EA01 and EA02 in solution.*

The PL spectra exhibit one single peak for all the small molecules at 385 nm, 426 nm, and 416 for EADR01, EA01, and EA02 respectively, when small molecules are excited in solution at the absorption maximum wavelengths. The optical bandgaps of truxene-based small molecules are estimated from the $\lambda_{a.e.}$ using UV-vis measurement (**Figure 7.2** and **Table 7.2**).

Table 7.2. *Optical properties of EADR01, EA01, and EA02.*

Small Molecule	$\lambda_{abs.}$ ***(nm)***	$\lambda_{em.}$ ***(nm)***	$\lambda_{a.e.}$ ***(nm)***	E_g^{opt} ***(eV)***
EADR01	306/350	385	368	3.37
EA01	310/375	456	426	2.91
EA02	330/360	440	416	2.98

The LUMO energy levels of the small molecules are calculated from CV and UV-vis measurements by estimating their electronic and optical bandgap (as calculated in Chapter 5 and 6).[242] As shown in **Figure 7.3**, EA01, and EA02 exhibit three reversible oxidation waves while EADR01 has two reversible oxidation wave, with the first $E_{p\text{-}doping}{}^{p}$ values of 1.20 V, 0.59 V and 0.73 V *versus* vacuum, respectively. The first two oxidation waves of EA01 and EA02 are assigned to a sequential extraction from diphenylamine unit, corresponding mainly to one- and one-electron processes.[294] None of the small molecules show a reduction peak due to their electron-donating properties. The estimated LUMO energy levels are found to be -2.00 eV, -1.88 eV and -1.52 eV, respectively for EADR01, EA01 and EA02.

In general, the corresponding HOMO energy levels of EADR01, EA01, and EA02 are higher than the VBM of the CsFAMA perovskite absorber, so these molecules are more suitable for the hole selective layer in PSCs. However, when we compare their HOMO energy levels with Spiro-OMeTAD, EADR01 presents the deepest HOMO energy level while EA01 and EA02 have the highest. The coherent energy alignment between the

perovskite layer and HSLs is critical for charge transport, extraction, and interface recombination and profoundly the performance of PSCs.[297] Despite all the advantages that the CsFAMA absorber has, it can be replaced with a different type of perovskite absorber to avoid mismatch in further studies, as it has HOMO energy level differences of more than 0.5 eV with EA01. On the other side, EA01 and EA02 have higher LUMO energy levels than EADR01 and Spiro-OMeTAD, which gives them electron blocking capability.

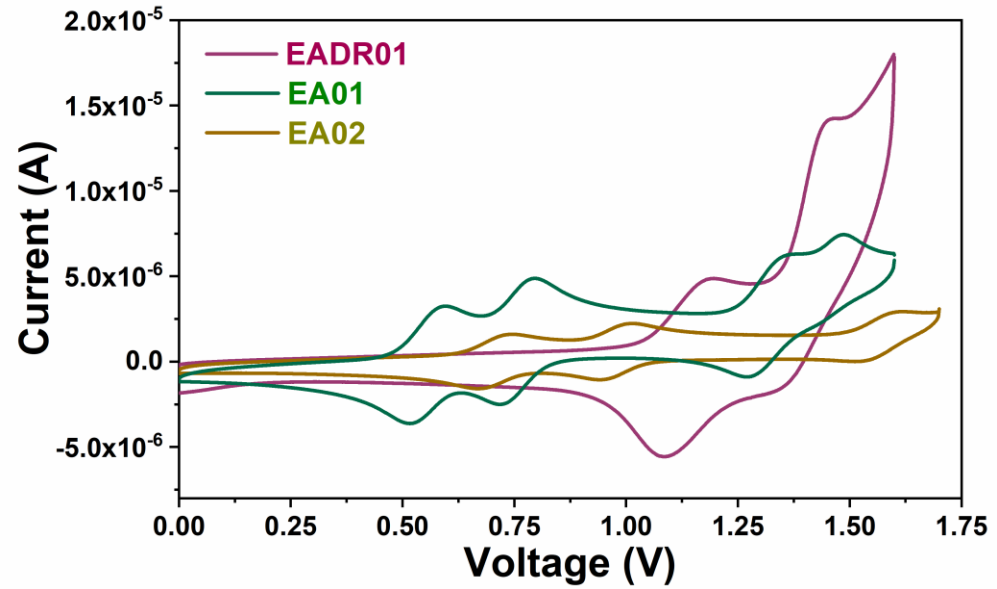

Figure 7.3. *Cyclic voltammetry of EADR01, EA01, and EA02, measured using ferrocene as an internal reference.*

Table 7.3. *Optical and energetic properties of truxene-based small molecules.*

Small Molecule	$E_{p\text{-}doping}^{p}$ ***(V)***	$E_{p\text{-}dedoping}^{p}$ ***(V)***	***HOMO (eV)***	***LUMO (eV)***	$E_{g}^{opt.}$ ***(eV)***
EADR01	1.20/1.48	1.07/1.32	-5.38	2.00	3.37
EA01	0.59/0.79	0.52/0.72	-4.80	1.88	2.91
EA02	0.73/1.00	0.66/0.94	-4.95	1.52	2.97

The hole mobilities of the HSLs are determined using the SCLC method, briefly explained in Chapter 2. We employed the state-of-the-art device architecture with ITO/PEDOT:PSS/HSLs/Au, using one electrode hole-injection creating an ohmic contact to determine the device performance. In other words, the recombination processes do not contribute to the device performance, however, the mobility, electric field and concentration of charges become the determinant factors. The calculation of the hole mobility values is explained in section 2.3.7.

The hole mobility values of EA01 and Spiro-OMeTAD are summarised in **Table 7.4**, and the obtained values are calculated from multiple devices (4 diodes) without chemical dopants in **Figure 2.3**. EADR01 and EA02 showed poor hole mobility and they could not stand the measurement conditions. The hole mobility of HSLs is determined at high voltages (> 2 V), the small molecule and metal contact probably could not resist

these conditions and the active area of EADR01 and EA02 is damaged. EA01 and Spiro-OMeTAD based devices are shown in **Figure 7.4.**

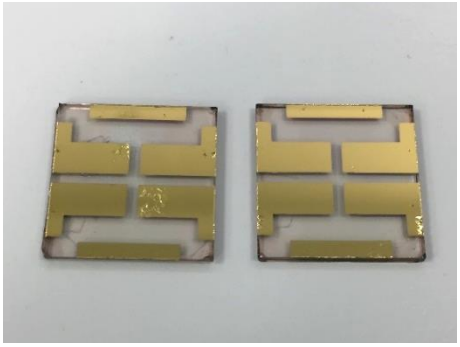

Figure 7.4. *Picture of an only-hole device fabricated with EADR01 (left) and Spiro-OMeTAD (right) for hole mobility measurements without chemical dopants.*

Table 7.4. *Hole mobility values for EA01 and Spiro-OMeTAD without chemical dopants.*

	EADR01	*EA01*	*EA02*	*Spiro-OMeTAD*
μ x10^{-4} (cm^2/Vs)	-	0.47	-	3.55

After completing their photoelectrical characterisation, we employed them in n-i-p configuration PSCs to study their performance as hole selective layer.

7.3.3. Photovoltaic Properties of Perovskite-Based Devices

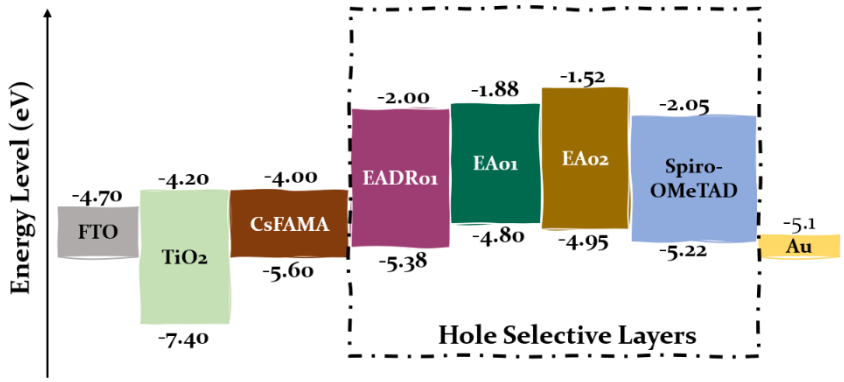

Figure 7.5. *Energy alignment of the related materials in the n-i-p configuration perovskite solar cells. The band edge positions of EADR01, EA01 and EA02 layers from CV measurements in the schematic representation. Note that the CsFAMA, TiO_2, FTO and Au layer values are reported from literature.*

The HOMO and VBM values of EADR01, EA01, AE02 and the other materials are schematically displayed in **Figure 7.5**.[298] In order to determine the capability of these new hole selective materials as HSL with chemical dopants on top of the perovskite layer, the photoluminescence spectrum of the perovskite and perovskite/HSL films are performed. **Figure 7.6a** shows the PL of the perovskite film in a variety of bilayer configurations, including CsFAMA/PMMA, CsFAMA/Spiro-OMeTAD, CsFAMA/EADR01, CsFAMA/EA01, and CsFAMA/EA02. The typical photoluminescence peak of CsFAMA is observed at 750 nm what completely agrees with previous reports.[243] Upon the deposition of HSLs on top of the perovskite layer, we noted that the PL intensities are quenched except for EADR01. Remarkably,

EA01 shows a significantly larger PL quenching in comparison to EA02. The larger PL quenching value of the HSL-coated perovskite layer with respect to the bare perovskite layer demonstrates a more efficient hole extraction process at the perovskite-HSL interface. Spiro-OMeTAD still exhibits a larger PL quenching than truxene-based HSLs.

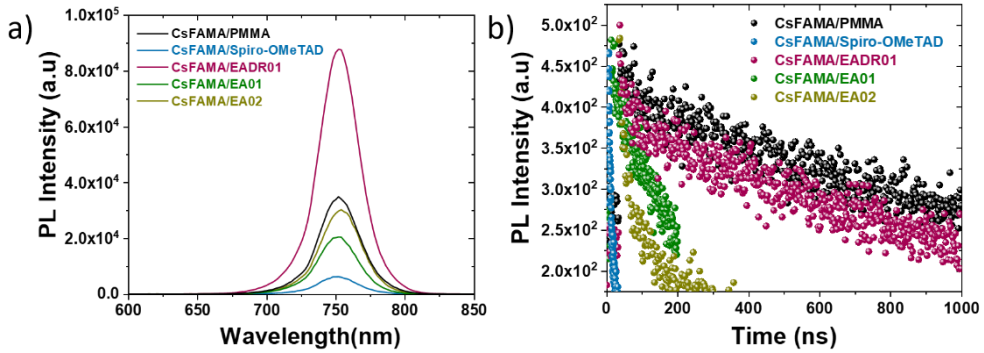

Figure 7.6. *a) Luminescence emission band upon excitation at λ_{ex}=470 nm for CsFAMA/PMMA, CsFAMA/Spiro-OMeTAD, CsFAMA/EADR01, CsFAMA/EA01, and CsFAMA/EA02 (total thickness of 550-600 nm) at room temperature. b) Luminescence emission decays (λ_{ex}=470 nm) measured for 1000 ns for the CsFAMA/PMMA, CsFAMA/Spiro-OMeTAD, CsFAMA/EADR01, CsFAMA/EA01, and CsFAMA/EA02 on FTO coated glass substrate at room temperature.*

Additionally, to understand the carrier dynamics of perovskite thin films incorporating HSLs, we performed TCSPC measurement. All films are deposited on top of the glass and bare perovskite thin film is protected with PMMA layer. The TCSPC spectra are measured upon 470 nm excitation wavelength and plotted in **Figure 7.6b**. The TCSPC spectra are fitted according to the stretched exponential decay function (see for details section 2.3.10). Among the HSLs, EA01 has a slightly similar lifetime as Spiro-OMeTAD, while EADR01 and EA02 have longer lifetimes. Interestingly, EADR01 had just two different decay profile and

its slower decay can be assigned to the bimolecular recombination, while the fast decay likely corresponds to trap filling for EA01 covered perovskite films that have been observed in Chapter 5 and 6 as well. The calculated lifetimes τ_1 (τ_2) of perovskite with and without HSLs are summarised in **Table 7.5**.

Table 7.5. *Fitting values are obtained from the de-convolution of the luminescence decays in* ***Figure 7.4b****.*

Films	***τ_1 (ns)***	***τ_2 (ns)***
CsFAMA/PMMA	32	1760
CsFAMA/Spiro-OMeTAD	5	-
CsFAMA/EADR01	16	1533
CsFAMA/EA01	6	244
CsFAMA/EA02	13	181

The state-of-the-art device structure with FTO/m-TiO_2/c-mTiO_2/LiTFSI/CsFAMA/HSLs/Au sandwich architecture is used in this study.[255] m-TiO_2 and c-TiO_2 layers are deposited on top of the UV-O_3 treated FTO substrates using spin-coating process. Then, LiTFSI thin layer is placed by spin-coater to dope the TiO_2 right before CsFAMA perovskite deposition. The one-step deposition technique is used to deposit perovskite layer on top of the ESLs. Later, HSLs are deposited on top of the annealed perovskite layer using dynamic spin-coating process. For preliminary studies, we have used the optimal concentration for Spiro-OMeTAD is 28.4 mM[255] and HSLs are 15 mM and the speed of the

deposition, 1800 rpm 200 acceleration for 30s. The optimised HSLs are doped with chemical dopants to improve their p-type properties (see section 2.5 for detailed fabrication processes of the PSCs). They are doped using 53.7 mol% of LiTFSI, 333.2 mol% of *t*BP and 9.8 mol% of Co(II)TFSI. For instance, LiTFSI improve the hole mobility of Spiro-OMeTAD, Li^+ react with oxygen and Spiro-OMeTAD to facilitate the formation of oxidized Spiro-OMeTAD, while the $TFSI^-$ stabilises the oxidised Spiro-OMeTAD.[299] To complete the device, a layer of 80 nm gold is evaporated using thermal evaporator under ultra-high vacuum ($1x10^{-6}$ mbar).

The preliminary studies of small molecules optimisation are carried out by preparing devices under the same conditions with Spiro-OMeTAD as HSL reference but changing the molarity of EADR01, EA01, and EA02. The optimised molarity of small molecules for hole mobility studies is used to have suitable film thickness. While EA01 had a good performance with 20 mM, EADR01 and EA02 did not permit an efficient hole injection from perovskite in pre-studies due to having a lower HOMO energy level than EA01. EA01 showed a lower performance than Spiro-OMeTAD with low FF and V_{OC}. **Figure 7.7** shows the current density versus voltage (J-V) scans of the best devices with Spiro-OMeTAD and EA01 measured at a scan rate of 40 mV/s from forward to reverse bias. The photovoltaic data are summarised in **Table 7.6**.

For further studies, to improve the device performance of EA01 in n-i-p configuration PSCs, the molarity of the EA01 solution will be changed and it will be prepared without chemical dopant to obtain stable PSCs.

Truxene Derivatives as Hole Transporting Materials in Perovskite Solar Cells

EADR01 and EA02 will be used as a HSL in p-i-n configuration PSCs and their long-term stability performance will be tested.

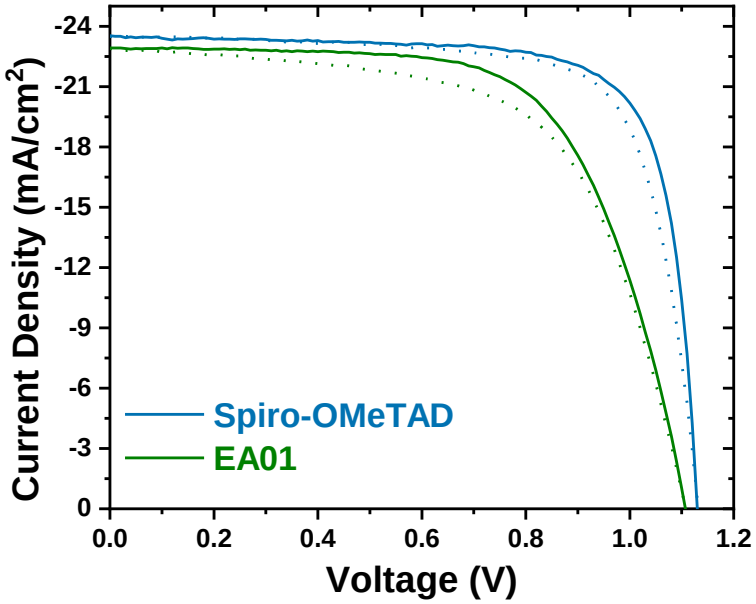

Figure 7.7. *Best J-V curve of the preliminary studies of Spiro-OMeTAD and EA01 in n-i-p configuration PSCs with chemical dopants.*

Table 7.6. *The preliminary studies photovoltaic device parameters from Spiro-OMeTAD and EA01 in different solvents.*

HSLs	*Molarity (mM)*	*Scan Direction*	*Jsc (mA/cm²)*	*V_{OC} (mV)*	*FF (%)*	*PCE (%)*	*HI (%)*
Spiro-OMeTAD	28.4	forward	23.4	1132	74	19.7	0.02
		reverse	23.5	1130	76	20.3	
EA01	20	forward	22.8	1108	62	15.7	0.06
		reverse	22.9	1107	66	16.7	

7.4. Conclusion

In this work, we synthesised new three truxene-based molecules with different electron donating moieties. Their thermal, optical, and electrochemical characterisations are carried out by TGA, DSC, UV-vis, PL, and CV, respectively. The charge transfer properties of truxene-based small molecules are determined with TCSPC measurements. After determining the charge selective properties of small molecules, they have been employed as HSL in n-i-p configuration PSCs. For pre-work studies, the triple cation perovskite layer is used as an absorber and Spiro-OMeTAD is used as a reference HSL. We have obtained comparable PCE result just from EA01 with ~17%, while Spiro-OMeTAD has >20%. In further studies, different EA01 molarities will be used in order to optimise the film thickness and see if it is possible to obtain better performance from the EA01 layer. After that, we will do further characterisation on the completed devices to figure out the role of a thermal stable small molecule (EA01) on long-term device stability.

7.5. Synthetic Method and Procedures

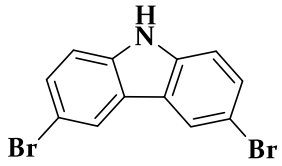

Carbazole-Br

3,6-dibromo-9H-carbazole (Carbazole-Br)

A solution of N-bromosuccinimide (NBS) (6.40 g, 35.88 mmol, 2 equiv.) in 15.0 mL DMF is added dropwise with stirring 9*H*-carbazole (3.00 g, 17.94 mmol, 1 equiv.) in 20.0 mL DMF with ice bath. After for 3 h, the reaction mixture is poured into 250.0 mL ice water, and the crude product is collected by filtration to give beige powder. Recrystallisation from H2O/EtOH to afford beige powder (4.60 g, 80% yield).

^{1}H NMR (400 MHz, DMSO) δ 11.60 (s, 1H), 8.43 (d, J = 2.0 Hz, 1H), 7.54 (dd, J = 8.6, 2.0 Hz, 1H), 7.48 (d, J = 8.6 Hz, 1H).

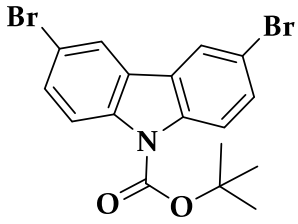

Carbazole-Boc

3,6-dibromo-9h-carbazole-9-carboxylate (Carbazole-Boc)

3,6-Dibromo-9*H*-Carbazole (0.50 g, 1.54 mmol, 1 equiv.) and di-*tert*-butyl dicarbonate (0.50 g, 2.30 mmol, 1.5 equiv.) are dissolved in freshly dried THF (15.0 mL) with stirring. 4-(dimethylamino)pyridine (0.04 g, 0.31 mmol, 0.2 equiv.) is dissolved in different one-necked round bottomed flask and the solution is added to the solution dropwise. Then the reaction mixture is heated to 85 ˚C to reflux for 3h with stirring. After cooling, the solvent is removed under reduced pressure. The crude product is filtered through a pad of silica gel using dichloromethane as the eluent and concentrated *in vacuo* (0.53g, 81% yield).

^{1}H NMR (400 MHz, $CDCl_3$) δ 8.16 (d, J = 8.9 Hz, 2H), 8.03 (d, J = 2.0 Hz, 2H), 7.57 (dd, J = 8.9, 2.1 Hz, 2H), 1.75 (s, 9H).

^{13}C NMR (101 MHz, $CDCl_3$) δ 150.47, 137.50, 130.52, 126.30, 122.60, 117.86, 116.40, 84.84, 28.34.

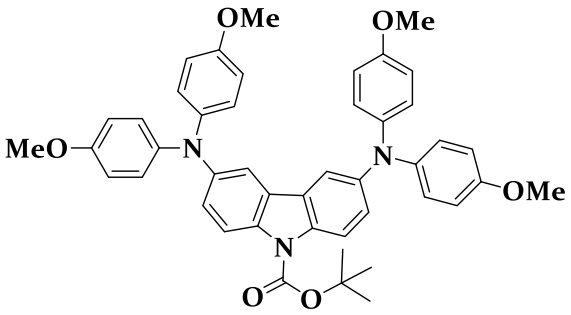

Carbazole-Boc-DAMP

3,6-bis(bis(4-methoxyphenyl)amino)-9h-carbazole-9H-carboxylate (Carbazole-Boc-DAMP)

To a two-necked round bottomed flask, *tert*-butyl 3,6-dibromo-9*h*-carbazole-9-carboxylate (0.50 g, 1.17 mmol, 1 equiv.), bis(4-methoxyphenyl)amine (0.57 g, 2.46 mmol, 2.1 mmol) and sodium *tert*-butoxide (0.34 g, 3.49 mmol, 3 equiv.) and freshly distilled toluene (15.0 mL) are added. The solution is bubbled with argon for 30 min. and then [(t-Bu)$_3$PH·BF$_4$)] (0.07 g, 0.23 mmol, 20%) and [$Pd_2(dba)_3$] (0.11 g, 0.12 mmol, 10%) are added one portion. The reaction mixture is heated to reflux overnight under argon. After cooling, the reaction is poured into water, extracted with toluene and brine. The solvent is concentrated in vacuo. The combined extracts are dried over anhydrous $MgSO_4$, filtered and concentrated under vacuum. The compound is purified by column chromatography (Hexane:EtOAc, 10:1, v:v). Recrystallisation is performed in hexane to give a white solid (0.45 g, 58% yield).

^{1}H NMR (400 MHz, DMSO) δ 8.06 (d, J = 9.0 Hz, 2H), 7.46 (d, J = 2.5 Hz, 2H), 7.03 (dd, J = 9.0, 2.4 Hz, 2H), 6.93 – 6.79 (m, 16H), 3.70 (s, 12H), 1.66 (s, 9H).

^{13}C NMR (101 MHz, DMSO) δ 155.33, 150.58, 144.62, 141.71, 133.95, 126.34, 125.36, 123.78, 117.28, 115.29, 114.27, 84.25, 55.65, 28.27.

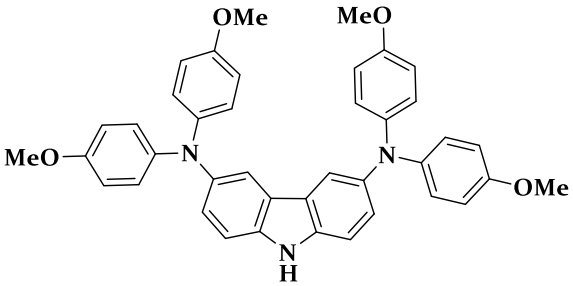

Carbazole-DAMP

N^3,N^3,N^6,N^6-tetrakis(4-methoxyphenyl)-9H-carbazole-3,6-diamine (Carbazole-DAMP)

To a 250.0 mL two-necked round-bottom flask, compound *tert*-butyl 3,6-bis(bis(4-methoxyphenyl)amino)-9h-carbazole-9H-carboxylate (0.50 g, 0.69 mmol, 1 equiv.), potassium *tert*-butoxide (0.24 g, 2.08 mmol, 3 equiv.) and 60.0 mL dry toluene and 20.0 mL absolute ethanol are added. The temperature of reaction mixture is heated to 85 ˚C to reflux overnight. After cooling, the solution is poured into water and extracted with ethyl acetate (3x50 mL). The combined organic phase is dried over anhydrous Na_2SO_4 and concentrated in vacuo. Recrystallisation is performed in methanol to give a light green colour solid (0.42g, 97% yield).

^{1}H NMR (400 MHz, DMSO) δ 11.15 (s, 1H), 7.64 (d, J = 2.2 Hz, 2H), 7.40 (d, J = 8.6 Hz, 2H), 7.06 (dd, J = 8.6, 2.2 Hz, 2H), 6.88 – 6.77 (m, 16H), 3.69 (s, 12H).

^{13}C NMR (101 MHz, DMSO) δ 154.56, 142.68, 140.17, 137.57, 124.95, 124.04, 123.55, 117.42, 115.08, 112.45, 55.65.

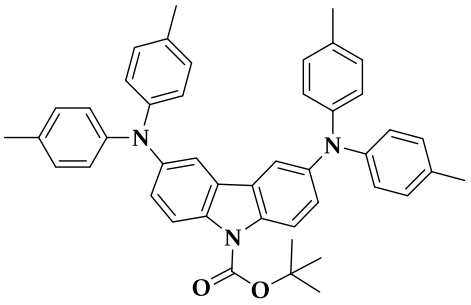

Carbazole-Boc-DAP

3,6-bis(di-p-tolylamino)-9H-carbazole-9-carboxylate (Carbazole-Boc-DAP)

To a two-necked round bottomed flask, *tert*-butyl 3,6-dibromo-9h-carbazole-9-carboxylate (1.75 g, 4.11 mmol, 1 equiv.), di-*p*-tolylamine (1.70 g, 8.64 mmol, 2.1 mmol) and sodium *tert*-butoxide (1.12 g, 12.29 mmol, 3 equiv.) and freshly distilled toluene (50.0 mL) are added. The solution is bubbled with argon for 30 min. and then [(t-Bu)$_3$PH·BF$_4$)] (0.24 g, 0.82 mmol, 20%) and [Pd$_2$(dba)$_3$] (0.38 g, 0.42 mmol, 10%) are added one portion. The reaction mixture is heated to reflux overnight under argon. After cooling, the reaction is poured into water, extracted with toluene and brine. The solvent is concentrated in vacuo. The combined extracts are dried over anhydrous magnesium sulfate, filtered and concentrated under vacuum. The compound is purified by column chromatography (Hexane:EtOAc, 5:1, v:v). Recrystallisation is performed in hexane to give a green solid (1.60 g, 59% yield).

^{1}H NMR (400 MHz, CDCl$_3$) δ 8.16 (d, J = 8.9 Hz, 2H), 7.55 (d, J = 2.3 Hz, 2H), 7.19 (dd, J = 9.0, 2.3 Hz, 8H), 7.05 (d, J = 7.7 Hz, 8H), 6.97 (d, J = 8.4 Hz, 8H), 2.32 (s, 12H), 1.74 (s, 9H).

^{13}C NMR (101 MHz, $CDCl_3$) δ 145.93, 143.73, 134.95, 131.59, 129.79, 126.62, 124.99, 123.40, 117.04, 115.93, 83.70, 28.37, 20.74.

Calc. for $C_{45}H_{43}N_3O_2^+$. (M^+.):680.3247; found: 680.3253.

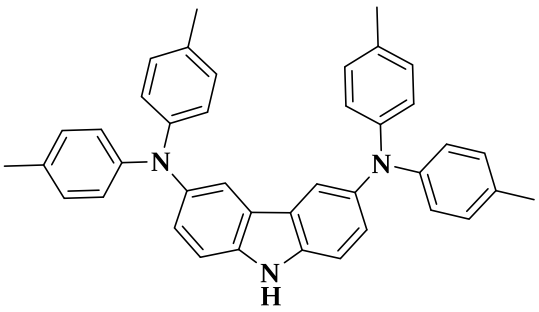

Carbazole-DAP

N3,N3,N6,N6-tetra-p-tolyl-9H-carbazole-3,6-diamine (Carbazole-DAP)

To a 250.0 mL two-necked round-bottom flask, compound *tert*-butyl 3,6-bis(di-*p*-tolylamino)-9*H*-carbazole-9-carboxylate (1.60 g, 2.43 mmol, 1 equiv.), potassium *tert*-butoxide (0.82 g, 7.30 mmol, 3 equiv.) and 60.0 mL dry toluene and 20.0 mL absolute EtOH are added. The temperature of reaction mixture is heated to 85 ˚C to reflux overnight. After cooling, the solution is poured into water and extracted with ethyl acetate (3X100 mL). The combined organic phase is dried over anhydrous Na_2SO_4 and concentrated in vacuo. Recrystallisation is performed in methanol to give a dark green colour solid (1.31 g, 97% yield).

^{1}H NMR (400 MHz, Acetone) δ 10.33 (s, 1H), 7.74 (d, J = 2.1 Hz, 2H), 7.49 (d, J = 8.6 Hz, 2H), 7.17 (dd, J = 8.6, 2.1 Hz, 2H), 7.03 (d, J = 8.3 Hz, 8H), 6.90 (d, J = 8.4 Hz, 8H), 2.25 (s, 12H).

^{13}C NMR (101 MHz, Acetone) δ 146.62, 140.05, 137.79, 130.58, 129.54, 125.31, 123.87, 122.53, 117.96, 111.88, 19.77.

Truxene Derivatives as Hole Transporting Materials in Perovskite Solar Cells

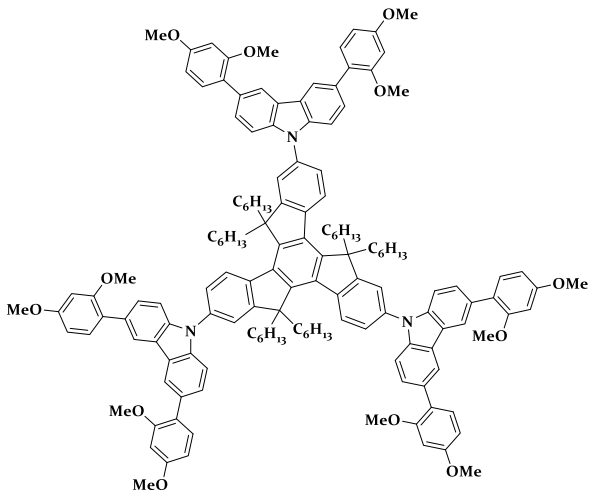

EADR01

9,9′,9″-(5,5,10,10,15,15-hexahexyl-10,15-dihydro-5H-diindeno[1,2-a:1′,2′-c]fluorene-2,7,12-triyl)tris(3,6-bis(2,4-dimethoxyphenyl)-9H-carbazole) (EADR01)

A mixture of 2,7,12-tribromo-5,5,10,10,15,15-hexahexyl-10,15-dihydro-5*H*-diindeno[1,2-a:1',2'-c]fluorine **(1)** (0.25 g, 0.23 mmol), 3,6-bis(2,4-dimethoxyphenyl)-9*H*-carbazole **(Carbazole-DMP)** (0.40 g, 0.89 mmol), $Pd_2(dba)_3$ (0.02 g 0.02 mmol), tri-*tert*-butylphosphine tetrafluoroborate (0.012 g, 0.02 mmol), sodium *tert*-butoxide (0.086 g, 0.89 mmol) are dissolved in 20.0 mL freshly dried toluene in a 50.0 mL two-neck flask under argon atmosphere. The system is purged with argon for 30 minutes. Then, the mixture is refluxed at 115 °C for two days. After 48 h, the reaction is gradually cooled to room temperature and the solution is concentrated under vacuum. A brine solution (100.0 mL) is added, and the solution is extracted with EtOAc (2x100 mL). The combined extracts are dried over anhydrous Na_2SO_4, filtered and concentrated under vacuum. The compound is purified by column chromatography (Hexane: EtOAc, 2:1, v:v). Recrystallisation is performed in hexane to give a beige colour solid (235 mg, 47% yield).

^{1}H NMR (400 MHz, Chloroform-d) δ 8.63 (d, J = 8.5 Hz, 3H), 8.32 (dd, J = 1.7, 0.7 Hz, 6H), 7.80 (d, J = 2.1 Hz, 3H), 7.76 – 7.70 (m, 3H), 7.68 – 7.59

(m, 12H), 7.43 (d, *J* = 9.0 Hz, 6H), 6.70 – 6.63 (m, 12H), 3.92 (s, 18H), 3.88 (s, 18H), 3.19 – 3.08 (m, 6H), 2.28 – 2.18 (m, 6H), 1.09 (dt, *J* = 17.7, 5.3 Hz, 36H), 0.74 (t, *J* = 6.8 Hz, 18H).

^{13}C NMR (101 MHz, $CDCl_3$) δ 160.00, 157.59, 155.61, 145.47, 140.15, 139.02, 138.12, 136.43, 131.59, 130.30, 127.75, 125.77, 124.45, 123.72, 121.28, 109.35, 104.69, 99.14, 56.12, 55.68, 55.49, 37.00, 31.59, 29.50, 24.13, 22.38, 14.03.

MALDI-TOF m/z calc. for $C_{147}H_{159}N_3O_{12}^+(M^+)$: 2158.1918; found: 2158.1896.

Elemental Anal. calcd. for $C_{147}H_{159}N_3O_{12}$: C, 81.75; H, 7.42; N, 1.95. Found: C, 81.25; H, 7.45; N, 1.92.

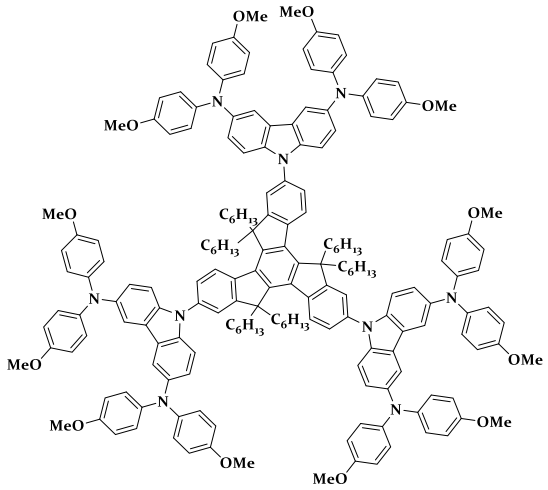

EA01

9,9′,9″-(5,5,10,10,15,15-hexahexyl-10,15-dihydro-5H-diindeno[1,2-a:1′,2′-c]fluorene-2,7,12-triyl)tris(N3,N3,N6,N6-tetrakis(4-methoxyphenyl)-9H-carbazole-3,6-diamine) (EA01)

A mixture of 2,7,12-tribromo-5,5,10,10,15,15-hexahexyl-10,15-dihydro-5H-diindeno[1,2-a:1′,2′-c]fluorine **(1)** (0.30 g, 0.27 mmol, 1 equiv.), $N3,N_3,N_6,N_6$-tetrakis(4-methoxyphenyl)-9*H*-carbazole-3,6-diamine **(Carbazole-DAMP)** 0.65 g, 1.05 mmol, 3.9 equiv.), $Pd_2(dba)_3$ (0.05 mg 20%), tri-*tert*-butylphosphine tetrafluoroborate (0.03 mg, 40%), sodium *tert*-butoxide (0.10 mg, 1.05 mmol, 3.9 equiv.) are dissolved in 20.0 mL freshly dried toluene in a 100.0

mL two-neck flask under argon atmosphere. The system is purged with argon for 1 hour. Then, the mixture is refluxed at 115 °C overnight. The reaction is cooled to the room temperature and concentrated under vacuum. The concentrated solution is extracted with ethyl acetate (EtOAc) (2x100 mL). The combined extracts are dried over anhydrous Na_2SO_4, filtered and concentrated under vacuum. The compound is purified by column chromatography (Hexane:EtOAc, 4:1, v:v). Recrystallisation is performed in hexane to give a light green solid (0.56 g, 74 % yield).

^{1}H NMR (500 MHz, DMSO) δ 8.57 (d, J = 8.6 Hz, 3H), 7.81 (d, J = 2.0 Hz, 3H), 7.71 (s, 6H), 7.68 – 7.62 (m, 3H), 7.29 (d, J = 8.8 Hz, 6H), 7.08 (d, J = 8.8 Hz, 6H), 6.91 (d, J = 8.4 Hz, 24H), 6.81 (d, J = 8.8 Hz, 24H), 3.70 (s, 36H), 3.02 – 2.96 (m, 6H), 2.30 – 2.21 (m, 6H), 0.98 – 0.85 (m, 36H), 0.54 (t, 18H).

Calc. for $C_{183}H_{189}N_9O_{12}^+$. ($M^+$.): 2704.4450; found: 2704.4458.

Elemental Anal. calcd. for $C_{183}H_{189}N_9O_{12}$: C, 81.21; H, 7.04; N, 4.66. Found: C, 80.94; H, 7.16; N, 4.60.

Truxene Derivatives as Hole Transporting Materials in Perovskite Solar Cells

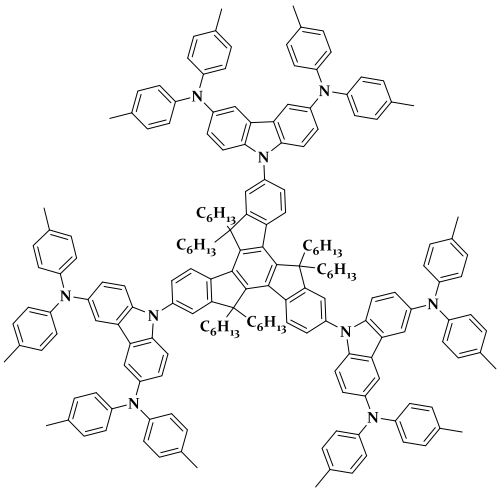

EA02

9,9′,9″-(5,5,10,10,15,15-hexahexyl-10,15-dihydro-5H-diindeno[1,2-a:1′,2′-c]fluorene-2,7,12-triyl)tris(N³,N³,N⁶,N⁶-tetra-p-tolyl-9H-carbazole-3,6-diamine) (EA02)

A mixture of 2,7,12-tribromo-5,5,10,10,15,15-hexahexyl-10,15-dihydro-5H-diindeno[1,2-a:1′,2′-c]fluorine **(1)** (0.30 g, 0.27 mmol, 1 equiv.), N3,N3,N6,N6-tetra-p-tolyl-9H-carbazole-3,6-diamine **(Carbazole-DAP)** (0.48 g, 0.87 mmol, 3.1 equiv.), $Pd_2(dba)_3$ (0.05 mg 20%), tri-*tert*-butylphosphine tetrafluoroborate (0.03 mg, 40%), sodium *tert*-butoxide (0.10 mg, 1.05 mmol, 3.9 equiv.) are dissolved in 20.0 mL freshly dried toluene in a 100.0 mL two-neck flask under argon atmosphere. The system is purged with argon for 1 hour. Then, the mixture is refluxed at 115 °C overnight. The reaction is cooled to the room temperature and concentrated under vacuum. The concentrated solution is extracted with EtOAc (2x200 mL). The combined extracts are dried over anhydrous Na_2SO_4, filtered and concentrated under vacuum. Recrystallisation is performed in hexane to give a light grey solid (0.50 g, 74 % yield).

^{1}H NMR (500 MHz, DMSO) δ 8.62 (d, J = 8.6 Hz, 3H), 7.84 (d, J = 2.2 Hz, 9H), 7.70 (dd, J = 8.4, 2.1 Hz, 3H), 7.35 (d, J = 8.7 Hz, 6H), 7.17 (dd, J = 8.7, 2.2 Hz, 6H), 7.05 (d, J = 8.1 Hz, 24H), 6.90 (d, J = 8.5 Hz, 24H), 3.10 – 2.98

(m, 6H), 2.35 – 2.27 (m, 6H), 2.25 (s, 36H), 1.04 – 0.87 (m, 36H), 0.82 – 0.66 (m, 12H), 0.58 (t, *J* = 6.9 Hz, 18H).

Calc. for $[C_{183}H_{189}N_9^{+}.]$,$[M^{+}.]$: 2512.5060; found: 2512.5087.

Elemental Anal. calcd. for $C_{183}H_{189}N_9$: C, 87.41; H, 7.58; N, 5.01. Found: C, 85.25; H, 7.71; N, 4.69.

Chapter 8

General Conclusions

General Conclusions

The general aim of this thesis was to analyse the potential and improve the efficiency and long-term stability of PCS with an interfacial layer and self-assembled small molecules. To achieve these goals, the designs, syntheses, and characterisations of new truxene & Lewis base-based interfacial layer, self-assembled hole selective small molecules, and truxene-based p-type small molecules have been described with their photovoltaic applications in PSCs.

Moreover, we have demonstrated that the use of photo-induced transient optoelectronic techniques, such as PI-TPV, PI-TPC, and PI-CE is extremely useful for obtaining the information about the charge carrier recombination in PSCs. Additionally, we carried out MMP tracking to measure the stability of the perovskite-based devices at the real working conditions and reported these data from multiple diodes for giving average T_{80}% values.

In this section, the general conclusion of this thesis will be explained briefly for each chapter.

In Chapter 3, we designed and synthesised a new Lewis base based on a truxene core interfacial small molecule to passivate surface defects in the MAPI perovskite layer, specifically the non-coordinated lead. The truxene-based small molecule decreased the number of defects at the MAPI surface, increasing luminescence lifetime by carrying out interfacial charge transfer processes with the MAPI thin film upon illumination. Moreover, we improved the potential of Trux-FPy interfacial layer in lead-based perovskite device by showing its interaction with the uncoordinated lead ions by using UV-vis absorption.

However, the Trux-FPy interfacial layer did not ensure improvement in the interfacial carrier recombination processes as expected, when PI-CE, PI-TPV and PI-TPC techniques are applied to the completed perovskite device.

In Chapter 4, we used TT1 as a self-assembled hole-transporting monolayer in p-i-n configuration PSCs. In this study, TT1 is synthesised by using a novel synthetic route to increase the yield of phthalocyanine derivative. Then, TT1 is used as a self-assembled hole selective monolayer in MAPI PSCs with PCE close to 15%, while PEDOT:PSS-based PSCs' PCE is close to 14% at 1 sun illumination conditions. We observed that TT1-based perovskite devices showed higher V_{OC} than PEDOT:PSS, due to having higher HOMO energy values. To support our results, we measured the differential capacitance of the complete devices, including the evaluation of the carrier recombination order under *operando* conditions. We concluded that, the differences observed in the V_{OC} value might be attributed on the variations in HOMO energy values and not due to differences in charge carrier recombination at the device. As a consequence, using phthalocyanine derivative as SAMs in perovskite devices can give a new perspective to design a new charge selective layer for PSCs.

In Chapter 5, we demonstrated that the molecular design of the SAMs as a charge selective layer is an important key for having stable and efficient PSCs. We designed carbazole-based small molecule (EADR03) with benzoic acid substituent because of its good electron donor properties and passivating effects on the perovskite surface. This small

molecule is modified with an extra phenyl ring (EADR04) for increasing the decomposition temperature of the small molecule, increasing the device stability at 85 °C. Additionally, the 1,3-dimethoxybenzene is added to these molecules to promote a hydrophilic surface once the SAMs are deposited and thus, obtaining more homogenous and compact perovskite film. The perovskite devices based on EADR03 and EADR04 exhibited excellent PCE over 21% when compared to PTAA based cells. Moreover, the EADR04 based devices T_{80}% reached more than 2000 h. We have shown that, after proper optimisation, the SAMs enhanced tremendously the long-term stability of the completed perovskite devices.

In Chapter 6, the perovskite-based device optimisation and performance using three new SAMs based on triphenylamine core synthesised had been described. The optimisation process indicated that the selection of different solvents used for the dip-coating process of SAMs deposition plays a critical role in the device performance. We found that the methoxy group position affects the wettability, consequently increasing the average grain size and decrease the grain boundaries density in the perovskite layer. The perovskite device performance with triphenylamine-based SAMs have the best PCE is 19.8%, 19.6%, and 19.7% for a terminated dimethoxy group at position *para-&ortho-* (RC24), *ortho-&meta-* (RC25), and *para-&meta-* (RC34), respectively. Moreover, we demonstrated that the terminal moieties impact the stability of the device and RC24, RC25, and RC34 based perovskite cells that lose around 3%, 4%, and 5% of their initial PCE after 120 seconds.

General Conclusions

In Chapter 7, we report the design and synthesis of three new truxene-based charge selective small molecules terminated with carbazole and diphenylamine-based electron-donating moieties. They are characterised thermally, optically, and electrochemically and their charge transfer properties are determined with TCSPC measurements. After having strong evidence about their hole selective properties, they have been employed as HSL in n-i-p configuration PSCs. For preliminary studies, the triple cation perovskite layer is used as an absorber, and Spiro-OMeTAD is used as a reference HSL. We obtained a good photovoltaic performance from EA01 PCE of ~17%, while Spiro-OMeTAD PCE is more than >20%. Unfortunately, EADR01 and EA02 did not show interesting results when applied with the same conditions studied for EA01. In future studies, we will change the thickness of HSLs by playing with the solution concentration of small molecules or chemical dopants to obtain better performance from HSLs. Moreover, we will replace the CsFAMA with another perovskite composition for having better energy alignment with HSLs. In addition, the role of the thermally stable small molecules in the long-term device stability of PSCs will be checked.

General Conclusions

References

1. Ekwurzel, B. *et al.* The rise in global atmospheric CO2, surface temperature, and sea level from emissions traced to major carbon producers. *Clim. Change* **144**, 579–590 (2017).

2. Lacis, A. A., Schmidt, G. A., Rind, D. & Ruedy, R. A. Atmospheric CO2: Principal Control Knob Governing Earth's Temperature. *Science (80-.).* **330**, 356–359 (2010).

3. Allen, M. Liability for climate change. *Nature* **421**, 891–892 (2003).

4. Victoria, M., Zhu, K., Brown, T., Andresen, G. B. & Greiner, M. Early decarbonisation of the European energy system pays off. *Nat. Commun.* **11**, 6223 (2020).

5. Global electricity generation mix, 2010-2020. *IEA* https://www.iea.org/data-and-statistics/charts/global-electricity-generation-mix-2010-2020 (2020).

6. Ye, M., Hong, X., Zhang, F. & Liu, X. Recent advancements in perovskite solar cells: flexibility, stability and large scale. *J. Mater. Chem. A* **4**, 6755–6771 (2016).

7. Kippelen, B. & Brédas, J.-L. Organic photovoltaics. *Energy Environ. Sci.* **2**, 251 (2009).

8. O'Regan, B. & Grätzel, M. A low-cost, high-efficiency solar cell based on dye-sensitized colloidal TiO2 films. *Nature* **353**, 737–740 (1991).

9. Yao, Z. *et al.* Dithienopicenocarbazole as the kernel module of low-energy-gap organic dyes for efficient conversion of sunlight to electricity. *Energy Environ. Sci.* **8**, 3192–3197 (2015).

10. Chawla, P. & Tripathi, M. Novel improvements in the sensitizers of dye-sensitized solar cells for enhancement in efficiency-a review. *Int. J. Energy Res.* **39**, 1579–1596 (2015).

11. Kojima, A., Teshima, K., Shirai, Y. & Miyasaka, T. Organometal

References

Halide Perovskites as Visible-Light Sensitizers for Photovoltaic Cells. *J. Am. Chem. Soc.* **131**, 6050–6051 (2009).

12. NREL. Best Research-Cell Efficiency Chart. https://www.nrel.gov/pv/cell-efficiency.html (2021).

13. Goldschmidt, V. M. Die Gesetze der Krystallochemie. *Naturwissenschaften* **14**, 477–485 (1926).

14. Mitzi, D. B. Templating and structural engineering in organic-inorganic perovskites. *J. Chem. Soc. Dalt. Trans.* 1–12 (2001) doi:10.1039/b007070j.

15. Saliba, M. *et al.* Cesium-containing triple cation perovskite solar cells: improved stability, reproducibility and high efficiency. *Energy Environ. Sci.* **9**, 1989–1997 (2016).

16. Green, M. A., Ho-Baillie, A. & Snaith, H. J. The emergence of perovskite solar cells. *Nat. Photonics* **8**, 506–514 (2014).

17. Zhang, F., Yang, B., Li, Y., Deng, W. & He, R. Extra long electron–hole diffusion lengths in CH3NH 3 PbI3–xCl x perovskite single crystals. *J. Mater. Chem. C* **5**, 8431–8435 (2017).

18. Marchioro, A. *et al.* Unravelling the mechanism of photoinduced charge transfer processes in lead iodide perovskite solar cells. *Nat. Photonics* **8**, 250–255 (2014).

19. Zhao, X. & Wang, M. Organic hole-transporting materials for efficient perovskite solar cells. *Mater. Today Energy* **7**, 208–220 (2018).

20. Stolterfoht, M. *et al.* The impact of energy alignment and interfacial recombination on the internal and external open-circuit voltage of perovskite solar cells. *Energy Environ. Sci.* **12**, 2778–2788 (2019).

21. Johnston, M. B. & Herz, L. M. Hybrid Perovskites for Photovoltaics: Charge-Carrier Recombination, Diffusion, and Radiative Efficiencies. *Acc. Chem. Res.* **49**, 146–154 (2016).

22. Shockley, W. & Read, W. T. Statistics of the Recombinations of

References

Holes and Electrons. *Phys. Rev.* **87**, 835–842 (1952).

23. Hall, R. N. Electron-Hole Recombination in Germanium. *Phys. Rev.* **87**, 387–387 (1952).

24. Stolterfoht, M. *et al.* Approaching the fill factor Shockley–Queisser limit in stable, dopant-free triple cation perovskite solar cells. *Energy Environ. Sci.* **10**, 1530–1539 (2017).

25. Wolff, C. M., Caprioglio, P., Stolterfoht, M. & Neher, D. Nonradiative Recombination in Perovskite Solar Cells: The Role of Interfaces. *Adv. Mater.* **31**, 1902762 (2019).

26. Guo, Y. *et al.* Enhanced performance of perovskite solar cells via anti-solvent nonfullerene Lewis base IT-4F induced trap-passivation. *J. Mater. Chem. A* **6**, 5919–5925 (2018).

27. Lee, J.-W. *et al.* A Bifunctional Lewis Base Additive for Microscopic Homogeneity in Perovskite Solar Cells. *Chem* **3**, 290–302 (2017).

28. Wetzelaer, G.-J. A. H. *et al.* Trap-Assisted Non-Radiative Recombination in Organic-Inorganic Perovskite Solar Cells. *Adv. Mater.* **27**, 1837–1841 (2015).

29. Davies, C. L. *et al.* Bimolecular recombination in methylammonium lead triiodide perovskite is an inverse absorption process. *Nat. Commun.* **9**, 293 (2018).

30. Bridgman, P. W. Note on the Principle of Detailed Balancing. *Phys. Rev.* **31**, 101–102 (1928).

31. Kirchartz, T., Krückemeier, L. & Unger, E. L. Research Update: Recombination and open-circuit voltage in lead-halide perovskites. *APL Mater.* **6**, 100702 (2018).

32. Stranks, S. D. *et al.* Electron-Hole Diffusion Lengths Exceeding 1 Micrometer in an Organometal Trihalide Perovskite Absorber. *Science (80-.).* **342**, 341–344 (2013).

33. Wolf, C., Cho, H., Kim, Y.-H. & Lee, T.-W. Polaronic Charge Carrier-Lattice Interactions in Lead Halide Perovskites. *ChemSusChem* **10**, 3705–3711 (2017).

References

34. Herz, L. M. Charge-Carrier Dynamics in Organic-Inorganic Metal Halide Perovskites. *Annu. Rev. Phys. Chem.* **67**, 65–89 (2016).

35. Yang, W. S. *et al.* High-performance photovoltaic perovskite layers fabricated through intramolecular exchange. *Science (80-.).* **348**, 1234–1237 (2015).

36. Ogomi, Y. *et al.* CH3NH3SnxPb(1– x)I3 Perovskite Solar Cells Covering up to 1060 nm. *J. Phys. Chem. Lett.* **5**, 1004–1011 (2014).

37. Stoumpos, C. C., Malliakas, C. D. & Kanatzidis, M. G. Semiconducting Tin and Lead Iodide Perovskites with Organic Cations: Phase Transitions, High Mobilities, and Near-Infrared Photoluminescent Properties. *Inorg. Chem.* **52**, 9019–9038 (2013).

38. Noh, J. H., Im, S. H., Heo, J. H., Mandal, T. N. & Seok, S. Il. Chemical Management for Colorful, Efficient, and Stable Inorganic–Organic Hybrid Nanostructured Solar Cells. *Nano Lett.* **13**, 1764–1769 (2013).

39. Xing, G. *et al.* Low-temperature solution-processed wavelength-tunable perovskites for lasing. *Nat. Mater.* **13**, 476–480 (2014).

40. Tan, Z.-K. *et al.* Bright light-emitting diodes based on organometal halide perovskite. *Nat. Nanotechnol.* **9**, 687–692 (2014).

41. Fang, Y., Dong, Q., Shao, Y., Yuan, Y. & Huang, J. Highly narrowband perovskite single-crystal photodetectors enabled by surface-charge recombination. *Nat. Photonics* **9**, 679–686 (2015).

42. Shockley, W. & Queisser, H. J. Detailed Balance Limit of Efficiency of p-n Junction Solar Cells. *J. Appl. Phys.* **32**, 510–519 (1961).

43. Al-Ashouri, A. *et al.* Monolithic perovskite/silicon tandem solar cell with >29% efficiency by enhanced hole extraction. *Science (80-.).* **370**, 1300–1309 (2020).

44. Matsui, T., Seo, J.-Y., Saliba, M., Zakeeruddin, S. M. & Grätzel, M. Room-Temperature Formation of Highly Crystalline Multication Perovskites for Efficient, Low-Cost Solar Cells. *Adv. Mater.* **29**, 1606258 (2017).

References

45. Chopra, K. L., Major, S. & Pandya, D. K. Transparent conductors—A status review. *Thin Solid Films* **102**, 1–46 (1983).

46. Elangovan, E. & Ramamurthi, K. Studies on micro-structural and electrical properties of spray-deposited fluorine-doped tin oxide thin films from low-cost precursor. *Thin Solid Films* **476**, 231–236 (2005).

47. Thampy, A. S. & Dhamodharan, S. K. Performance analysis and comparison of ITO- and FTO-based optically transparent terahertz U-shaped patch antennas. *Phys. E Low-dimensional Syst. Nanostructures* **66**, 52–58 (2015).

48. Domanski, K. *et al.* Not All That Glitters Is Gold: Metal-Migration-Induced Degradation in Perovskite Solar Cells. *ACS Nano* **10**, 6306–6314 (2016).

49. Wang, J. C., Ren, X. C., Shi, S. Q., Leung, C. W. & Chan, P. K. L. Charge accumulation induced S-shape J-V curves in bilayer heterojunction organic solar cells. *Org. Electron.* **12**, 880–885 (2011).

50. Chen, C. *et al.* Effect of BCP buffer layer on eliminating charge accumulation for high performance of inverted perovskite solar cells. *RSC Adv.* **7**, 35819–35826 (2017).

51. Leijtens, T. *et al.* Electronic Properties of Meso-Superstructured and Planar Organometal Halide Perovskite Films: Charge Trapping, Photodoping, and Carrier Mobility. *ACS Nano* **8**, 7147–7155 (2014).

52. Kim, H.-S. *et al.* Lead Iodide Perovskite Sensitized All-Solid-State Submicron Thin Film Mesoscopic Solar Cell with Efficiency Exceeding 9%. *Sci. Rep.* **2**, 591 (2012).

53. Giordano, F. *et al.* Enhanced electronic properties in mesoporous TiO2 via lithium doping for high-efficiency perovskite solar cells. *Nat. Commun.* **7**, 1–6 (2016).

54. Schloemer, T. H., Christians, J. A., Luther, J. M. & Sellinger, A. Doping strategies for small molecule organic hole-transport

References

materials: impacts on perovskite solar cell performance and stability. *Chem. Sci.* **10**, 1904–1935 (2019).

55. Snaith, H. J. *et al.* Anomalous Hysteresis in Perovskite Solar Cells. *J. Phys. Chem. Lett.* **5**, 1511–1515 (2014).

56. Liu, X. *et al.* Novel efficient C60-based inverted perovskite solar cells with negligible hysteresis. *Electrochim. Acta* **288**, 115–125 (2018).

57. Chong, W. K., Giovanni, D. & Sum, T.-C. *Halide Perovskites Photovoltaics, Light Emitting Devices, and Beyond*. *Halide Perovskites* (2018).

58. Willems, R. E. M., Weijtens, C. H. L., de Vries, X., Coehoorn, R. & Janssen, R. A. J. Relating Frontier Orbital Energies from Voltammetry and Photoelectron Spectroscopy to the Open-Circuit Voltage of Organic Solar Cells. *Adv. Energy Mater.* **9**, 1803677 (2019).

59. Aktas, E., Jiménez-López, J., Azizi, K., Torres, T. & Palomares, E. Self-assembled Zn phthalocyanine as a robust p-type selective contact in perovskite solar cells. *Nanoscale Horizons* **5**, 1415–1419 (2020).

60. Bi, C. *et al.* Non-wetting surface-driven high-aspect-ratio crystalline grain growth for efficient hybrid perovskite solar cells. *Nat. Commun.* **6**, 1–7 (2015).

61. Yalcin, E. *et al.* Semiconductor self-assembled monolayers as selective contacts for efficient PiN perovskite solar cells. *Energy Environ. Sci.* **12**, 230–237 (2019).

62. Rodríguez-Seco, C. *et al.* Minimization of Carrier Losses for Efficient Perovskite Solar Cells through Structural Modification of Triphenylamine Derivatives. *Angew. Chemie Int. Ed.* **59**, 5303–5307 (2020).

63. Mesquita, I., Andrade, L. & Mendes, A. Temperature Impact on Perovskite Solar Cells Under Operation. *ChemSusChem* **12**, 2186–2194 (2019).

References

64. Bai, Y. *et al.* Effects of a Molecular Monolayer Modification of NiO Nanocrystal Layer Surfaces on Perovskite Crystallization and Interface Contact toward Faster Hole Extraction and Higher Photovoltaic Performance. *Adv. Funct. Mater.* **26**, 2950–2958 (2016).

65. Bach, U., De Cloedt, K., Spreitzer, H. & Grätzel, M. Characterization of Hole Transport in a New Class of Spiro-Linked Oligotriphenylamine Compounds. *Adv. Mater.* **12**, 1060–1063 (2000).

66. Jeon, N. J. *et al.* o -Methoxy Substituents in Spiro-OMeTAD for Efficient Inorganic–Organic Hybrid Perovskite Solar Cells. *J. Am. Chem. Soc.* **136**, 7837–7840 (2014).

67. Jeon, N. J. *et al.* Efficient Inorganic–Organic Hybrid Perovskite Solar Cells Based on Pyrene Arylamine Derivatives as Hole-Transporting Materials. *J. Am. Chem. Soc.* **135**, 19087–19090 (2013).

68. Juarez-Perez, E. J. *et al.* Role of the Dopants on the Morphological and Transport Properties of Spiro-MeOTAD Hole Transport Layer. *Chem. Mater.* **28**, 5702–5709 (2016).

69. Wang, S. *et al.* Role of 4-tert-Butylpyridine as a Hole Transport Layer Morphological Controller in Perovskite Solar Cells. *Nano Lett.* **16**, 5594–5600 (2016).

70. Guo, Y. *et al.* n-Type doping for efficient polymeric electron-transporting layers in perovskite solar cells. *J. Mater. Chem. A* **4**, 18852–18856 (2016).

71. Wang, S. *et al.* Unveiling the Role of tBP-LiTFSI Complexes in Perovskite Solar Cells. *J. Am. Chem. Soc.* **140**, 16720–16730 (2018).

72. Walzer, K., Maennig, B., Pfeiffer, M. & Leo, K. Highly Efficient Organic Devices Based on Electrically Doped Transport Layers. *Chem. Rev.* **107**, 1233–1271 (2007).

73. Habisreutinger, S. N., Noel, N. K., Snaith, H. J. & Nicholas, R. J. Investigating the Role of 4- Tert Butylpyridine in Perovskite Solar Cells. *Adv. Energy Mater.* **7**, 1601079 (2017).

References

74. Wang, S., Yuan, W. & Meng, Y. S. Spectrum-Dependent Spiro-OMeTAD Oxidization Mechanism in Perovskite Solar Cells. *ACS Appl. Mater. Interfaces* **7**, 24791–24798 (2015).

75. Burschka, J., Kessler, F., Nazeeruddin, M. K. & Grätzel, M. Co(III) Complexes as p-Dopants in Solid-State Dye-Sensitized Solar Cells. *Chem. Mater.* **25**, 2986–2990 (2013).

76. Nguyen, W. H., Bailie, C. D., Unger, E. L. & McGehee, M. D. Enhancing the hole-conductivity of spiro-OMeTAD without oxygen or lithium salts by using spiro(TFSI)2 in perovskite and dye-sensitized solar cells. *J. Am. Chem. Soc.* **136**, 10996–11001 (2014).

77. Goubard, F. & Dumur, F. Truxene: A promising scaffold for future materials. *RSC Adv.* **5**, 3521–3551 (2015).

78. Boorum, M. M. Groundwork for a Rational Synthesis of C60: Cyclodehydrogenation of a C60H30 Polyarene. *Science (80-.).* **294**, 828–831 (2001).

79. Li, L.-L. *et al.* Synthesis and mesomorphism of ether–ester mixed tail C3-symmetrical truxene discotic liquid crystals. *Liq. Cryst.* **37**, 499–506 (2010).

80. Wang, L. *et al.* Highly Efficient and Color-Stable Deep-Blue Organic Light-Emitting Diodes Based on a Solution-Processible Dendrimer. *Adv. Mater.* **21**, 4854–4858 (2009).

81. Huang, C. *et al.* Dopant-Free Hole-Transporting Material with a C3hSymmetrical Truxene Core for Highly Efficient Perovskite Solar Cells. *J. Am. Chem. Soc.* **138**, 2528–2531 (2016).

82. Cao, X. Y. *et al.* Extended π-conjugated dendrimers based on truxene. *J. Am. Chem. Soc.* **125**, 12430–12431 (2003).

83. Li, H. *et al.* Enhancing Efficiency of Perovskite Solar Cells via Surface Passivation with Graphene Oxide Interlayer. *ACS Appl. Mater. Interfaces* **9**, 38967–38976 (2017).

84. Tiep, N. H., Ku, Z. & Fan, H. J. Recent Advances in Improving the Stability of Perovskite Solar Cells. *Adv. Energy Mater.* **6**, 1–19 (2016).

References

85. Wang, B., Zeng, Q., Sun, Z., Xue, S. & Liang, M. Molecularly engineering of truxene-based dopant-free hole-transporting materials for efficient inverted planar perovskite solar cells. *Dye. Pigment.* **165**, 81–89 (2019).

86. Dai, Z. *et al.* Interfacial toughening with self-assembled monolayers enhances perovskite solar cell reliability. **622**, 618–622 (2021).

87. Magomedov, A. *et al.* Self-Assembled Hole Transporting Monolayer for Highly Efficient Perovskite Solar Cells. *Adv. Energy Mater.* **8**, (2018).

88. Bigelow, W. C., Pickett, D. L. & Zisman, W. A. Oleophobic monolayers. *J. Colloid Sci.* **1**, 513–538 (1946).

89. Ulman, A. Formation and Structure of Self-Assembled Monolayers. *Chem. Rev.* **96**, 1533–1554 (1996).

90. Kaliginedi, V. *et al.* Promising anchoring groups for single-molecule conductance measurements. *Phys. Chem. Chem. Phys.* **16**, 23529–23539 (2014).

91. Brennan, B. J. *et al.* Comparison of silatrane, phosphonic acid, and carboxylic acid functional groups for attachment of porphyrin sensitizers to TiO2 in photoelectrochemical cells. *Phys. Chem. Chem. Phys.* **15**, 16605–16614 (2013).

92. Park, H., Bae, E., Lee, J.-J., Park, J. & Choi, W. Effect of the Anchoring Group in Ru–Bipyridyl Sensitizers on the Photoelectrochemical Behavior of Dye-Sensitized TiO2 Electrodes: Carboxylate versus Phosphonate Linkages. *J. Phys. Chem. B* **110**, 8740–8749 (2006).

93. Silberzan, P., Leger, L., Ausserre, D. & Benattar, J. J. Silanation of silica surfaces. A new method of constructing pure or mixed monolayers. *Langmuir* **7**, 1647–1651 (1991).

94. Mutin, P. H., Guerrero, G. & Vioux, A. Organic–inorganic hybrid materials based on organophosphorus coupling molecules: from metal phosphonates to surface modification of oxides. *Comptes*

References

Rendus Chim. **6**, 1153–1164 (2003).

95. Chen, F., Li, X., Hihath, J., Huang, Z. & Tao, N. Effect of Anchoring Groups on Single-Molecule Conductance: Comparative Study of Thiol-, Amine-, and Carboxylic-Acid-Terminated Molecules. *J. Am. Chem. Soc.* **128**, 15874–15881 (2006).

96. Kim, S. Y., Cho, S. J., Byeon, S. E., He, X. & Yoon, H. J. Self-Assembled Monolayers as Interface Engineering Nanomaterials in Perovskite Solar Cells. *Adv. Energy Mater.* **10**, (2020).

97. Wojciechowski, K. *et al.* Heterojunction modification for highly efficient organic-inorganic perovskite solar cells. *ACS Nano* **8**, 12701–12709 (2014).

98. Valles-Pelarda, M. *et al.* Analysis of the Hysteresis Behavior of Perovskite Solar Cells with Interfacial Fullerene Self-Assembled Monolayers. *J. Phys. Chem. Lett.* **7**, 4622–4628 (2016).

99. Li, L. *et al.* Self-assembled naphthalimide derivatives as an efficient and low-cost electron extraction layer for n-i-p perovskite solar cells. *Chem. Commun.* **55**, 13239–13242 (2019).

100. Guldi, D. M. *et al.* Nanoscale Organization of a Phthalocyanine–Fullerene System: Remarkable Stabilization of Charges in Photoactive 1-D Nanotubules. *J. Am. Chem. Soc.* **127**, 5811–5813 (2005).

101. Gouloumis, A. *et al.* Control over charge separation in phthalocyanine-anthraquinone conjugates as a function of the aggregation status. *J. Am. Chem. Soc.* **128**, 12674–12684 (2006).

102. Ballesteros, B. *et al.* Single-Wall Carbon Nanotubes Bearing Covalently Linked Phthalocyanines – Photoinduced Electron Transfer. *J. Am. Chem. Soc.* **129**, 5061–5068 (2007).

103. Reddy, P. Y. *et al.* Efficient Sensitization of Nanocrystalline TiO2 Films by a Near-IR-Absorbing Unsymmetrical Zinc Phthalocyanine. *Angew. Chemie* **119**, 377–380 (2007).

104. Cid, J. J. *et al.* Molecular cosensitization for efficient panchromatic

References

dye-sensitized solar cells. *Angew. Chemie - Int. Ed.* **46**, 8358–8362 (2007).

105. Laibinis, P. E. & Whitesides, G. M. .omega.-Terminated alkanethiolate monolayers on surfaces of copper, silver, and gold have similar wettabilities. *J. Am. Chem. Soc.* **114**, 1990–1995 (1992).

106. Ma, H., Yip, H.-L., Huang, F. & Jen, A. K.-Y. Interface Engineering for Organic Electronics. *Adv. Funct. Mater.* **20**, 1371–1388 (2010).

107. Haruyama, J., Sodeyama, K., Han, L. & Tateyama, Y. Termination Dependence of Tetragonal CH3NH3PbI3 Surfaces for Perovskite Solar Cells. *J. Phys. Chem. Lett.* **5**, 2903–2909 (2014).

108. Zuo, L. *et al.* Enhanced Photovoltaic Performance of CH3NH3PbI3 Perovskite Solar Cells through Interfacial Engineering Using Self-Assembling Monolayer. *J. Am. Chem. Soc.* **137**, 2674–2679 (2015).

109. Ogomi, Y. *et al.* All-Solid Perovskite Solar Cells with HOCO-R-NH3+I – Anchor-Group Inserted between Porous Titania and Perovskite. *J. Phys. Chem. C* **118**, 16651–16659 (2014).

110. Cao, J. *et al.* Thiols as interfacial modifiers to enhance the performance and stability of perovskite solar cells. *Nanoscale* **7**, 9443–9447 (2015).

111. Wang, Q. *et al.* Effects of Self-Assembled Monolayer Modification of Nickel Oxide Nanoparticles Layer on the Performance and Application of Inverted Perovskite Solar Cells. *ChemSusChem* **10**, 3794–3803 (2017).

112. Zuo, L. *et al.* Tailoring the Interfacial Chemical Interaction for High-Efficiency Perovskite Solar Cells. *Nano Lett.* **17**, 269–275 (2017).

113. Wolff, C. M. *et al.* Perfluorinated Self-Assembled Monolayers Enhance the Stability and Efficiency of Inverted Perovskite Solar Cells. *ACS Nano* **14**, 1445–1456 (2020).

114. Tarkuc, S., Udum, Y. A. & Toppare, L. Tailoring the optoelectronic properties of donor-acceptor-donor type ??-conjugated polymers

References

via incorporating different electron-acceptor moieties. *Thin Solid Films* **520**, 2960–2965 (2012).

115. Han, J. *et al.* Interfacial engineering of a ZnO electron transporting layer using self-Assembled monolayers for high performance and stable perovskite solar cells. *J. Mater. Chem. A* **8**, 2105–2113 (2020).

116. Dou, L. *et al.* Atomically thin two-dimensional organic-inorganic hybrid perovskites. *Science (80-.).* **349**, 1518–1521 (2015).

117. Liang, J. *et al.* All-Inorganic Perovskite Solar Cells. *J. Am. Chem. Soc.* **138**, 15829–15832 (2016).

118. Jiang, J. *et al.* Polymer Doping for High-Efficiency Perovskite Solar Cells with Improved Moisture Stability. *Adv. Energy Mater.* **8**, 1701757 (2018).

119. Yang, S. *et al.* Functionalization of perovskite thin films with moisture-tolerant molecules. *Nat. Energy* **1**, 15016 (2016).

120. Calado, P. *et al.* Evidence for ion migration in hybrid perovskite solar cells with minimal hysteresis. *Nat. Commun.* **7**, 13831 (2016).

121. Bryant, D. *et al.* Observable Hysteresis at Low Temperature in "Hysteresis Free" Organic–Inorganic Lead Halide Perovskite Solar Cells. *J. Phys. Chem. Lett.* **6**, 3190–3194 (2015).

122. Ono, L. K., Raga, S. R., Wang, S., Kato, Y. & Qi, Y. Temperature-dependent hysteresis effects in perovskite-based solar cells. *J. Mater. Chem. A* **3**, 9074–9080 (2015).

123. Christians, J. A., Manser, J. S. & Kamat, P. V. Best Practices in Perovskite Solar Cell Efficiency Measurements. Avoiding the Error of Making Bad Cells Look Good. *J. Phys. Chem. Lett.* **6**, 852–857 (2015).

124. Pellet, N. *et al.* Hill climbing hysteresis of perovskite-based solar cells: a maximum power point tracking investigation. *Prog. Photovoltaics Res. Appl.* **25**, 942–950 (2017).

125. Cimaroli, A. J. *et al.* Tracking the maximum power point of hysteretic perovskite solar cells using a predictive algorithm. *J.*

References

Mater. Chem. C **5**, 10152–10157 (2017).

126. Wang, Q. *et al.* Managing Phase Purities and Crystal Orientation for High-Performance and Photostable Cesium Lead Halide Perovskite Solar Cells. *Sol. RRL* **4**, 2000213 (2020).

127. Khenkin, M. V. *et al.* Consensus statement for stability assessment and reporting for perovskite photovoltaics based on ISOS procedures. *Nat. Energy* **5**, 35–49 (2020).

128. Sharma, V., Sastry, O. S., Kumar, A., Bora, B. & Chandel, S. S. Degradation analysis of a-Si, (HIT) hetro-junction intrinsic thin layer silicon and m-C-Si solar photovoltaic technologies under outdoor conditions. *Energy* **72**, 536–546 (2014).

129. Han, Y. *et al.* Degradation observations of encapsulated planar CH3NH3PbI3 perovskite solar cells at high temperatures and humidity. *J. Mater. Chem. A* **3**, 8139–8147 (2015).

130. Frost, J. M. *et al.* Atomistic Origins of High-Performance in Hybrid Halide Perovskite Solar Cells. *Nano Lett.* **14**, 2584–2590 (2014).

131. Wu, C.-G. *et al.* High efficiency stable inverted perovskite solar cells without current hysteresis. *Energy Environ. Sci.* **8**, 2725–2733 (2015).

132. You, J. *et al.* Moisture assisted perovskite film growth for high performance solar cells. *Appl. Phys. Lett.* **105**, 183902 (2014).

133. Aristidou, N. *et al.* The Role of Oxygen in the Degradation of Methylammonium Lead Trihalide Perovskite Photoactive Layers. *Angew. Chemie Int. Ed.* **54**, 8208–8212 (2015).

134. Aristidou, N. *et al.* Fast oxygen diffusion and iodide defects mediate oxygen-induced degradation of perovskite solar cells. *Nat. Commun.* **8**, 15218 (2017).

135. Bryant, D. *et al.* Light and oxygen induced degradation limits the operational stability of methylammonium lead triiodide perovskite solar cells. *Energy Environ. Sci.* **9**, 1655–1660 (2016).

136. Alsari, M. *et al.* Degradation Kinetics of Inverted Perovskite Solar

References

Cells. *Sci. Rep.* **8**, 5977 (2018).

137. Schwenzer, J. A. *et al.* Temperature Variation-Induced Performance Decline of Perovskite Solar Cells. *ACS Appl. Mater. Interfaces* **10**, 16390–16399 (2018).

138. Tenuta, E., Zheng, C. & Rubel, O. Thermodynamic origin of instability in hybrid halide perovskites. *Sci. Rep.* **6**, 37654 (2016).

139. Beal, R. E. *et al.* Cesium Lead Halide Perovskites with Improved Stability for Tandem Solar Cells. *J. Phys. Chem. Lett.* **7**, 746–751 (2016).

140. Wei, Y., Audebert, P., Galmiche, L., Lauret, J.-S. & Deleporte, E. Photostability of 2D Organic-Inorganic Hybrid Perovskites. *Materials (Basel).* **7**, 4789–4802 (2014).

141. Jemli, K. *et al.* Using Low Temperature Photoluminescence Spectroscopy to Investigate CH3NH3PbI3 Hybrid Perovskite Degradation. *Molecules* **21**, 885 (2016).

142. Azpiroz, J. M., Mosconi, E., Bisquert, J. & De Angelis, F. Defect migration in methylammonium lead iodide and its role in perovskite solar cell operation. *Energy Environ. Sci.* **8**, 2118–2127 (2015).

143. Haruyama, J., Sodeyama, K., Han, L. & Tateyama, Y. First-Principles Study of Ion Diffusion in Perovskite Solar Cell Sensitizers. *J. Am. Chem. Soc.* **137**, 10048–10051 (2015).

144. Leijtens, T. *et al.* Overcoming ultraviolet light instability of sensitized TiO2 with meso-superstructured organometal tri-halide perovskite solar cells. *Nat. Commun.* **4**, 2885 (2013).

145. Zhang, L. Q. *et al.* Highly efficient and stable planar heterojunction perovskite solar cells via a low temperature solution process. *J. Mater. Chem. A* **3**, 12133–12138 (2015).

146. Leijtens, T. *et al.* Hydrophobic Organic Hole Transporters for Improved Moisture Resistance in Metal Halide Perovskite Solar Cells. *ACS Appl. Mater. Interfaces* **8**, 5981–5989 (2016).

References

147. Hou, Y. *et al.* A generic interface to reduce the efficiency-stability-cost gap of perovskite solar cells. *Science (80-.).* **358**, 1192–1197 (2017).

148. Nguyen, W. H., Bailie, C. D., Unger, E. L. & McGehee, M. D. Enhancing the Hole-Conductivity of Spiro-OMeTAD without Oxygen or Lithium Salts by Using Spiro(TFSI)2 in Perovskite and Dye-Sensitized Solar Cells. *J. Am. Chem. Soc.* **136**, 10996–11001 (2014).

149. Chen, W.-Y. *et al.* Low-cost solution-processed copper iodide as an alternative to PEDOT:PSS hole transport layer for efficient and stable inverted planar heterojunction perovskite solar cells. *J. Mater. Chem. A* **3**, 19353–19359 (2015).

150. Jørgensen, M. *et al.* Stability of Polymer Solar Cells. *Adv. Mater.* **24**, 580–612 (2012).

151. Deng, Y., Dong, Q., Bi, C., Yuan, Y. & Huang, J. Air-Stable, Efficient Mixed-Cation Perovskite Solar Cells with Cu Electrode by Scalable Fabrication of Active Layer. *Adv. Energy Mater.* **6**, 1600372 (2016).

152. Zhao, J. *et al.* Is Cu a stable electrode material in hybrid perovskite solar cells for a 30-year lifetime? *Energy Environ. Sci.* **9**, 3650–3656 (2016).

153. Besleaga, C. *et al.* Iodine Migration and Degradation of Perovskite Solar Cells Enhanced by Metallic Electrodes. *J. Phys. Chem. Lett.* **7**, 5168–5175 (2016).

154. Gholipour, S. *et al.* Highly Efficient and Stable Perovskite Solar Cells based on a Low-Cost Carbon Cloth. *Adv. Energy Mater.* **6**, 1601116 (2016).

155. Loganathan, S., Valapa, R. B., Mishra, R. K., Pugazhenthi, G. & Thomas, S. Thermogravimetric Analysis for Characterization of Nanomaterials. in *Thermal and Rheological Measurement Techniques for Nanomaterials Characterization* 67–108 (Elsevier, 2017). doi:10.1016/B978-0-323-46139-9.00004-9.

156. Kasap, S., Málek, J. & Svoboda, R. Thermal Properties and Thermal

References

Analysis: Fundamentals, Experimental Techniques and Applications. in *Springer Handbook of Electronic and Photonic Materials* 1–1 (Springer International Publishing, 2017). doi:10.1007/978-3-319-48933-9_19.

157. Koshy, O., Subramanian, L. & Thomas, S. Differential Scanning Calorimetry in Nanoscience and Nanotechnology. in *Thermal and Rheological Measurement Techniques for Nanomaterials Characterization* 109–122 (Elsevier, 2017). doi:10.1016/B978-0-323-46139-9.00005-0.

158. Gauglitz, G. Ultraviolet and Visible Spectroscopy. in *Handbook of Analytical Techniques* 419–463 (Wiley-VCH Verlag GmbH). doi:10.1002/9783527618323.ch16.

159. Perkampus, H.-H. *UV-VIS Spectroscopy and Its Applications*. (Springer Berlin Heidelberg, 1992). doi:10.1007/978-3-642-77477-5.

160. Giridhar, G., Manepalli, R. K. N. R. & Apparao, G. Contact Angle Measurement Techniques for Nanomaterials. in *Thermal and Rheological Measurement Techniques for Nanomaterials Characterization* 173–195 (Elsevier, 2017). doi:10.1016/B978-0-323-46139-9.00008-6.

161. Law, K.-Y. & Zhao, H. *Surface Wetting Characterization, Contact Angle, and Fundamentals*. (Springer International Publishing, 2016). doi:10.1007/978-3-319-25214-8.

162. Bersier, J. *et al. Electrochemistry V. Topics In Current Chemistry* (1994).

163. Cynthia G. Zoski. *Handbook of Electrochemistry*. (Elsevier, 2007). doi:10.1016/B978-0-444-51958-0.X5000-9.

164. Dandrade, B. *et al.* Relationship between the ionization and oxidation potentials of molecular organic semiconductors. *Org. Electron.* **6**, 11–20 (2005).

165. Leckey, R. Ultraviolet Photoelectron Spectroscopy of Solids. in 291–300 (1992). doi:10.1007/978-3-662-02767-7_14.

References

166. Ozawa, K. Ultraviolet Photoelectron Spectroscopy. in *Compendium of Surface and Interface Analysis* 783–790 (Springer Singapore, 2018). doi:10.1007/978-981-10-6156-1_125.

167. Sworakowski, J. How accurate are energies of HOMO and LUMO levels in small-molecule organic semiconductors determined from cyclic voltammetry or optical spectroscopy? *Synth. Met.* **235**, 125–130 (2018).

168. Toney, M. F. & Brennan, S. Observation of the effect of refraction on x rays diffracted in a grazing-incidence asymmetric Bragg geometry. *Phys. Rev. B* **39**, 7963–7966 (1989).

169. *Advanced Characterization Techniques for Thin Film Solar Cells*. (Wiley-VCH Verlag GmbH & Co. KGaA, 2011). doi:10.1002/9783527636280.

170. Lee, H.-L. & Flynn, N. T. X-RAY PHOTOELECTRON SPECTROSCOPY. in *Handbook of Applied Solid State Spectroscopy* 485–507 (Springer US). doi:10.1007/0-387-37590-2_11.

171. Stevie, F. A. & Donley, C. L. Introduction to x-ray photoelectron spectroscopy. *J. Vac. Sci. Technol. A* **38**, 063204 (2020).

172. Lauermann, I. & Steigert, A. CISSY: A station for preparation and surface/interface analysis of thin film materials and devices. *J. large-scale Res. Facil. JLSRF* **2**, A67 (2016).

173. Shippony, Z. & Read, W. G. A highly accurate Voigt function algorithm. *J. Quant. Spectrosc. Radiat. Transf.* **50**, 635–646 (1993).

174. D., J. V. Electronic processes in ionic crystals (Mott, N. F.; Gurney, R. W.). *J. Chem. Educ.* **42**, A692 (1965).

175. Nichols, K. G. & Vernon, E. V. Space-Charge-Limited Currents in Semiconductors and Insulators. Majority Carrier Transistors. in *Transistor Physics* 283–311 (Springer Netherlands, 1966). doi:10.1007/978-94-010-9916-5_9.

176. Montcada, N. F., Cabau, L., Kumar, C. V., Cambarau, W. & Palomares, E. Indoline as electron donor unit in “Push–Pull”

References

organic small molecules for solution processed organic solar cells: Effect of the molecular π-bridge on device efficiency. *Org. Electron.* **20**, 15–23 (2015).

177. *Springer Handbook of Microscopy*. (Springer International Publishing, 2019). doi:10.1007/978-3-030-00069-1.

178. Desmond O'Connor. *Time-Correlated Single Photon Counting*. (Elsevier, 1984). doi:10.1016/B978-0-12-524140-3.X5001-1.

179. Yu, P. Y. & Cardona, M. *Fundamentals of Semiconductors*. (Springer Berlin Heidelberg, 2005). doi:10.1007/b137661.

180. Makovetskaya, A. *et al.* Photocatalytic properties of hybrid structures based on Titania nanoparticles and semiconductor quantum dots. *Opt. Quantum Electron.* **52**, 147 (2020).

181. Cojocaru, L. *et al.* Determination of unique power conversion efficiency of solar cell showing hysteresis in the I-V curve under various light intensities. *Sci. Rep.* **7**, 11790 (2017).

182. Riordan, C. & Hulstron, R. What is an air mass 1.5 spectrum? (solar cell performance calculations). in *IEEE Conference on Photovoltaic Specialists* 1085–1088 (IEEE). doi:10.1109/PVSC.1990.111784.

183. Habisreutinger, S. N., Noel, N. K. & Snaith, H. J. Hysteresis Index: A Figure without Merit for Quantifying Hysteresis in Perovskite Solar Cells. *ACS Energy Lett.* **3**, 2472–2476 (2018).

184. Unger, E. L. *et al.* Hysteresis and transient behavior in current-voltage measurements of hybrid-perovskite absorber solar cells. *Energy Environ. Sci.* **7**, 3690–3698 (2014).

185. Eames, C. *et al.* Ionic transport in hybrid lead iodide perovskite solar cells. *Nat. Commun.* **6**, 2–9 (2015).

186. Lopez-Varo, P. *et al.* Effects of Ion Distributions on Charge Collection in Perovskite Solar Cells. *ACS Energy Lett.* **2**, 1450–1453 (2017).

187. Azpiroz, J. M., Mosconi, E., Bisquert, J. & De Angelis, F. Defect migration in methylammonium lead iodide and its role in

References

perovskite solar cell operation. *Energy Environ. Sci.* **8**, 2118–2127 (2015).

188. Meloni, S. *et al.* Ionic polarization-induced current-voltage hysteresis in CH3NH3PbX3 perovskite solar cells. *Nat. Commun.* **7**, (2016).

189. Shao, Y., Xiao, Z., Bi, C., Yuan, Y. & Huang, J. Origin and elimination of photocurrent hysteresis by fullerene passivation in CH3NH3PbI3 planar heterojunction solar cells. *Nat. Commun.* **5**, 1–7 (2014).

190. Chen, B., Yang, M., Priya, S. & Zhu, K. Origin of J-V Hysteresis in Perovskite Solar Cells. *J. Phys. Chem. Lett.* **7**, 905–917 (2016).

191. Rakocevic, L. *et al.* Reliable Performance Comparison of Perovskite Solar Cells Using Optimized Maximum Power Point Tracking. *Sol. RRL* **3**, 1800287 (2019).

192. Birnie, D. P. Spin Coating Technique. in *Sol-Gel Technologies for Glass Producers and Users* 49–55 (Springer US, 2004). doi:10.1007/978-0-387-88953-5_4.

193. Puetz, J. & Aegerter, M. A. Dip Coating Technique. in *Sol-Gel Technologies for Glass Producers and Users* 37–48 (Springer US, 2004). doi:10.1007/978-0-387-88953-5_3.

194. Jergel, M. *et al.* Preliminary studies of thin metal oxide films prepared by deposition of an aerosol generated ultrasonically from aqueous nitrate solutions. *Thin Solid Films* **305**, 157–163 (1997).

195. Jergel, M., Conde-Gallardo, A., García, M., Falcony, C. & Jergel, M. Metal oxide Co and Co-Fe-Cr films deposited on glass substrates from a metal-organic aerosol atomised by means of ultrasonic excitations. *Thin Solid Films* **305**, 210–218 (1997).

196. Sorensen, C. M. *et al.* Aerosol Spray Pyrolysis Synthesis Techniques. in *Nanophase Materials* 109–116 (Springer Netherlands, 1994). doi:10.1007/978-94-011-1076-1_15.

197. Duffy, N. W., Peter, L. M., Rajapakse, R. M. G. & Wijayantha, K. G.

References

U. Investigation of the Kinetics of the Back Reaction of Electrons with Tri-Iodide in Dye-Sensitized Nanocrystalline Photovoltaic Cells. *J. Phys. Chem. B* **104**, 8916–8919 (2000).

198. Palomares, E. *et al.* Photovoltage/photocurrent transient techniques. in *Characterization Techniques for Perovskite Solar Cell Materials* 161–180 (Elsevier, 2020). doi:10.1016/B978-0-12-814727-6.00007-4.

199. Barnes, P. R. F. *et al.* Factors controlling charge recombination under dark and light conditions in dye sensitised solar cells. *Phys. Chem. Chem. Phys.* **13**, 3547–3558 (2011).

200. Ryan, J. W., Marin-Beloqui, J. M., Albero, J. & Palomares, E. Nongeminate recombination dynamics-device voltage relationship in hybrid PbS quantum Dot/C60 solar cells. *J. Phys. Chem. C* **117**, 17470–17476 (2013).

201. Gelmetti, I. *et al.* Energy alignment and recombination in perovskite solar cells: Weighted influence on the open circuit voltage. *Energy Environ. Sci.* **12**, 1309–1316 (2019).

202. Kiermasch, D. *et al.* Unravelling steady-state bulk recombination dynamics in thick efficient vacuum-deposited perovskite solar cells by transient methods. *J. Mater. Chem. A* **7**, 14712–14722 (2019).

203. Kirchartz, T. & Nelson, J. Meaning of reaction orders in polymer:fullerene solar cells. *Phys. Rev. B - Condens. Matter Mater. Phys.* **86**, 1–12 (2012).

204. Gelmetti, I. Advanced Characterization and Modelling of Charge Transfer in Perovskite Solar Cells. (2019).

205. Jiménez-López, J. Analysis of the Different Kinetic Processes in Perovskite Solar Cells. (2019).

206. Pazoki, M., Cappel, U. B., Johansson, E. M. J., Hagfeldt, A. & Boschloo, G. Characterization techniques for dye-sensitized solar cells. *Energy Environ. Sci.* **10**, 672–709 (2017).

207. Walker, A. B., Peter, L. M., Lobato, K. & Cameron, P. J. Analysis of

References

photovoltage decay transients in dye-sensitized solar cells. *J. Phys. Chem. B* **110**, 25504–25507 (2006).

208. Ryan, J. W. & Palomares, E. Photo-Induced Charge Carrier Recombination Kinetics in Small Molecule Organic Solar Cells and the Influence of Film Nanomorphology. *Adv. Energy Mater.* **7**, (2017).

209. O'Regan, B. C. *et al.* Optoelectronic Studies of Methylammonium Lead Iodide Perovskite Solar Cells with Mesoporous TiO2 : Separation of Electronic and Chemical Charge Storage, Understanding Two Recombination Lifetimes, and the Evolution of Band Offsets during J – V Hysteresis. *J. Am. Chem. Soc.* **137**, 5087–5099 (2015).

210. Du, T. *et al.* Elucidating the Origins of Subgap Tail States and Open-Circuit Voltage in Methylammonium Lead Triiodide Perovskite Solar Cells. *Adv. Funct. Mater.* **28**, 1801808 (2018).

211. Shuttle, C. G. *et al.* Experimental determination of the rate law for charge carrier decay in a polythiophene: Fullerene solar cell. *Appl. Phys. Lett.* **92**, 093311 (2008).

212. Jiménez-López, J., Puscher, B. M. D., Guldi, D. M. & Palomares, E. Improved Carrier Collection and Hot Electron Extraction Across Perovskite, C60 , and TiO2 Interfaces. *J. Am. Chem. Soc.* **142**, 1236–1246 (2020).

213. Aktas, E. *et al.* Supramolecular Coordination of Pb2+ Defects in Hybrid Lead Halide Perovskite Films Using Truxene Derivatives as Lewis Base Interlayers. *ChemPhysChem* **20**, 2702–2711 (2019).

214. Kimura, M. *et al.* New 9-fluorene-type trispirocyclic compounds for thermally stable hole transport materials in OLEDs. *J. Mater. Chem.* **15**, 2393 (2005).

215. Wang, J. *et al.* A new thermal-stable truxene-based hole-transporting material for perovskite solar cells. *Dye. Pigment.* **125**, 399–406 (2016).

216. Tsuji, H. *et al.* Tripyridyltruxenes: Thermally Stable Cathode Buffer

References

Materials for Organic Thin-Film Solar Cells. *Asian J. Org. Chem.* **1**, 34–37 (2012).

217. Liu, L. & Telfer, S. G. Systematic ligand modulation enhances the moisture stability and gas sorption characteristics of quaternary metal-organic frameworks. *J. Am. Chem. Soc.* **137**, 3901–3909 (2015).

218. Grisorio, R. *et al.* Rational Design of Molecular Hole-Transporting Materials for Perovskite Solar Cells: Direct versus Inverted Device Configurations. *ACS Appl. Mater. Interfaces* **9**, 24778–24787 (2017).

219. Ye, M. *et al.* Recent advances in interfacial engineering of perovskite solar cells. *J. Phys. D. Appl. Phys.* **50**, 373002 (2017).

220. Knight, A. J. *et al.* Electronic Traps and Phase Segregation in Lead Mixed-Halide Perovskite. *ACS Energy Lett.* **4**, 75–84 (2019).

221. Pockett, A. & Carnie, M. J. Ionic Influences on Recombination in Perovskite Solar Cells. *ACS Energy Lett.* **2**, 1683–1689 (2017).

222. Aktas, E., Jiménez-López, J., Azizi, K., Torres, T. & Palomares, E. Self-assembled Zn phthalocyanine as a robust p-type selective contact in perovskite solar cells. *Nanoscale Horizons* **5**, 1415–1419 (2020).

223. García-Iglesias, M. *et al.* Increasing the efficiency of zinc-phthalocyanine based solar cells through modification of the anchoring ligand. *Energy Environ. Sci.* **4**, 189–194 (2011).

224. Zhang, Y. *et al.* Unsymmetrical and Symmetrical Zn(II) Phthalocyanines as Hole-Transporting Materials for Perovskite Solar Cells. *ACS Appl. Energy Mater.* **1**, 2399–2404 (2018).

225. Monda, F. & Madsen, R. Zinc Oxide-Catalyzed Dehydrogenation of Primary Alcohols into Carboxylic Acids. *Chem. - A Eur. J.* **24**, 17832–17837 (2018).

226. Jiménez-López, J. & Palomares, E. Interfacial recombination kinetics in aged perovskite solar cells measured using transient photovoltage techniques. *Nanoscale* **11**, 20024–20029 (2019).

227. Aktas, E. *et al.* Understanding the perovskite/self-assembled

References

selective contact interface for ultra-stable and highly efficient p–i–n perovskite solar cells. *Energy Environ. Sci.* (2021) doi:10.1039/D0EE03807E.

228. Can, M. *et al.* Electrical properties of SAM-modified ITO surface using aromatic small molecules with double bond carboxylic acid groups for OLED applications. *Appl. Surf. Sci.* **314**, 1082–1086 (2014).

229. Pudi, R., Rodríguez-Seco, C., Vidal-Ferran, A., Ballester, P. & Palomares, E. o,p -Dimethoxybiphenyl Arylamine Substituted Porphyrins as Hole-Transport Materials: Electrochemical, Photophysical, and Carrier Mobility Characterization. *European J. Org. Chem.* **2018**, 2064–2070 (2018).

230. Zhu, X. *et al.* Hole-Transporting Materials Incorporating Carbazole into Spiro-Core for Highly Efficient Perovskite Solar Cells. *Adv. Funct. Mater.* 1807094 (2018) doi:10.1002/adfm.201807094.

231. Lu, C., Choi, I. T., Kim, J. & Kim, H. K. Simple synthesis and molecular engineering of low-cost and star-shaped carbazole-based hole transporting materials for highly efficient perovskite solar cells. *J. Mater. Chem. A* **5**, 20263–20276 (2017).

232. Yin, X. *et al.* One-step facile synthesis of a simple carbazole-cored hole transport material for high-performance perovskite solar cells. *Nano Energy* **40**, 163–169 (2017).

233. Rodríguez-Seco, C. *et al.* Minimization of Carrier Losses for Efficient Perovskite Solar Cells through Structural Modification of Triphenylamine Derivatives. *Angew. Chemie* **132**, 5341–5345 (2020).

234. Jeon, N. J. *et al.* o-Methoxy Substituents in Spiro-OMeTAD for Efficient Inorganic–Organic Hybrid Perovskite Solar Cells. *J. Am. Chem. Soc.* **136**, 7837–7840 (2014).

235. Krishna, A. & Grimsdale, A. C. Hole transporting materials for mesoscopic perovskite solar cells – towards a rational design? *J. Mater. Chem. A* **5**, 16446–16466 (2017).

References

236. Tozlu, C. *et al.* Effect of TiO 2 modification with amino-based self-assembled monolayer on inverted organic solar cell. *Appl. Surf. Sci.* **422**, 1129–1138 (2017).

237. Moulder, J. F., Stickle, W. F., Sobol, P. E. & Bomben, K. D. Handbook of X-ray Photoelectron Spectroscopy. *Chastain, Publ. by Perkin-Elmer Corp.* (1992).

238. Montagne, F., Polesel-Maris, J., Pugin, R. & Heinzelmann, H. Poly(N-isopropylacrylamide) thin films densely grafted onto gold surface: preparation, characterization, and dynamic AFM study of temperature-induced chain 'conformational changes. *Langmuir* **25**, 983–991 (2009).

239. Yan, C., Zharnikov, M., Gölzhäuser, A. & Grunze, M. Preparation and characterization of self-assembled monolayers on indium tin oxide. *Langmuir* **16**, 6208–6215 (2000).

240. Arkan, E. *et al.* Effect of functional groups of self assembled monolayer molecules on the performance of inverted perovskite solar cell. *Mater. Chem. Phys.* 123435 (2020) doi:10.1016/j.matchemphys.2020.123435.

241. Nazeeruddin, M. K., Humphry-Baker, R., Liska, P. & Grätzel, M. Investigation of sensitizer adsorption and the influence of protons on current and voltage of a dye-sensitized nanocrystalline TiO2 solar cell. *J. Phys. Chem. B* **107**, 8981–8987 (2003).

242. Costa, J. C. S., Taveira, R. J. S., Lima, C. F. R. A. C., Mendes, A. & Santos, L. M. N. B. F. Optical band gaps of organic semiconductor materials. *Opt. Mater. (Amst).* **58**, 51–60 (2016).

243. Saliba, M. *et al.* Cesium-containing triple cation perovskite solar cells: Improved stability, reproducibility and high efficiency. *Energy Environ. Sci.* **9**, 1989–1997 (2016).

244. Al-Ashouri, A. *et al.* Conformal monolayer contacts with lossless interfaces for perovskite single junction and monolithic tandem solar cells. *Energy Environ. Sci.* **12**, 3356–3369 (2019).

245. Zuo, L. *et al.* Enhanced photovoltaic performance of $CH_3NH_3PbI_3$

References

perovskite solar cells through interfacial engineering using self-assembling monolayer. *J. Am. Chem. Soc.* **137**, 2674–2679 (2015).

246. Safari, Z. *et al.* Optimizing the interface between hole transporting material and nanocomposite for highly efficient perovskite solar cells. *Nanomaterials* **9**, (2019).

247. Roose, B., Dey, K., Chiang, Y.-H., Friend, R. H. & Stranks, S. D. A Critical Assessment of the Use of Excess Lead Iodide in Lead Halide Perovskite Solar Cells. *J. Phys. Chem. Lett.* (2020) doi:10.1021/acs.jpclett.0c01820.

248. Kim, J. *et al.* Excitation Density Dependent Photoluminescence Quenching and Charge Transfer Efficiencies in Hybrid Perovskite / Organic Semiconductor Bilayers. **1802474**, 1–11 (2018).

249. Wen, X. *et al.* Defect trapping states and charge carrier recombination in organic-inorganic halide perovskites. *J. Mater. Chem. C* **4**, 793–800 (2015).

250. Hutter, E. M., Kirchartz, T., Ehrler, B., Cahen, D. & von Hauff, E. Pitfalls and prospects of optical spectroscopy to characterize perovskite-transport layer interfaces. *Appl. Phys. Lett.* **116**, 100501 (2020).

251. Okada, W., Suga, T., Oyaizu, K., Segawa, H. & Nishide, H. Perovskite/TiO2 Interface Passivation Using Poly(vinylcarbazole) and Fullerene for the Photovoltaic Conversion Efficiency of 21%. *ACS Appl. Energy Mater.* **2**, 2848–2853 (2019).

252. Stolterfoht, M. *et al.* Visualization and suppression of interfacial recombination for high-efficiency large-area pin perovskite solar cells. *Nat. Energy* **3**, 847–854 (2018).

253. Wojciechowski, K. *et al.* C60 as an Efficient n-Type Compact Layer in Perovskite Solar Cells. *J. Phys. Chem. Lett.* **6**, 2399–2405 (2015).

254. Yang, T. Y. *et al.* Achieving Long-Term Operational Stability of Perovskite Solar Cells with a Stabilized Efficiency Exceeding 20% after 1000 h. *Adv. Sci.* **6**, 1–7 (2019).

References

255. Saliba, M. *et al.* How to Make over 20% Efficient Perovskite Solar Cells in Regular (n-i-p) and Inverted (p-i-n) Architectures. *Chem. Mater.* **30**, 4193–4201 (2018).

256. Habisreutinger, S. N. *et al.* Enhanced Hole Extraction in Perovskite Solar Cells Through Carbon Nanotubes. *J. Phys. Chem. Lett.* **5**, 4207–4212 (2014).

257. Lin, Y. *et al.* Self-Assembled Monolayer Enables Hole Transport Layer-Free Organic Solar Cells with 18% Efficiency and Improved Operational Stability. *ACS Energy Lett.* **5**, 2935–2944 (2020).

258. Wang, L., McCleese, C., Kovalsky, A., Zhao, Y. & Burda, C. Femtosecond time-resolved transient absorption spectroscopy of CH 3NH3PbI3 perovskite films: Evidence for passivation effect of pbi2. *J. Am. Chem. Soc.* **136**, 12205–12208 (2014).

259. Wang, Q., Phung, N., Di Girolamo, D., Vivo, P. & Abate, A. Enhancement in lifespan of halide perovskite solar cells. *Energy Environ. Sci.* **12**, 865–886 (2019).

260. Li, Z. *et al.* Side-Chain Engineering for Enhancing the Thermal Stability of Polymer Solar Cells. *Adv. Mater.* **27**, 6999–7003 (2015).

261. Petrović, M. *et al.* Limitations of a polymer-based hole transporting layer for application in planar inverted perovskite solar cells. *Nanoscale Adv.* **1**, 3107–3118 (2019).

262. Gijsman, P., Meijers, G. & Vitarelli, G. Comparison of the UV-degradation chemistry of polypropylene, polyethylene, polyamide 6 and polybutylene terephthalate. *Polym. Degrad. Stab.* **65**, 433–441 (1999).

263. Saliba, M. *et al.* Incorporation of rubidium cations into perovskite solar cells improves photovoltaic performance. *Science (80-.).* **354**, 206–209 (2016).

264. Farooq, A. *et al.* Spectral Dependence of Degradation under Ultraviolet Light in Perovskite Solar Cells. *ACS Appl. Mater. Interfaces* **10**, 21985–21990 (2018).

References

265. Li, W. *et al.* Enhanced UV-light stability of planar heterojunction perovskite solar cells with caesium bromide interface modification. *Energy Environ. Sci.* **9**, 490–498 (2016).

266. Roose, B., Dey, K., Chiang, Y.-H., Friend, R. H. & Stranks, S. D. Critical Assessment of the Use of Excess Lead Iodide in Lead Halide Perovskite Solar Cells. *J. Phys. Chem. Lett.* **11**, 6505–6512 (2020).

267. Zheng, X. *et al.* Enhanced thermal stability of inverted perovskite solar cells by interface modification and additive strategy. *RSC Adv.* **10**, 18400–18406 (2020).

268. Canil, L. *et al.* Tuning halide perovskite energy levels. *Energy Environ. Sci.* (2021) doi:10.1039/d0ee02216k.

269. Choi, K. *et al.* A Short Review on Interface Engineering of Perovskite Solar Cells: A Self-Assembled Monolayer and Its Roles. *Sol. RRL* **4**, 1–20 (2020).

270. Cao, B. *et al.* Role of Interfacial Layers in Organic Solar Cells: Energy Level Pinning versus Phase Segregation. *ACS Appl. Mater. Interfaces* acsami.6b02712 (2016) doi:10.1021/acsami.6b02712.

271. Li, Z. *et al.* Incorporating self-assembled silane-crosslinked carbon dots into perovskite solar cells to improve efficiency and stability. *J. Mater. Chem. A* **8**, 5629–5637 (2020).

272. Yang, G. *et al.* Interface engineering in planar perovskite solar cells: energy level alignment, perovskite morphology control and high performance achievement. *J. Mater. Chem. A* **5**, 1658–1666 (2017).

273. Agarwala, P. & Kabra, D. A review on triphenylamine (TPA) based organic hole transport materials (HTMs) for dye sensitized solar cells (DSSCs) and perovskite solar cells (PSCs): Evolution and molecular engineering. *J. Mater. Chem. A* **5**, 1348–1373 (2017).

274. Shen, S. *et al.* A star-shaped oligothiophene with triphenylamine as core and octyl cyanoacetate as end groups for solution-processed organic solar cells. *Org. Electron. physics, Mater. Appl.* **14**, 875–881 (2013).

References

275. Ke, L., Chen, P. & Chua, S. J. Photoluminescence degradation in organic light-emitting devices. *Appl. Phys. Lett.* **80**, 697–699 (2002).

276. Thelakkat, M. Star-Shaped, Dendrimeric and Polymeric Triarylamines as Photoconductors and Hole Transport Materials for Electro-Optical Applications. *Macromol. Mater. Eng.* **287**, 442 (2002).

277. Ishikawa, W., Noguchi, K., Kuwabaru, Y. & Shirota, Y. Novel amorphous molecular materials: The starburst molecule 1,3,5-tris[N-(4-diphenyl- aminophenyl)phenylamino]benzene. *Adv. Mater.* **5**, 559–561 (1993).

278. Hammett, L. P. The Effect of Structure upon the Reactions of Organic Compounds. Benzene Derivatives. *J. Am. Chem. Soc.* **59**, 96–103 (1937).

279. Al-Ashouri, A. *et al.* Conformal monolayer contacts with lossless interfaces for perovskite single junction and monolithic tandem solar cells. *Energy Environ. Sci.* **12**, 3356–3369 (2019).

280. Chen, Y. *et al.* Mechanism of PbI2 in Situ Passivated Perovskite Films for Enhancing the Performance of Perovskite Solar Cells. *ACS Appl. Mater. Interfaces* **11**, 44101–44108 (2019).

281. Muscarella, L. A. *et al.* Crystal Orientation and Grain Size: Do They Determine Optoelectronic Properties of MAPbI3 Perovskite? *J. Phys. Chem. Lett.* **10**, 6010–6018 (2019).

282. Le Bail, A. & Jouanneaux, A. A Qualitative Account for Anisotropic Broadening in Whole-Powder-Diffraction-Pattern Fitting by Second-Rank Tensors. *J. Appl. Crystallogr.* **30**, 265–271 (1997).

283. Saliba, M. *et al.* Cesium-containing triple cation perovskite solar cells: Improved stability, reproducibility and high efficiency. *Energy Environ. Sci.* **9**, 1989–1997 (2016).

284. Ran, J. *et al.* Triphenylamine–Polystyrene Blends for Perovskite Solar Cells with Simultaneous Energy Loss Suppression and Stability Improvement. *Sol. RRL* **4**, 1–8 (2020).

References

285. Yang, L. *et al.* Enhanced stability and efficiency of perovskite solar cells via bifunctional group passivation with thiosalicylic acid. *Org. Electron.* **81**, 105681 (2020).

286. Noel, N. K. *et al.* Enhanced Photoluminescence and Solar Cell Performance via Lewis Base Passivation of Organic–Inorganic Lead Halide Perovskites. *ACS Nano* **8**, 9815–9821 (2014).

287. Chen, R. *et al.* Efficient and Stable Inverted Planar Perovskite Solar Cells Using a Triphenylamine Hole-Transporting Material. *ChemSusChem* **11**, 1467–1473 (2018).

288. Chen, C. *et al.* Effect of BCP buffer layer on eliminating charge accumulation for high performance of inverted perovskite solar cells. *RSC Adv.* **7**, 35819–35826 (2017).

289. An, Q. *et al.* Small grains as recombination hot spots in perovskite solar cells. *Matter* **4**, 1683–1701 (2021).

290. Saliba, M. & Etgar, L. Current density mismatch in Perovskite solar cells. *ACS Energy Lett.* **5**, 2886–2888 (2020).

291. Chakravarthi, N. *et al.* Substituent position engineering of phosphine oxide functionalized triazine-based cathode interfacial materials for flexible organic and perovskite solar cells. *Org. Electron.* **54**, 54–63 (2018).

292. Correa-Baena, J.-P. *et al.* Unbroken Perovskite: Interplay of Morphology, Electro-optical Properties, and Ionic Movement. *Adv. Mater.* **28**, 5031–5037 (2016).

293. Phung, N. *et al.* The Role of Grain Boundaries on Ionic Defect Migration in Metal Halide Perovskites. *Adv. Energy Mater.* **10**, 1903735 (2020).

294. Rodriguez-Seco, C. Low-Molecular Weight Organic Semiconductors for Organic and Perovskite Solar Cells. (2019).

295. Zheng, H. *et al.* The influence of perovskite layer and hole transport material on the temperature stability about perovskite solar cells. *Sol. Energy* **159**, 914–919 (2018).

References

296. Dhingra, P., Singh, P., Rana, P. J. S., Garg, A. & Kar, P. Hole-Transporting Materials for Perovskite-Sensitized Solar Cells. *Energy Technol.* **4**, 891–938 (2016).

297. Raoui, Y., Ez-Zahraouy, H., Kazim, S. & Ahmad, S. Energy level engineering of charge selective contact and halide perovskite by modulating band offset: Mechanistic insights. *J. Energy Chem.* **54**, 822–829 (2021).

298. Jiménez-López, J., Cambarau, W., Cabau, L. & Palomares, E. Charge Injection, Carriers Recombination and HOMO Energy Level Relationship in Perovskite Solar Cells. *Sci. Rep.* **7**, 6101 (2017).

299. Zhou, Y. *et al.* Doping and alloying for improved perovskite solar cells. *J. Mater. Chem. A* **4**, 17623–17635 (2016).

Appendix

$^{1}H/^{13}C$ NMR Spectra

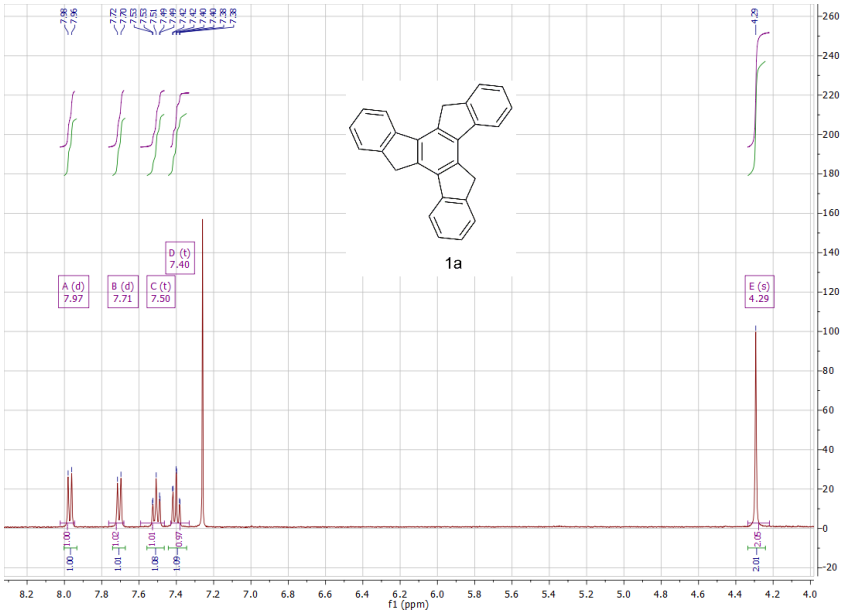

Figure A1. *^{1}H NMR spectrum of compound 1a*

Appendix

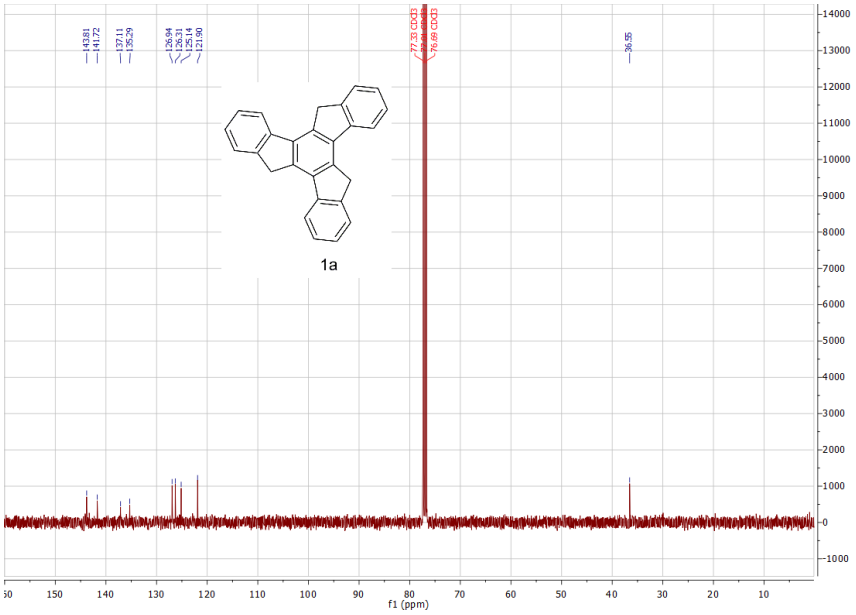

Figure A2. *¹³ C NMR spectrum of compound 1a*

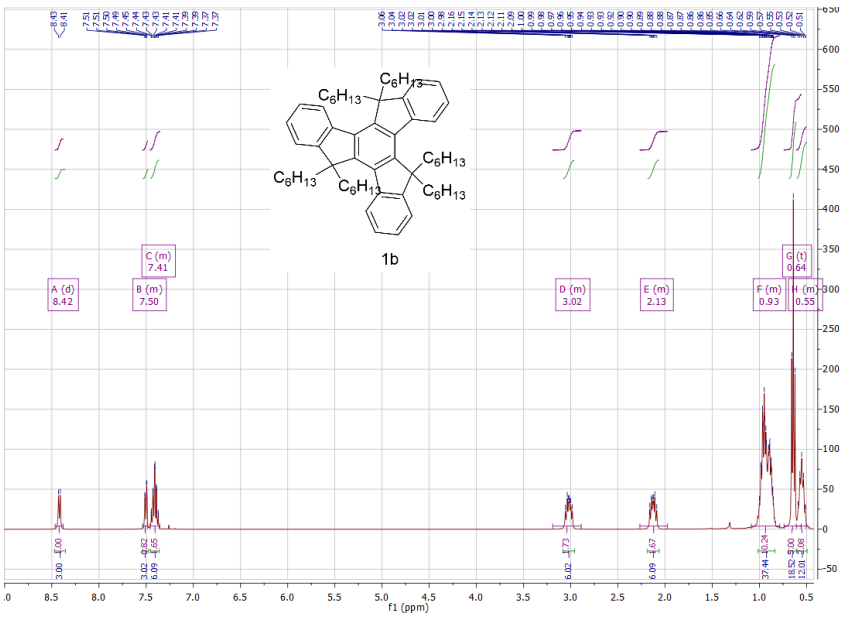

Figure A3. *¹H NMR spectrum of compound 1b*

Appendix

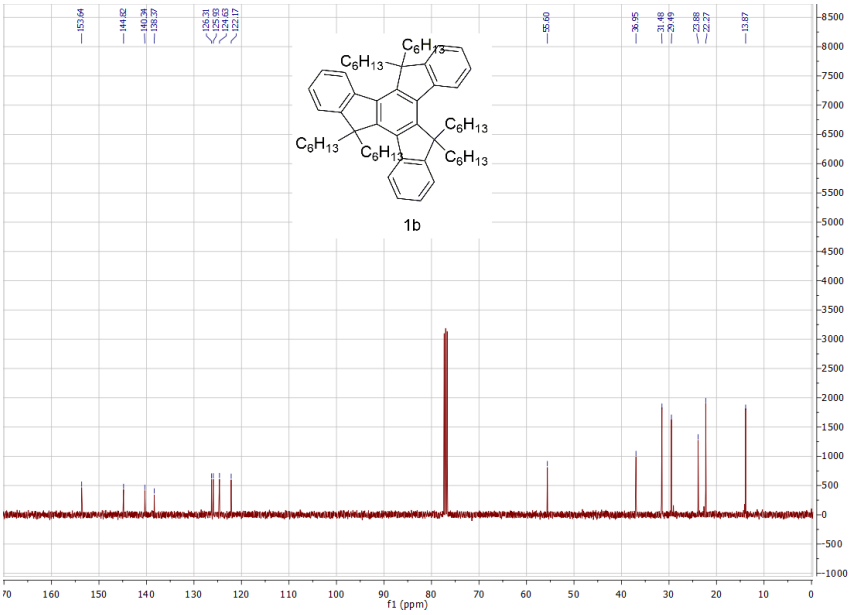

Figure A4. *^{13}C NMR spectrum of compound 1b*

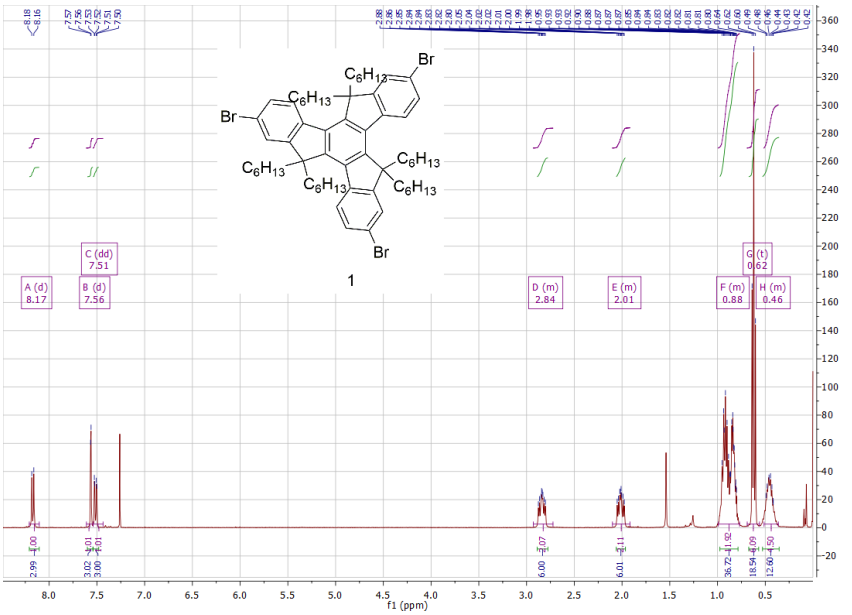

Figure A5. *^{1}H NMR spectrum of compound 1*

Appendix

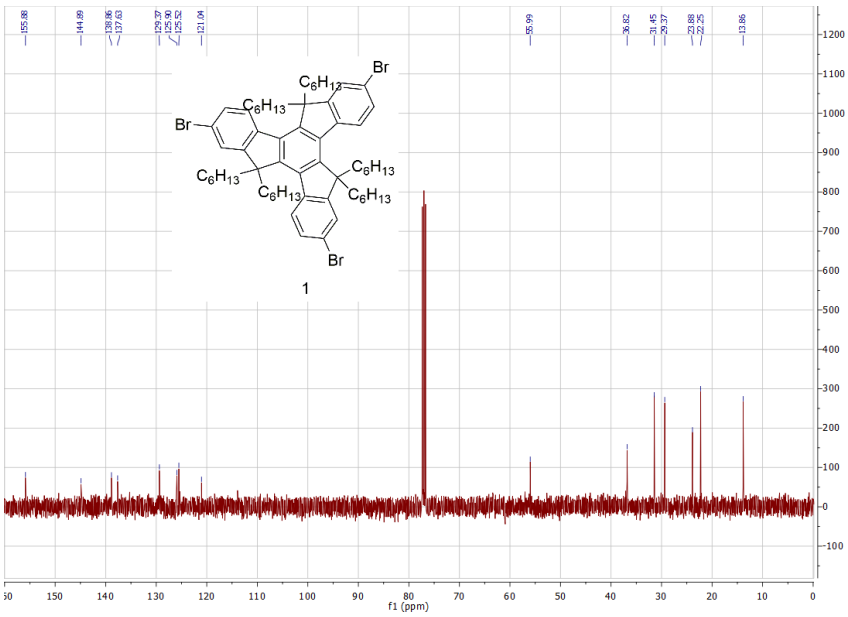

Figure A6. *^{13}C NMR spectrum of compound 1*

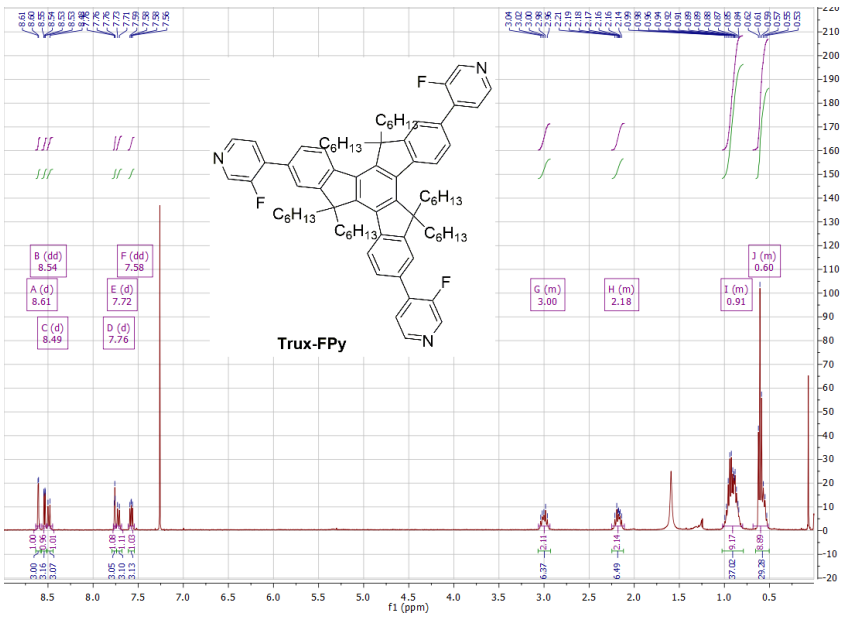

Figure A7. *^{1}H NMR spectrum of compound Trux-FPy*

Appendix

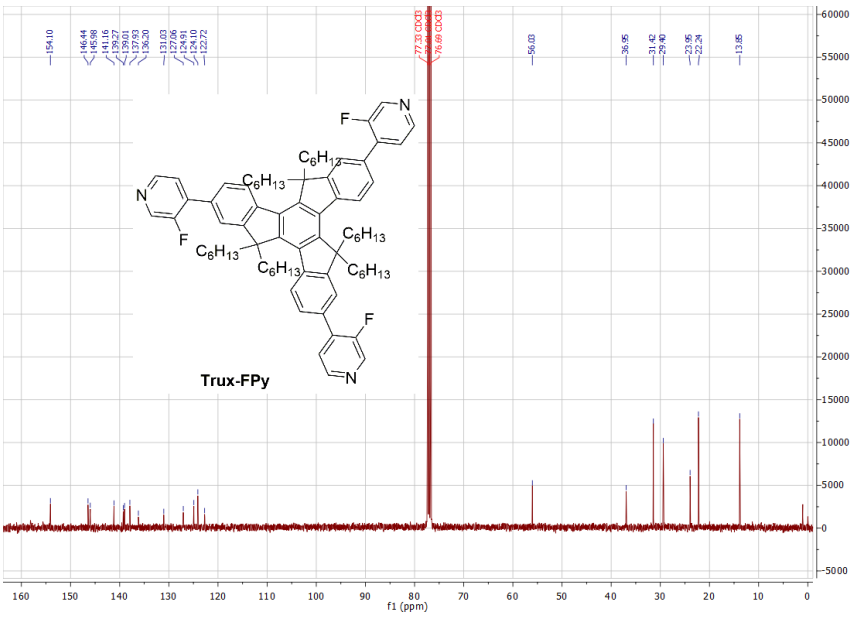

Figure A8. *^{13}C NMR spectrum of compound Trux-FPy*

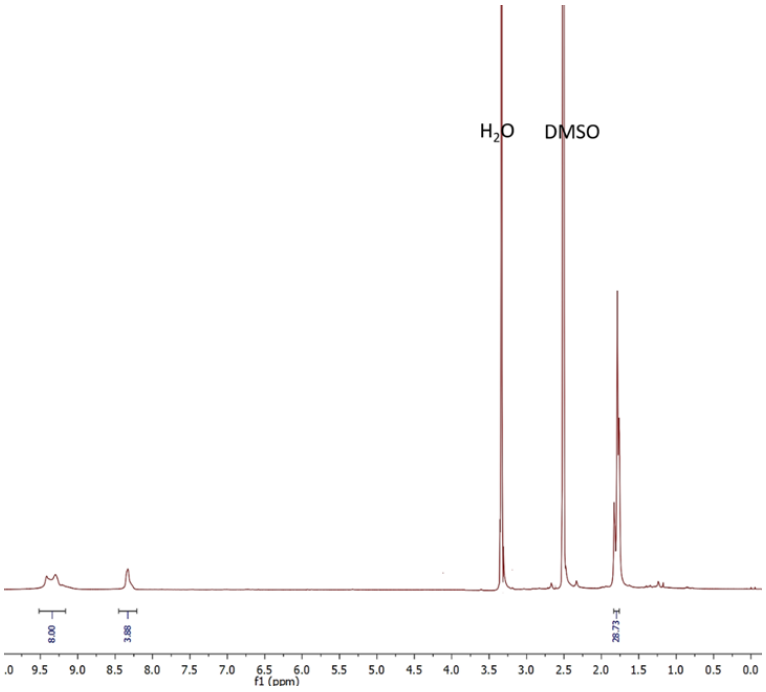

Figure A9. *^{1}H NMR of TT1*

Appendix

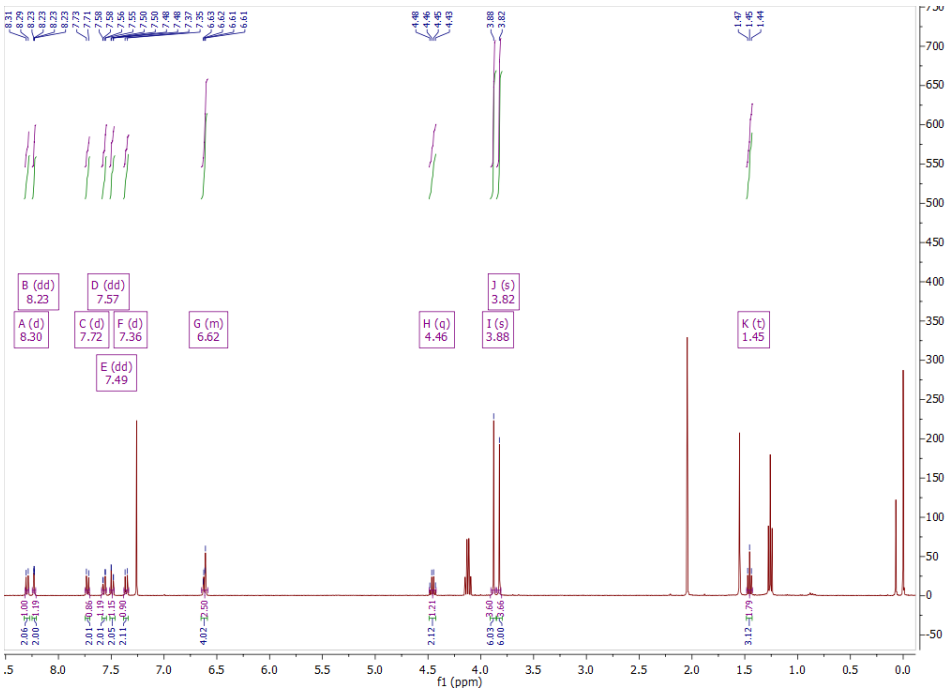

Figure A10. *¹H NMR spectrum of EADR03-COOEt*

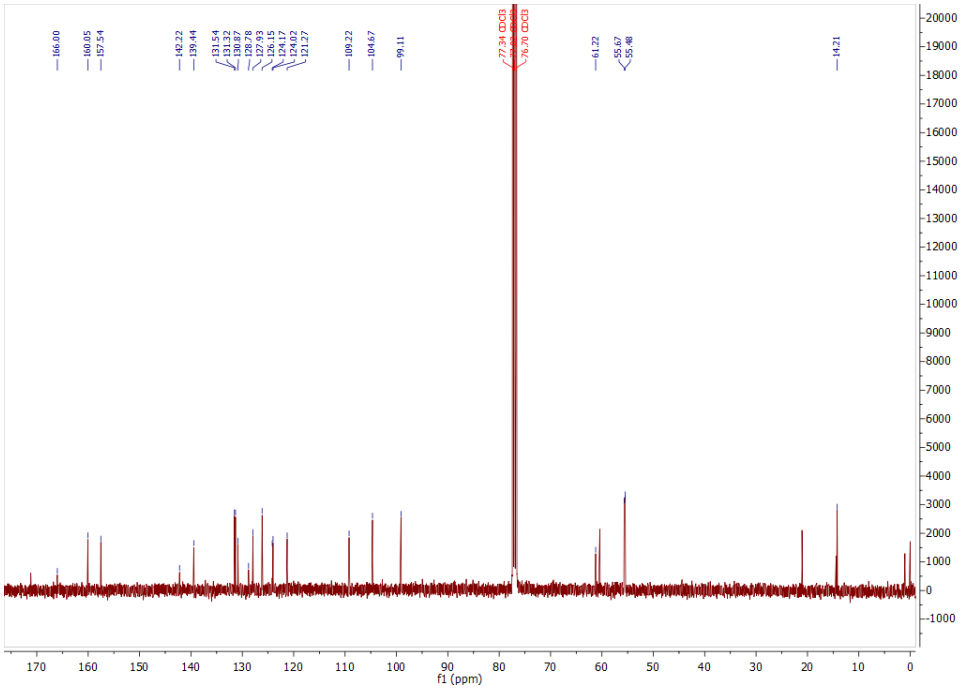

Figure A11. *¹³C NMR spectrum of EADR03-COOEt*

Appendix

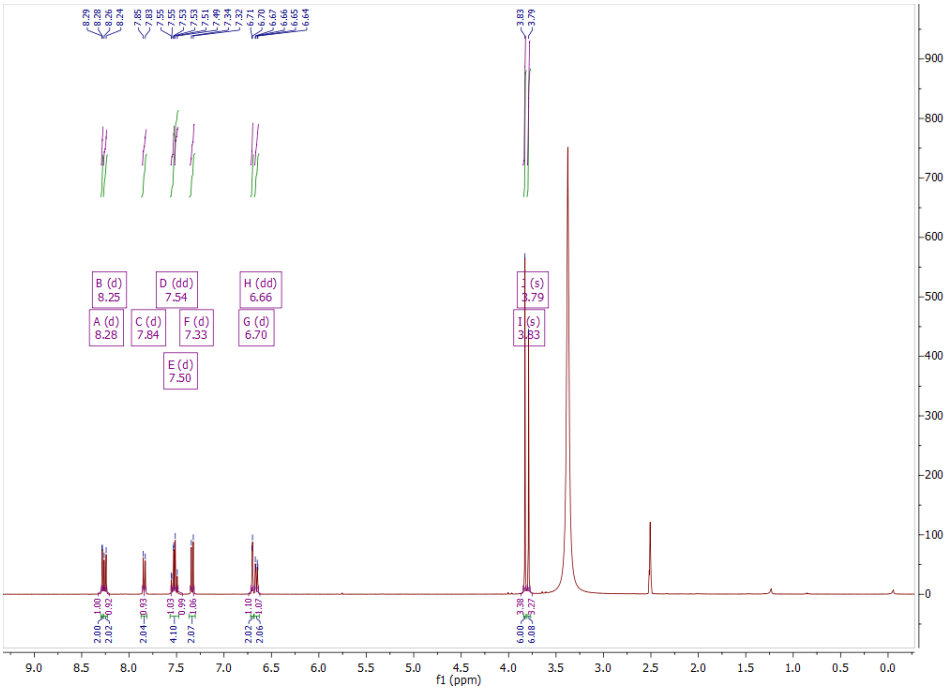

Figure A12. *[1]H NMR spectrum of EADR03*

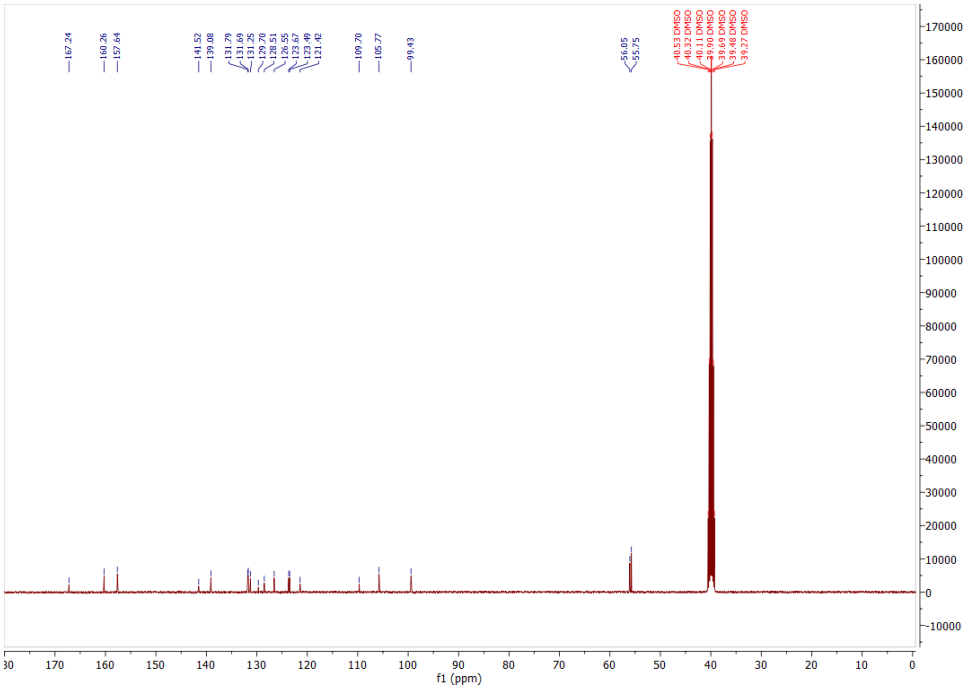

Figure A13. *[13]C NMR spectrum of EADR03*

Appendix

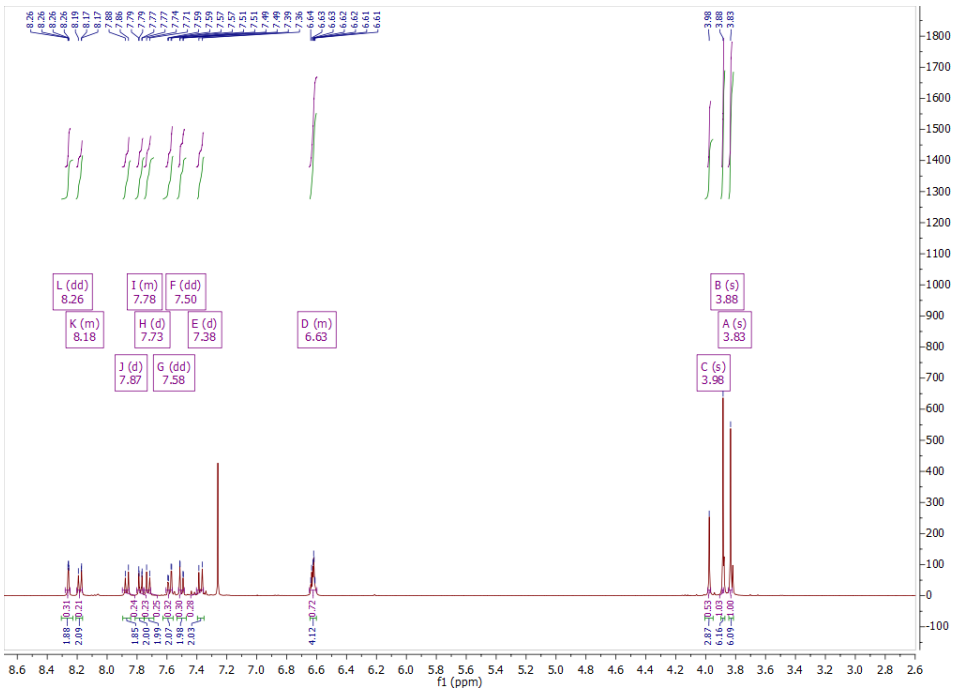

Figure A14. *[1]H NMR spectrum of EADR04-COOMe*

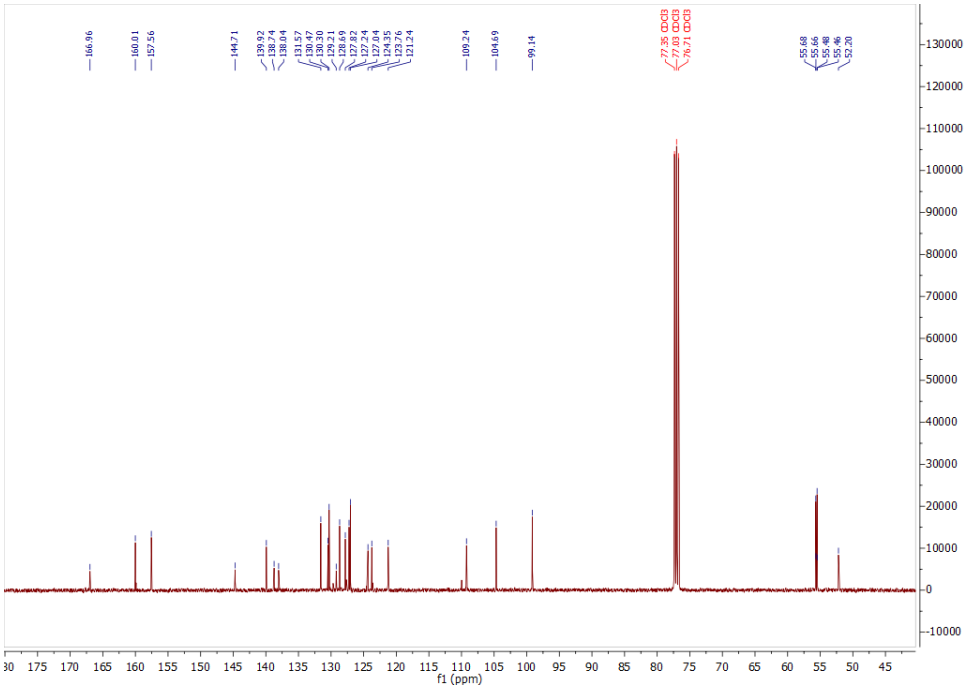

Figure A15. *[13]C NMR spectrum of EADR04-COOMe*

Appendix

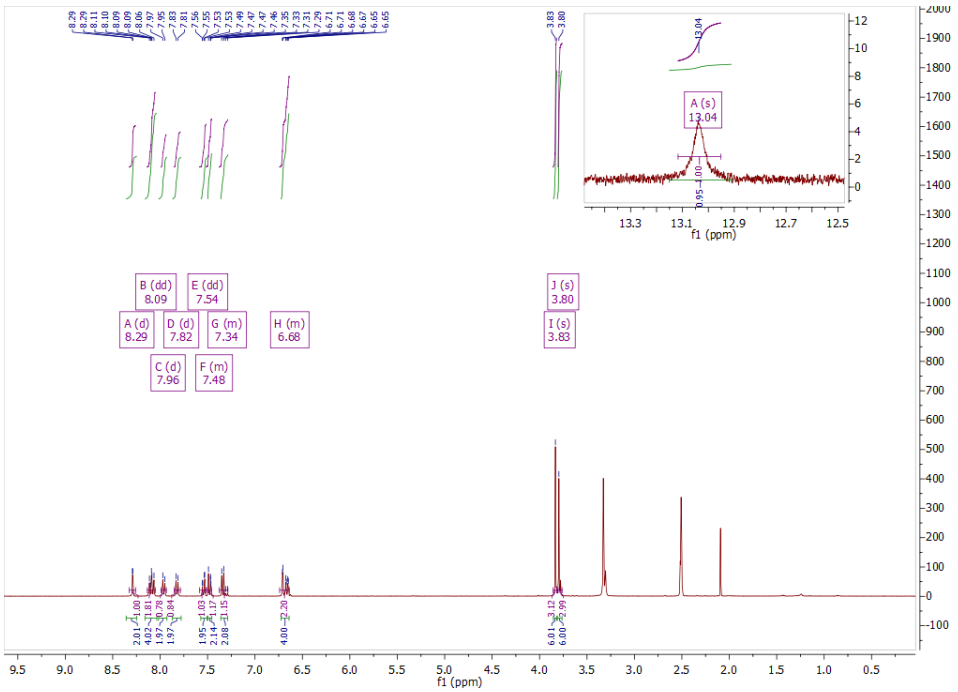

Figure A16. *[1]H NMR spectrum of EADR04*

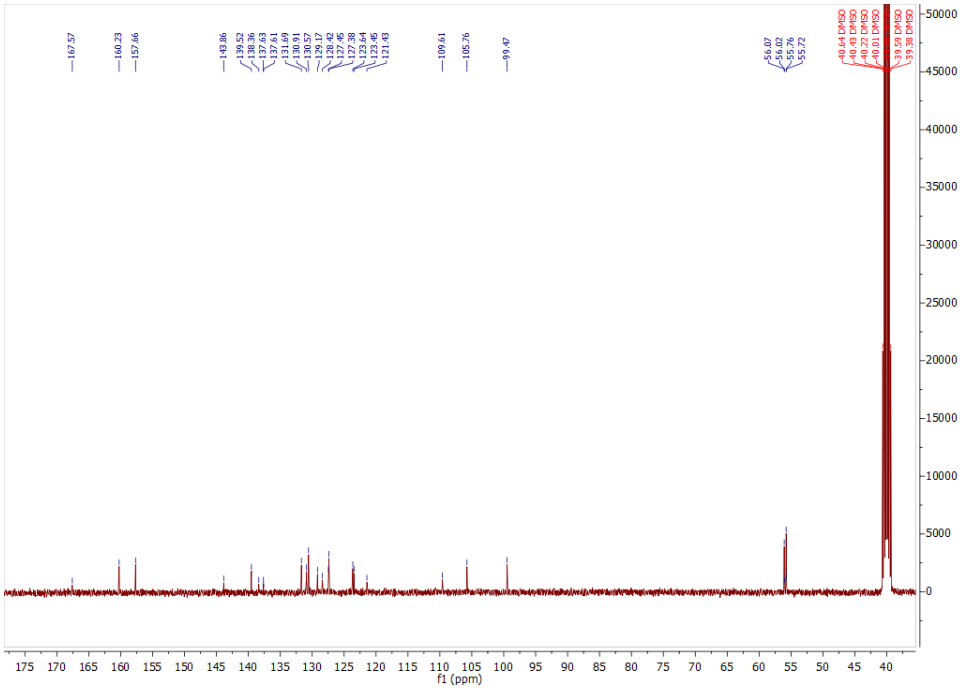

Figure A17. *[13]C NMR spectrum of EADR04*

Appendix

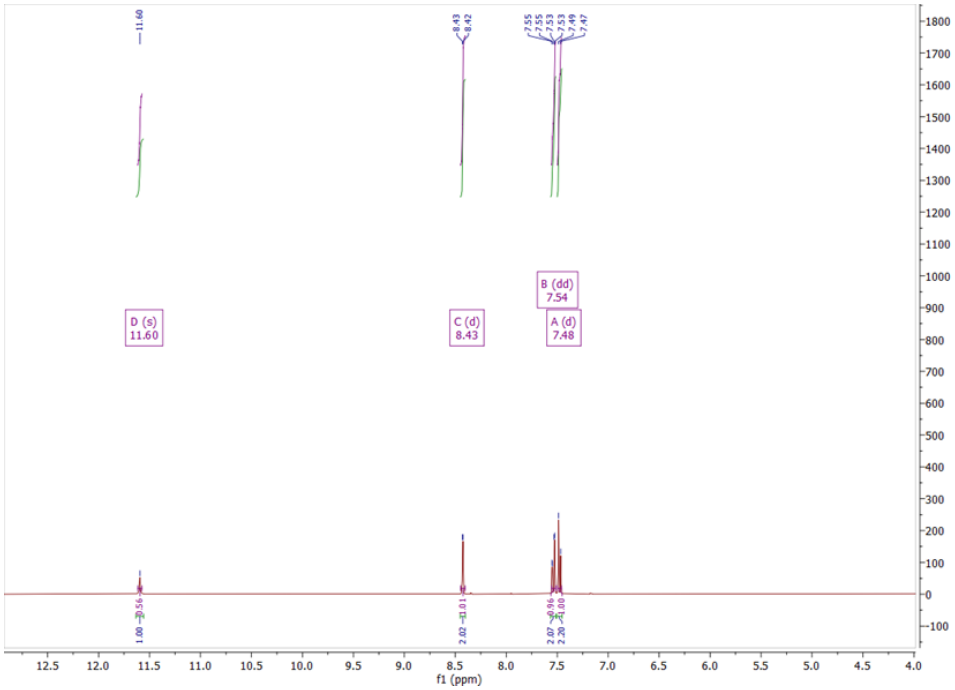

Figure A18. *^{1}H NMR of 3,6-Dibromo-9H-Carbazole*

Appendix

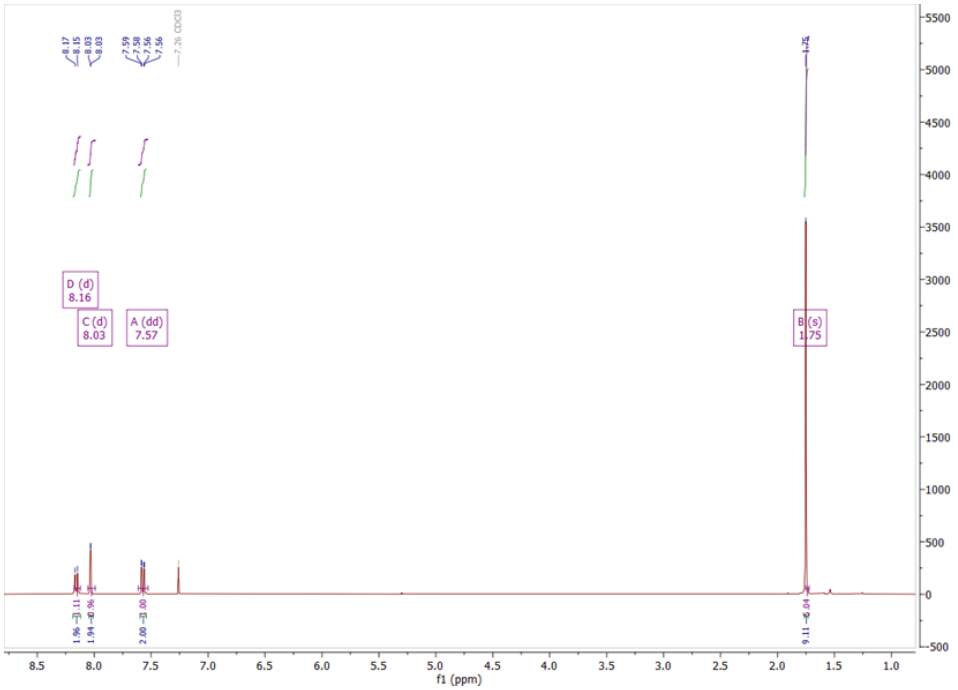

Figure A19. *^{1}H NMR of tert-butyl 3,6-dibromo-9h-carbazole-9-carboxylate (Carbazole-Boc)*

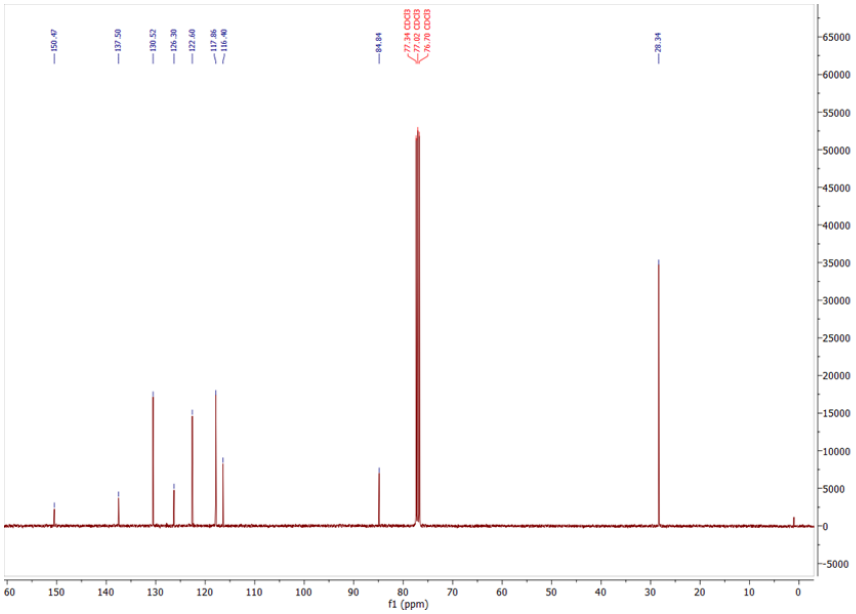

Figure A20. *^{13}C NMR of tert-butyl 3,6-dibromo-9h-carbazole-9-carboxylate (Carbazole-Boc)*

Appendix

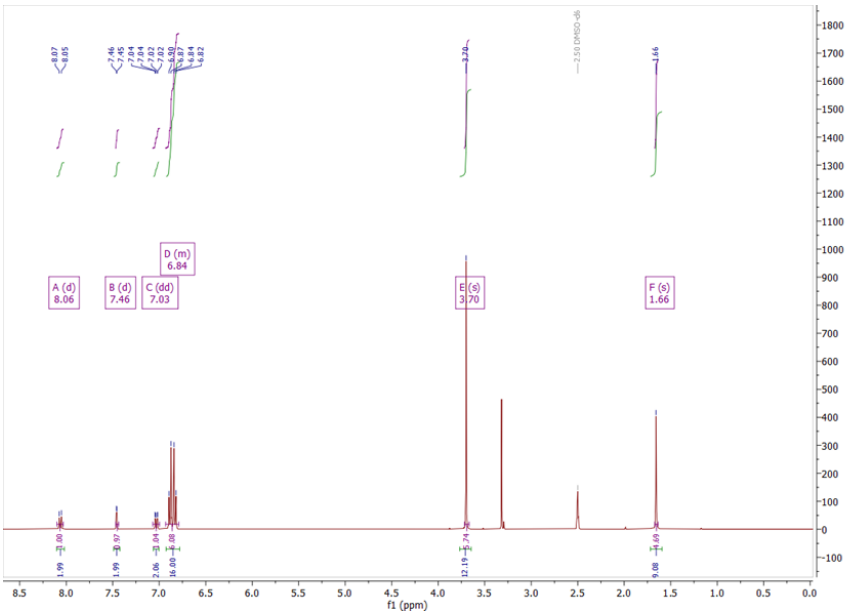

Figure A21. *[1]H NMR of tert-butyl 3,6-bis(bis(4-methoxyphenyl)amino)-9h-carbazole-9H-carboxylate (Carbazole-Boc-DAMP)*

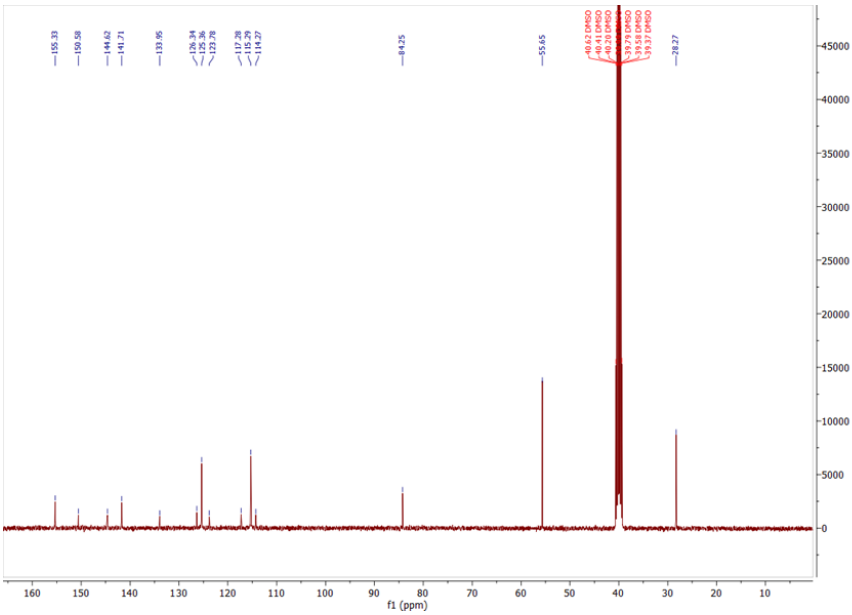

Figure A22. *[13]C NMR of tert-butyl 3,6-bis(bis(4-methoxyphenyl)amino)-9h-carbazole-9H-carboxylate (Carbazole-Boc-DAMP)*

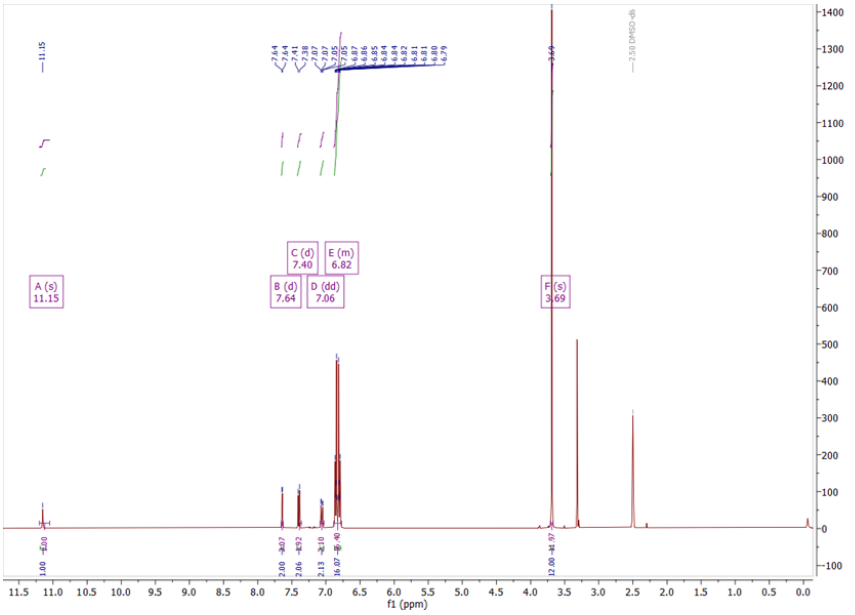

Figure A23. *[1]H NMR of N3,N3,N6,N6-tetrakis(4-methoxyphenyl)-9H-carbazole-3,6-diamine (Carbazole-DAMP)*

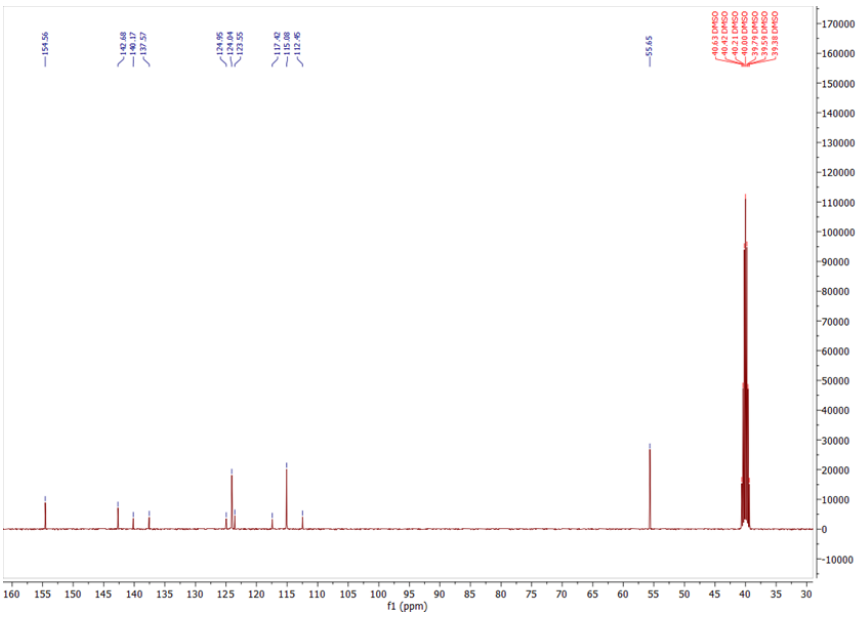

Figure A24. *[13]C NMR of N3,N3,N6,N6-tetrakis(4-methoxyphenyl)-9H-carbazole-3,6-diamine (Carbazole-DAMP)*

Appendix

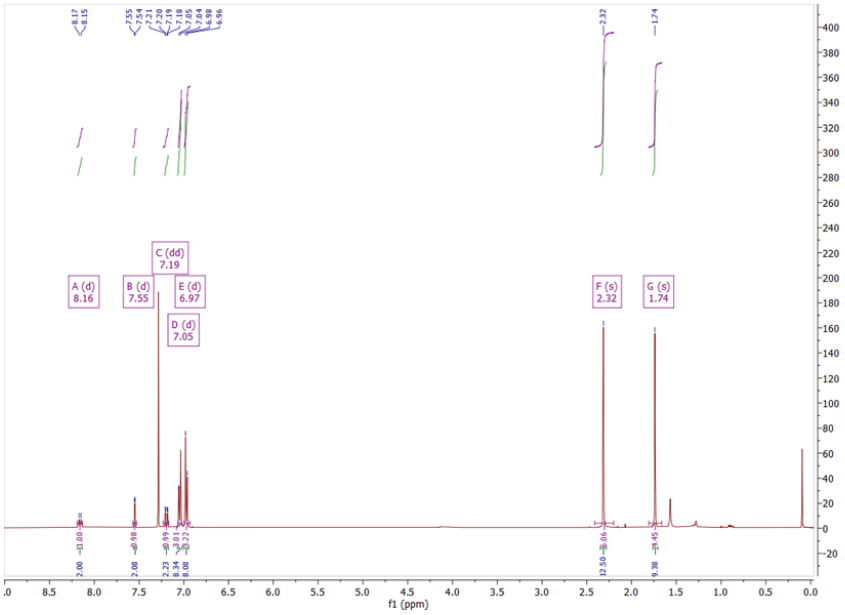

Figure A25. *[1]H NMR of tert-butyl 3,6-bis(di-p-tolylamino)-9H-carbazole-9-carboxylate (Carbazole-Boc-DAP)*

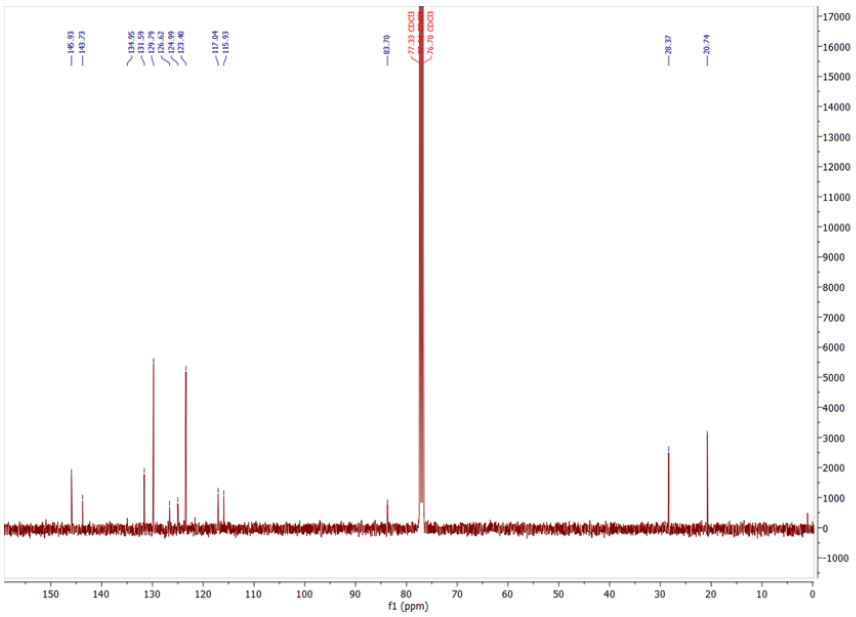

Figure A26. *[13]C NMR of tert-butyl 3,6-bis(di-p-tolylamino)-9H-carbazole-9-carboxylate (Carbazole-Boc-DAP)*

Appendix

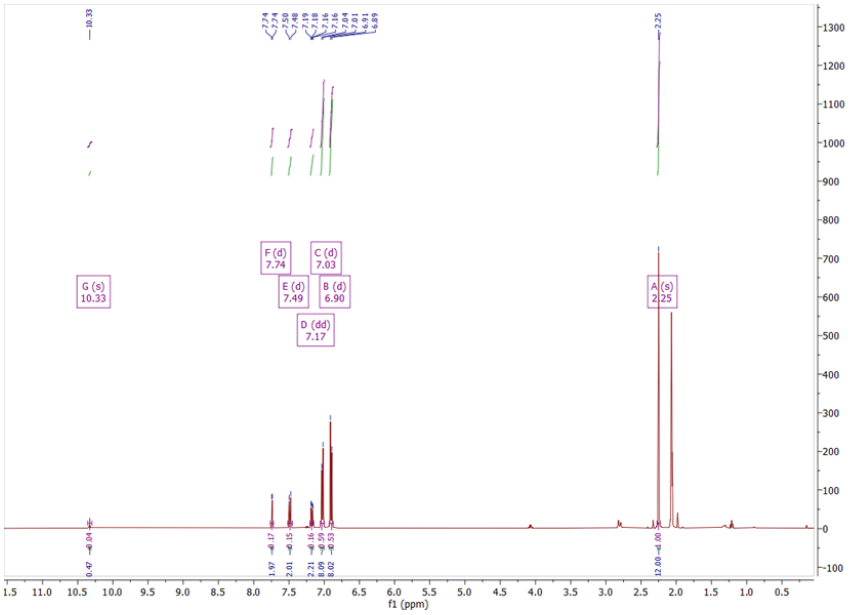

Figure A27. *^{1}H NMR of N^{3},N^{3},N^{6},N^{6}-tetra-p-tolyl-9H-carbazole-3,6-diamine (Carbazole-DAP)*

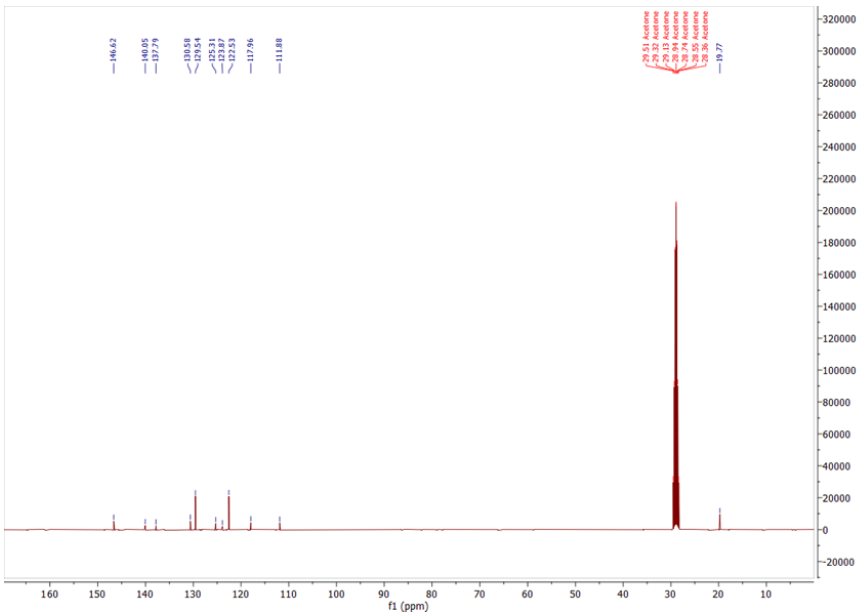

Figure A28. *^{13}C NMR of N^{3},N^{3},N^{6},N^{6}-tetra-p-tolyl-9H-carbazole-3,6-diamine (Carbazole-DAP)*

Appendix

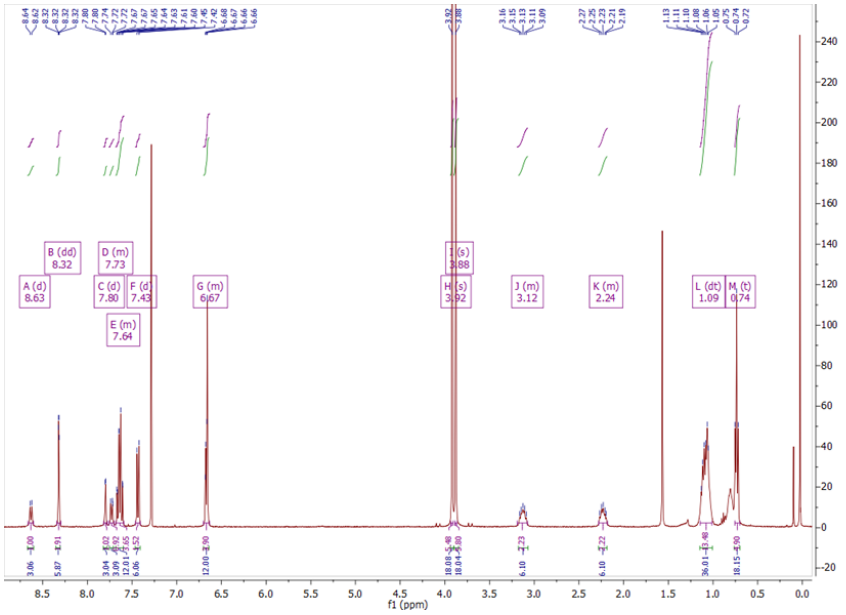

Figure A29. *^{1}H NMR spectrum of EADR01*

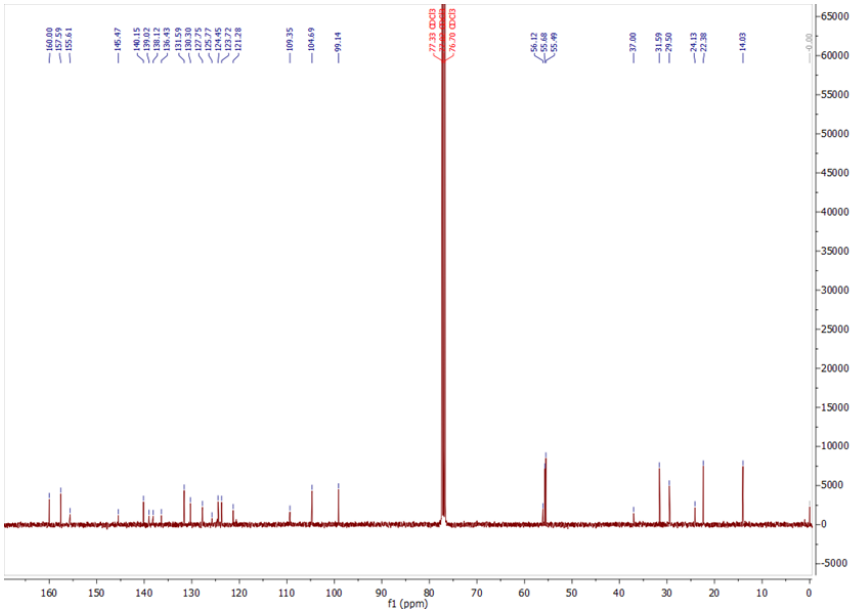

Figure A30. *^{13}C NMR spectrum of EADR01*

Appendix

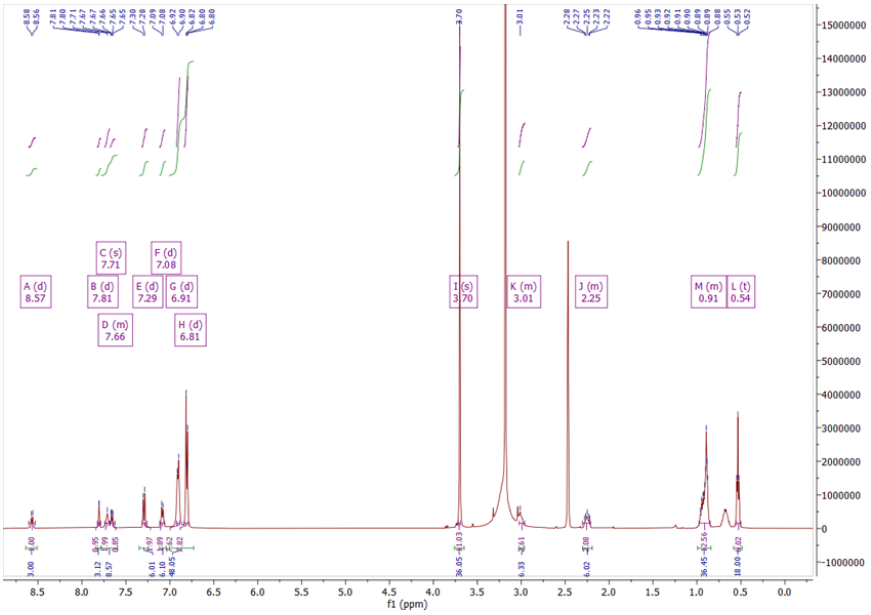

Figure A31. *^{1}H NMR of 9,9',9''-(5,5,10,10,15,15-hexahexyl-10,15-dihydro-5H-diindeno[1,2-a:1',2'-c]fluorene-2,7,12-triyl)tris(N^3,N^3,N^6,N^6-tetrakis(4-methoxyphenyl)-9H-carbazole-3,6-diamine) (EA01)*

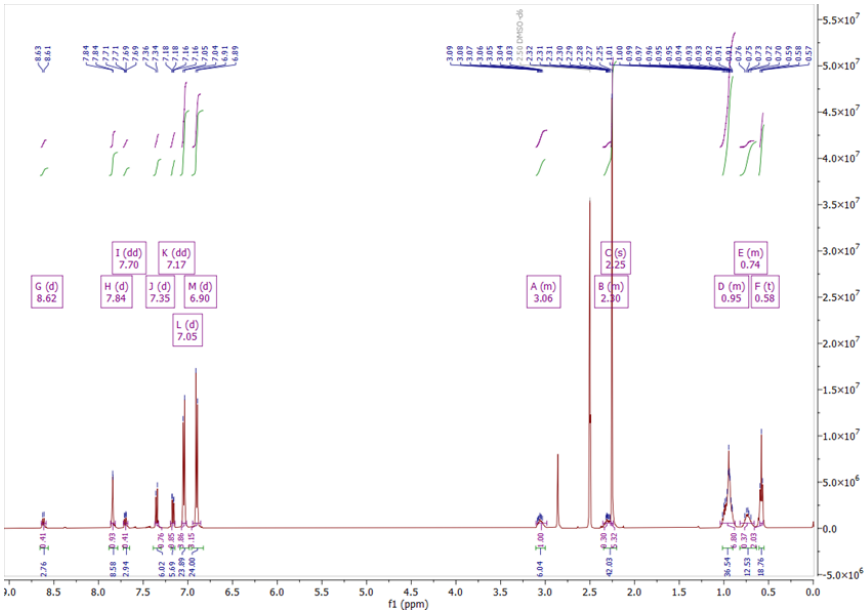

Figure A32. *¹H NMR of 9,9',9''-(5,5,10,10,15,15-hexahexyl-10,15-dihydro-5H-diindeno[1,2-a:1',2'-c]fluorene-2,7,12-triyl)tris(N³,N³,N⁶,N⁶-tetra-p-tolyl-9H-carbazole-3,6-diamine) (EA02)*

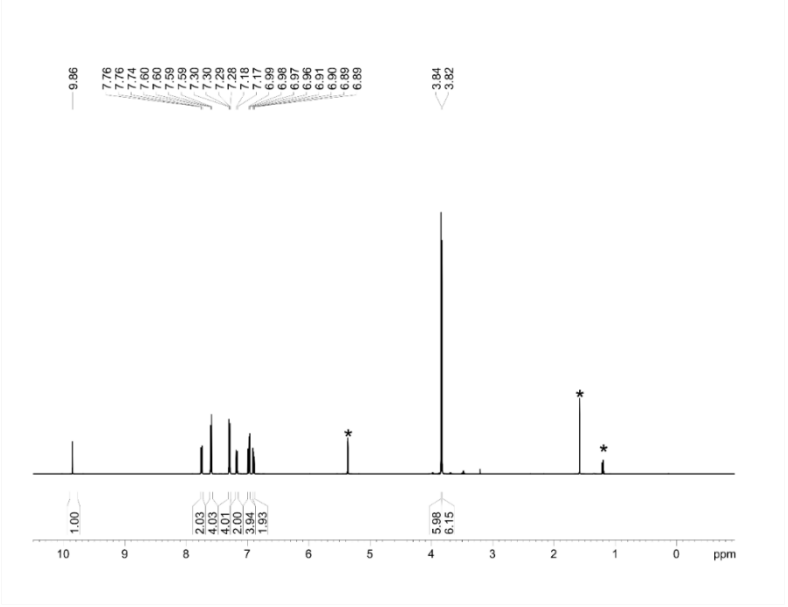

Figure A33. *¹H NMR spectra of RC25-CHO in CD_2Cl_2. *Residual solvent peaks.*

Appendix

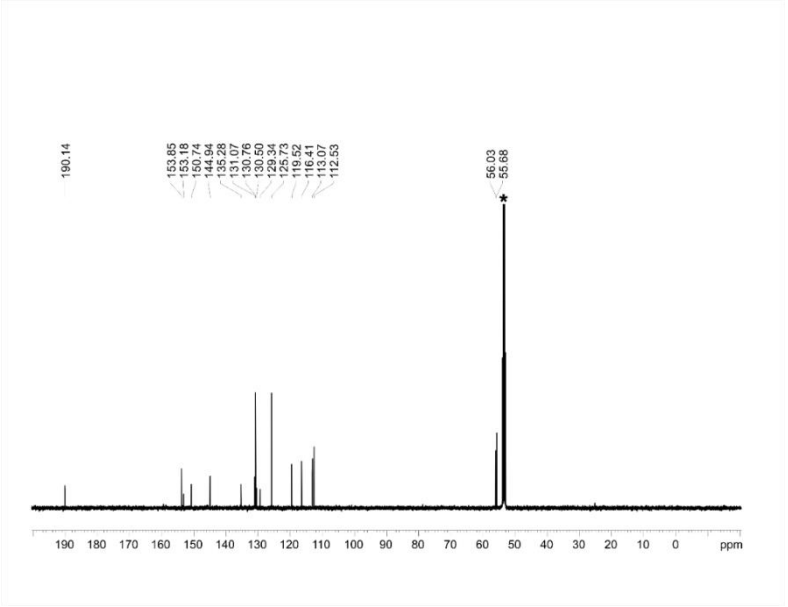

Figure A34. *^{13}C NMR spectra of RC25-CHO in CD_2Cl_2. *Residual solvent peaks.*

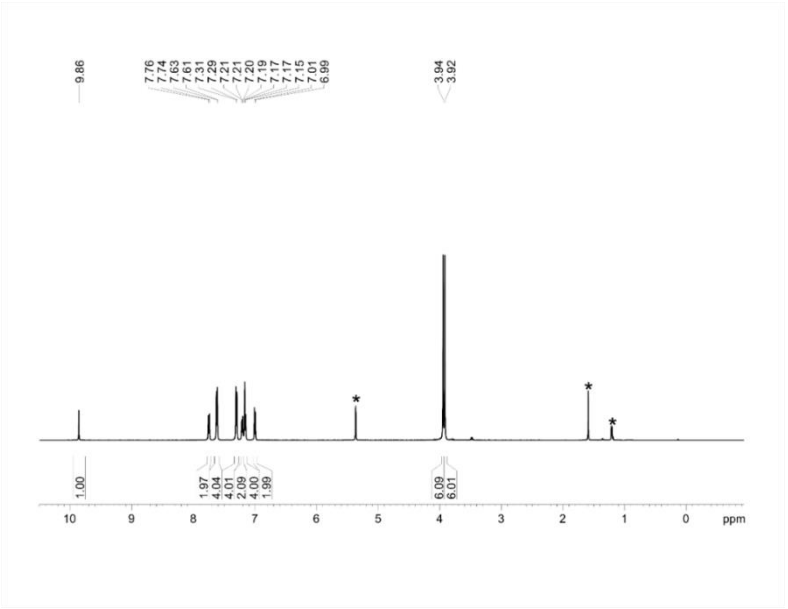

Figure A35. *^{1}H NMR spectra of RC34-CHO in CD_2Cl_2. *Residual solvent peaks.*

Appendix

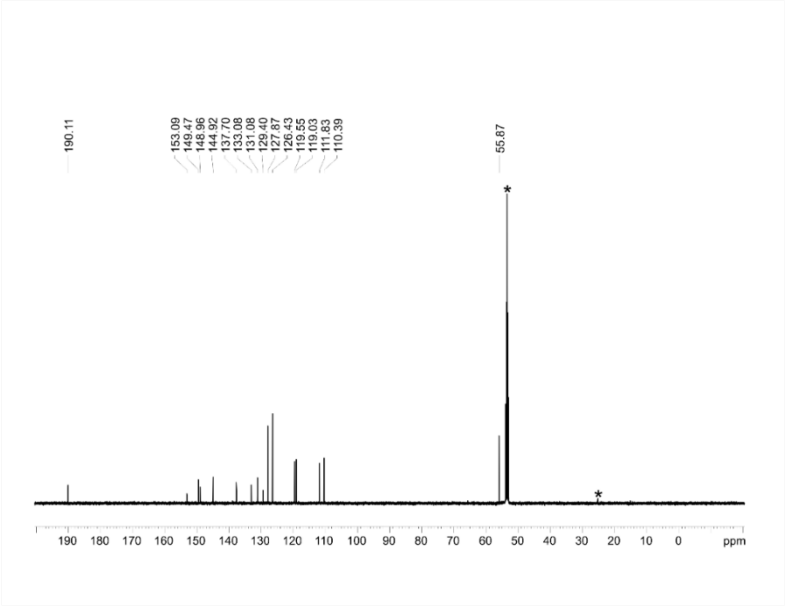

Figure A36. *^{13}C NMR spectra of RC34-CHO in CD_2Cl_2. *Residual solvent peaks.*

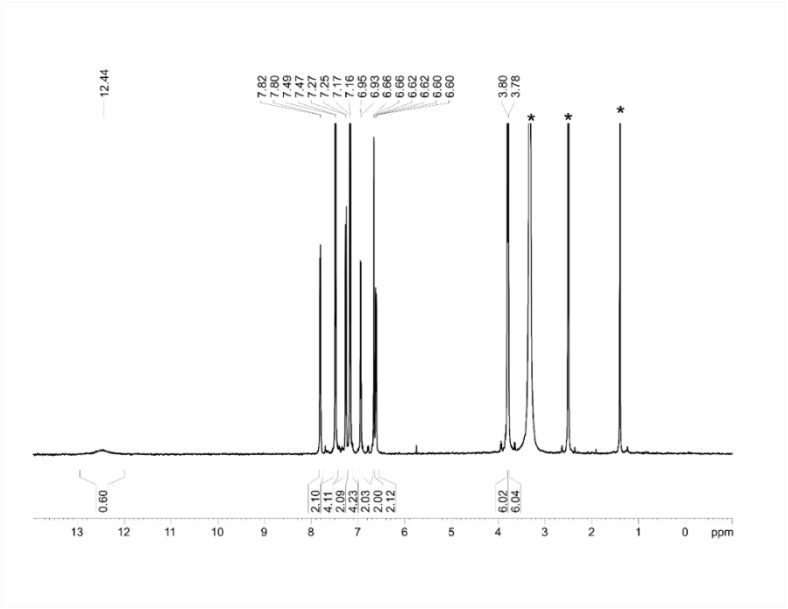

Figure A37. *^{1}H NMR spectra of RC24 in DMSO-d_6. *Residual solvent peaks.*

Appendix

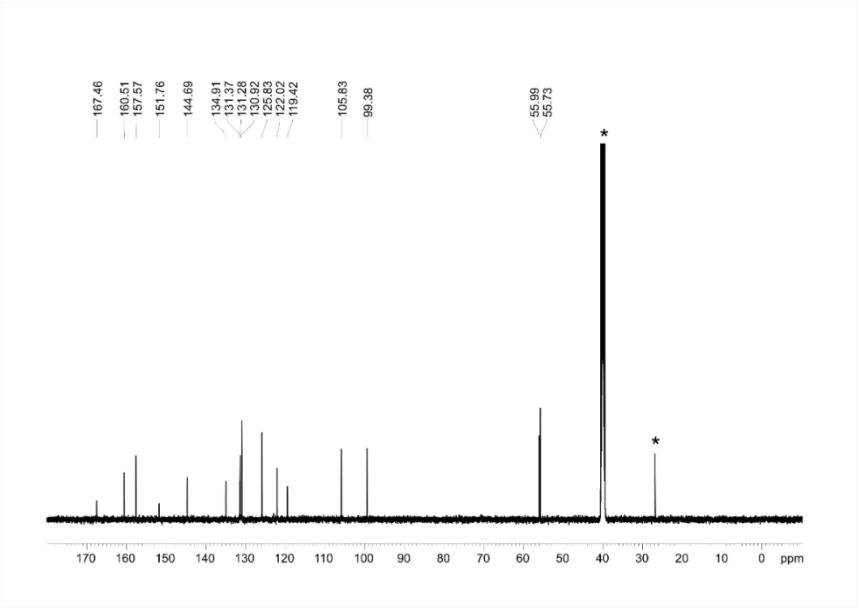

Figure A38. *^{13}C NMR spectra of RC24 in DMSO-d6. *Residual solvent peaks.*

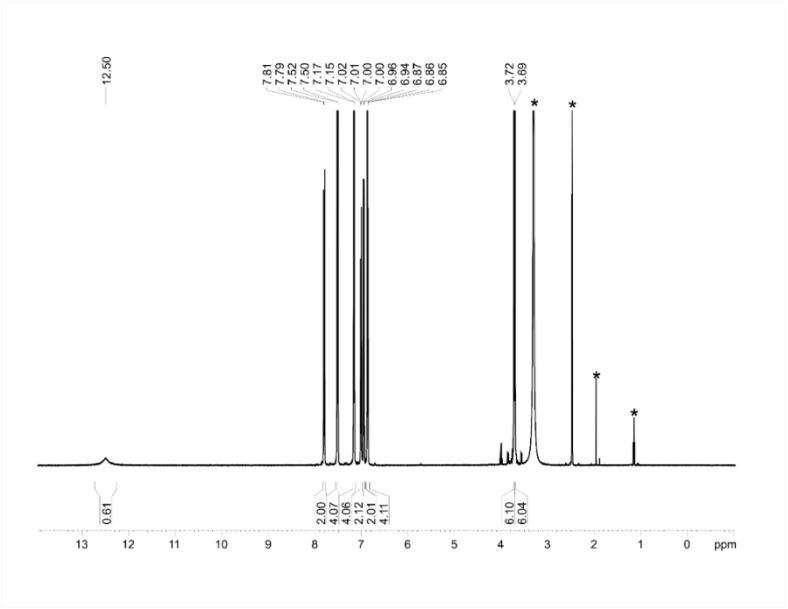

Figure A39. *^{1}H NMR spectra of RC25 in DMSO-d$_6$. *Residual solvent peaks.*

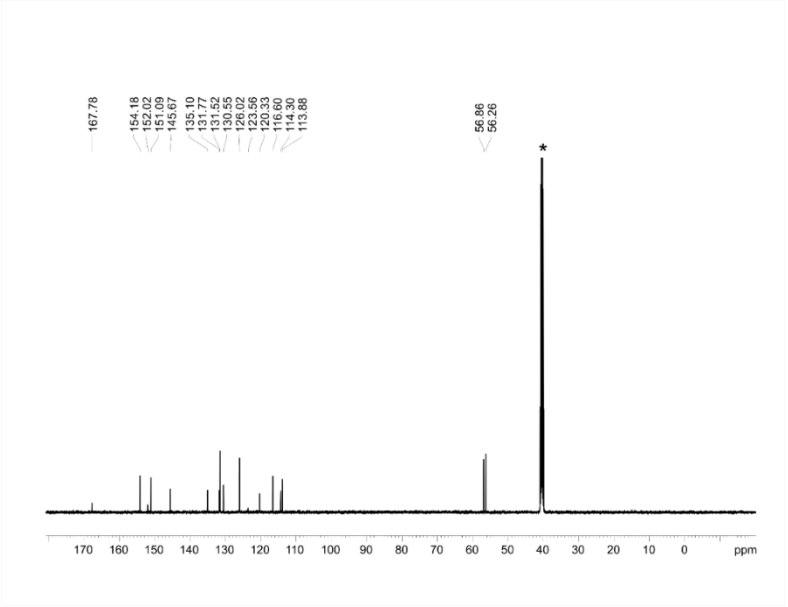

Figure A40. *^{13}C NMR spectra of RC25 in DMSO-d_6. *Residual solvent peaks.*

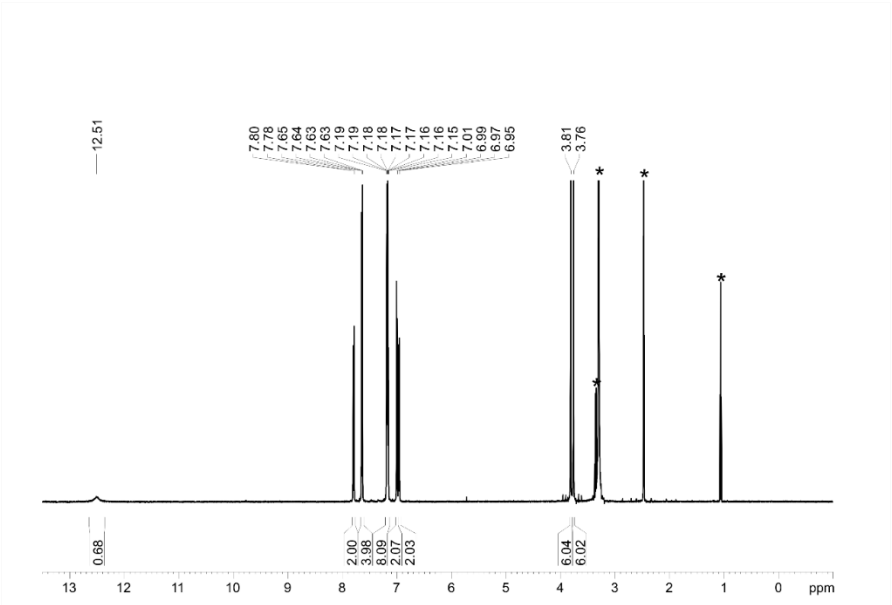

Figure A41. *^{1}H NMR spectra of RC34 in DMSO-d_6. *Residual solvent peaks.*

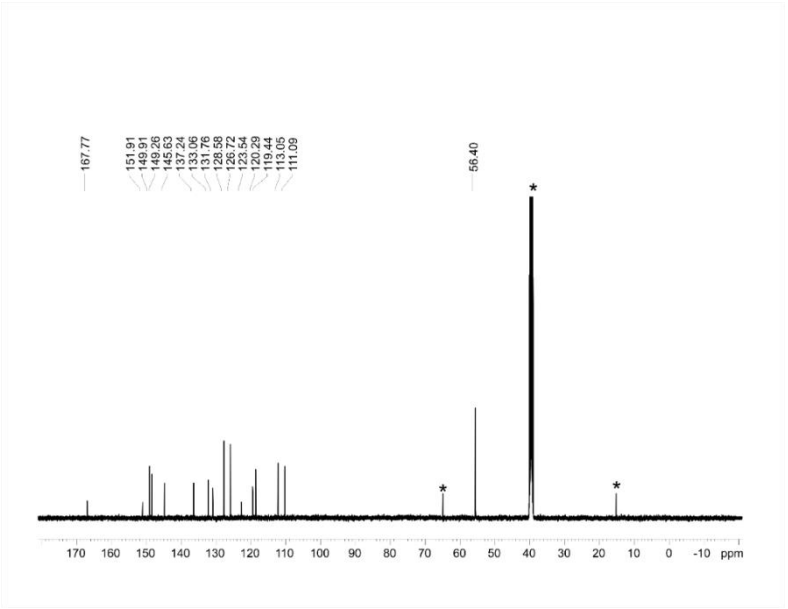

Figure A42. *^{13}C NMR spectra of RC34 in DMSO-d_6. *Residual solvent peaks.*

MS Spectra

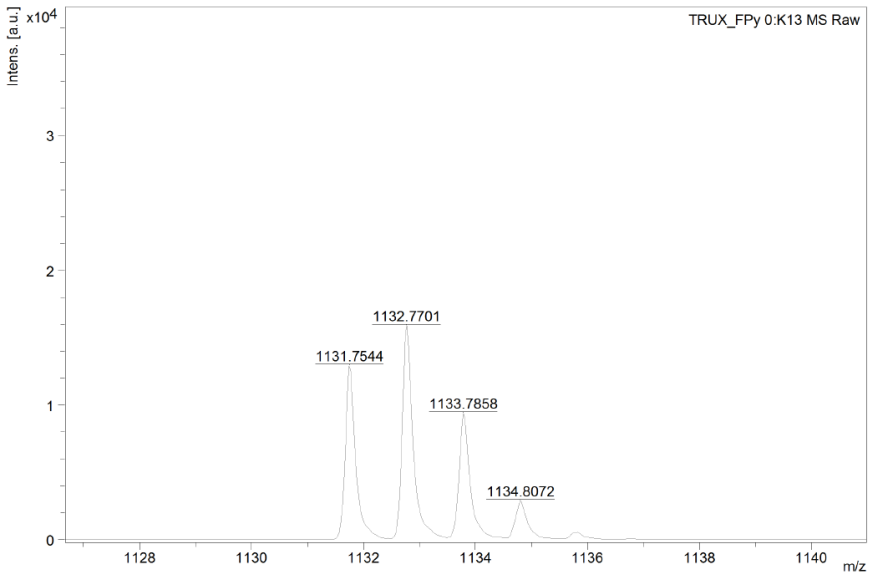

Figure A43. *MALDI-TOF-MS spectra in wide and narrow mass ranges of Trux-FPy*

Appendix

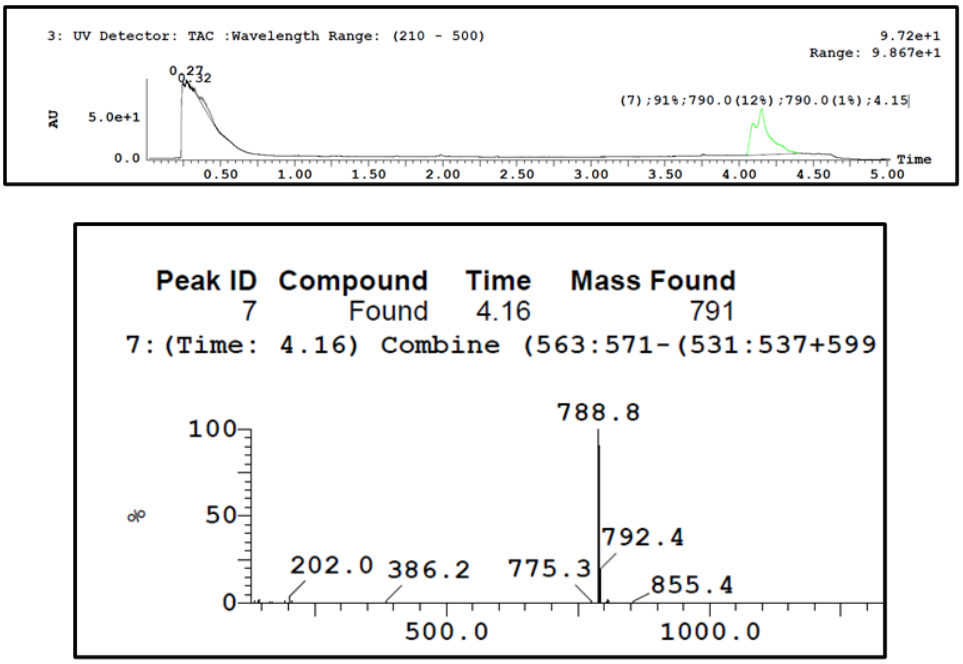

Figure A44. *LC-Mass of TT1 in ACN*

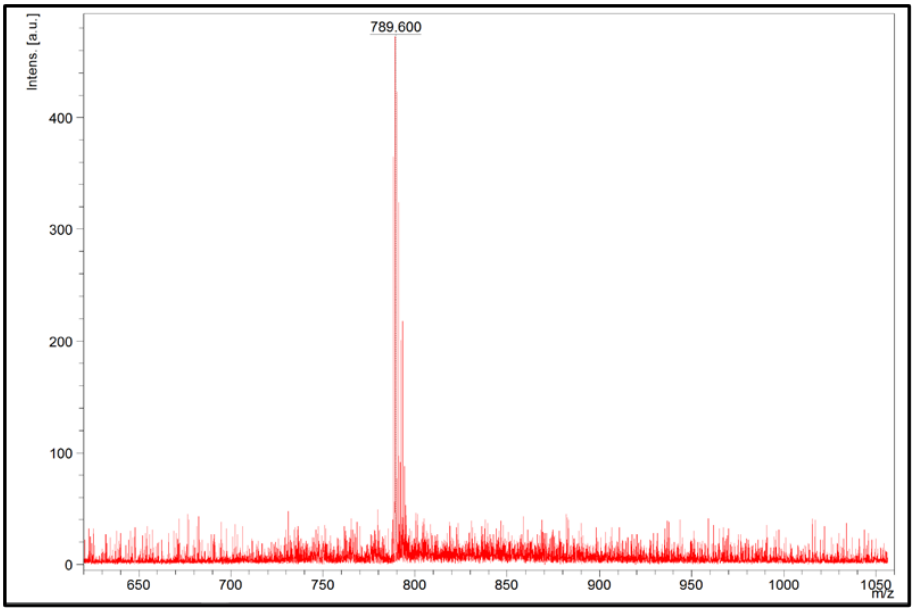

Figure A45. *The MALDI-TOF-MS of TT1 on ground steel plate.*

Appendix

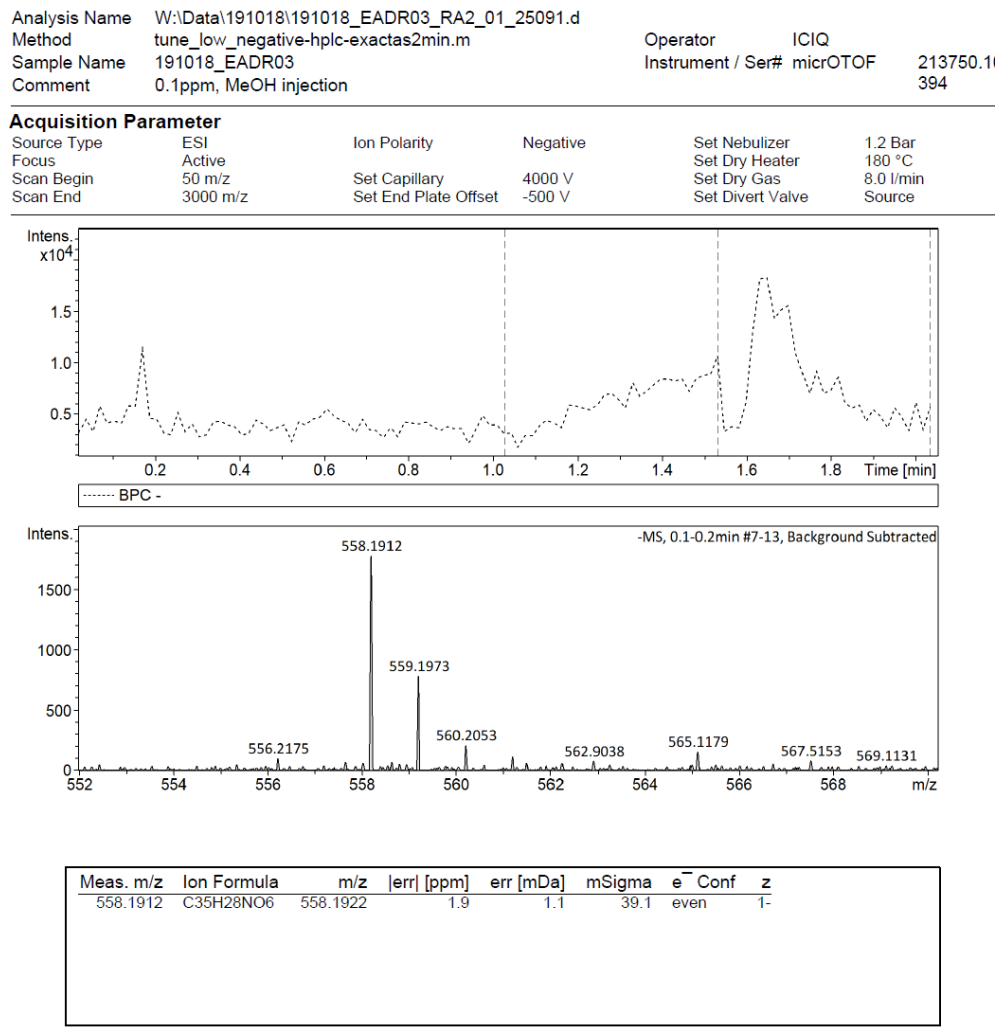

Figure A46. *ESI-MS of EADR03*

Appendix

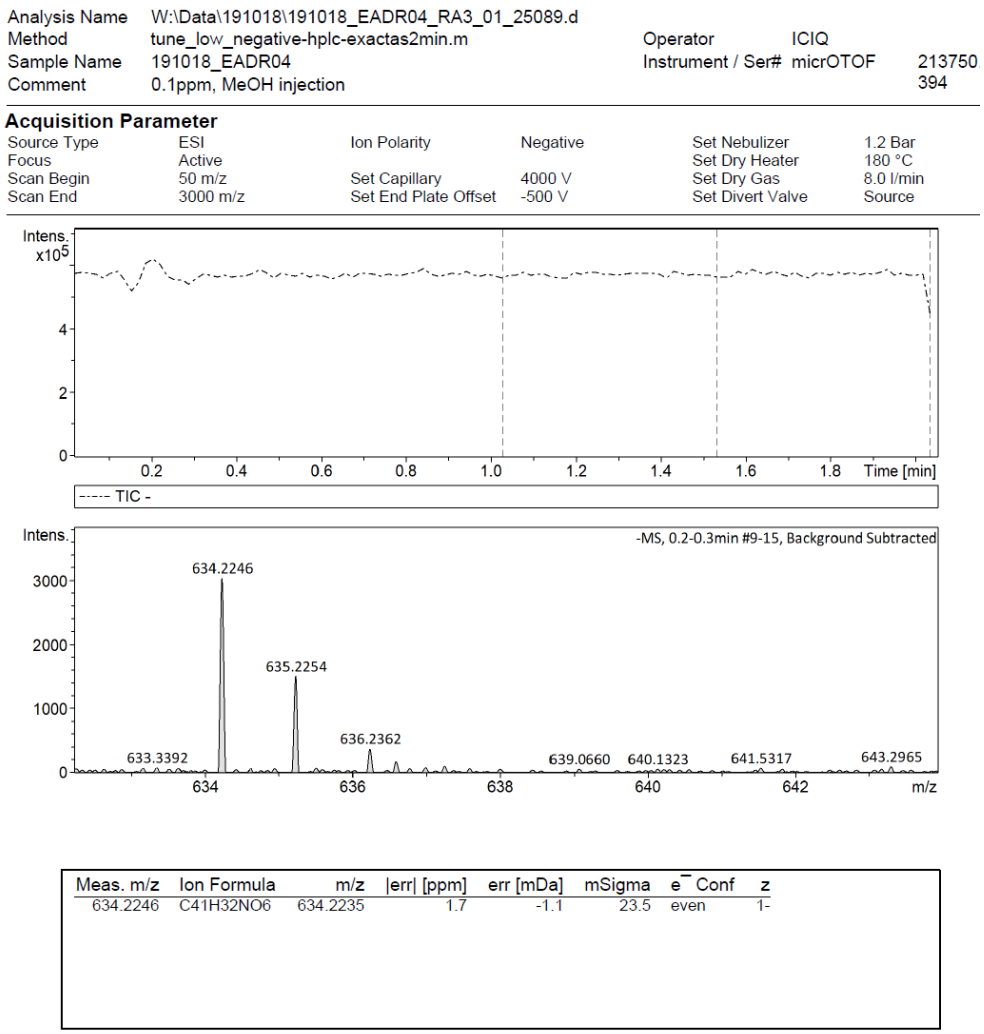

Figure A47. *ESI-MS of EADR04*

Appendix

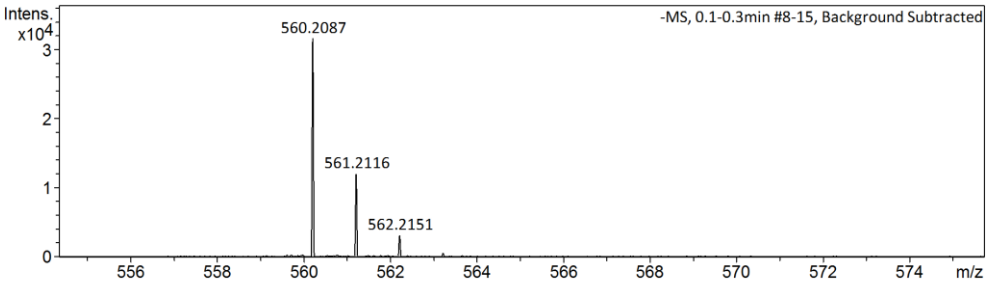

Meas. m/z	Ion Formula	m/z	|err| [ppm]	err [mDa]	mSigma	e¯ Conf	z
560.2087	C35H30NO6	560.2079	1.5	0.9	8.2	even	1-

Figure A48. *ESI-mass spectra of RC24*

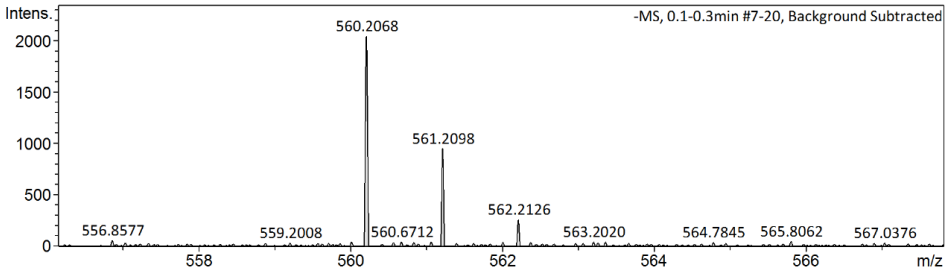

Meas. m/z	Ion Formula	m/z	|err| [ppm]	err [mDa]	mSigma	e¯ Conf	z
560.2068	C35H30NO6	560.2079	1.8	-1.0	43.6	even	1-

Figure A49. *ESI-mass spectra of RC25*

Appendix

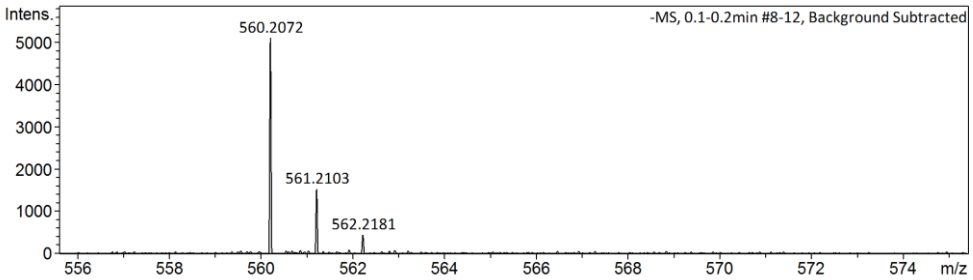

Meas. m/z	Ion Formula	m/z	|err| [ppm]	err [mDa]	mSigma	e¯ Conf	z
560.2072	C35H30NO6	560.2079	1.1	0.6	44.3	even	1-

Figure A50. *ESI-mass spectra of RC34*

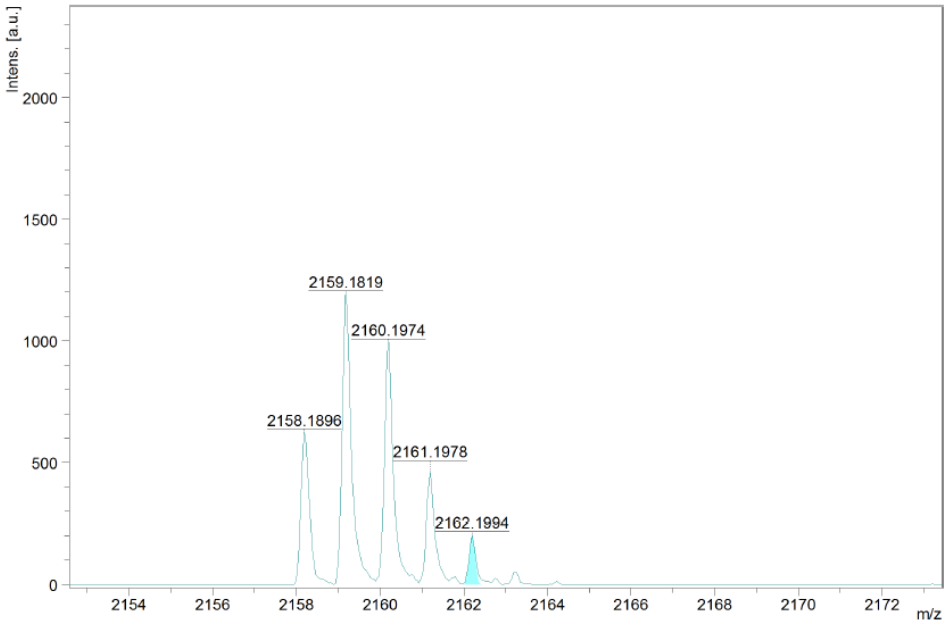

Figure A51. *MALDI-TOF-MS spectra in wide and narrow mass ranges of EADR01*

Appendix

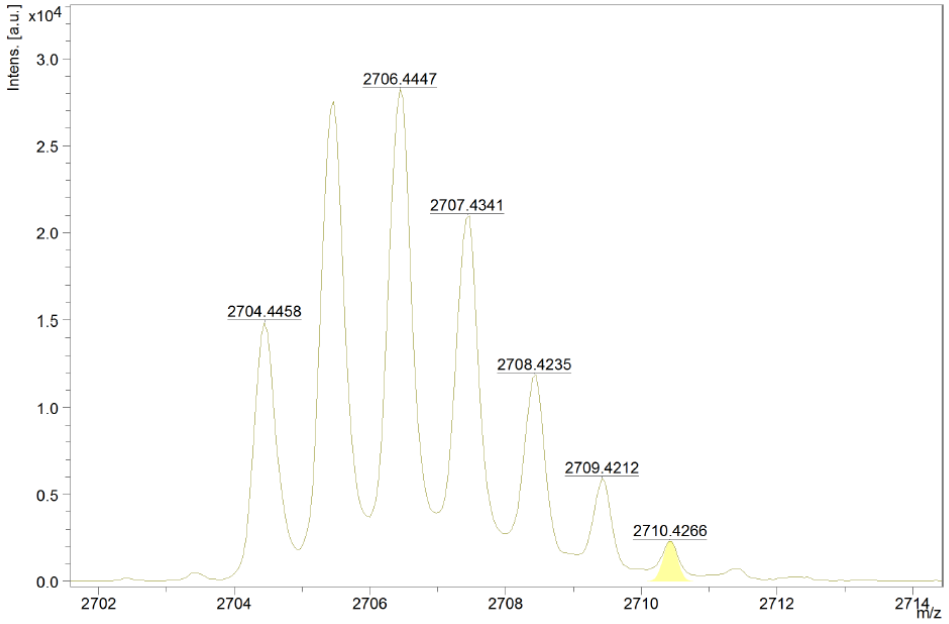

Figure A52. *MALDI-TOF-MS spectra in wide and narrow mass ranges of EA01*

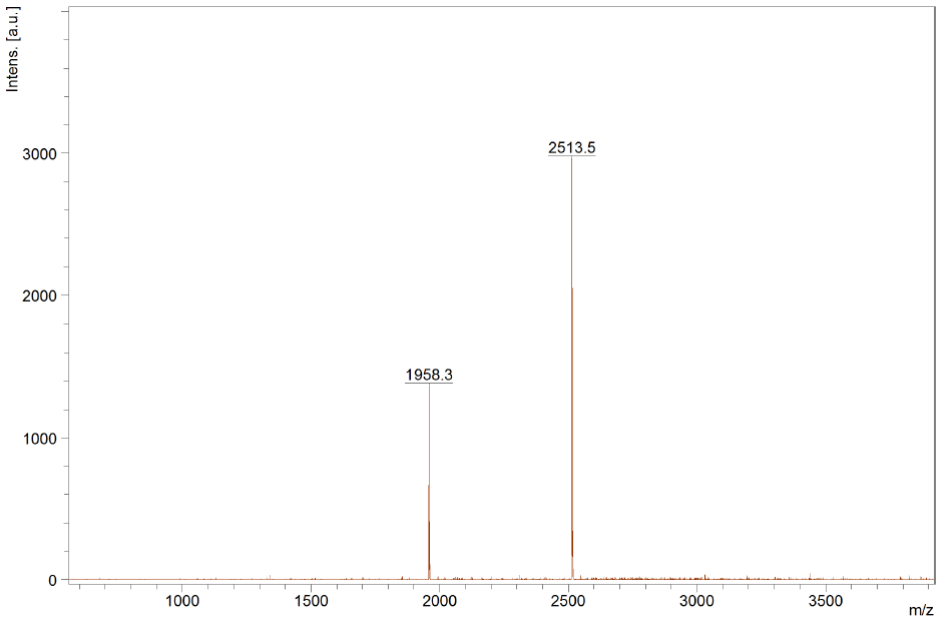

Figure A53. *MALDI-TOF-MS spectra in wide and narrow mass ranges of EA02*

Appendix

IR Spectra

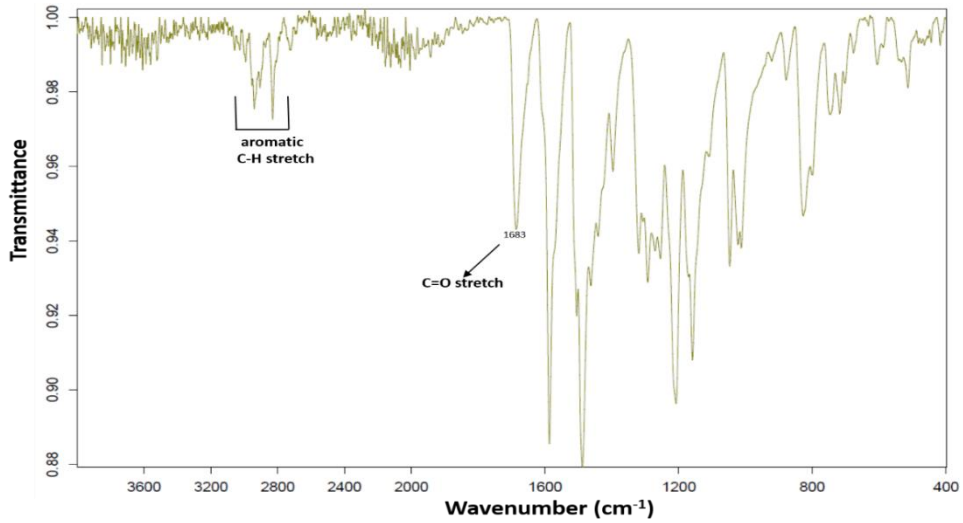

Figure A54. *ATR-IR spectrum of RC24-CHO*

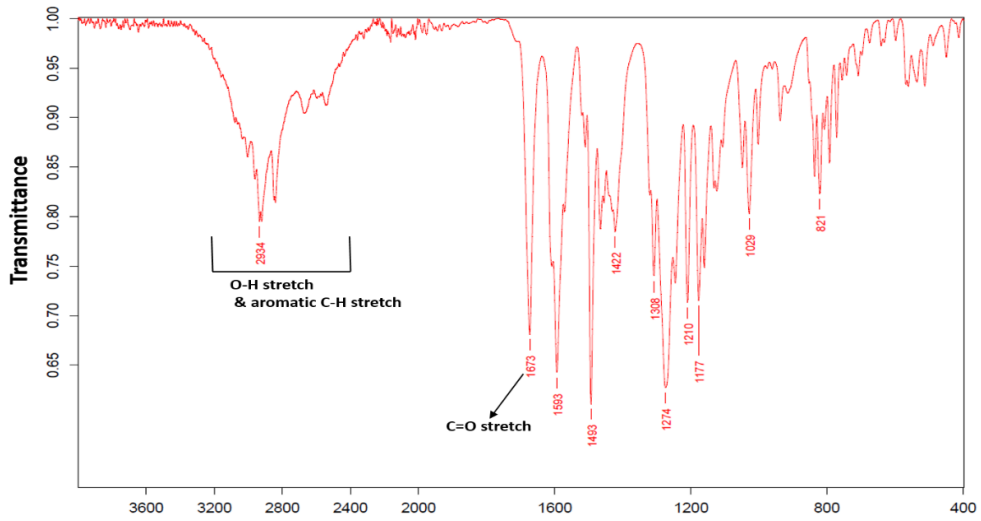

Figure A55. *ATR-IR spectrum of RC24*

Appendix

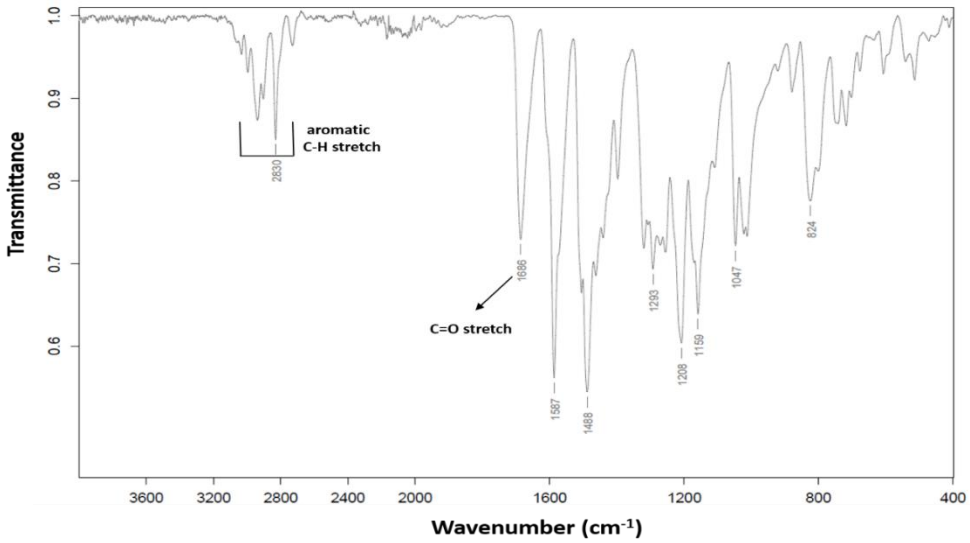

Figure A56. *ATR-IR spectrum of RC25-CHO*

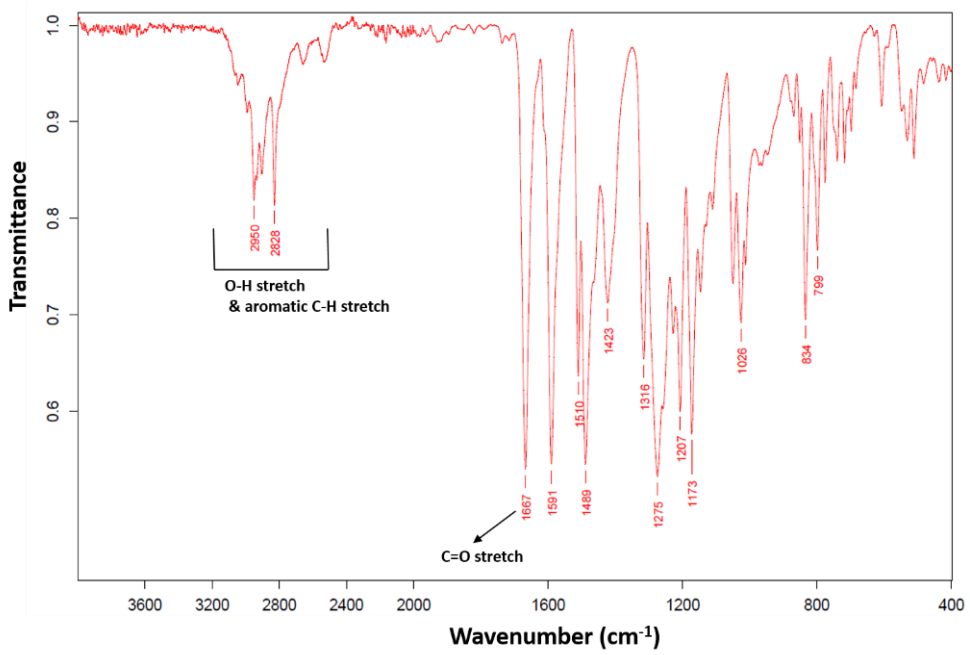

Figure A57. *ATR-IR spectrum of RC25*

Appendix

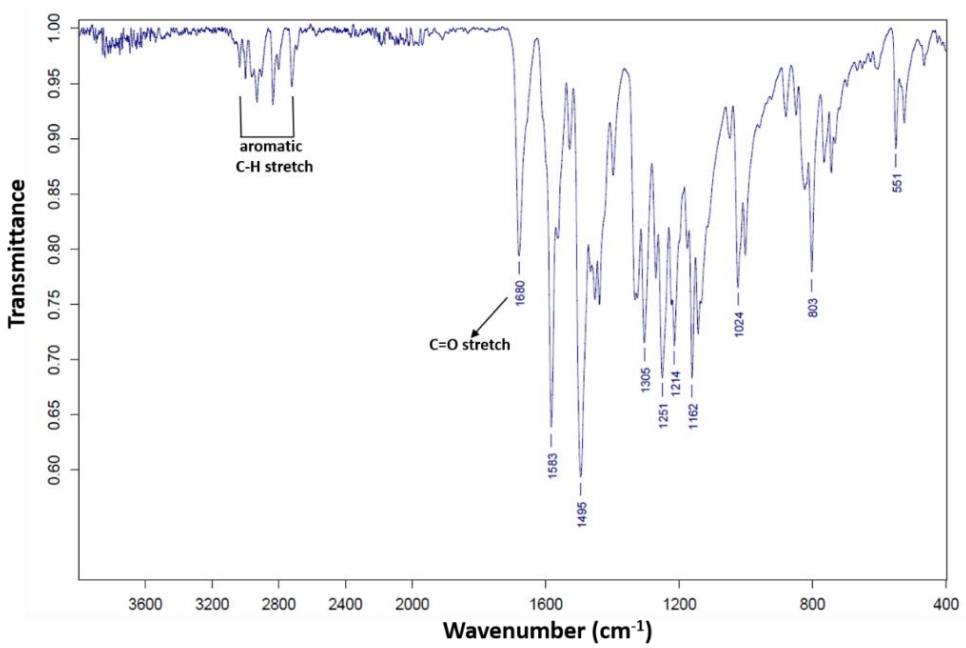

Figure A58. *ATR-IR spectrum of RC34-CHO*

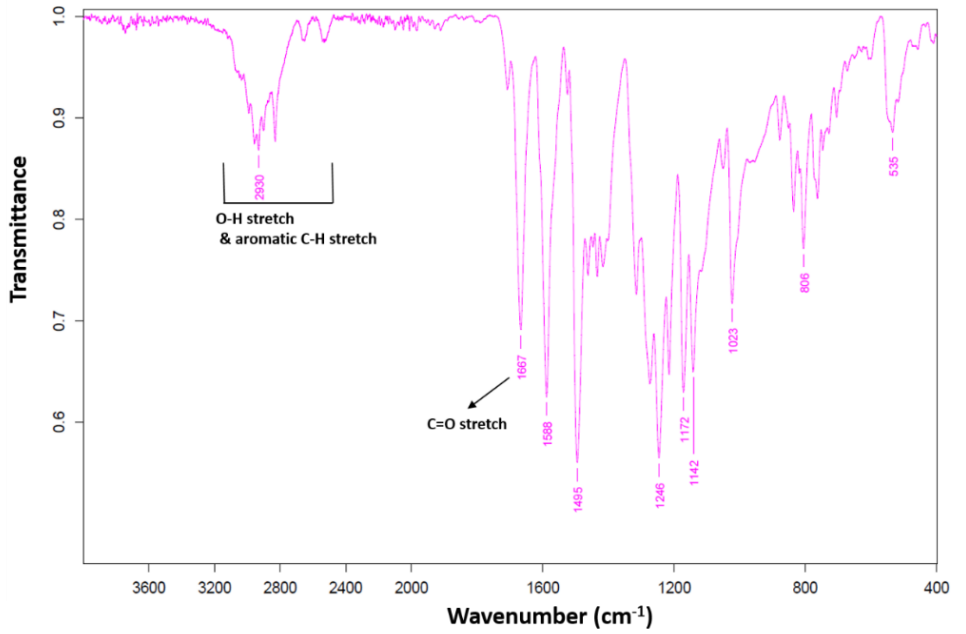

Figure A59. *ATR-IR spectrum of RC34*

Appendix

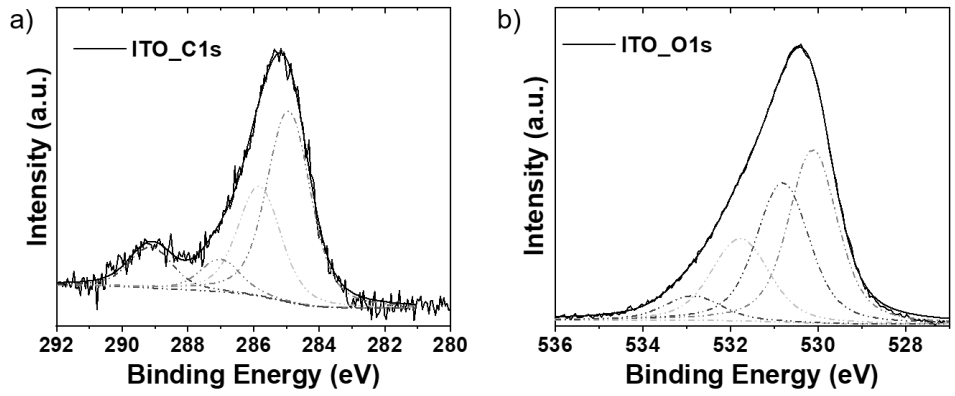

Figure A60. *The XPS high-resolution survey spectra of a) C1s and b) O1s for UV-Ozone treated ITO.*

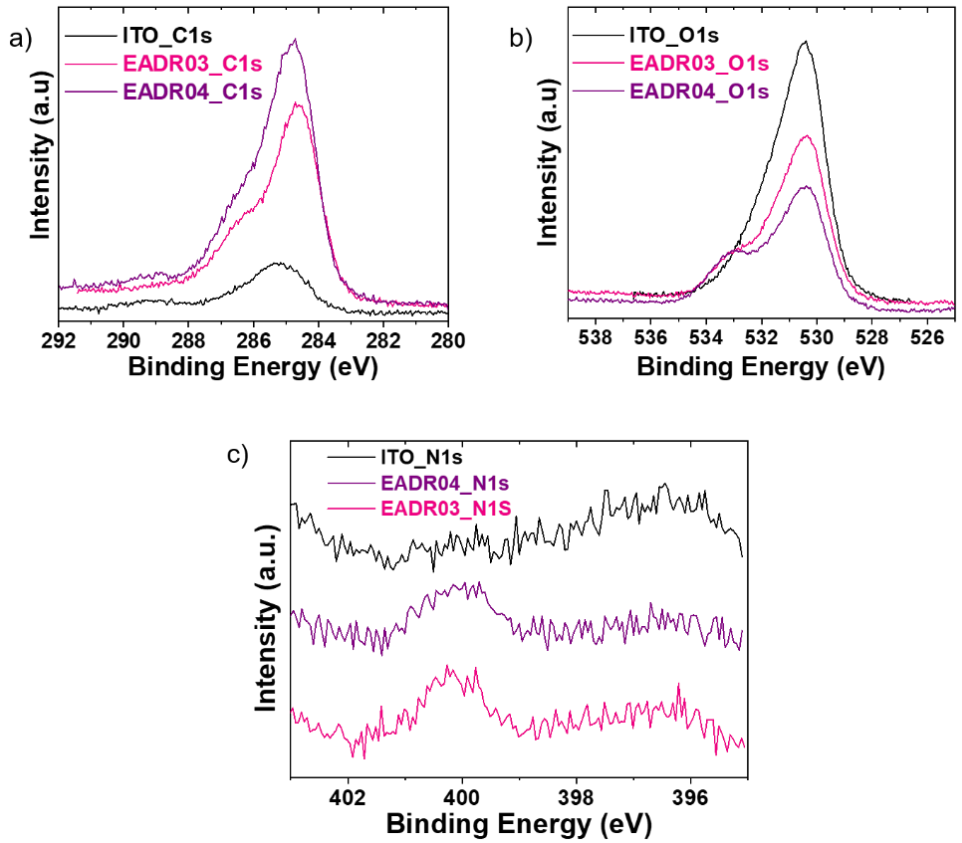

Figure A61. *The X-ray photoelectron spectroscopy at the a) C1s and b) O1s c) N1s regions of ITO glass with and without EAR03 and EADR04. The bare*

ITO has residual signals in these regions due to transferring samples between glovebox.

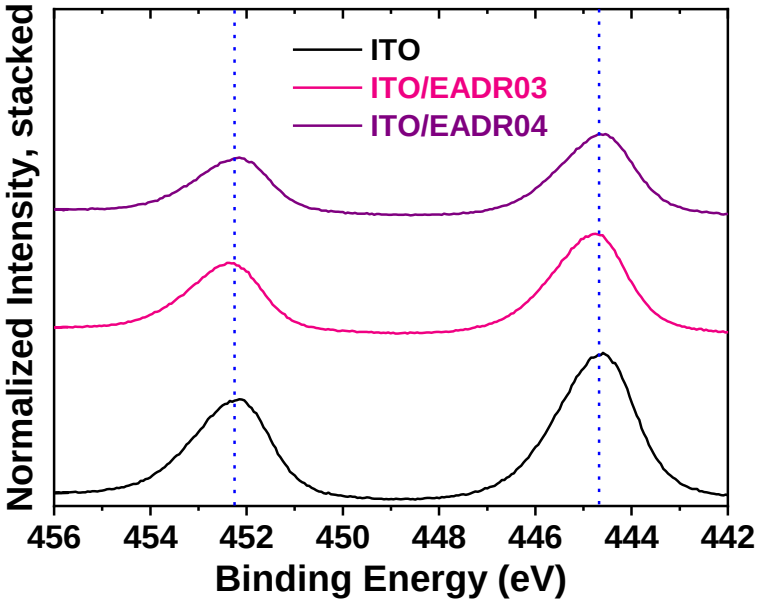

Figure A62. *The In peaks of the ITO substrates with and without EADR03 and EADR04, which are measured using XPS after finishing the UPS measurement.*

Table A. 1. *Fit results for the C1s and O1s regions*

ITO C1s

Peak	*BE (eV)*	*Intensity (a.u.)*	*Gaussian FWHM (eV)*	*Lorentzian FWHM (eV)*	*Total FWHM (eV)*
C-C/C-H	284.9	2959	0.6	1.20	1.55
C-O	285.8	1701	0.6	1.20	1.55
O-C=O att.	287.0	482	0.6	1.20	1.48
O-C=O	289.1	635	0.6	1.20	1.55

ITO O1s

Peak	*BE (eV)*	*intensity (a.u.)*	*Gaussian FWHM (eV)*	*Lorentzian FWHM (eV)*	*Total FWHM (eV)*
ITO	530.1	34747	0.6	0.95	1.31
hydroxides	530.8	29983	0.6	1.07	1.43
C=O	531.8	18990	0.6	1.20	1.55
C-O	532.9	5591	0.6	1.20	1.55

EADR03 C1s

Peak	*BE (eV)*	*Intensity (a.u.)*	*Gaussian FWHM (eV)*	*Lorentzian FWHM (eV)*	*Total FWHM (eV)*
C-C/C-H	284.6	14194	0.6	1.10	1.45
C-O	286.0	4712	0.6	1.20	1.55
O-C=O att.	287.0	1438	0.6	0.94	1.30
O-C=O	288.5	120	0.6	0.80	1.17

Appendix

EADR03 O1s

Peak	*BE (eV)*	*Intensity (a.u.)*	*Gaussian FWHM (eV)*	*Lorentzian FWHM (eV)*	*Total FWHM (eV)*
ITO	530.1	25875	0.6	1.04	1.40
hydroxides	530.9	18607	0.6	1.20	1.55
C=O	531.8	8765	0.6	1.20	1.55
C-O	533.1	7968	0.6	1.16	1.51

EADR04 C1s

Peak	*BE (eV)*	*Intensity (a.u.)*	*Gaussian FWHM (eV)*	*Lorentzian FWHM (eV)*	*Total FWHM (eV)*
C-C/C-H	284.7	17351	0.6	1.05	1.41
C-O	285.9	7293	0.6	1.20	1.55
O-C=O att.	287.0	2340	0.6	0.87	1.24
O-C=O	289.2	636	0.6	1.08	1.44

Appendix

EADR04 O1s

Peak	*BE (eV)*	*Intensity (a.u.)*	*Gaussian FWHM (eV)*	*Lorentzian FWHM (eV)*	*Total FWHM (eV)*
ITO	530.1	15265	0.6	0.96	1.32
hydroxides	530.8	17432	0.6	1.20	1.55
C=O	531.9	7454	0.6	1.20	1.55
C-O	533.2	10129	0.6	1.20	1.55

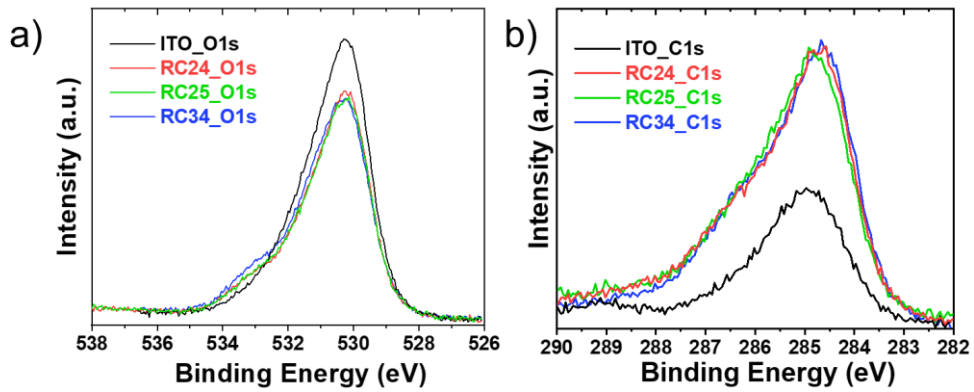

Figure A63. *The X-ray photoelectron spectroscopy at the a) C1s and b) O1s of ITO glass with and without RC24, RC25 and RC34. The bare ITO has residual signals in these regions due to transferring samples between glovebox.*

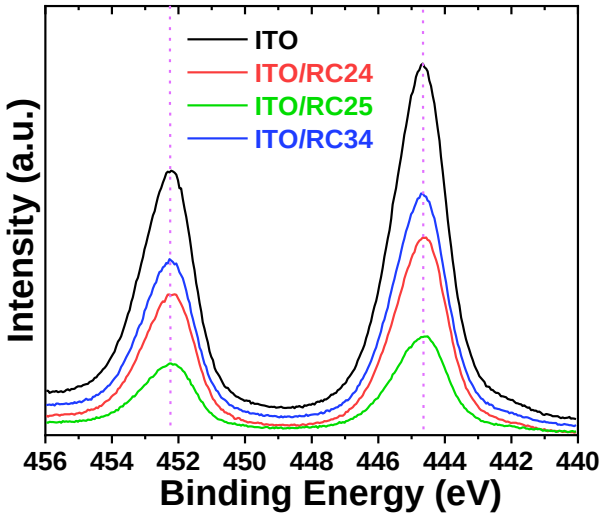

Figure A64. *The In peaks of the bare ITO glass, ITO/RC24, ITO/RC25 and ITO/RC34 substrates, which are measured using XPS after finishing the UPS measurement.*

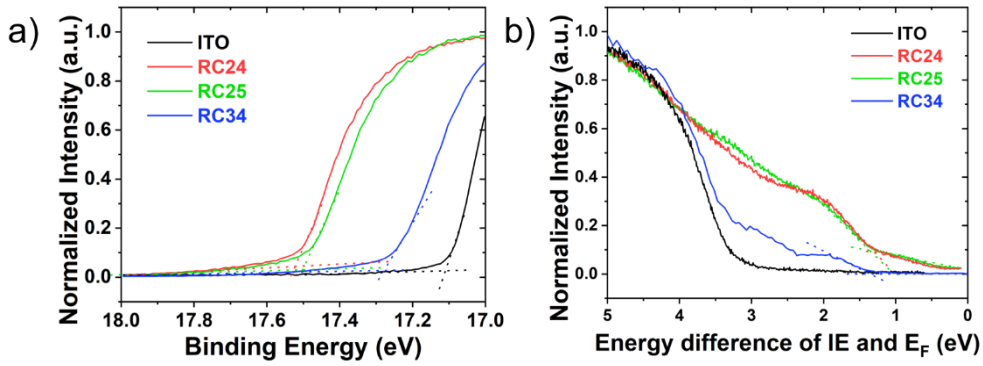

Figure A65. *Ultra-violet photoelectron spectra (UPS) of the SAMs on ITO a) the work function and b) valence band onset values are extracted for the energy band edge diagram in Fig. 1b of the main text (the excitation energy is 21.22 eV).*

Appendix

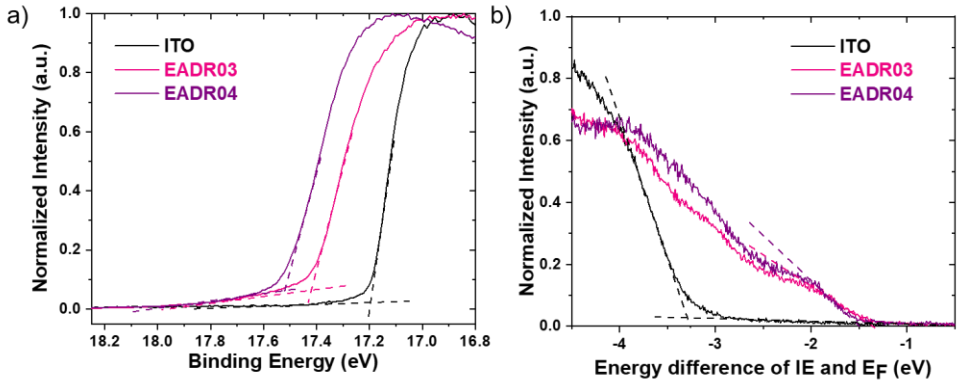

Figure A66. *UPS of the SAMs on ITO a) the work function and b) valence band onset values are extracted for the energy band edge diagram in Fig. 1b of the main text (the excitation energy is 21.22 eV).*

Table A.2. *The summarised fitting data for the C1s and O1s regions.*

RC24 C1s

Peak	*BE (eV)*	*Intensity (a.u.)*	*Gaussian FWHM (eV)*	*Lorentzian FWHM (eV)*	*Total FWHM (eV)*
C-C/C-H	284.7	1604	0.6	1.20	1.46
C-O	285.7	475	0.6	1.20	1.46
O-C=O att.	286.7	337	0.6	1.20	1.46
O-C=O	288.9	93	0.6	1.20	1.46

RC24 O1s

Peak	*BE (eV)*	*Intensity (a.u.)*	*Gaussian FWHM (eV)*	*Lorentzian FWHM (eV)*	*Total FWHM (eV)*
ITO	530.0	1518	0.6	1.20	1.46
hydroxides	530.9	663	0.6	1.20	1.46
C=O	531.8	296	0.6	1.20	1.46
C-O	533.1	200	0.6	1.20	1.46

RC25 C1s

Peak	*BE (eV)*	*Intensity (a.u.)*	*Gaussian FWHM (eV)*	*Lorentzian FWHM (eV)*	*Total FWHM (eV)*
C-C/C-H	284.8	1521	0.6	1.20	1.46
C-O	285.8	556	0.6	1.20	1.46
O-C=O att.	286.8	322	0.6	1.20	1.46
O-C=O	289.1	67	0.6	1.20	1.46

RC25 O1s

Peak	*BE (eV)*	*Intensity (a.u.)*	*Gaussian FWHM (eV)*	*Lorentzian FWHM (eV)*	*Total FWHM (eV)*
ITO	530.0	1431	0.6	1.20	1.46
hydroxides	530.9	642	0.6	1.20	1.46
C=O	531.8	295	0.6	1.20	1.46
C-O	533.0	189	0.6	1.20	1.46

Appendix

RC34 C1s

Peak	*BE (eV)*	*Intensity (a.u.)*	*Gaussian FWHM (eV)*	*Lorentzian FWHM (eV)*	*Total FWHM (eV)*
C-C/C-H	284.5	3100	0.6	1.20	1.46
C-O	285.6	1100	0.6	1.20	1.46
O-C=O att.	286.6	773	0.6	1.20	1.46
O-C=O	289.0	212	0.6	1.20	1.46

RC34 O1s

Peak	*BE (eV)*	*Intensity (a.u.)*	*Gaussian FWHM (eV)*	*Lorentzian FWHM (eV)*	*Total FWHM (eV)*
ITO	530.0	1377	0.6	1.20	1.46
hydroxides	530.9	790	0.6	1.20	1.46
C=O	531.8	309	0.6	1.20	1.46
C-O	533.0	260	0.6	1.20	1.46

Appendix

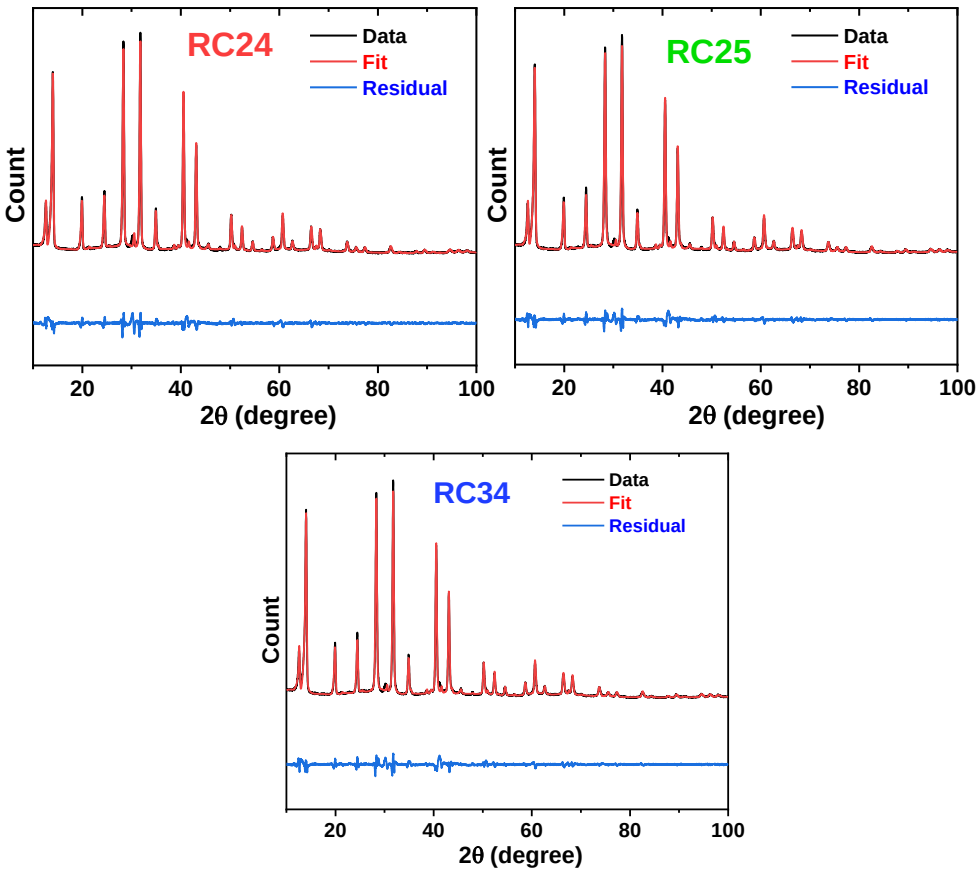

Figure A67. *Le-Bail refinement from a laboratory XRD pattern at RT of perovskite layers grown on bare ITO, ITO/RC24, ITO/RC25, and ITO/RC34.*

Appendix

UNIVERSITAT ROVIRA I VIRGILI
LOW-MOLECULAR WEIGHT MOLECULES AS SELECTIVE CONTACTS FOR PEROVSKITE SOLAR CELLS
Ece Aktaş

UNIVERSITAT ROVIRA i VIRGILI

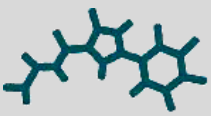

ICIQ

Institut
Català
d'Investigació
Química

HZB Helmholtz
Zentrum Berlin